

**UCLA**

**UCLA Electronic Theses and Dissertations**

**Title**

The Mechanism and Origins of Reactivities and Selectivities in Transition-metal-catalyzed and Organocatalyzed Cycloadditions

**Permalink**

<https://escholarship.org/uc/item/9dh130b7>

**Author**

Hong, Xin

**Publication Date**

2014

Peer reviewed|Thesis/dissertation

UNIVERSITY OF CALIFORNIA

Los Angeles

The Mechanism and Origins of Reactivities and Selectivities in Transition-metal-catalyzed and  
Organocatalyzed Cycloadditions

A dissertation submitted in partial satisfaction of the  
requirements for the degree Doctor of Philosophy  
in Chemistry

by

Xin Hong

2014

© Copyright by

Xin Hong

2014

## ABSTRACT OF THE DISSERTATION

The Mechanism and Origins of Reactivities and Selectivities in Transition-metal-catalyzed and Organocatalyzed Cycloadditions

by

Xin Hong

Doctor of Philosophy in Chemistry

University of California, Los Angeles, 2014

Professor Kendall N. Houk, Chair

A preeminent goal of organic synthesis is to achieve structural complexity with functional value in a step, atom, and time economical fashion. Cycloadditions, as exemplified by the Diels-Alder reaction, represent uniquely powerful processes to achieve this goal. Most of widely-used cycloadditions require transition metal or organic catalysts to achieve the desired control of reactivity and selectivity, which rely on mechanistic understandings at the molecular level. Modern density functional theory (DFT) calculations provide the foundation to achieve such level of understanding, and my PhD research focuses on studying the mechanism and selectivities of a series of important transition-metal-catalyzed and organocatalytic cycloadditions through DFT calculations.



The first part of the thesis includes my studies on the mechanism and selectivities of transition-metal-catalyzed cycloadditions. Chapter 1 focuses on the mechanism and origins of selectivities in Ru(II)-catalyzed intramolecular (5+2) cycloadditions and ene reactions of vinylcyclopropanes and alkynes. The favored mechanism involves an initial ene-yne oxidative cyclization to form a ruthenacyclopentene intermediate, which is different from that found earlier with rhodium catalysts. Based on this new mechanism, solvent effect, chemoselectivity, diastereoselectivity and regioselectivity are explained. Chapter 2 includes the study of mechanism and ligand-controlled selectivities in [Ni(NHC)]-catalyzed intramolecular (5+2) cycloadditions and homo-ene reactions of vinylcyclopropanes and alkynes. The reaction mechanism of nickel catalysts is similar to that of ruthenium catalysts, which involves the alkyne-alkene cyclization to form a metallacyclopentene intermediate. The selectivity between the (5+2) and homo-ene products is determined in the subsequent competing reductive elimination and  $\beta$ -hydride elimination steps. The anisotropic steric environments of SIPr and *It*Bu ligands are the major reasons for the reversed selectivity of these two similar-sized ligands. Chapter 3 emphasizes the study of terminal methyl effects in Rh(I)-catalyzed intermolecular (5+2) cycloadditions of vinylcyclopropanes and allenes. A competitive allene dimerization is found to irreversibly sequester the rhodium catalyst. This explains the necessity of methyl substituents on the reacting double bond of allenes to achieve the desired cycloadditions.

The second part of the thesis focuses on my studies of the organocatalyzed cycloadditions. Chapter 4 illustrates the explorations of the mechanism and controlling factors of the organocatalyzed carbonyl-olefin metathesis. In the (3+2) cycloadditions between hydrazone and alkenes, the distortion of reactants controls the reactivities. In the subsequent cycloreversions, the

strain-release of the five-membered ring intermediates determines the reaction barriers. For these two reasons, the cyclopropene derivatives are found to be the most reactive in experiments. Chapter 5 discusses the distortion-acceleration effect of alkynyl substituents in the stepwise hexadehydro-Diels-Alder (HDDA) Reaction. The HDDA reaction follows a stepwise mechanism with a diradical intermediate. The alkynyl substituent dramatically accelerates the HDDA reaction mainly by decreasing the distortion energy required to achieve the diradical transition state. Chapter 6 focuses on the mechanism and selectivity of N-triflylphosphoramidate catalyzed ( $3^++2$ ) cycloaddition between hydrazones and alkenes. The protonation of hydrazones by Brønsted acid catalysts are found to be crucial for the facile ( $3^++2$ ) cycloaddition. This explains the acidity-dependent catalytic activities of this reaction. Based on the mechanism, we have also explained the origins of enantioselectivities when a chiral N-triflylphosphoramidate catalyst is employed. Chapter 7 includes the study of mechanism and origins of switchable chemoselectivity of Ni-catalyzed C(aryl)-O and C(acyl)-O activation of aryl esters with phosphine ligands. For aryl esters, nickel with bidentate phosphine ligands cleaves C(acyl)-O and C(aryl)-O bonds via three-centered transition states, and this cleavage favors the weak C(acyl)-O bond. However, when monodentate phosphine ligands are used, the five-centered C(aryl)-O cleavage transition state makes C(aryl)-O activation favorable. In the case of aryl pivalates, nickel with bidentate phosphine ligands still favors the C(acyl)-O activation, but the subsequent decarbonylation requires very high barrier and the alternative C(aryl)-O activation occurs.

The dissertation of Xin Hong is approved.

Craig A. Merlic

Pei Yuin Keng

Kendall N. Houk, Committee Chair

University of California, Los Angeles

2014

I want to thank my mentor, Prof. Kendall N. Houk, for his guidance and support all these years. He taught me what research is and how to make contributions to society by academic research. His intelligence and diligence set the example for not only me, but the hundreds of Houk group members and all the chemists in the world.

I want to thank my parents for all their support and education in my life. They taught me right from wrong. Even though I'm more educated, I feel that it is very difficult for me to achieve their parenthood and that unconditional love, and this makes me feel incredibly lucky to be their son and spend the life with them.

I want to thank my fiancée, Yunfang, for always being there with me. She is one of the kindest people I have ever met, and her support gives me the strength to move forward. She makes me a better person and I enjoy every day with her.

I want to thank all my family members, my friends, my mentors, my collaborators, my co-workers, and my students. I cannot describe how lucky and grateful I am to have you in my life and benefit so much from you.

## TABLE OF CONTENTS

<b>ABSTRACT OF THE DISSERTATION .....</b>	<b>ii</b>
<b>TABLE OF CONTENTS .....</b>	<b>vii</b>
<b>LIST OF SCHEMES .....</b>	<b>xi</b>
<b>LIST OF FIGURES .....</b>	<b>xiv</b>
<b>LIST OF TABLES .....</b>	<b>xviii</b>
<b>ACKNOWLEDGEMENTS .....</b>	<b>xix</b>
<b>VITA.....</b>	<b>xxi</b>
<b>Chapter 1. The Mechanism and Origins of Selectivities in Ru(II)-catalyzed Intramolecular (5+2) Cycloadditions and Ene Reactions of Vinylcyclopropanes and Alkynes .....</b>	<b>1</b>
1.1 Abstract .....	1
1.2 Introduction.....	2
1.3 Computational Details .....	8
1.4 Results and Discussion .....	8
1.4.1 Metallacyclohexene Pathway vs. Metallacyclopentene Pathway .....	8
1.4.2 Acetonitrile Coordination and Solvent Effects .....	14
1.4.3 Selectivity of Cycloaddition and Ene Reaction with the <i>Trans</i> -VCP .....	18
1.4.4 Selectivity of Cycloaddition and Ene Reaction with the <i>Cis</i> -VCP .....	21
1.4.5 Origins of Diastereoselectivities .....	25
1.4.6 Origins of Regioselectivities .....	29
1.5 Conclusions.....	32
1.6 References.....	34

**Chapter 2. The Mechanism and Origins of Ligand-Controlled Selectivities in [Ni(NHC)]-catalyzed Intramolecular (5+2) Cycloadditions and Homo-Ene Reactions: A Theoretical**

**Study.....37**

2.1 Abstract..... 37

2.2 Introduction..... 38

2.3 Computational Details ..... 41

2.4 Results and Discussion ..... 42

    2.4.1 Mechanism of Formation of the Metallacyclooctadiene Intermediate.... 42

    2.4.2 Mechanism of Formation of (5+2) Cycloaddition and Homo-Ene Products 46

    2.4.3 The Catalytic Cycle..... 49

    2.4.4 Selectivities between (5+2) and Homo-Ene Products with SIPr Ligand 50

    2.4.5 Selectivities between (5+2) and Homo-Ene Products with ItBu Ligand 54

2.5 Conclusions..... 56

2.6 References..... 56

**Chapter 3. The Terminal Methyl Effects in Rh(I)-catalyzed Intermolecular (5+2) Cycloadditions of Vinylcyclopropanes: Origins of Substituent Effects on Reactivity and**

**Chemoselectivity of Allenes.....63**

3.1 Abstract..... 63

3.2 Introduction..... 64

3.3 Computational Details ..... 71

3.4 Results and Discussion ..... 72

    3.4.1 Reactions with Terminally Unsubstituted Allene ..... 72

    3.4.2 Terminal Methyl Effects on Allene Dimerization..... 76

    3.4.3 Origins of Chemoselectivities ..... 80

3.5 Conclusions.....	83
3.6 References.....	85
<b>Chapter 4. Distortion-accelerated Cycloadditions and Strain-Release-Promoted Cycloreversions in the Organocatalytic Carbonyl-Olefin Metathesis .....</b>	<b>922</b>
4.1 Abstract.....	92
4.2 Introduction.....	92
4.3 Computational Details .....	94
4.4 Results and Discussion .....	95
4.4.1 The Mechanism of Organocatalytic Carbonyl-Olefin Metathesis .....	95
4.4.2 The Distortion Control of Cycloadditions.....	98
4.4.3 The Strain-Release Control of Cycloreversions.....	102
4.5 Conclusions.....	104
4.6 References.....	105
<b>Chapter 5. Distortion-Acceleration Effect of Alkynyl Substituents in the Stepwise Hexadehydro-Diels-Alder Reaction .....</b>	<b>108</b>
5.1 Abstract.....	108
5.2 Introduction.....	108
5.3 Computational Details .....	111
5.4 Results and Discussion .....	111
5.5 Conclusions.....	117
5.6 References.....	117

## **Chapter 6. The Mechanism and Selectivity of N-triflylphosphoramidate Catalyzed (3<sup>+</sup>+2)**

### **Cycloaddition between Hydrazones and Alkenes .....122**

6.1 Abstract.....	122
6.2 Introduction.....	123
6.3 Computational Details .....	126
6.4 Results and Discussion .....	126
6.4.1 Complexation between Hydrazone and Phosphoramidate.....	126
6.4.2 Catalytic Activities of Phosphoramidate and Phosphoric Acid .....	132
6.4.3 Origins of Regioselectivity.....	135
6.4.4 Origins of Enantioselectivity.....	136
6.5 Conclusions.....	141
6.6 References.....	142

## **Chapter 7. The Mechanisms and Origins of Switchable Chemoselectivity of Ni-catalyzed**

### **C(aryl)-O and C(acyl)-O Activation of Aryl Esters with Phosphine Ligands.....147**

7.1 Abstract.....	147
7.2 Introduction.....	148
7.3 Computational Details .....	151
7.4 Results and Discussion .....	152
7.4.1 Aryl Esters of Aromatic Carboxylic Acids: Origins of Ligand-Controlled Chemoselectivity of C-O Activation.....	152
7.4.2 Aryl Pivalates: Origins of Substrate-Dependent Chemoselectivity of C-O Activation.....	161
7.5 Conclusions.....	168
7.6 References.....	169



## LIST OF SCHEMES

<b>Scheme 1.1.</b> Representative natural products and drug molecules that contain seven-membered rings.....	2
<b>Scheme 1.2.</b> General transition-metal-catalyzed intramolecular (5+2) cycloaddition of vinylcyclopropane and alkyne.....	3
<b>Scheme 1.3.</b> Proposed mechanisms for transition-metal-catalyzed (5+2) cycloadditions .....	4
<b>Scheme 1.4.</b> Ru(II)-catalyzed Alder-ene reaction and (5+2) cycloaddition.....	4
<b>Scheme 1.5.</b> Selectivity between Ru(II)-catalyzed intramolecular (5+2) cycloaddition and ene reaction of <i>trans</i> - and <i>cis</i> -VCP .....	5
<b>Scheme 1.6.</b> Selected examples of diastereoselectivities of Ru(II)-catalyzed intramolecular (5+2) cycloaddition .....	7
<b>Scheme 1.7.</b> Selected examples of regioselectivities of Ru(II)-catalyzed intramolecular (5+2) cycloaddition .....	7
<b>Scheme 1.8.</b> Metallacyclohexene and metallacyclopentene intermediates in Ru(II)-catalyzed (5+2) cycloaddition .....	9
<b>Scheme 1.9.</b> Thermodynamic equilibrium of acetonitrile coordination of ruthenium complexes that involved in the Ru(II)-catalyzed intramolecular (5+2) cycloaddition in gas phase and solution .....	17
<b>Scheme 1.10.</b> Key intermediates of (5+2) cycloaddition and ene reaction with <i>cis</i> -VCP substrate.....	23
<b>Scheme 1.11.</b> Reaction pathways that generate the <i>trans</i> - and <i>cis</i> -diastereomers of Ru(II)-catalyzed (5+2) cycloaddition .....	26
<b>Scheme 1.12.</b> Reaction pathways that cleave the more and less substituted C-C bond of cyclopropane in 1,2-disubstituted cyclopropane of Ru(II)-catalyzed (5+2) cycloaddition .....	30
<b>Scheme 2.1.</b> Postulated mechanisms for transition metal-catalyzed (5+2) cycloadditions .....	39
<b>Scheme 2.2.</b> Nickel-NHC catalyzed intramolecular (5+2) cycloaddition and homo-ene reaction of alkyne and VCP .....	40
<b>Scheme 3.1.</b> Selected examples of Rh(I)-catalyzed intramolecular ( <i>m+n</i> ) and ( <i>m+n+o</i> ) cycloadditions with allenes .....	66

<b>Scheme 3.2.</b> Examples of terminal methyl effects on allene reactivities in Rh(I)-catalyzed intermolecular cycloadditions .....	67
<b>Scheme 3.3.</b> Experimental and theoretical studies of uncatalyzed thermal dimerization of allenes.....	69
<b>Scheme 3.4.</b> Selected examples of Rh(I)-catalyzed dimerization of allenes and derived methodologies .....	69
<b>Scheme 3.5.</b> Proposed competing mechanisms for the Rh(I)-catalyzed (5+2) cycloaddition and allene dimerization with allene-yne .....	70
<b>Scheme 3.6.</b> Chemoselectivity of [Rh(CO) <sub>2</sub> Cl] <sub>2</sub> -catalyzed intermolecular (5+2) cycloaddition of VCP and allene-yne .....	71
<b>Scheme 3.7.</b> The computational model of Rh(I)-catalyzed (5+2) cycloaddition and dimerization of the terminally unsubstituted allene-yne .....	72
<b>Scheme 3.8.</b> Possible 2 $\pi$ insertion transition states in the (5+2) cycloaddition pathway with allene-yne .....	81
<b>Scheme 3.9.</b> 2 $\pi$ insertion barriers (5+2) cycloaddition pathway with different allenes, alkynes and allene-yne .....	83
<b>Scheme 4.1.</b> The (2+2) and (3+2) strategies for carbonyl-olefin metathesis .....	93
<b>Scheme 4.2.</b> Catalytic carbonyl-olefin metathesis between aldehydes and cyclopropenes and the proposed mechanism .....	94
<b>Scheme 5.1.</b> a) Formation of benzyne through the HDDA reactions and subsequent trapping reactions to generate various benzene derivatives. b) Representative substrates and conditions for the HDDA reactions.....	110
<b>Scheme 5.2.</b> Effects of the ester and alkynyl groups on the DA reactivities of dienophiles with cyclopentadiene .....	111
<b>Scheme 6.1.</b> Lewis acid and Brønsted acid facilitated enantioselective (3+2) cycloadditions between hydrazones and alkenes .....	124
<b>Scheme 6.2.</b> Proposed monopolar (3 <sup>+</sup> +2) pathway of Brønsted acid catalyzed cycloaddition between hydrazones and alkenes .....	125
<b>Scheme 6.3.</b> Experimental results and computational models of selectivities of chiral phosphoramidate catalyzed cycloaddition between hydrazone and $\alpha$ -methylstyrene .....	135
<b>Scheme 7.1.</b> Representative Reactions Involving Ni-Catalyzed C(aryl)-O Activation .....	149

<b>Scheme 7.2.</b> Chemoselectivity of Ni-Catalyzed C-O Activation of Aryl Esters with Phosphine Ligands .....	150
<b>Scheme 7.3.</b> Proposed Mechanisms for Ni-Catalyzed C-O Activation of Aryl Esters and Subsequent C-C Coupling with Azoles .....	151
<b>Scheme 7.4.</b> DFT-Computed Gibbs Free Energies for Reaction Using Naphthalen-2-yl Pivalate.....	165
<b>Scheme 7.5.</b> Comparisons of Reaction Free Energies of Decarbonylation Involving Benzoate and Pivalate .....	168

## LIST OF FIGURES

<b>Figure 1.1.</b> Free energy profiles of metallacyclohexene and metallacyclopentene pathways in Ru(II)-catalyzed (5+2) cycloaddition.....	10
<b>Figure 1.2.</b> Optimized structures of intermediates and transition states in metallacyclohexene and metallacyclopentene pathways of Ru(II)-catalyzed (5+2) cycloaddition. ....	12
<b>Figure 1.3.</b> Optimized structures of intermediates and transition states in metallacyclohexene and metallacyclopentene pathways of Ru(II)-catalyzed (5+2) cycloaddition .....	13
<b>Figure 1.4.</b> Free energy profiles of metallacyclopentene pathway with (blue) and without acetonitrile coordination (black) in Ru(II)-catalyzed intramolecular (5+2) cycloaddition with VCP and alkyne .....	15
<b>Figure 1.5.</b> Optimized structures of intermediates and transition states with additional acetonitrile coordination in metallacyclopentene pathways of Ru(II)-catalyzed intramolecular (5+2) cycloaddition .....	16
<b>Figure 1.6.</b> Free energy profiles of metallacyclopentene pathway with (blue) and without acetonitrile coordination in Ru(II)-catalyzed (5+2) cycloaddition .....	18
<b>Figure 1.7.</b> Free energy profiles of reductive elimination and $\beta$ -hydride elimination in Ru(II)-catalyzed (5+2) cycloaddition with <i>trans</i> -VCP .....	20
<b>Figure 1.8.</b> Free energies and structures of selectivity determining transition states in <i>trans</i> -VCP .....	21
<b>Figure 1.9.</b> Free energy profiles of reductive elimination and $\beta$ -hydride elimination in Ru(II)-catalyzed (5+2) cycloaddition with the <i>cis</i> -VCP .....	24
<b>Figure 1.10.</b> Optimized structures, Newman projection of C5-C6 and relative Gibbs free energies of intermediate <b>22</b> and <b>22-C2</b> .....	25
<b>Figure 1.11.</b> Optimized structures and relative Gibbs free energies of diastereomeric oxidative cyclization post-intermediates with various allylic substituents in Ru(II)-catalyzed (5+2) cycloaddition .....	29
<b>Figure 1.12.</b> Optimized structures and relative Gibbs free energies of cyclopropane cleavage transition states in Ru(II)-catalyzed (5+2) cycloaddition with <i>trans</i> - and <i>cis</i> -1,2-disubstituted cyclopropanes .....	32
<b>Figure 2.1.</b> Gibbs free energies for [Ni(NHC)]-catalyzed cycloaddition from substrate coordinated complex to metallacyclooctadiene intermediate.....	42
<b>Figure 2.2.</b> Optimized structures and bond distances of selected intermediates and transition states in Figure 2.1.....	45

<b>Figure 2.3.</b> Gibbs free energies of the [Ni(NHC)]-catalyzed (5+2) cycloaddition and homo-ene reaction from the metallacyclooctadiene intermediate <b>14</b> .....	46
<b>Figure 2.4.</b> Optimized structures and bond distances of selected intermediates and transition states in Figure 2.3.....	48
<b>Figure 2.5.</b> Gibbs free energies of preferred mechanism for [Ni(NHC)]-catalyzed (5+2) cycloaddition and homo-ene reaction .....	49
<b>Figure 2.6.</b> Optimized transition structures of Me and TMS substituted <b>TS21</b> and <b>TS23</b> with the SIPr ligand.....	53
<b>Figure 2.7.</b> Optimized transition structures of <i>t</i> -Bu substituted <b>TS21</b> and <b>TS23</b> with the <i>It</i> Bu ligand.....	55
<b>Figure 3.1.</b> Free energy surface of favored pathways of [Rh(CO) <sub>2</sub> Cl] <sub>2</sub> -catalyzed (5+2) cycloaddition and allene dimerization with terminally unsubstituted allene-yne .....	73
<b>Figure 3.2.</b> Optimized structures of selected intermediates and transition states in the favored pathways of [Rh(CO) <sub>2</sub> Cl] <sub>2</sub> -catalyzed (5+2) cycloaddition and allene dimerization with terminally unsubstituted allene-yne .....	75
<b>Figure 3.3.</b> Free energy surface of [Rh(CO) <sub>2</sub> Cl] <sub>2</sub> -catalyzed (5+2) cycloaddition and allene dimerization with dimethyl-substituted allene-yne .....	77
<b>Figure 3.4.</b> Transition states of [Rh(CO) <sub>2</sub> Cl]-catalyzed dimerization of allene-ynes .....	79
<b>Figure 4.1.</b> DFT-computed Gibbs free energies for the ring-opening metathesis of cyclopropene with benzaldehyde using hydrazine catalyst .....	97
<b>Figure 4.2.</b> The (3+2) cycloaddition transition states <i>E</i> - <b>TS12</b> and <i>Z</i> - <b>TS12</b> and the cycloreversion transition state <b>TS15</b> .....	98
<b>Figure 4.3.</b> Optimized transition-state structures of the (3+2) cycloadditions of various alkenes with <i>E</i> - <b>10</b> and the corresponding retro-(3+2) cycloadditions.....	99
<b>Figure 4.4.</b> Plot of activation free energy $\Delta G_{\text{act}}$ for cycloadditions versus strain release $\Delta E_{\text{strain}}$ .....	101
<b>Figure 4.5.</b> Plot of activation free energy $\Delta G_{\text{act}}$ for cycloadditions versus distortion energy $\Delta E_{\text{dist}}$ .....	102
<b>Figure 4.6.</b> Plot of activation free energy $\Delta G_{\text{act}}$ for cycloreversions versus strain release $\Delta E_{\text{strain}}$ .....	103
<b>Figure 5.1.</b> (U)M06-2X/6-311+G(d,p)-optimized transition-state structures for the stepwise or concerted HDDA reactions of butadiyne with dienophiles .....	112

<b>Figure 5.2.</b> M06-2X/6-311+G(d,p)-optimized transition-state structures for the concerted DA reactions of butadiene with ethene and cyclopentadiene with dienophiles .....	113
<b>Figure 6.1.</b> Optimized structures and Gibbs free energies of complexes between hydrazone and phosphoramidate.....	128
<b>Figure 6.2.</b> Optimized structures and Gibbs free energies of (3+2) cycloaddition transition states between the hydrazone-phosphoramidate complexes and ethylenes .....	130
<b>Figure 6.3.</b> Free energy changes of the phosphoramidate catalyzed monopolar (3 <sup>+</sup> +2) cycloaddition pathway and the 1, 3-dipolar cycloaddition pathway between hydrazone and ethylene .....	131
<b>Figure 6.4.</b> Free energy changes and distortion/interaction analysis of transition states of phosphoramidate and phosphoric acid catalyzed (3+2) cycloadditions between hydrazone and ethylene .....	134
<b>Figure 6.5.</b> Transition states and relative Gibbs free energies of phosphoramidate catalyzed cycloaddition between hydrazone and $\alpha$ -methylstyrene .....	136
<b>Figure 6.6.</b> Optimized structures and relative stabilities of chiral N-triflylphosphoramidate anion and anion-hydrazone complex .....	139
<b>Figure 6.7.</b> Optimized structures and relative stabilities of chiral N-triflylphosphoramidate catalyzed (3+2) cycloaddition transition states between hydrazone and $\alpha$ -methylstyrene .....	140
<b>Figure 7.1.</b> DFT-computed Gibbs free energies for the Ni/dcype-catalyzed decarbonylative C-C coupling of benzoxazole and phenyl benzoate .....	154
<b>Figure 7.2.</b> DFT-optimized structures of selected intermediates and transition states for the Ni/dcype-catalyzed decarbonylative C-C coupling of benzoxazole and phenyl benzoate .....	155
<b>Figure 7.3.</b> DFT-computed Gibbs free energies for the Ni/dcype-catalyzed C(acyl)-O and C(aryl)-O activation pathways of phenyl benzoate .....	156
<b>Figure 7.4.</b> The distortion/interaction analysis of the C(aryl)-O and C(acyl)-O activation transition states involving the Ni/dcype catalyst .....	158
<b>Figure 7.5.</b> DFT-computed Gibbs free energies for the Ni/PCy <sub>3</sub> -catalyzed C(acyl)-O and C(aryl)-O activation pathways of phenyl benzoate .....	160
<b>Figure 7.6.</b> The distortion/interaction analysis of the C(aryl)-O and C(acyl)-O activation transition states involving the Ni/PCy <sub>3</sub> catalyst .....	161
<b>Figure 7.7.</b> DFT-computed Gibbs free energies for the Ni/dcype-catalyzed C-C coupling between benzoxazole and phenyl pivalate .....	162

**Figure 7.8.** DFT-optimized structures of selected intermediates and transition states for the C(acyl)-O and C(aryl)-O activation pathways of the Ni/dcype-catalyzed C-C coupling between benzoxazole and phenyl pivalate.....163

**Figure 7.9.** DFT-computed Gibbs free energies for the Ni/dcype-catalyzed decarbonylative C-C coupling of benzoxazole and phenyl pivalate .....166

## LIST OF TABLES

<b>Table 1.1.</b> Gibbs free energies of key intermediates and transition states that generate the <i>trans</i> - and <i>cis</i> -diastereomeric cycloadducts in Ru(II)-catalyzed (5+2) cycloadditions with various allylic substituents .....	28
<b>Table 1.2.</b> Gibbs free energies of key intermediates and transition states that undergo the cleavage A and cleavage B pathways in Ru(II)-catalyzed (5+2) cycloadditions with <i>trans</i> - and <i>cis</i> -1,2-disubstituted cyclopropanes.....	31
<b>Table 2.1</b> Theoretical and experimental selectivities between triene and cycloheptadiene with SIPr and <i>i</i> TBu ligands and substrates with various terminal substituents .....	51
<b>Table 4.1</b> Activation free energy ( $\Delta G_{\text{act}}$ ) and reaction free energy ( $\Delta G_{\text{rxn}}$ ) for the (3+2) cycloadditions of hydrazonium with various alkenes in dichloroethane, the strain release ( $\Delta E_{\text{strain}}$ ) from the alkene to the corresponding alkane, and the transition-state distortion energy ( $\Delta E_{\text{dist}}$ ).....	101
<b>Table 4.2.</b> Activation free energy ( $\Delta G_{\text{act}}$ ) and reaction free energy ( $\Delta G_{\text{rxn}}$ ) for the (3+2) cycloreversions in dichloroethane and the strain release ( $\Delta E_{\text{strain}}$ ) of the alkane moiety from the alkene .....	104
<b>Table 5.1.</b> (U)M06-2X/6-311+G(d,p)-computed activation, distortion, and interaction energies.....	114



## ACKNOWLEDGEMENTS

### Chapter 1

This chapter is a version of:

Hong, X.; Trost, B. M.; Houk, K. N. *J. Am. Chem. Soc.* **2013**, *135*, 6588.

Permission was given for use of this work in this thesis.

### Chapter 2

This chapter is a version of:

Hong, X.; Liu, P.; Houk, K. N. *J. Am. Chem. Soc.* **2013**, *135*, 1456.

Permission was given for use of this work in this thesis.

### Chapter 4

This chapter is a version of:

Hong, X.; Liang, Y.; Griffith, A. K.; Lambert, T. H.; Houk, K. N. *Chem. Sci.* **2014**, *5*, 471.

Permission was given for use of this work in this thesis.

### Chapter 7

This chapter is a version of:

Hong, X.; Liang, Y.; Houk, K. N. *J. Am. Chem. Soc.* **2014**, *136*, 2017.

Permission was given for use of this work in this thesis.

## **Funding**

This work was supported by the National Science Foundation (CHE-0548209 and CHE-1059084). Computer time was provided in part by the UCLA Institute for Digital Research and Education (IDRE) Hoffman2 cluster, and the Extreme Science and Engineering Discovery Environment (XSEDE), which is supported by the NSF (OCI-1053575).



# Chapter 1. The Mechanism and Origins of Selectivities in Ru(II)-catalyzed Intramolecular (5+2) Cycloadditions and Ene Reactions of Vinylcyclopropanes and Alkynes

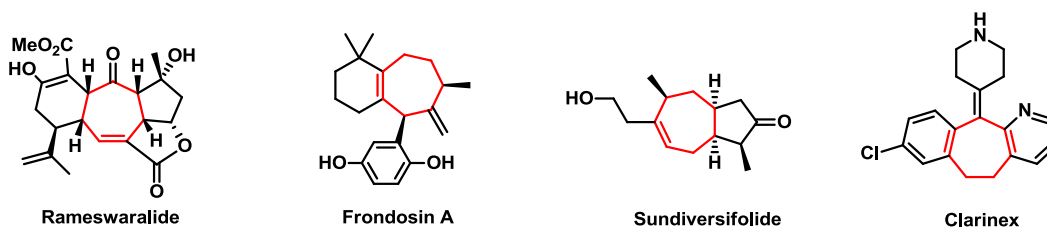
## 1.1 Abstract

The mechanism, solvent effects and origins of selectivities in Ru(II)-catalyzed intramolecular (5+2) cycloaddition and ene reaction of vinylcyclopropanes (VCP) and alkynes have been studied using density functional theory. B3LYP/6-31G(d)/LANL2DZ optimized structures were further evaluated with the M06 functional, 6-311+G(2d,p) and LANL2DZ basis sets and the SMD solvent model. The favored mechanism involves an initial ene-yne oxidative cyclization to form a ruthenacyclopentene intermediate. This mechanism is different from that found earlier with rhodium catalysts. The subsequent  $\beta$ -hydride elimination and cyclopropane cleavage are competitive, determining the experimental selectivity. In *trans*-VCP, the cyclopropane cleavage is intrinsically favored and leads to the (5+2) cycloaddition product. Although the same intrinsic preferences occur with the *cis*-VCP, an unfavorable rotation is required in order to generate the *cis*-double bond in seven-membered ring product, which reverses the selectivity. Acetone solvent is found to facilitate the acetonitrile dissociation from the precatalyst, destabilizing the resting state of the catalyst and leading to a lower overall reaction barrier. In addition, the origins of diastereoselectivities that allylic hydroxyl group is *trans* to the bridgehead hydrogen are found to be the electrostatic interactions. In the pathway that generates the favored diastereomer, the oxygen lone pairs from the substituent are closer to the cationic catalyst center and provide stabilizing electrostatic interactions. Similar pathways also determine the regioselectivities that whether the more or less substituted C-C bond of cyclopropane is cleaved. In the *trans*-1,2-disubstituted cyclopropane substrate, the substituent from the cyclopropane is away from the reaction center in

both pathways and low regioselectivity is found. In contrast, the cleavage of the more substituted C-C bond of the *cis*-1,2-disubstituted cyclopropane has steric repulsions from the substituent and thus higher regioselectivity is found.

## 1.2 Introduction

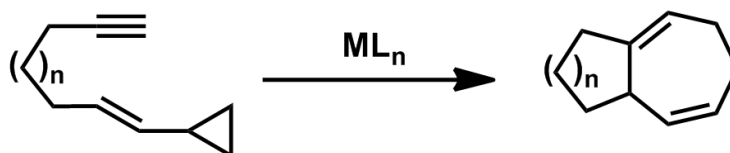
Seven-membered carbocycles are presented in many natural products and drugs and have been targets for a number of synthetic studies (Scheme 1.1).<sup>1</sup> The synthesis of seven-membered rings often requires ring-closing bond formation or ring expansion reactions.<sup>2</sup> These transformations typically need multi-step synthesis of precursor and thus difficult to achieve atom and step economy as well as application in total synthesis of fused ring systems.



**Scheme 1.1.** Representative natural products and drug molecules that contain seven-membered rings.

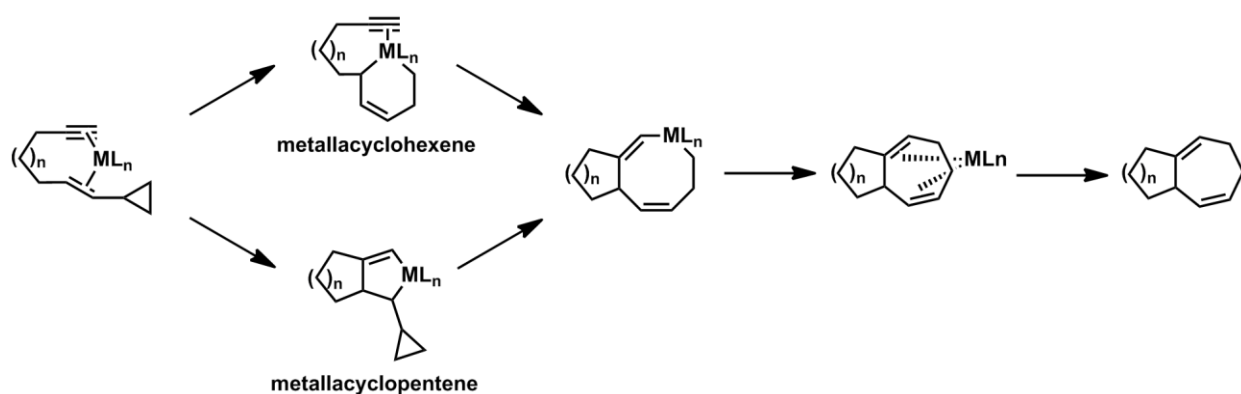
Although the synthesis of seven-membered ring still lags behind that for smaller rings (especially for catalytic and intermolecular reactions), remarkable progress has been made.<sup>3</sup> As a homolog of the Diels-Alder (4+2) cycloaddition, transition-metal-catalyzed (5+2) cycloaddition of vinylcyclopropanes (VCPs) and  $2\pi$  components provides a practical and efficient way for functionalized seven-membered ring formation (Scheme 1.2).<sup>4</sup> In 1995, the Wender group reported the first examples of intramolecular (5+2) cycloaddition of VCPs catalyzed by  $[\text{Rh}(\text{Cl})(\text{PPh}_3)_3]$

and successfully applied this methodology with various catalysts, VCPs and substrates.<sup>5</sup> The (5+2) cycloaddition has also provided a conceptual foundation and led to the application in total synthesis<sup>6</sup> and the discovery of many new cycloaddition reactions such as (5+2+1),<sup>7</sup> (5+1+2+1),<sup>8</sup> (3+2),<sup>9</sup> and (5+1)<sup>10</sup> reactions.



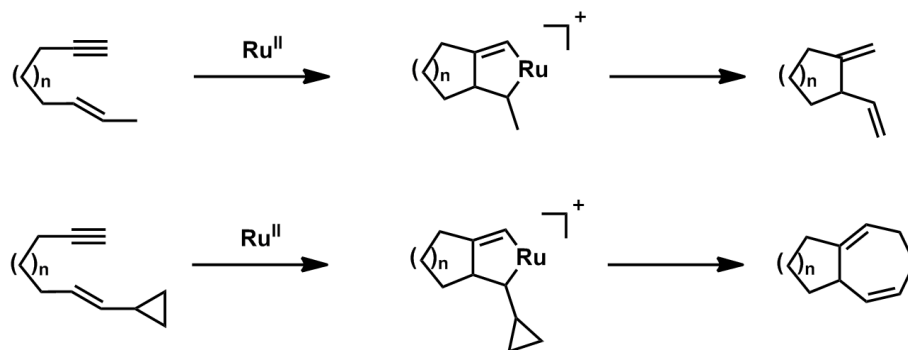
**Scheme 1.2.** General transition-metal-catalyzed intramolecular (5+2) cycloaddition of vinylcyclopropane and alkyne.

There are two general mechanisms proposed for the transition-metal-catalyzed (5+2) cycloaddition (Scheme 1.3). One involves the formation of a metallacyclohexene intermediate followed by the  $2\pi$  insertion and reductive elimination. The other proceeds through the oxidative cyclization followed by the cyclopropane cleavage and reductive elimination. Our previous theoretical studies have revealed that the metallacyclohexene pathway is preferred with rhodium catalysts and the rate-determining step is the  $2\pi$  insertion to form the metallacyclooctadiene intermediate.<sup>11</sup> Later experimental and theoretical collaborations demonstrated a delicate electronic and steric control of regioselectivities in Rh(I)-catalyzed (5+2) cycloadditions.<sup>12</sup>



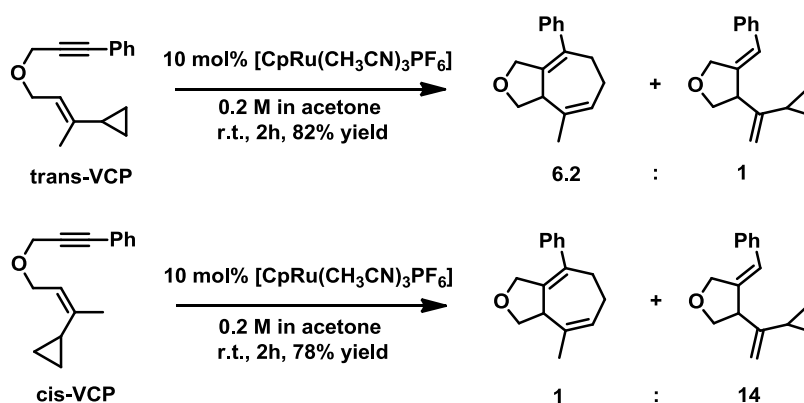
**Scheme 1.3.** Proposed mechanisms for transition-metal-catalyzed (5+2) cycloadditions.

Inspired by the Rh(I)-catalyzed (5+2) cycloaddition and Ru(II)-catalyzed Alder-ene reaction,<sup>13</sup> Trost proposed a Ru(II)-catalyzed (5+2) cycloaddition involving a ruthenacyclopentene intermediate (Scheme 1.4).<sup>14</sup> By replacing the terminal methyl group of the alkene with cyclopropane, a ruthenacyclopentene intermediate could be generated and lead to a seven-membered ring product by ring expansion. This chemical transformation was indeed achieved by  $[\text{CpRu}(\text{CH}_3\text{CN})_3\text{PF}_6]$  catalyst, the same complex that catalyzes the alkene-alkyne coupling.<sup>15</sup> Later, Trost et al. systematically studied the scope of this reaction including the functional group tolerance, the type and length of the tether between alkyne and VCP, and the substituent effects on the regio- and diastereoselectivities.<sup>14(d)</sup>



**Scheme 1.4.** Ru(II)-catalyzed Alder-ene reaction and (5+2) cycloaddition.

The preliminary experimental studies of mechanism pointed to the metallacyclopentene intermediate, and the discovery of the  $\beta$ -hydride elimination side product also supported the hypothesis of the ruthenacyclopentene intermediate (Scheme 1.5).<sup>14(d)</sup> The  $\beta$ -hydride elimination product is quite common in Ru(II)-catalyzed (5+2) cycloaddition if the internal alkene carbon of VCP contains a substituent with  $\alpha$ -hydrogen, and the selectivity between (5+2) cycloaddition and ene reaction relies heavily on the substrates. The *trans*-VCP favors the (5+2) cycloaddition and the *cis*-VCP favors the ene reaction (Scheme 1.5). Although the metallacyclopentene intermediate is achievable with ruthenium catalysts, the same ruthenium catalyst is also known to catalyze the vinylcyclopropane cleavage under similar conditions.<sup>16</sup> Therefore, the ruthenacyclohexene intermediate might still compete with the ruthenacyclopentene intermediate. To understand the detailed mechanism of Ru(II)-catalyzed (5+2) cycloaddition was a principal goal of this work.



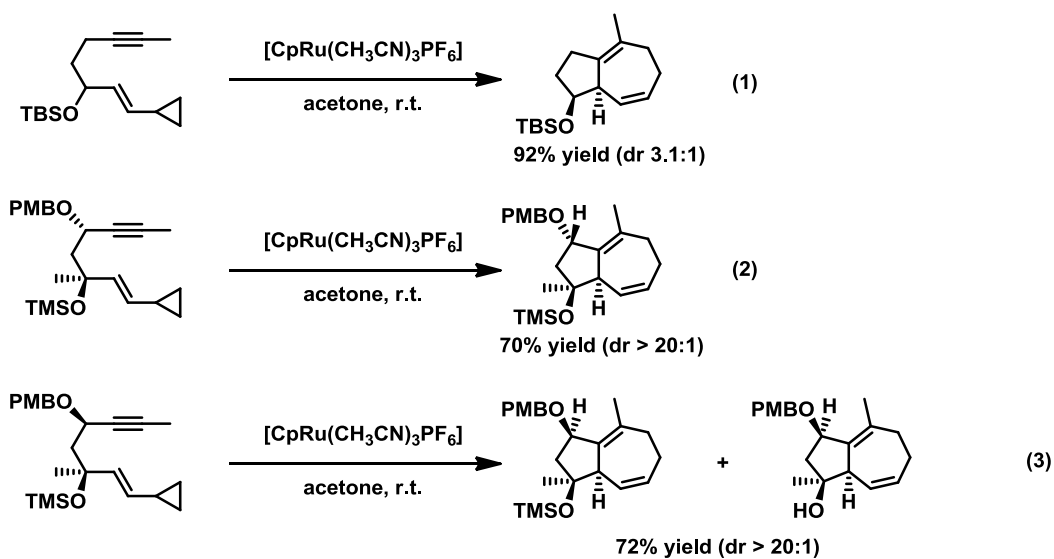
**Scheme 1.5.** Selectivity between Ru(II)-catalyzed intramolecular (5+2) cycloaddition and ene reaction of *trans*- and *cis*-VCP.

In addition to the questions of mechanism, distinct solvent effect was found experimentally: the reaction requires a polar solvent, and acetone was found especially effective.<sup>14(d)</sup> Does acetone just provide a polar solvent environment that facilitates the catalytic transformation or is the

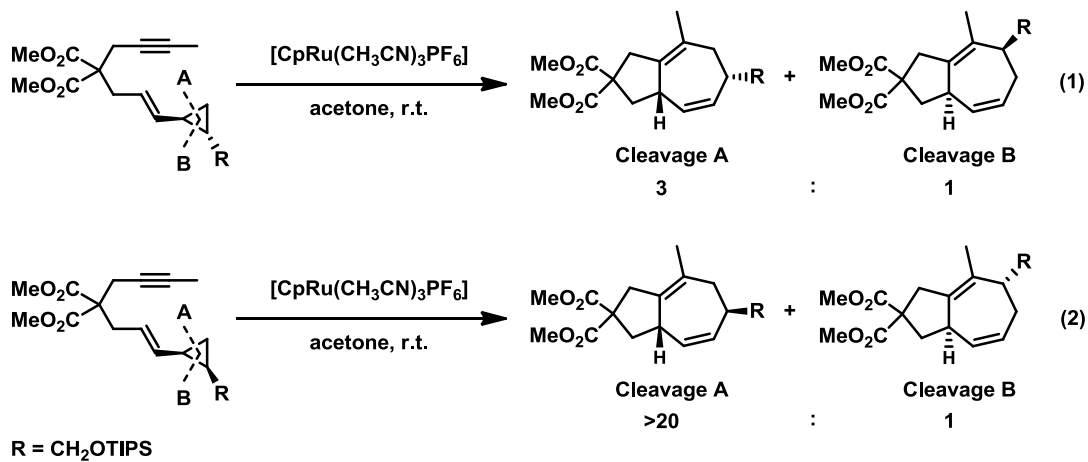


acetone acting as a ligand? Is acetone stabilizing the rate-determining transition state or destabilizing the resting state to lower the overall reaction barrier? Although solvent effect is very crucial and common in transition-metal-catalyzed reactions, there is not a thorough understanding of such effects.

Diastereo- and regioselectivities are also intriguing: (1) the stereochemistry of allylic substituents in the tether strongly affects the created bridgehead stereogenic center. In all investigated cases, the allylic hydroxyl group is *trans* to the bridgehead hydrogen and disubstitution on allylic position increases the diastereoselectivities (Scheme 1.6). (2) the *trans*-1,2-disubstituted cyclopropane has a small preference to cleave the less substituted C-C bond and the regioselectivity increases dramatically in the *cis*-disubstituted cyclopropane (Scheme 1.7). What are the origins of the diastereo- and regioselectivities? In order to understand the above questions, we used density functional theory (DFT) calculations to explore the mechanism, solvent effects and the origins of selectivities involved in Ru(II)-catalyzed intramolecular (5+2) cycloaddition and ene reaction between vinylcyclopropanes and alkynes.



**Scheme 1.6.** Selected examples of diastereoselectivities of Ru(II)-catalyzed intramolecular (5+2) cycloaddition.



**Scheme 1.7.** Selected examples of regioselectivities of Ru(II)-catalyzed intramolecular (5+2) cycloaddition.

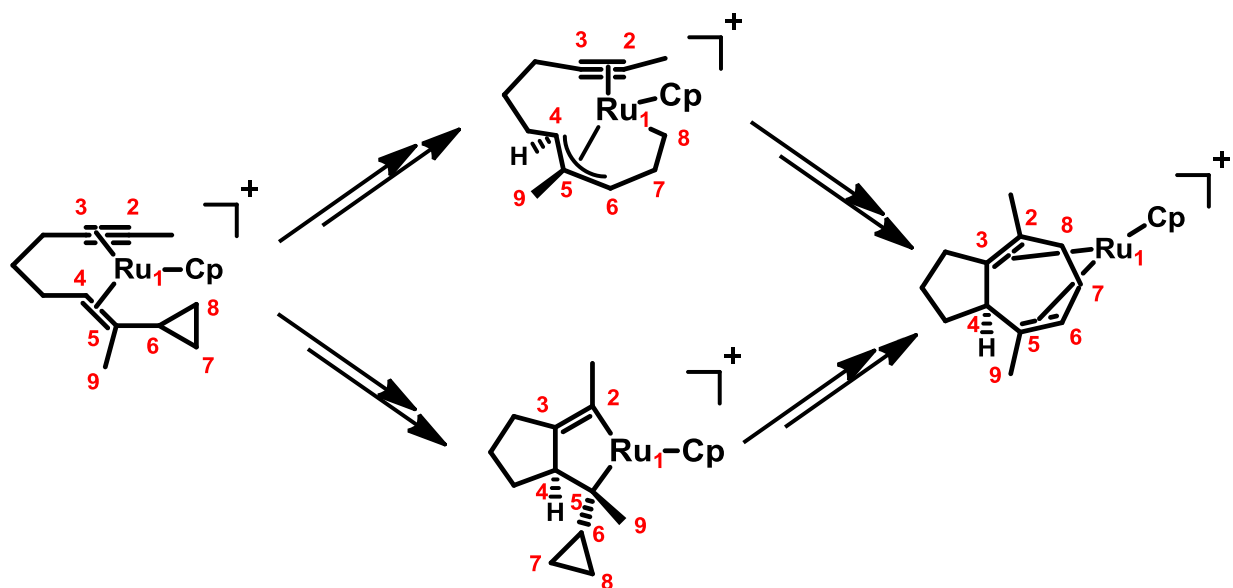
### **1.3 Computational Details**

Geometry optimizations, frequencies, and thermal energy corrections were performed with the B3LYP functional, 6-31G(d) basis set for all main group elements and LANL2DZ basis set for ruthenium implemented in Gaussian 09.<sup>17</sup> Energies were evaluated with the M06 method,<sup>18</sup> the 6-311+G(2d,p) basis set for all main group elements and LANL2DZ basis set for ruthenium. All reported free energies involve zero-point vibrational energy corrections and thermal corrections to Gibbs free energy at 298 K. The solvation free energy corrections were computed with SMD model on gas-phase optimized geometries and acetone was chosen as the solvent for consistency with the experiment. Computed structures are illustrated using CYLVIEW drawings.<sup>19</sup>

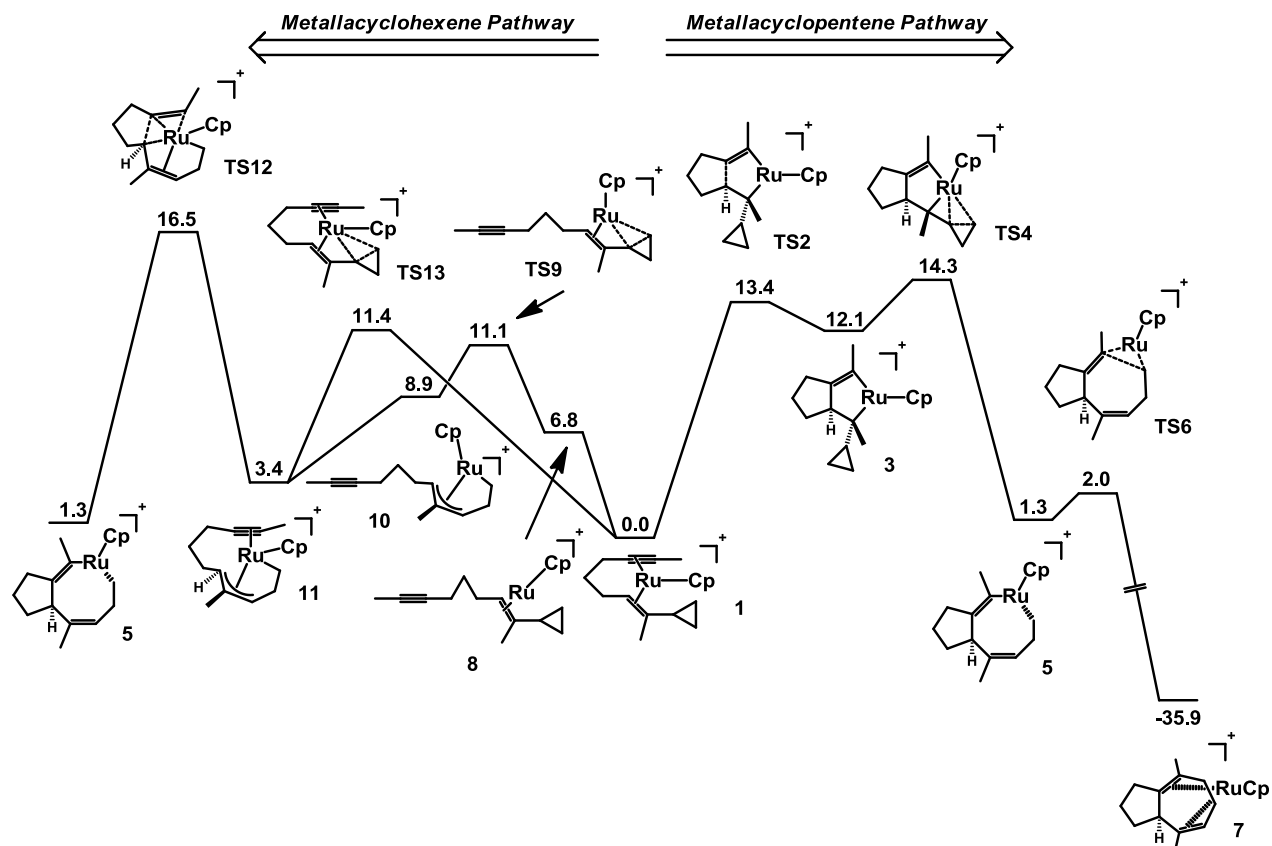
### **1.4 Results and Discussion**

#### **1.4.1 Metallacyclohexene Pathway vs. Metallacyclopentene Pathway**

To study the feasibility of metallacyclohexene and metallacyclopentene pathways, we first calculated the free energy profiles of both pathways starting from the substrate coordinated complex to the seven-membered ring product coordinated complex (atom labeling is shown in Scheme 1.8, detailed free energy profiles are provided in Figure 1 and optimized structures are shown in Figure 1.2 and 1.3).



**Scheme 1.8.** Metallacyclohexene and metallacyclopentene intermediates in Ru(II)-catalyzed (5+2) cycloaddition.



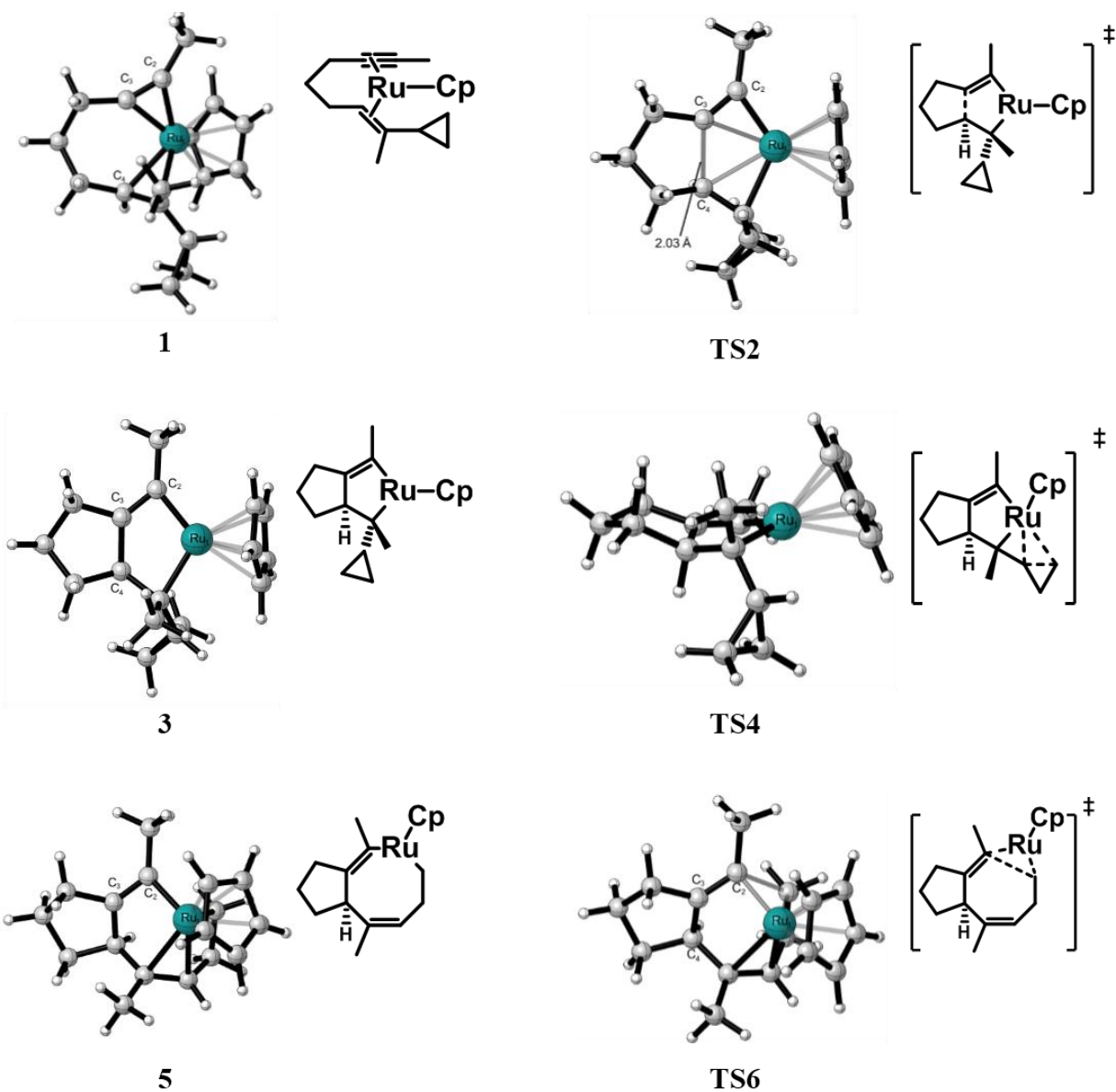
**Figure 1.1.** Free energy profiles of metallacyclohexene and metallacyclopentene pathways in Ru(II)-catalyzed (5+2) cycloaddition.

Complex **1** can undergo the metallacyclopentene pathway with an initial ene-yne oxidative cyclization via **TS2** (13.4 kcal/mol). From intermediate **3** (12.1 kcal/mol), the cyclopropane cleavage could occur with a 2.2 kcal/mol barrier (**TS4**) to give the ruthenacyclooctadiene intermediate **5** (1.3 kcal/mol). The overall barrier of ruthenacyclopentene pathway from complex **1** is 14.3 kcal/mol, and the rate determining step is the cyclopropane cleavage step with **TS4**. This conclusion is consistent with the studies of the alkene-alkyne coupling where formation of the ruthenacyclopentene is reversible and the product determining step is the  $\beta$ -hydrogen insertion.<sup>13</sup>

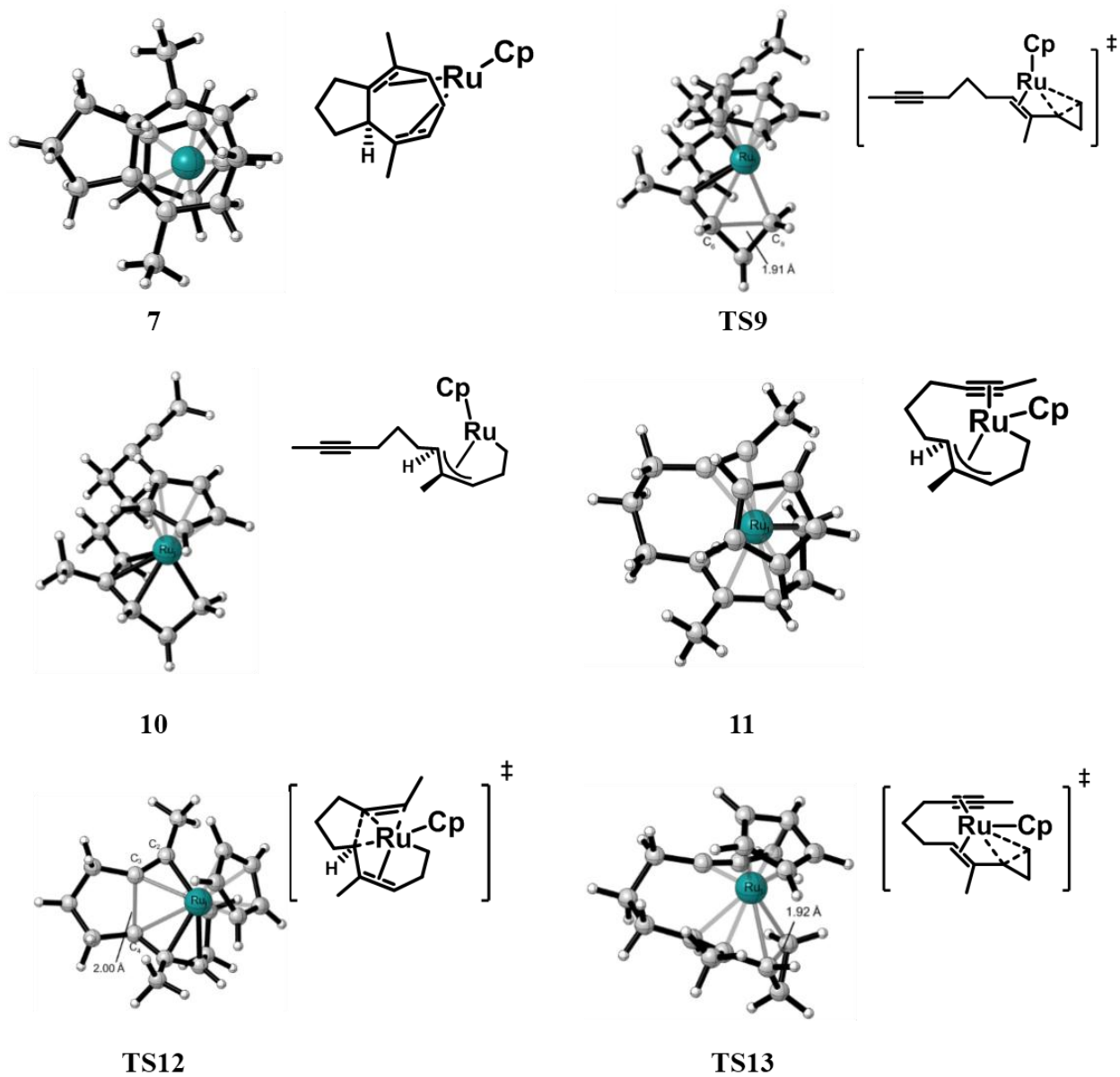
Alternatively, the metallacyclohexene pathway can occur with an initial cyclopropane cleavage (Figure 1.1). The cyclopropane cleavage can proceed with or without the intramolecular alkyne coordination. With alkyne coordination, ruthenacyclohexene intermediate **11** (3.4 kcal/mol) can be formed via **TS13** (11.4 kcal/mol). Alternatively, the alkyne can dissociate from ruthenium first to give the intermediate **8** (6.8 kcal/mol). Then the electron-deficient ruthenium catalyzes the cyclopropane cleavage through **TS9** (11.1 kcal/mol) to give the post-intermediate **10** (8.9 kcal/mol). Subsequently, the alkyne can coordinate to ruthenium again to generate the same ruthenacyclohexene intermediate **11**. Complex **11** will further undergo  $2\pi$  insertion via **TS12** (16.5 kcal/mol) to give the same ruthenaoctadiene intermediate **5**. The metallacyclohexene pathway requires a 16.5 kcal/mol barrier and the rate-determining step is the  $2\pi$  insertion of alkyne.

Consistent with the Trost's experimental studies, the metallacyclopentene pathway is preferred by 2.2 kcal/mol. The two complexes, **1** (0.0 kcal/mol) and **11** (3.4 kcal/mol), are somewhat different in energy but have more similar reaction barriers (14.3 kcal/mol for **1** and 13.1 kcal/mol for **11**). Thus, the relative stabilities of **1** and **11** mainly lead to the small preference for the metallacyclopentene pathway, **1** to **TS2**. The preference to metallacyclopentene pathway is in contrast to the rhodium catalyst, which significantly favors the metallacyclohexene pathway. The major difference between ruthenium and rhodium catalysts is the barrier difference between the  $2\pi$  insertion of metallacyclohexene intermediate (**11** to **TS12**) and ene-yne oxidative cyclization of substrate coordinated complex (**1** to **TS2**). With the rhodium catalyst,<sup>10(a)</sup> the  $2\pi$  insertion step has a much lower barrier than the oxidative cyclization, while the two steps have very similar barriers to those of the ruthenium catalyst. The origins of the barrier difference may be due to differences in the redox potentials of different transition-metal catalysts. The oxidation state of the

transition metal increases in the metallacycle formation, but remains the same in the  $2\pi$  insertion. Therefore, the metal complex that has a lower oxidation potential should favor the ene-yne oxidative cyclization.<sup>20</sup>



**Figure 1.2.** Optimized structures of intermediates and transition states in metallacyclohexene and metallacyclopentene pathways of Ru(II)-catalyzed (5+2) cycloaddition (All species have one positive charge).



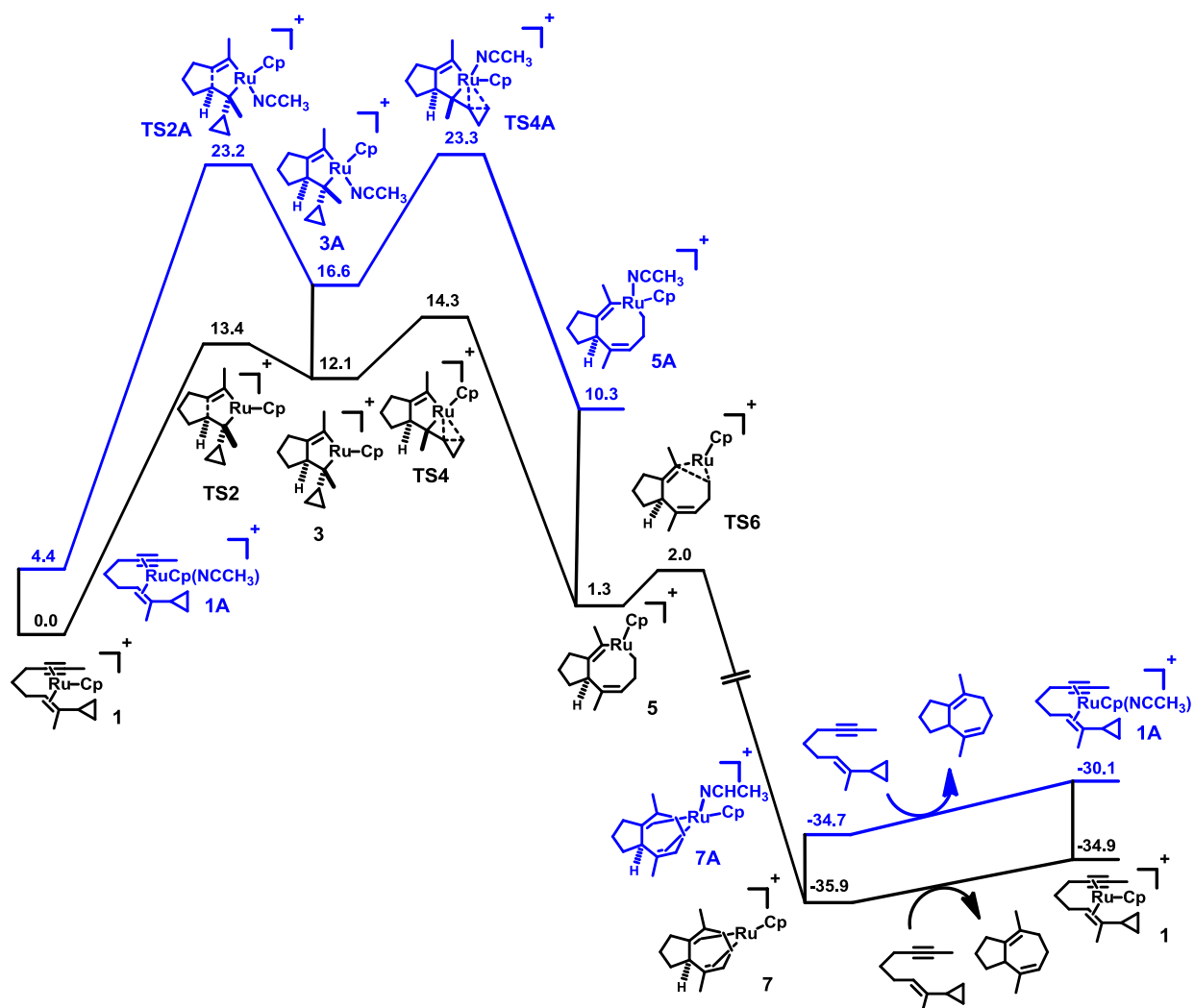
**Figure 1.3.** Optimized structures of intermediates and transition states in metallacyclohexene and metallacyclopentene pathways of Ru(II)-catalyzed (5+2) cycloaddition (All species have one positive charge).



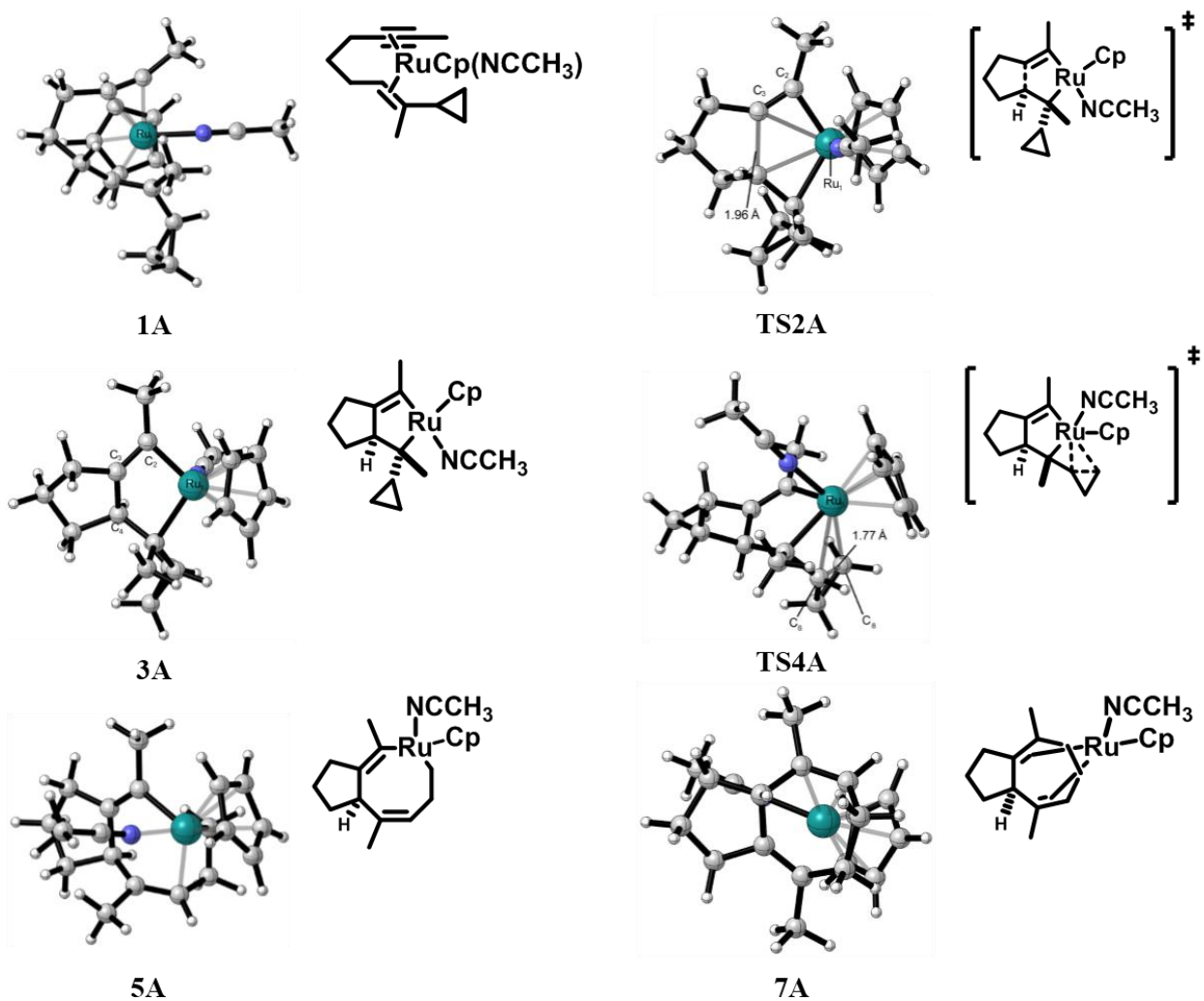
### 1.4.2 Acetonitrile Coordination and Solvent Effects

The possibility of acetonitrile coordination to the ruthenium catalyst was also studied. Figure 1.4 shows the free energy profiles for the reaction with only Cp as the ligand (black) and with additional acetonitrile coordination (blue). The optimized structures are provided in Figure 1.5. All the acetonitrile coordinated intermediates and transition states either have higher energies than in the absence of acetonitrile or cannot be located (**TS6A**)<sup>21</sup>. In addition, the acetone coordination is even less favorable than the acetonitrile coordination. Because the DFT calculations tend to overestimate the energy contribution from solvation entropy, the relative stabilities between **1** and **1A** is not conclusive based on the 4.4 kcal/mol free energy difference. Although the real structure of substrate coordinated complex is still in question, we believe the reaction will follow the pathway with only Cp as the ligand because of the large energy difference between **TS4** and **TS4A**. Therefore, all three acetonitriles in the precatalyst will dissociate to achieve the reaction.

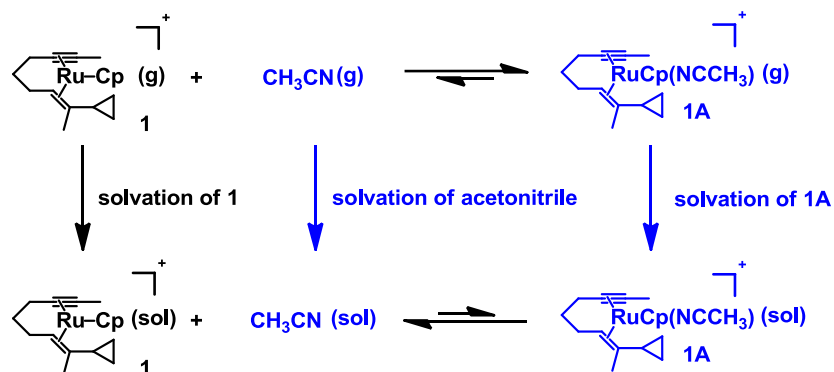
There are strong ruthenium-acetonitrile bonds in the optimized structures (the bond distances varies between 2.08Å to 2.23Å) and acetonitrile coordination is favorable in the gas phase. Scheme 1.9 gives an analysis of the thermodynamics of acetonitrile coordination at equilibrium. Because the pre- and post-coordination complexes have similar polarities, the difference of solvation energies between **1** (52.4 kcal/mol) and **1A** (50.1 kcal/mol) is only 2.3 kcal/mol. The major contributor to the equilibrium preference between the gas phase and solvent comes from the solvation energy of acetonitrile (6.8 kcal/mol). The solvation energy of acetonitrile is very strong in acetone and alters the complexation equilibrium and the reaction barriers. Therefore, we also calculated the free energy profiles with acetonitrile coordinated ruthenium complex in the gas phase (shown in Figure 1.6).



**Figure 1.4.** Free energy profiles of metallacyclopentene pathway with (blue) and without acetonitrile coordination (black) in Ru(II)-catalyzed intramolecular (5+2) cycloaddition with VCP and alkyne (in acetone).

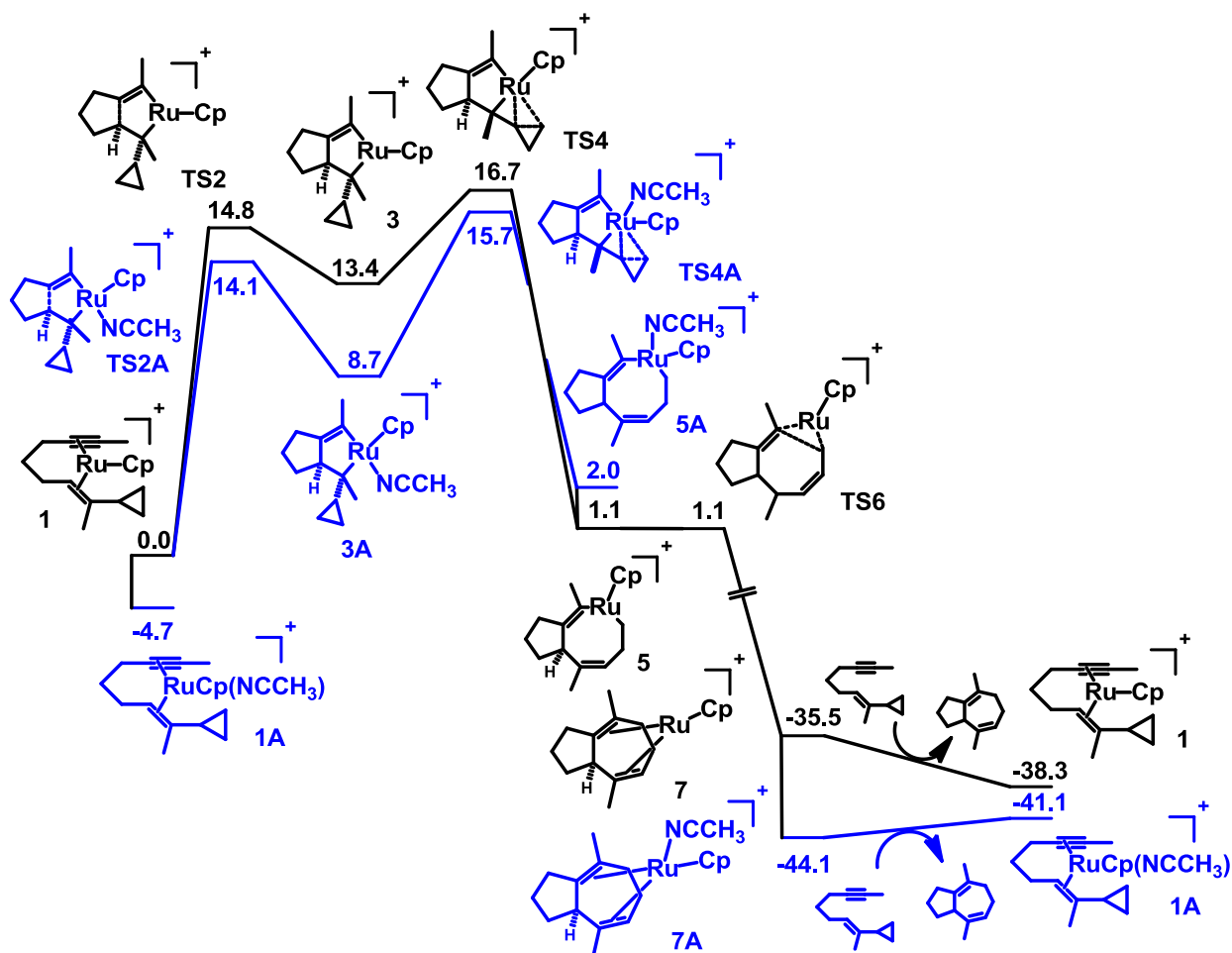


**Figure 1.5.** Optimized structures of intermediates and transition states with additional acetonitrile coordination in metallacyclopentene pathways of Ru(II)-catalyzed intramolecular (5+2) cycloaddition (All species have one positive charge).



**Scheme 1.9.** Thermodynamic equilibrium of acetonitrile coordination of ruthenium complexes that involved in the Ru(II)-catalyzed intramolecular (5+2) cycloaddition in gas phase and solution.

In the gas phase, acetonitrile coordination is favorable and the intermediates are more stabilized than the transition states. The reaction pathway without the acetonitrile coordination requires a 16.7 kcal/mol overall barrier, which is similar to the barrier in acetone. With the acetonitrile coordination, the barrier increases to 23.4 kcal/mol (from **7A** to **TS4A**) due to the significant stabilization of the resting state **7A**. Comparing the acetone solvent, the gas phase can be considered as an extreme of nonpolar solvent, and the difference of free energy profiles between gas phase and acetone solvent explains the origin of the superior solvent effect of acetone in this reaction. The polar solvent acetone facilitates the acetonitrile dissociation from the precatalyst, which destabilizes the resting state and lowers the overall reaction barrier. In a nonpolar solvent, the acetonitrile coordination is favorable and stabilizes the resting states of the catalytic cycle, resulting in a higher reaction barrier and lower efficiency.



**Figure 1.6.** Free energy profiles of metallacyclopentene pathway with (blue) and without acetonitrile coordination (black) in Ru(II)-catalyzed (5+2) cycloaddition (gas phase).

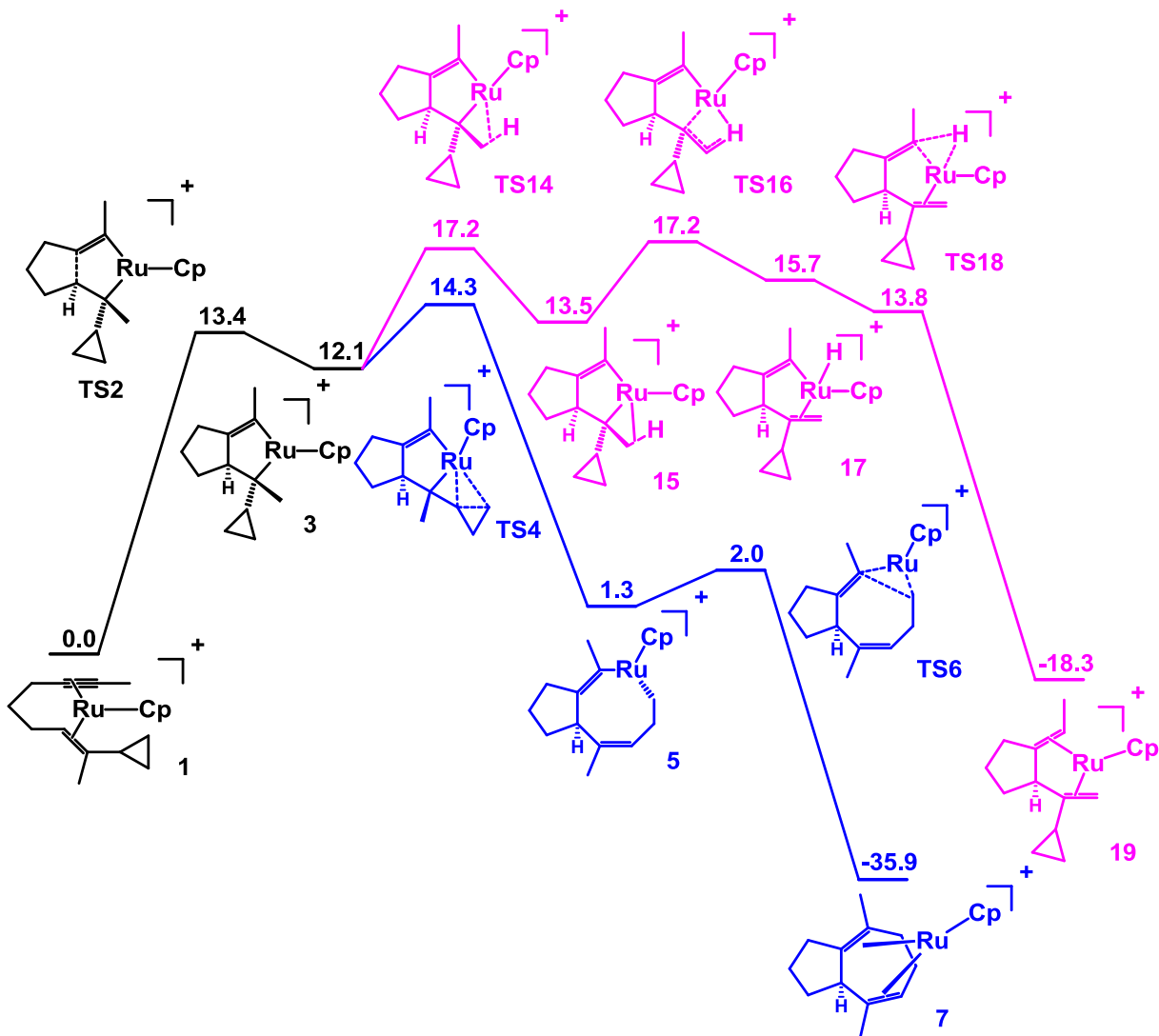
### 1.4.3 Selectivity of Cycloaddition and Ene Reaction with the *Trans*-VCP

As noted earlier, the *trans*-VCP substrate gives mainly (5+2) cycloaddition involving the ring-opening of the cyclopropane (Scheme 1.5). The *cis*-VCP produces mainly ene product, but some of the (5+2) product is formed as well. This seems obvious from the structure of substrate, but it should be noted that the intermediates involved from the *trans* vs *cis* substrates are diastereomeric.

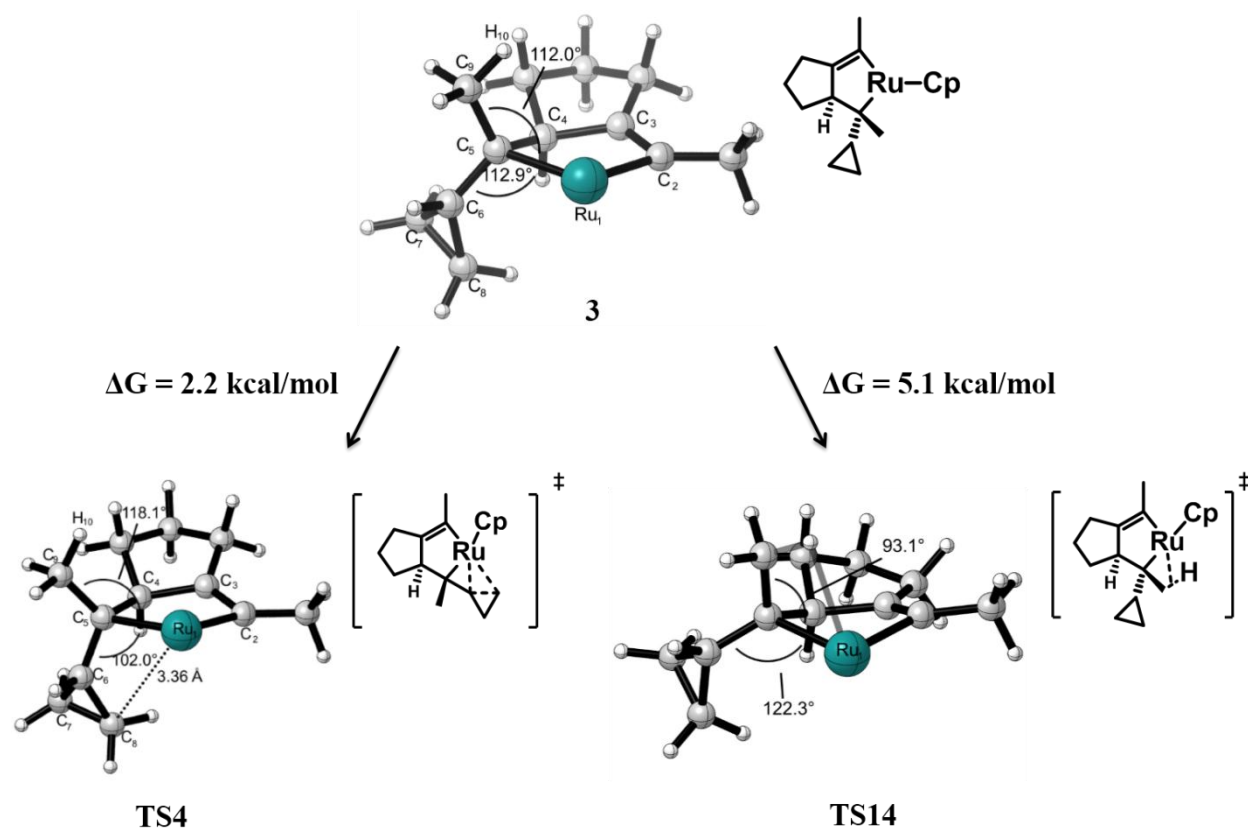
In order to explore the origins of such selectivity in more detail, we first calculated the free energy profiles for both (5+2) cycloaddition and ene reaction with *trans*-VCP (shown in Figure 1.7).

The ruthenacyclopentene intermediate **3** (12.1 kcal/mol) can undergo the cyclopropane cleavage via **TS4**; this requires only a 2.2 kcal/mol barrier. The ruthenacyclooctadiene intermediate **5** (1.3 kcal/mol) then generates the seven-membered ring product through a facile reductive elimination via **TS6** (2.0 kcal/mol). Alternatively, a  $\beta$ -hydride elimination can occur in the intermediate **3** initiated by an agostic intermediate **15** (13.5 kcal/mol) via **TS14** (17.2 kcal/mol). Then the  $\beta$ -hydride elimination through **TS16** gives the intermediate **17** (15.7 kcal/mol). Finally, the diene complex **19** can be formed via C-H reductive elimination. For the  $\beta$ -hydride elimination, both **TS14** and **TS16** are rate-determining and require 5.1 kcal/mol barriers from the intermediate **3**.

The calculations predicts a preference for (5+2) cycloaddition in *trans*-VCP, as is found experimentally. The difference between **TS4** and **TS14** explains the origins of selectivity; these transition structures are shown in Figure 1.8. The cyclopropane cleavage (**TS4**) is favored intrinsically. To achieve the Ru<sub>1</sub>-H<sub>10</sub> bond interaction and form an agostic intermediate, the methyl group must rotate to a larger degree in **TS14**, resulting in an unfavorable distortion and higher energy of **TS14** compared to **TS4**.



**Figure 1.7.** Free energy profiles of reductive elimination (blue) and  $\beta$ -hydride elimination (pink) in Ru(II)-catalyzed (5+2) cycloaddition with *trans*-VCP.



**Figure 1.8.** Free energies and structures of selectivity determining transition states in *trans*-VCP (The Cp ligand is hidden for clearance and all species have one positive charge).

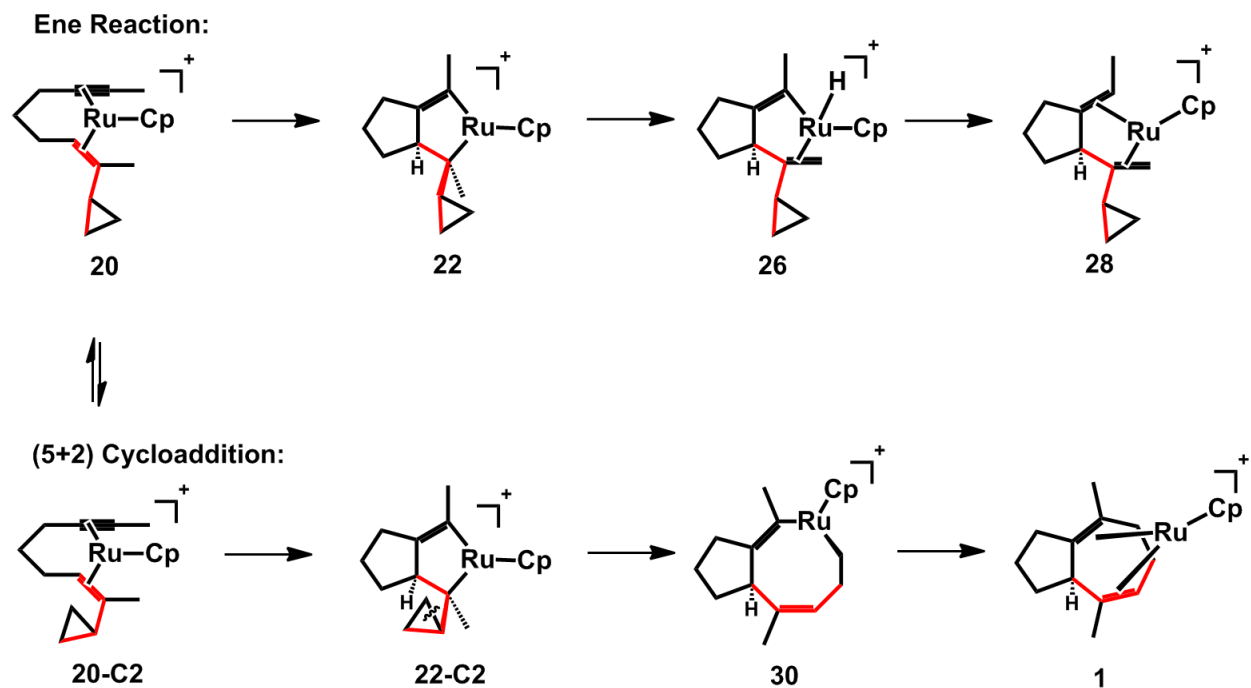
#### 1.4.4 Selectivity of Cycloaddition and Ene Reaction with the *Cis*-VCP

Subsequently, the origin of selectivity of *cis*-VCP was also studied. Here,  $\beta$ -hydride elimination has a lower barrier, and the ene product is preferred (free energy profile is shown in Figure 1.9). The key difference between *trans*- and *cis*-VCP is the position of the cyclopropyl group. The favored conformation of ruthenacyclopentene intermediate **22** in the *cis*-VCP requires rotation of the cyclopropyl group in order to form a *cis*-double bond in the cycloheptadiene (shown in Scheme 1.10). This rotation is not necessary for  $\beta$ -hydride elimination. Therefore, for the *cis*-

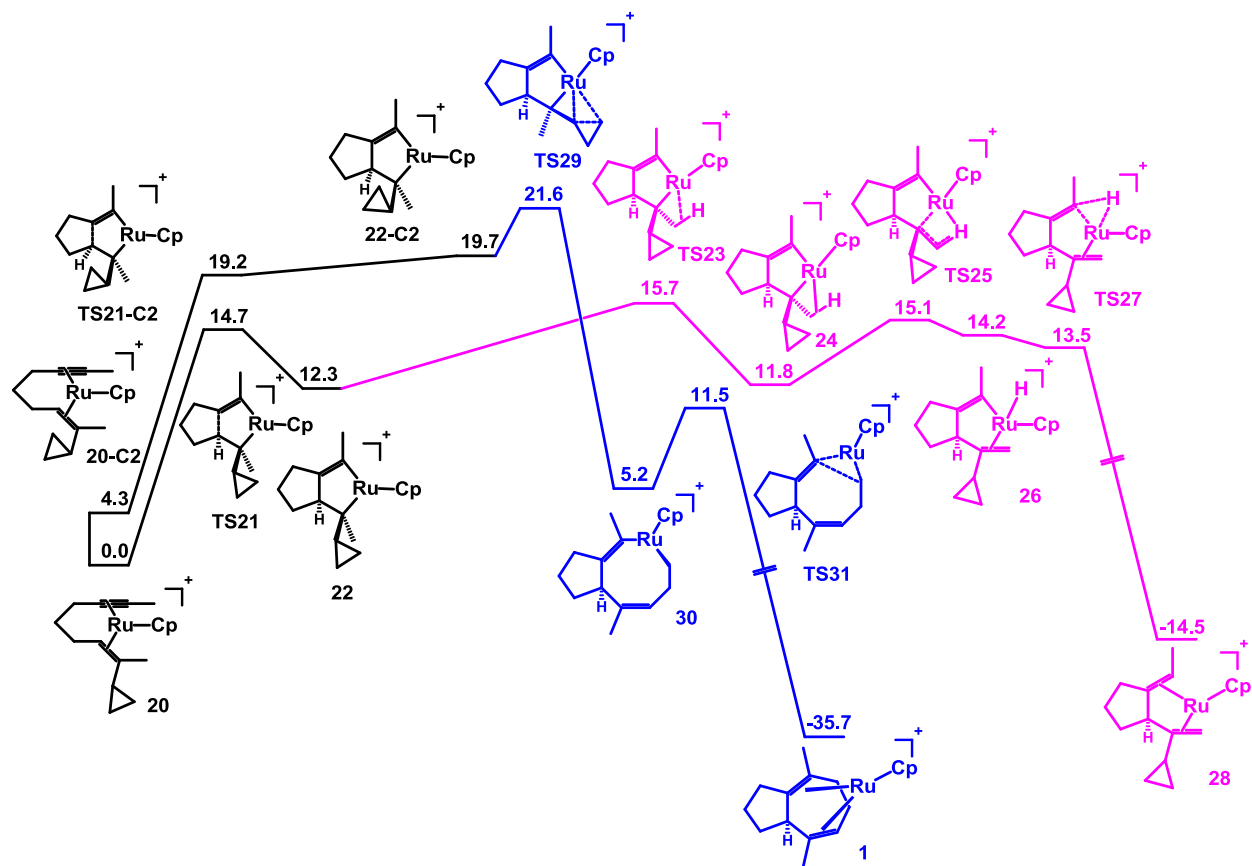


VCP, the (5+2) cycloaddition and ene reaction start from different intermediates (**20** and **20-C2** in Scheme 1.8 and Figure 1.9).

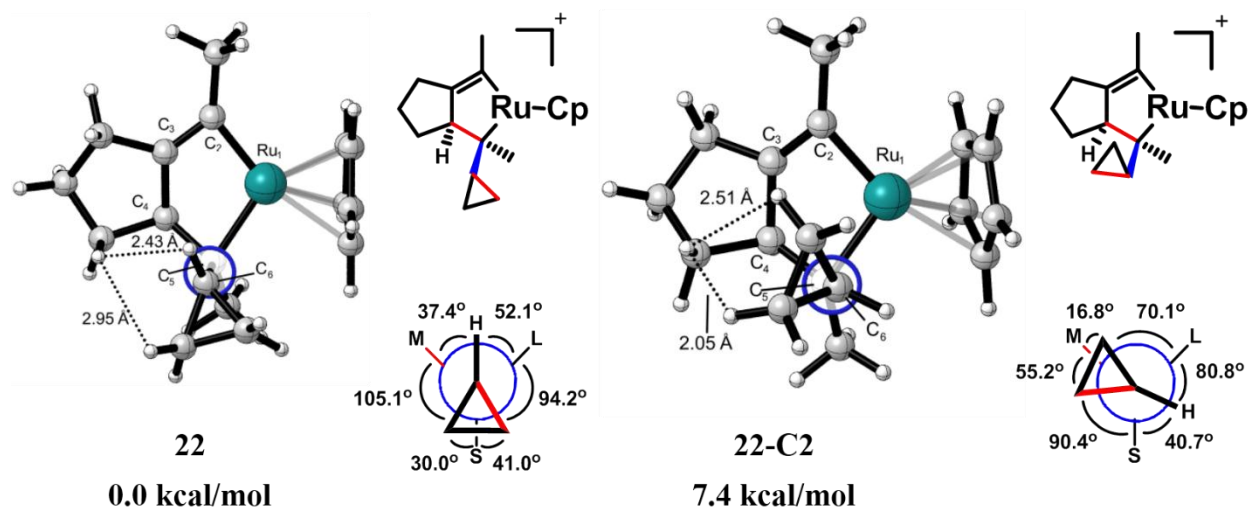
The ene reaction pathway of the *cis*-VCP is similar to that of the *trans*-VCP. The rate-determining step is **TS23** to form the agostic intermediate **24** which requires an overall barrier of 15.7 kcal/mol. To the (5+2) cycloaddition, the intermediate **20** has to adopt an unfavorable conformation, **20-C2**, in order to generate the *cis*-double bond in the cycloheptadiene. After oxidative cyclization, the formed intermediate, **22-C2** (19.7 kcal/mol), is much less stable than the favored conformation **22** (12.3 kcal/mol).<sup>22</sup> This instability is due to the steric repulsions between the formed five-membered ring and the cyclopropyl group, which are shown by the H-H distance and the Newman projection of C5-C6 (Figure 1.10). Therefore, although the cyclopropane cleavage still has a lower intrinsic barrier (1.9 kcal/mol from **22-C2** to **TS29**) compared to  $\beta$ -hydride elimination (3.4 kcal/mol from **22** to **TS23**), the relative stabilities of **22** and **22-C2** overruled the intrinsic barrier differences and lead to the  $\beta$ -hydride elimination and ene product eventually.



**Scheme 1.10.** Key intermediates of (5+2) cycloaddition and ene reaction with *cis*-VCP substrate (The carbons in one of the *cis*-double bonds of cycloheptadiene are labeled in red).



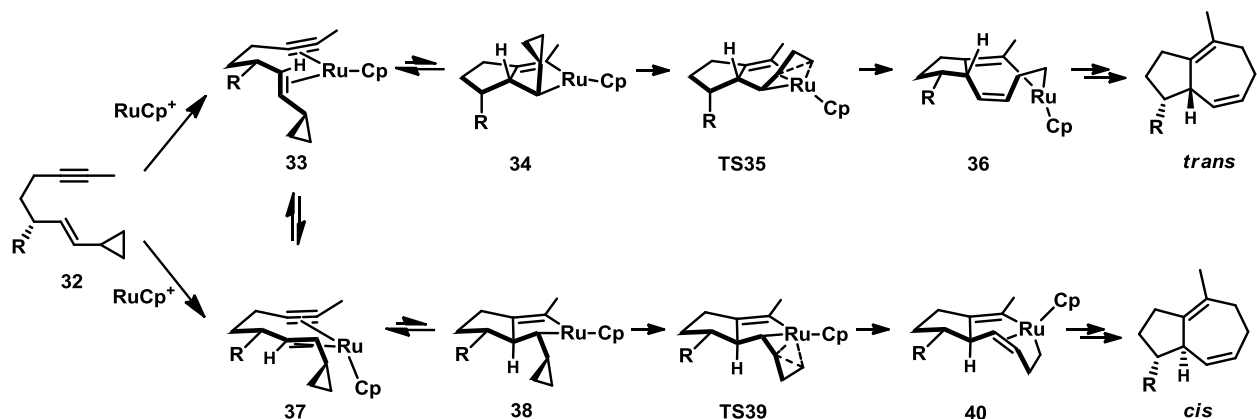
**Figure 1.9.** Free energy profiles of reductive elimination (blue) and  $\beta$ -hydride elimination (pink) in Ru(II)-catalyzed (5+2) cycloaddition with the *cis*-VCP.



**Figure 1.10.** Optimized structures, Newman projection of C5-C6 and relative Gibbs free energies of intermediate **22** and **22-C2** (S stands for the methyl group, M stands for the formed five-membered carbocycle and L stands for the ruthenium).

### 1.4.5 Origins of Diastereoselectivities

As noted earlier, the stereochemistry of allylic substituents in the tether strongly affects the formed bridgehead stereogenic center. The allylic hydroxyl group is *trans* to bridgehead hydrogen and disubstitution on allylic position dramatically increases the diastereoselectivities (Scheme 1.6). In order to explore the origins of the diastereoselectivities, we studied the reaction pathways that generate the diastereomeric (5+2) cycloadducts.



**Scheme 1.11.** Reaction pathways that generate the *trans*- and *cis*-diastereomers of Ru(II)-catalyzed (5+2) cycloaddition.

Scheme 1.11 shows the key intermediates and transition states that generate the diastereoselectivities. From enantiopure substrate **32**, substrate-catalyst complex **33** undergoes the oxidative cyclization to form the bicyclic post-intermediate **34** with the substituent R *trans* to the bridgehead hydrogen. The subsequent irreversible cyclopropane cleavage via **TS35** generates the eight-membered ring intermediate **36** and eventually the (5+2) cycloadduct with R *trans* to the bridgehead hydrogen. In the *cis*-pathway, the diastereomeric substrate-catalyst complex **37** generates the post-intermediate **38** with the allylic substituent R *cis* to the bridgehead hydrogen. Subsequent cyclopropane cleavage produces the eight-membered ring intermediate **40** through the **TS39** and eventually the (5+2) cycloadduct with R *cis* to the bridgehead hydrogen.

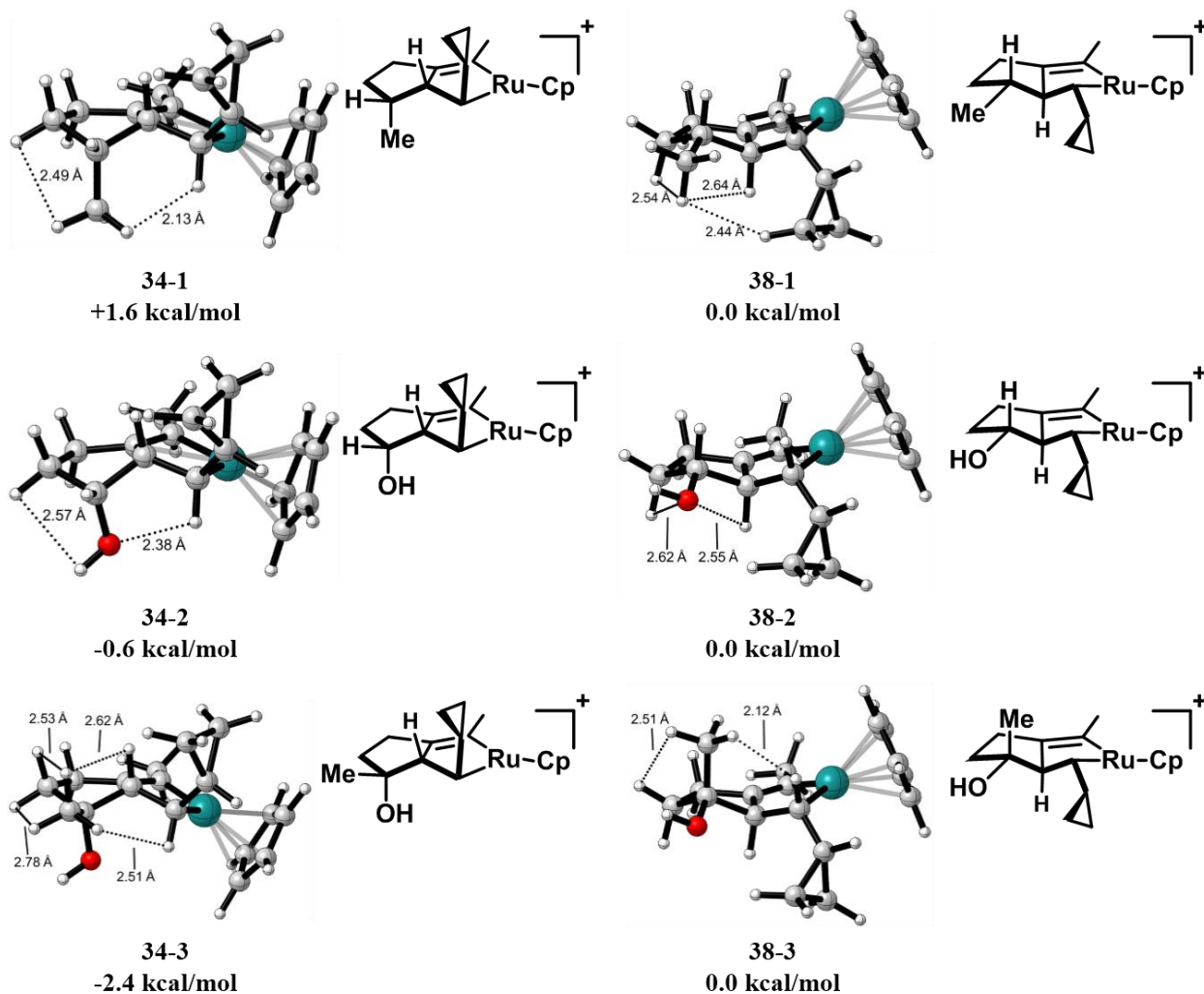
Table 1.1 shows the free energies of the intermediates and transition states from Scheme 1.11 with various allylic substituents. In the case that allylic position is mono-substituted by methyl group, the *trans*-cycloadduct is disfavored by 1.4 kcal/mol (Table 1.1, entry 1). Because the cyclopropane cleavage barriers are very similar in *trans*- and *cis*-pathways (1.8 kcal/mol from **34**-

**1** to **TS35-1** and 2.0 kcal/mol from **38-1** to **TS39-1**), the relative stabilities of **34-1** and **38-1** determine the diastereoselectivity. As shown in Figure 1.11, **34-1** has the steric repulsions between the methyl substituent and its  $\beta$ -hydrogen from the double bond while such repulsions are not presented in **38-1** (shown in Figure 1.11). Therefore, the steric effects lead to the preference to the *cis*-(5+2) cycloadduct when there is one allylic methyl substituent.

In contrast, the *trans*-cycloadduct is favored with allylic hydroxyl substituents. The predicted preference is consistent with the experimental diastereoselectivities. When substituted with one hydroxyl group, **34-2** (12.3 kcal/mol) is 0.6 kcal/mol less stable than **38-2** (12.9 kcal/mol) (Table 1.1, entry 2). The origins of the reversed stabilities and diastereoselectivities are electrostatic interactions. The oxygen in **34-2** is closer to the cationic catalyst center and thus the electrostatic stabilization from oxygen lone pairs makes the **34-2** more stable. Furthermore, when the allylic position is disubstituted with methyl and hydroxyl groups, both electrostatic and steric interactions favor the *trans*-(5+2) cycloadduct and produce a higher diastereoselectivity. In **34-3**, the oxygen lone pairs provide similar stabilization as in **34-2**, and the methyl substituent has no significant steric repulsions. However, the same methyl substituent in **38-3** has steric repulsions with its  $\beta$ -hydrogen from the double bond. Therefore, the combined electrostatic and steric effects generate the higher diastereoselectivity observed in experiments.

entry		<i>trans</i>			<i>cis</i>			$\Delta\Delta G(\text{TS35-TS39})$
		33	34	TS35	37	38	TS39	
<b>1</b>	<b>R<sub>1</sub>=Me;R<sub>2</sub>=H</b>	<b>0.0</b>	<b>14.6</b>	<b>16.4</b>	<b>3.0</b>	<b>13.0</b>	<b>15.0</b>	<b>+1.4</b>
<b>2</b>	<b>R<sub>1</sub>=OH;R<sub>2</sub>=H</b>	<b>0.0</b>	<b>12.3</b>	<b>14.5</b>	<b>2.3</b>	<b>12.9</b>	<b>15.0</b>	<b>-0.5</b>
<b>3</b>	<b>R<sub>1</sub>=OH;R<sub>2</sub>=Me</b>	<b>0.0</b>	<b>10.9</b>	<b>13.8</b>	<b>4.1</b>	<b>13.3</b>	<b>16.1</b>	<b>-2.3</b>

**Table 1.1.** Gibbs free energies of key intermediates and transition states that generate the *trans*- and *cis*-diastereomeric cycloadducts in Ru(II)-catalyzed (5+2) cycloadditions with various allylic substituents.



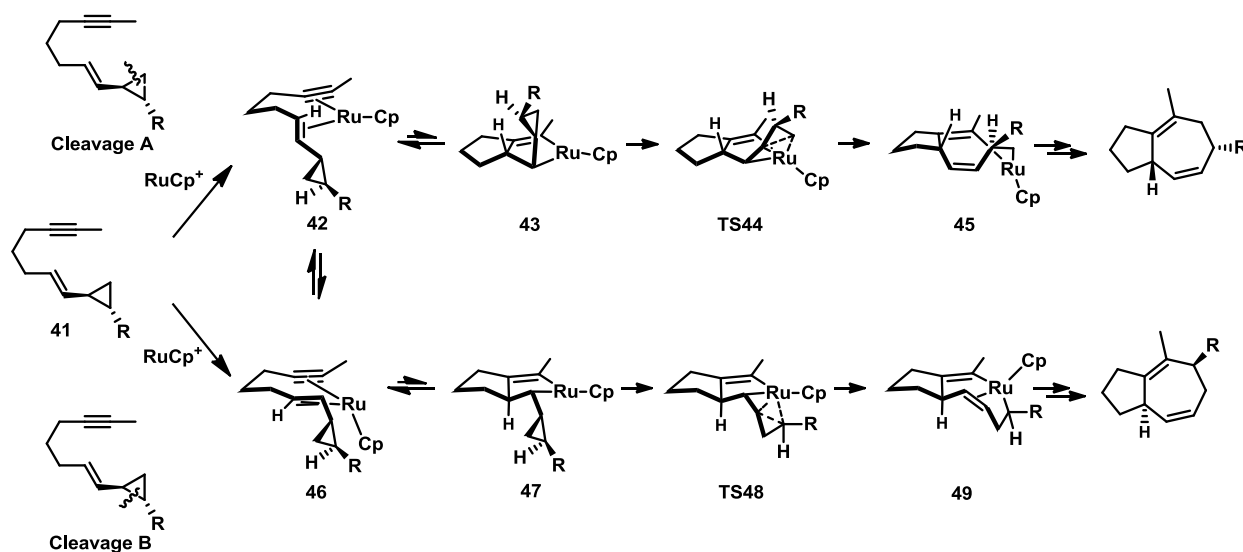
**Figure 1.11.** Optimized structures and relative Gibbs free energies of diastereomeric oxidative cyclization post-intermediates with various allylic substituents in Ru(II)-catalyzed (5+2) cycloaddition.

### 1.4.6 Origins of Regioselectivities

The origins of regioselectivities are also studied. The reaction pathways that generate the regioselectivities are very similar to the reaction pathways that generate the diastereoselectivities



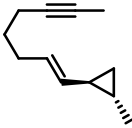
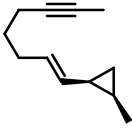
(Scheme 1.12). From *trans*-1,2-disubstituted cyclopropane substrate **41**, substrate-catalyst complex **42** undergoes the reversible oxidative cyclization to form the bicyclic post-intermediate **43**. The subsequent cyclopropane cleavage via **TS44** produces the eight-membered ring intermediate **45** and eventually the (5+2) cycloadduct with the less substituted C-C bond cleaved (Cleavage A). Alternatively, the substrate-catalyst complex **46** can undergo similar pathway to have the more substituted C-C bond cleaved (Cleavage B) and the determining transition state is **TS48**.



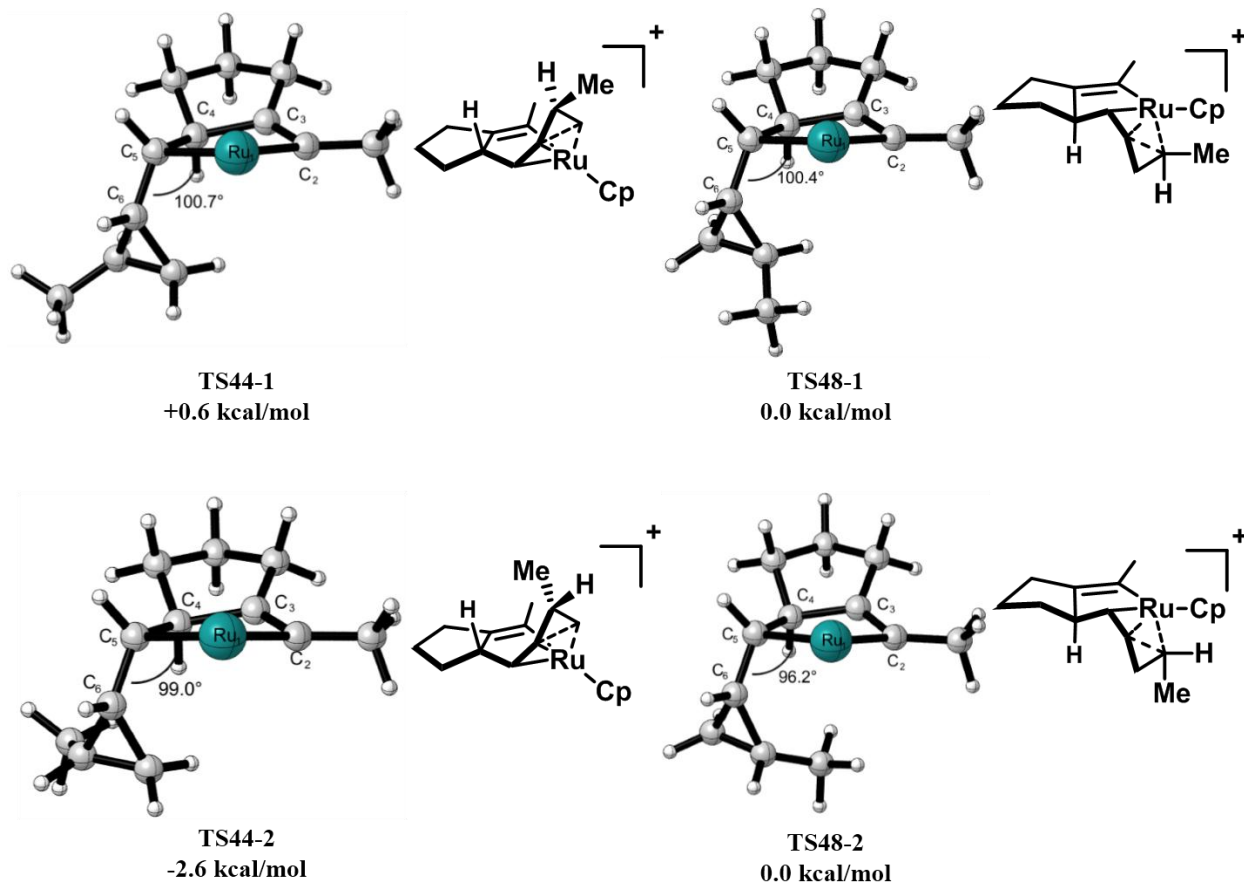
**Scheme 1.12.** Reaction pathways that cleave the more and less substituted C-C bond of cyclopropane in 1,2-disubstituted cyclopropane of Ru(II)-catalyzed (5+2) cycloaddition.

Table 1.2 shows the free energies of the intermediates and transition states from Scheme 1.12 with *trans*- and *cis*-1,2-disubstitution. With *trans*-disubstitution (Table 1.1, entry 1), the cleavage A and B have very similar barriers and the experimental regioselectivity is low (Scheme 1.7). Figure 1.12 showed the optimized structures of the regioselectivity-determining transition states. In **TS44-1** and **TS48-1**, the methyl substituent has no significant steric repulsions and is away from

reaction center in both cases and thus the cleavage A and B have very similar barriers and the regioselectivity is low. In contrast, the *cis*-disubstituted cyclopropane favors the cleavage A dramatically. The methyl substituent in **TS44-2** is still away from the reaction center and the cyclopropane cleavage barrier of cleavage A is low (3.0 kcal/mol). However, the methyl substituent in **TS48-2** is in a much sterically hindered position and close to the reaction center. Therefore, the steric repulsions from methyl substituent increase the cleavage barrier of cleavage B to 5.3 kcal/mol and generate the higher regioselectivity in *cis*-1,2-disubstituted cyclopropane.

entry	substrate	Cleavage A			Cleavage B			$\Delta\Delta G(\text{TS44-TS48})$
		42	43	TS44	46	47	TS48	
1		0.0	14.1	17.4	2.4	14.0	16.8	+0.6
2		0.0	16.6	19.6	6.4	16.9	22.2	-2.6

**Table 1.2.** Gibbs free energies of key intermediates and transition states that undergo the cleavage A and cleavage B pathways in Ru(II)-catalyzed (5+2) cycloadditions with *trans*- and *cis*-1,2-disubstituted cyclopropanes.



**Figure 1.12.** Optimized structures and relative Gibbs free energies of cyclopropane cleavage transition states in Ru(II)-catalyzed (5+2) cycloaddition with *trans*- and *cis*-1,2-disubstituted cyclopropanes (For clearance, cyclopentadienyl ligand is hidden and TS44-1, TS44-2 are the mirror images of their real structures).

## 1.5 Conclusions

The mechanism and solvent effects of Ru(II)-catalyzed intramolecular (5+2) cycloaddition and ene reaction have been studied theoretically. The favored catalytic cycle involves an initial

oxidative cyclization to produce a metallacyclopentene intermediate. Subsequent cyclopropane cleavage and C-C reductive elimination yield the (5+2) seven-membered ring product, while the  $\beta$ -hydride elimination and C-H reductive elimination gives the ene product. The acetone solvent is found to facilitate the acetonitrile dissociation from the precatalyst and destabilize the resting state, resulting in a lower reaction barrier. Quite noteworthy is the complementary mechanisms for the (5+2) cycloaddition between rhodium and ruthenium catalysis. Such a mechanistic dichotomy offers the opportunity to modulate the selectivity and reactivity for any given substrate by simply changing the metal catalyst which highlights the power of transition metal catalysis.

The origins of the reversed selectivity between (5+2) cycloaddition and ene reaction with *trans*- and *cis*-VCP were also revealed. In *trans*-VCP, the intrinsic lower barrier of cyclopropane cleavage leads to the seven-membered ring major product. The *cis*-VCP requires an unfavorable rotation of cyclopropyl group in order to generate the *cis*-double bond in the seven-membered ring product. This unfavorable rotation reverses the selectivity.

The origins of the diastereo- and regioselectivities have also been discovered. When the allylic position is substituted by hydroxyl group, the oxygen lone pair provides stabilizing electrostatic interactions with the cationic catalyst center in one diastereomer, and the favored diastereomer has the hydroxyl group *trans* to the bridgehead hydrogen. The origins of regioselectivities are from steric repulsions. In the *trans*-1,2-disubstituted cyclopropane, both the cleavages of more and less substituted C-C bond of the cyclopropane have no significant steric repulsions from the substituent. In contrast, the methyl substituent of the *cis*-1,2-disubstituted cyclopropane causes much steric repulsion in the transition state that cleaves the more substituted C-C bond, and thus a higher regioselectivity is found.

## 1.6 References

(1) (a) Wender, P. A.; Fuji, M.; Husfeld, C. O.; Love, J. A. *Org. Lett.* **1999**, *1*, 137. (b) Wender, P. A.; Zhang, L. *Org. Lett.* **2000**, *2*, 2323. (c) Trost, B. M.; Shen, H. C.; Surivet, J. P. *Angew. Chem., Int. Ed.* **2003**, *42*, 3943. (d) Padwa, A.; Boonsombat, J.; Rashatasakhon, P.; Willis, J. *Org. Lett.* **2005**, *7*, 3725. (e) Nakamura, S.; Sugano, Y.; Kikuchi, F.; Hashimoto, S. *Angew. Chem., Int. Ed.* **2006**, *45*, 6532. (f) Battiste, M. A.; Pelphrey, P. M.; Wright, D. L. *Chem. Eur. J.* **2006**, *12*, 3438. (g) Trost, B. M.; Hu, Y.; Horne, D. B. *J. Am. Chem. Soc.* **2007**, *129*, 11781. (h) Trost, B. M.; Waser, J.; Meyer, A. *J. Am. Chem. Soc.* **2008**, *130*, 16424. (i) Butenschön, H. *Angew. Chem., Int. Ed.* **2008**, *47*, 5287. (j) Shimada, N.; Hanari, T.; Kurosaki, Y.; Takeda, K.; Anada, M.; Nambu, H.; Shiro, M.; Hashimoto, S. *J. Org. Chem.* **2010**, *75*, 6039. (k) Wender, P. A.; Lesser, A. B.; Sirois, L. E. *Org. Synth.* **2011**, *88*, 109.

(2) (a) Kantorowski, E. J.; Kurth, M. J. *Tetrahedron* **2000**, *56*, 4317. (b) Byrne, L. A.; Gilheany, D. G. *Synlett* **2004**, *6*, 933. (c) Matsuda, T.; Makino, M.; Murakami, M. *Angew. Chem., Int. Ed.* **2005**, *44*, 4608. (d) Tite, T.; Tsimilaza, A.; Lallemand, M.; Tillequin, F.; Leproux, P.; Libot, F.; Husson, H. *Eur. J. Org. Chem.* **2006**, 863. (e) Hashimoto, T.; Naganawa, Y.; Maruoka, K. *J. Am. Chem. Soc.* **2009**, *131*, 6614. (f) Laventine, D. L.; Cullis, P. M.; Garcia, M. D.; Jenkins, P. R. *Tetrahedron Lett.* **2009**, *50*, 3657. (g) Yadav, D. B.; Morgans, G. L.; Aderibigbe, B. A.; Madeley, L. G.; Fernandes, M. A.; Michael, J. P.; de Koning, C. B.; van Otterlo, W. A. L. *Tetrahedron* **2011**, *67*, 2991. (h) Pulido, F. J.; Barbero, A.; Castreño, P. J. *Org. Chem.* **2011**, *76*, 5850. (i) Cao, H.; Vieira, T. O.; Alper, H. *Org. Lett.* **2011**, *13*, 11. (j) Li, X.; Zhang, M.; Shu, D.; Robichaux, P. J.; Huang, S.; Tang, W. P. *Angew. Chem., Int. Ed.* **2011**, *50*, 10421. (k) Usanov, D. L.; Yamamoto, H. *Org. Lett.* **2012**, *14*, 414.

(3) (a) Yet, L. *Chem. Rev.* **2000**, *100*, 2963. (b) Wender, P. A.; Croatt, M. P.; Deschamps, N. M. In *Comprehensive Organometallic Chemistry III*; Crabtree, R. H., Mingos, D. M. P., Eds.; Elsevier: Oxford, 2007; Vol. 10, pp 603-647.

(4) For reviews, see: (a) Wender, P. A.; Love, J. A. In: *Advances in Cycloaddition*; JAI Press, 1999, Vol. 5, pp 1-45. (b) Wender, P. A.; Gamber, G. G.; Williams, T. J. In: *Modern Rhodium-Catalyzed Organic Reactions*, Wiley-VCH, Weinheim, 2005, pp 263-299, and ref 1(g) and 3(b).

(5) For the first report by Wender, see: (a) Wender, P. A.; Takahashi, H.; Witulski, B. *J. Am. Chem. Soc.* **1995**, *117*, 4720. For intermolecular reactions involving alkynes, see: (b) Wender, P. A.; Rieck, H.; Fuji, M. *J. Am. Chem. Soc.* **1998**, *120*, 10976. (c) Wender, P. A.; Dyckman, A. J.; Husfeld, C. O.; Scanio, M. J. *Org. Lett.* **2000**, *2*, 1609. (d) Wender, P. A.; Barzilay, C. M.; Dyckman, A. J. *J. Am. Chem. Soc.* **2001**, *123*, 179. (e) Wender, P. A.; Gamber, G. G.; Scanio, M. J. *Angew. Chem., Int. Ed.* **2001**, *40*, 3895. (f) Wender, P. A.; Stemmler, R. T.; Sirois, L. E. *J. Am. Chem. Soc.* **2010**, *132*, 2532. (g) Wender, P. A.; Sirois, L. E.; Stemmler, R. T.; Williams, T. *J. Org. Lett.* **2010**, *12*, 1604. For intermolecular reactions involving allenes, see: (h) Wegner, H. A.; de Meijere, A.; Wender, P. A. *J. Am. Chem. Soc.* **2005**, *127*, 6530. For Ni and Fe-catalyzed

(5+2) cycloadditions, see: (i) Zuo, G.; Louie, J. *J. Am. Chem. Soc.* **2005**, *127*, 5798. (j) Fürstner, A.; Majima, K.; Martin, R.; Krause, H.; Kattnig, E.; Goddard, R.; Lehmann, C. W. *J. Am. Chem. Soc.* **2008**, *130*, 1992.

(6) (a) Wender, P. A.; Fuji, M.; Husfeld, C. O.; Love, J. A. *Org. Lett.* **1999**, *1*, 137. (b) Wender, P. A.; Zhang, L. *Org. Lett.* **2000**, *2*, 2323. (c) Wender, P. A.; Bi, F. C.; Brodney, M. A.; Gosselin, F. *Org. Lett.* **2001**, *3*, 2105. (d) Ashfeld, B. L.; Martin, S. F. *Tetrahedron* **2006**, *62*, 10497–10506. (e) Jiao, L.; Yuan, C.; Yu, Z. -X. *J. Am. Chem. Soc.* **2008**, *130*, 4421. (f) Yuan, C.; Jiao, L.; Yu, Z. -X. *Tetrahedron Lett.* **2010**, *51*, 5674. (g) Liang, Y.; Jiang, X.; Yu, Z. -X. *Chem. Commun.* **2011**, *47*, 6659. (h) Liang, Y.; Jiang, X.; Fu, X. -F.; Ye, S. -Y.; Wang, T.; Yuan, J.; Wang, Y.; Yu, Z. -X. *Chem. Asian. J.* **2012**, *7*, 593, and ref 1(g), 1(h) and 14(c).

(7) (a) Wender, P. A.; Gamber, G. G.; Hubbard, R. D.; Zhang, L. *J. Am. Chem. Soc.* **2002**, *124*, 2876. (b) Wang, Y.; Wang, J.; Su, J.; Huang, F.; Jiao, L.; Liang, Y.; Yang, D.; Zhang, S.; Wender, P. A.; Yu, Z.-X. *J. Am. Chem. Soc.* **2007**, *129*, 10060. (c) Huang, F.; Yao, Z.-K.; Wang, Y.; Wang, Y.; Zhang, J.; Yu, Z.-X. *Chem. Asian J.* **2010**, *5*, 1555.

(8) Wender, P. A.; Gamber, G. G.; Hubbard, R. D.; Pham, S. M.; Zhang, L. *J. Am. Chem. Soc.* **2005**, *127*, 2836.

(9) (a) Jiao, L.; Ye, S.-Y.; Yu, Z.-X. *J. Am. Chem. Soc.* **2008**, *130*, 7178. (b) Jiao, L.; Lin, M.; Yu, Z.-X. *Chem. Commun.* **2010**, *46*, 1059.

(10) Jiang, G.-J.; Fu, X.-F.; Li, Q.; Yu, Z.-X. *Org. Lett.* **2012**, *14*, 692.

(11) (a) Yu, Z.-X.; Wender, P. A.; Houk, K. N. *J. Am. Chem. Soc.* **2004**, *126*, 9154. (b) Yu, Z.-X.; Cheong, P. H.-Y.; Liu, P.; Legault, C. Y.; Wender, P. A.; Houk, K. N. *J. Am. Chem. Soc.* **2008**, *130*, 2378. (c) Liu, P.; Cheong, P. H.-Y.; Yu, Z.-X.; Wender, P. A.; Houk, K. N. *Angew. Chem., Int. Ed.* **2008**, *47*, 3939. (d) Hong, X.; Liu, P.; Houk, K. N. *J. Am. Chem. Soc.* **2013**, *135*, 1456.

(12) (a) Liu, P.; Sirois, L. E.; Cheong, P. H. -Y.; Yu, Z. -X.; Hartung, I. V.; Rieck, H.; Wender, P. A.; Houk, K. N. *J. Am. Chem. Soc.* **2010**, *132*, 10127. (b) Xu, X. F.; Liu, P.; Lesser, A.; Sirois, L. E.; Wender, P. A.; Houk, K. N. *J. Am. Chem. Soc.* **2012**, *134*, 11012.

(13) (a) Trost, B. M.; Indolese, A. *J. Am. Chem. Soc.* **1993**, *115*, 4361. (b) Trost, B. M.; Indolese, A.; Müller, T. J. J.; Treptow, B. *J. Am. Chem. Soc.* **1995**, *117*, 615. (c) Trost, B. M.; Krause, L.; Portnoy, M. *J. Am. Chem. Soc.* **1997**, *119*, 11319. (d) Trost, B. M.; Portnoy, M.; Kurihara, H. *J. Am. Chem. Soc.* **1997**, *119*, 836. (e) Trost, B. M.; Probst, G. D.; Schoop, A. *J. Am. Chem. Soc.*

**1998**, *120*, 9228. (f) Trost, B. M.; Toste, F. D. *Tetrahedron Lett.* **1999**, *40*, 7739. (g) Chen, H.; Li, S. *Organometallics* **2005**, *24*, 872.

(14) (a) Trost, B. M.; Toste, F. D.; Shen, H. C. *J. Am. Chem. Soc.* **2000**, *122*, 2379. (b) Trost, B. M.; Shen, H. C. *Org. Lett.* **2000**, *2*, 2523. (c) Trost, B. M.; Shen, H. C. *Angew. Chem., Int. Ed.* **2001**, *40*, 2313. (d) Trost, B. M.; Shen, H. C.; Horne, D. B.; Toste, E. D.; Steinmetz, B. G.; Koradin, C. *Chem. Eur. J.* **2005**, *11*, 2577.

(15) Trost, B. M.; Pinkerton, A. B.; Toste, F. D.; Sperrle, M. *J. Am. Chem. Soc.* **2001**, *123*, 12504.

(16) Trost, B. M.; Toste, F. D. *Angew. Chem., Int. Ed.* **2001**, *40*, 1114.

(17) Gaussian 09, *Rev. B.01*: Frisch, M. J.; *et al.*, Gaussian, Inc., Wallingford CT, 2010.

(18) Zhao, Y.; Truhlar, D. G. *Theor. Chem. Acc.* **2008**, *120*, 215.

(19) Legault, C. Y. CYLView, 1.0b; Universite ´ de Sherbrooke, Canada, 2009; <http://www.cylview.org>.

(20) This possibility is being explored computationally, and suggests that the preferred pathway might be controlled by influence of ligands to control the oxidation potential of the metal.

(21) Free energy surface scan from **5A** to **7A** indicates the dissociation of acetonitrile ligand with the C-C bond formation.

(22) The direct isomerization between **22** and **22-C2** is possible but requires a higher barrier (22.6 kcal/mol).

## **Chapter 2. The Mechanism and Origins of Ligand-Controlled Selectivities in [Ni(NHC)]-catalyzed Intramolecular (5+2) Cycloadditions and Homo-Ene Reactions: A Theoretical Study**

## 2.1 Abstract

The mechanism and origins of selectivities in [Ni(NHC)]-catalyzed intramolecular (5+2) cycloadditions and homo-ene reactions of vinylcyclopropanes (VCPs) and alkynes have been studied using density functional theory. The preferred mechanism involves oxidative alkyne-alkene cyclization to form a metallacyclopentene intermediate, in contrast to cyclopropane cleavage pathway in the reaction with Rh(I) catalysts. The selectivity between the (5+2) and homo-ene products is determined in the subsequent competing reductive elimination and  $\beta$ -hydride elimination steps. Two similar-sized N-heterocyclic carbene (NHC) ligands, SIPr and *I*tBu yielded reversed product selectivity, favoring the (5+2) and homo-ene products respectively. This is attributed to the anisotropic steric environment of these NHC ligands, which position the bulky substituents on the ligand to different directions and leads to distinct steric control in the reductive elimination and  $\beta$ -hydride elimination transition states.

## 2.2 Introduction

As a structural core in a large number of biologically important natural products, functionalized seven-membered rings are targets for numerous synthetic studies. Among the current methodologies, transition-metal-catalyzed (5+2) cycloadditions of vinylcyclopropanes (VCPs) with  $2\pi$  components such as alkynes, alkenes, and allenes provide a step-economical

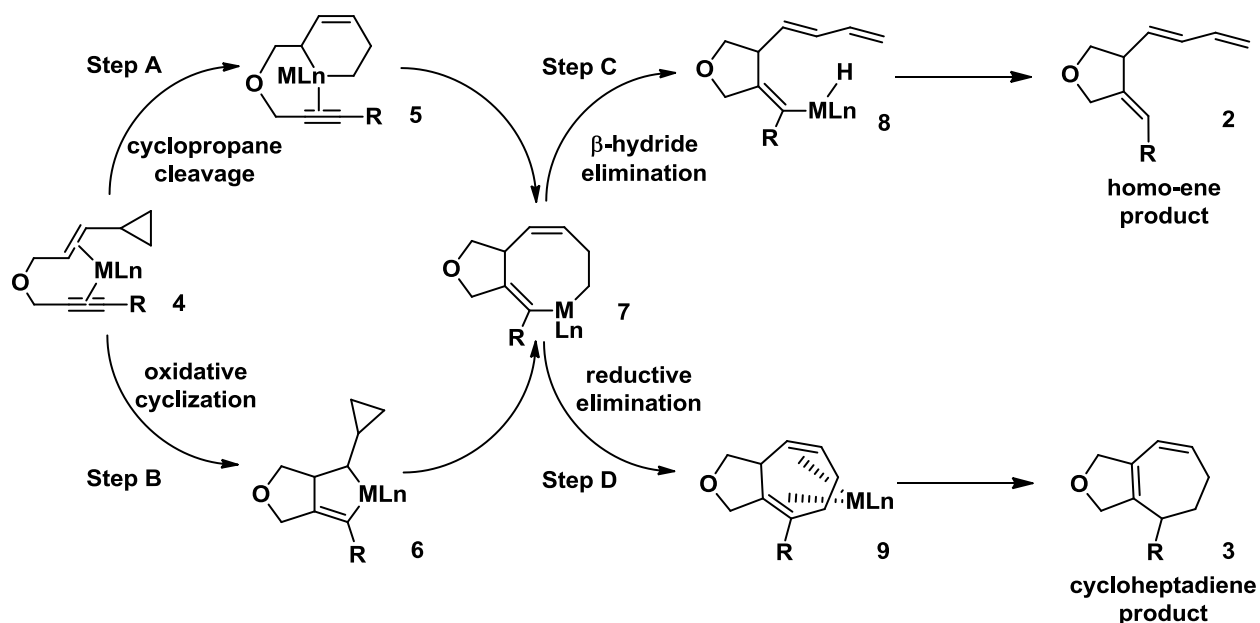


methodology for the synthesis of functionalized cycloheptadienes.<sup>1</sup> Since the first report using Rh(I) catalyst by Wender et al,<sup>2</sup> various transition metal catalysts including rhodium,<sup>3</sup> ruthenium,<sup>4</sup> nickel,<sup>5</sup> and iron<sup>6</sup> have shown promising catalytic activities in this methodology. The (5+2) reaction also led to the discovery of (5+1), (5+2+1) and other cycloadditions employing vinylcyclopropane or its analogues as building blocks.<sup>7</sup>

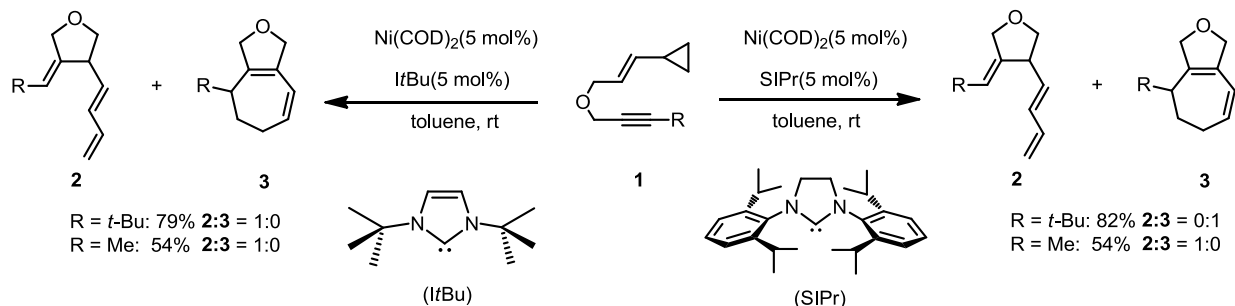
In contrast to the vast aspects of experimental investigations on this reaction, computational studies have only been focused on Rh-catalyzed reactions to date.<sup>8</sup> The effects of metal catalysts on the mechanism and selectivity are still not clear. Especially, although all (5+2) cycloadditions are likely to occur via a metallacyclooctadiene intermediate (**7**, Scheme 2.1), the mechanism leading to the formation of this intermediate may be different when different metal catalysts are employed. Previous computational studies indicated that the cycloadditions with Rh catalysts occur via cleavage of the cyclopropane to form the metallacyclohexene intermediate **5** followed by alkyne insertion to form intermediate **7** (Step A, Scheme 2.1). The alternative mechanism involving oxidative cyclization of alkyne and the alkenyl group on VCP to form the metallacyclopentene intermediate **6** (Step B) is not favorable with Rh. Since vinylcyclopropane is a widely used synthon, whether it behaves as a 2C or 5C component at the initial step with different transition metal catalysts not only directly relates to the mechanism in the (5+2) cycloadditions but also impacts the synthetic utility of VCPs in other transition-metal-catalyzed reactions.

In addition to the uncertainty of the initial steps in the mechanism, the metal catalysts may also affect the mechanism in the subsequent steps after formation of the metallacyclooctadiene intermediate. Unique among all metal catalysts for (5+2) cycloadditions, nickel shows strong ligand control on the selectivity of the (5+2) cycloaddition product (**3**) and a homo-ene product

(2).<sup>9</sup> Using the SIPr (1,3-bis(2,6-diisopropylphenyl)imidazolidene) ligand, the selectivity between the cycloheptadiene product **3** and homo-ene product **2** depends upon the nature of the terminal alkyne substituent. In contrast, the reaction with the *I*Bu ligand gives only the homo-ene product **2** regardless of the terminal alkyne substituent (Scheme 2.2). In addition, the tether between the VCP and  $2\pi$  component has no significant effect on the selectivity.<sup>10</sup>



**Scheme 2.1.** Postulated mechanisms for transition metal-catalyzed (5+2) cycloadditions.



**Scheme 2.2.** Nickel-NHC catalyzed intramolecular (5+2) cycloaddition and homo-ene reaction of alkyne and VCP.

Apparently, the selectivity between the cycloheptadiene and the homo-ene products is controlled by the preference for the  $\beta$ -hydride elimination and the reductive elimination pathways after the formation of the metallacyclooctadiene intermediate. Controlling the competition between reductive elimination and  $\beta$ -hydride elimination to prevent side reactions<sup>11</sup> and catalyst decomposition<sup>12</sup> is a persistent challenge in many transition metal-catalyzed C–C bond formation reactions. In order to achieve better synthetic utility, great efforts have been made to control these competitive steps by optimization of substrate,<sup>13</sup> counterion,<sup>14</sup> and especially the type and size of ligand.<sup>15</sup> Since SIPr and ItBu are both electron-rich NHC ligands, their steric properties are most likely controlling the selectivity. Based on the widely applied “buried volume” ( $\%V_{\text{bur}}$ ) model,<sup>16</sup> which describes the average bulkiness of the ligand, ItBu ( $35.5\% V_{\text{bur}}$ )<sup>15e</sup> and SIPr ( $35.7\% V_{\text{bur}}$ )<sup>16e</sup> have almost identical steric bulk. Why do these two NHC ligands with similar steric and electronic properties lead to reversed selectivity between  $\beta$ -hydride elimination and reductive elimination? Here we report DFT calculations on the transition states of the competing pathways and analyze the effects of the shape of NHC ligands, *i.e.* the orientation of the bulky substituents, with the steric contour model. We<sup>17</sup> and Cavallo<sup>18</sup> have employed the steric contour model to highlight the importance of the anisotropic steric environment of NHC ligands in determining regio- and

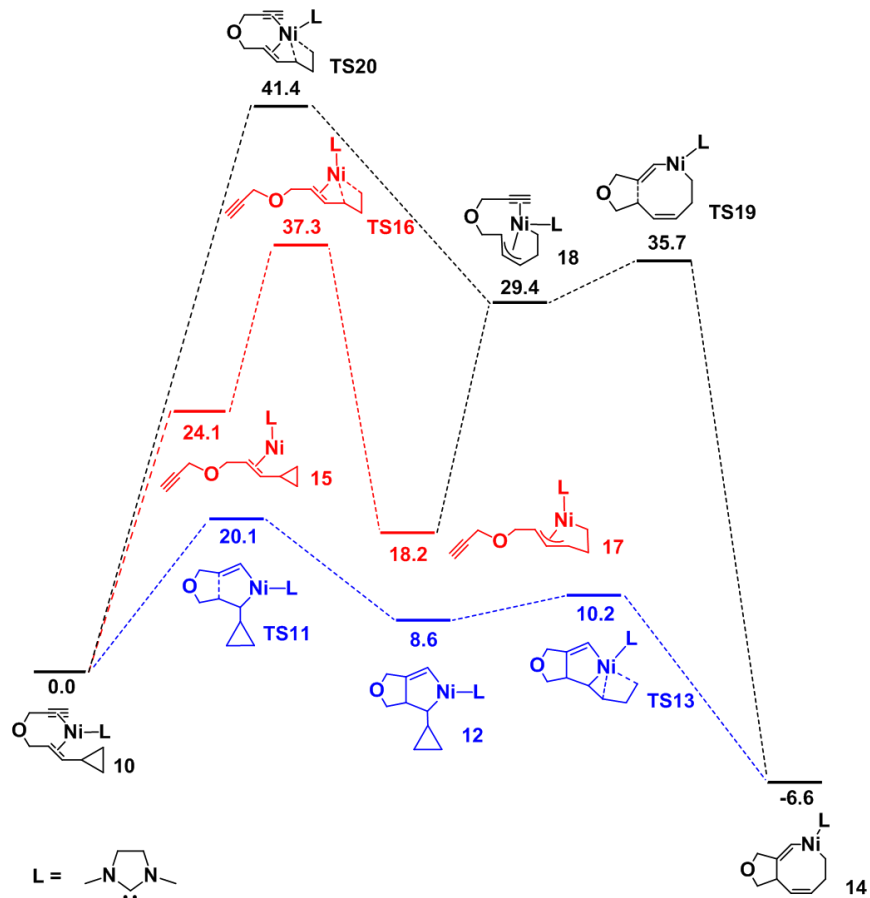
stereoselectivities. In this report, we present the first example that the shape and orientation of the NHC ligand affects the mechanism and prevents  $\beta$ -hydride elimination from the metallacycle.

### 2.3 Computational Details

Geometry optimizations, frequencies, and solvation energy calculations were performed with the B3LYP functional implemented in Gaussian 09.<sup>19</sup> The Stuttgart/Dresden effective core potential (SDD) was used for nickel. For all other atoms, the 6-31G(d) basis set was employed in geometry optimizations and the 6-311+G(2d,p) basis set was employed for all other atoms in single point solvation energy calculations. All reported free energies involve zero-point vibrational energy corrections, thermal corrections to Gibbs free energy at 298 K, DFT-D3 dispersion corrections,<sup>20</sup> and solvation free energy corrections computed by single point CPCM calculations on gas-phase optimized geometries. Toluene was used in the CPCM calculations for consistency with experiment. The molecular cavities were built up using the United Atom Topological Model (UAHF) and extra sphere was added on transferred hydrogen of **TS25** and **TS29**. Figures 2.2, 2.4, 2.6, and 2.7 were prepared using CYLView.<sup>21</sup>

## 2.4 Results and Discussion

### 2.4.1 Mechanism of Formation of the Metallacyclooctadiene Intermediate



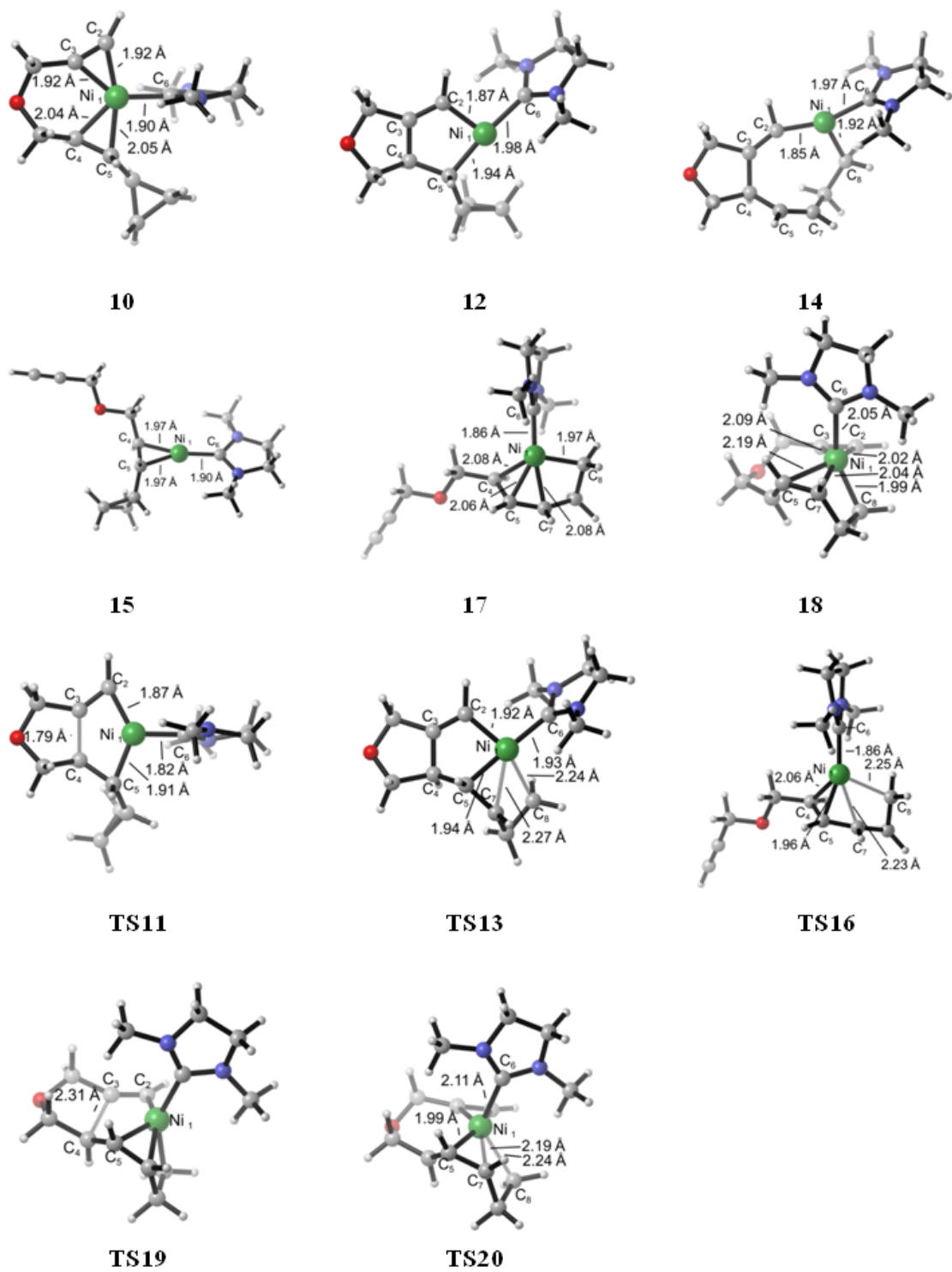
**Figure 2.1.** Gibbs free energies for [Ni(NHC)]-catalyzed cycloaddition from substrate coordinated complex to metallacyclooctadiene intermediate. The favored oxidative cyclization pathway is shown in blue, while the black and red indicate the cyclopropane cleavage pathway with alkyne coordination before (black) or after (red) VCP cleavage. Energies are given in kcal/mol.<sup>22</sup>

The possible pathways of the transformation of the substrate coordinated complex **10** to the metallacyclooctadiene intermediate **14** are computed and summarized in Figure 2.1. The

structures of selected intermediates and transition states are shown in Figure 2.2. A model NHC ligand, 1,3-dimethylimidazolidine, was employed in the investigation of mechanisms.

To form the metallacyclooctadiene intermediate, formation of one C–C bond and two Ni–C bonds are the fundamental steps, and the order of these steps determines whether the oxidative cyclization mechanism via the metallacyclopentene intermediate **12** or the cyclopropane cleavage mechanism via the metallacyclohexene intermediate **18** is involved.<sup>23</sup> In the oxidative cyclization mechanism (highlighted in blue in Figure 2.1), complex **10** initially undergoes C–C bond formation via transition state **TS11** (20.1 kcal/mol) to give the metallacyclopentene intermediate **12** (8.6 kcal/mol). Subsequent cleavage of the cyclopropane is more facile with a 1.6 kcal/mol barrier to give the stable metallacyclooctadiene intermediate **14** (-6.6 kcal/mol). On the other hand, initial cleavage of the cyclopropane to give the metallacyclohexene intermediate **18** (29.4 kcal/mol) is very different. The cyclopropane cleavage can occur in two ways.<sup>24</sup> Figure 2.1 shows that whether the alkyne is coordinated to the metal in the TS or not (**TS20** and **TS16**, respectively), the reaction requires a much higher barrier than the oxidative cyclization (**TS11**). Although [Ni(NHC)] can promote the rearrangement of vinylcyclopropane to cyclopentene via cyclopropane cleavage,<sup>24</sup> it is not likely to occur in this reaction. The main reason is the strong intramolecular coordination with alkyne. The dissociation of alkyne from the catalyst resting state **10** requires 24.1 kcal/mol. This contributes to the high barrier of cyclopropane cleavage transition state **TS16**. The cyclopropane cleavage transition state involves coordination of the alkyne (**TS20**) requires even higher activation energy than **TS16**. This is attributed to the formation of unstable intermediate (**18**) in this pathway. Thus the most preferred pathway in [Ni(NHC)] catalyzed (5+2) cycloadditions initiates via oxidative alkyne-alkene cyclization to form the metallacyclopentene intermediate **12**.<sup>25</sup> This is contrast to the Rh(I) catalyst from our previous theoretical studies.<sup>8</sup> In

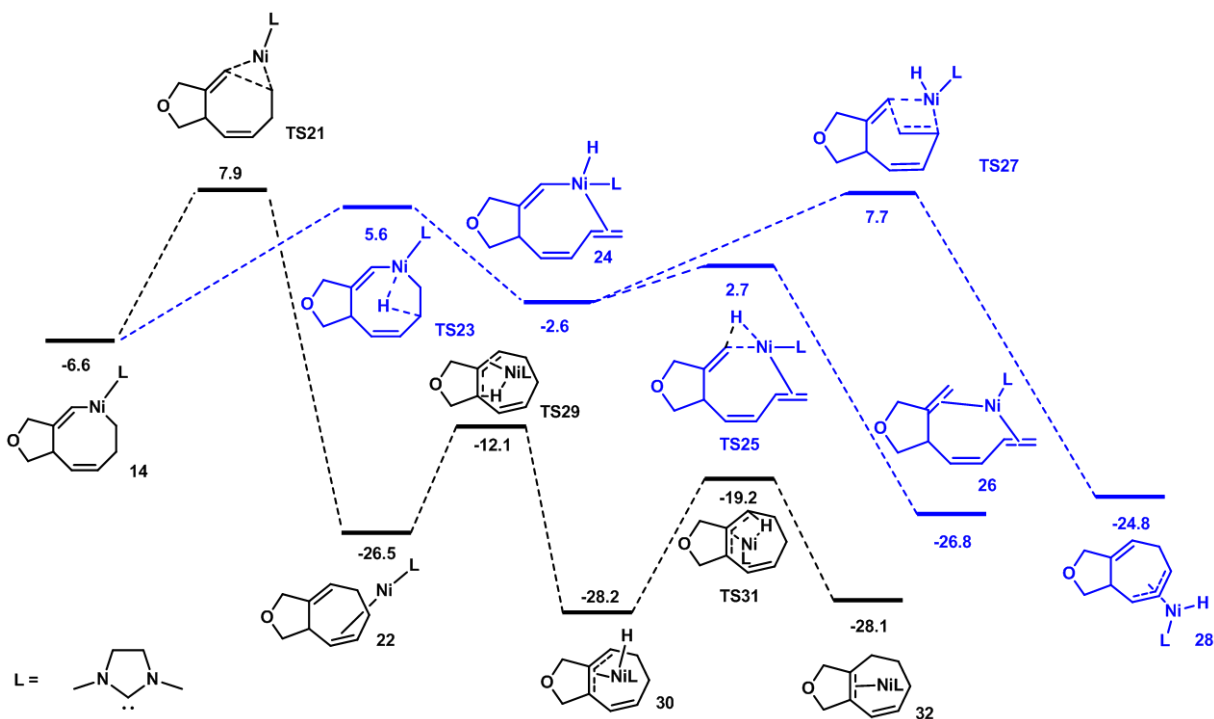
$[\text{Rh}(\text{CO})_2\text{Cl}]_2$  catalyzed intermolecular (5+2) cycloadditions of VCP and acetylene, the cyclopropane cleavage pathway is preferred by 7.8 kcal/mol. This reversed preference arises from two parts. First, the electron-rich NHC ligand stabilizes the 14 electron oxidative coupling transition states **TS11** dramatically with only 20.1 kcal/mol barrier. In  $[\text{Rh}(\text{CO})_2\text{Cl}]_2$ , this step requires a barrier of 29.7 kcal/mol in intermolecular reaction. Also, the relative stability between intermediate **10** and **15** are very different between nickel and rhodium complexes. From the triangular geometry **15**, the rotation of cyclopropane will not provide any favorable agostic interaction to replace alkyne coordination as in rhodium complex. Therefore, rhodium and nickel have different preference between metallacyclohexene and metallacyclopentene pathways.



**Figure 2.2.** Optimized structures and bond distances of selected intermediates and transition states in Figure 2.1.



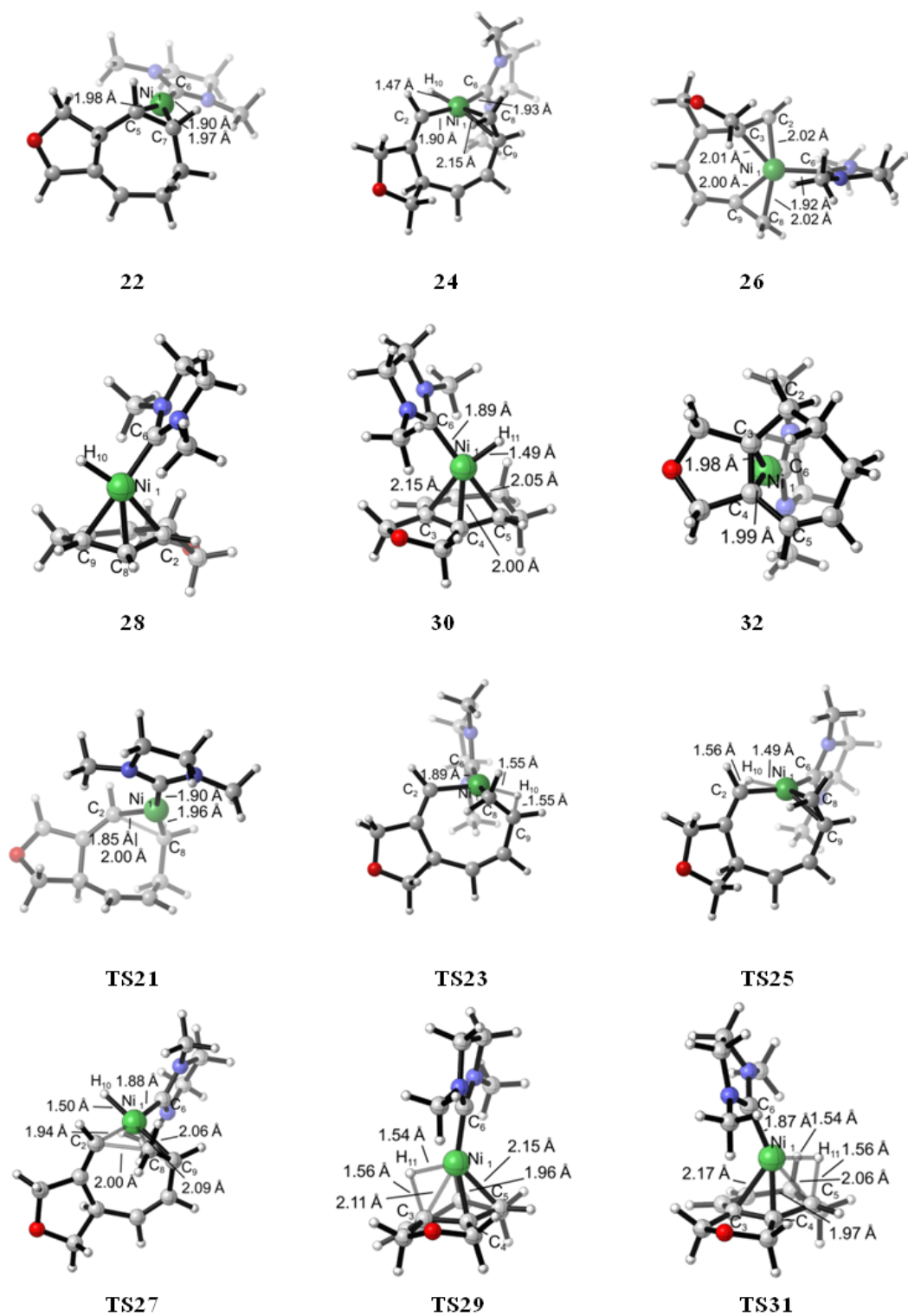
## 2.4.2 Mechanism of Formation of (5+2) Cycloaddition and Homo-Ene Products



**Figure 2.3.** Gibbs free energies of the [Ni(NHC)]-catalyzed (5+2) cycloaddition and homo-ene reaction from the metallacyclooctadiene intermediate **14**. The (5+2) cycloaddition pathway is shown in black and the homo-ene pathway is shown in blue. Energies are given in kcal/mol.

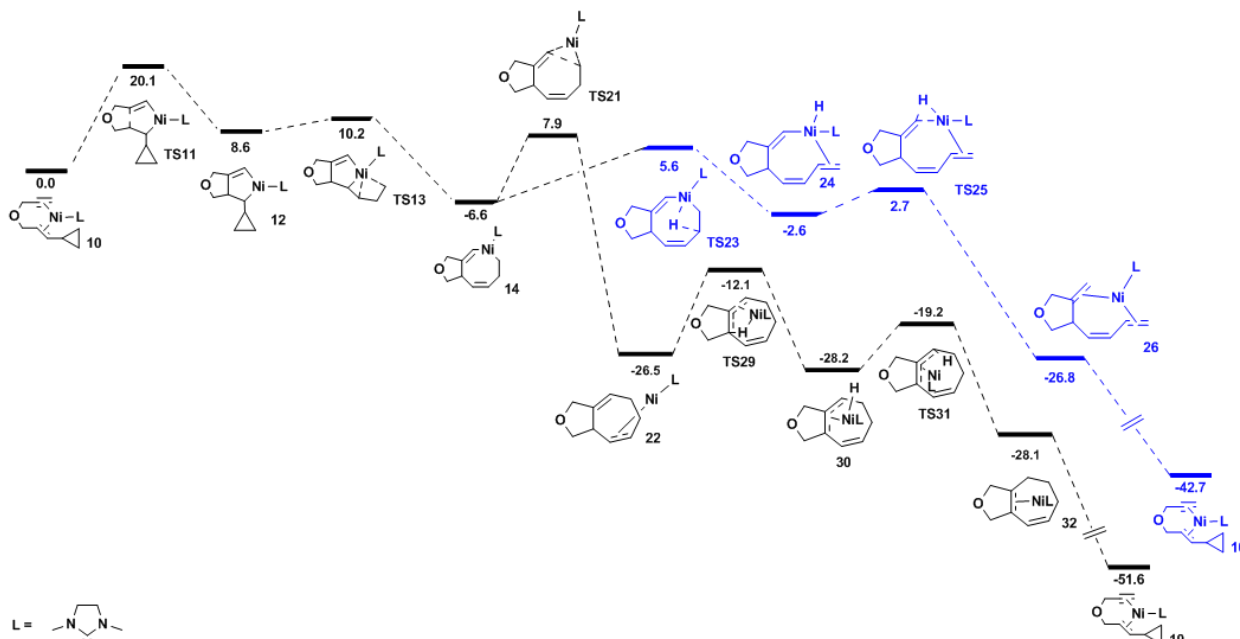
From the metallacyclooctadiene intermediate **14** (-6.6 kcal/mol with respect to the reactant complex **10**), there are two different pathways. First, direct C-C reductive elimination could occur via transition state **TS21** (7.9 kcal/mol), leading to the cycloheptadiene product **22** (-26.5 kcal/mol). Then diene isomerization occurs via transition state **TS29** (-12.1 kcal/mol), generating an allyl nickel(II) hydride intermediate **30** (-28.2 kcal/mol). From **30**, reductive elimination occurs via **TS31** (-19.2 kcal/mol), leading to a more stable conjugated diene product complex **32** (-28.1

kcal/mol). The overall barrier for cycloheptadiene generation is only 14.5 kcal/mol (**14** to **TS21**). Alternatively,  $\beta$ -hydride transfer could occur through **TS23** (5.6 kcal/mol), forming a tetracoordinated nickel(II) hydride complex **24** (-2.6 kcal/mol). This relatively unstable intermediate undergoes C-H reductive elimination to form the triene product **26** (-26.8 kcal/mol) via transition state **TS25** (2.7 kcal/mol). A possible alkene insertion transition state **TS27** (7.7 kcal/mol) from **24** was also located, generating a nickel hydride complex **28**. In principle, **28** can further undergo C-H reductive elimination and generate the intermediate **22** and eventually the seven-membered ring product. Therefore, **TS21** and **TS27** are very competitive with the model ligand and further calculations with the experimental ligand SIPr were conducted to determine the favored pathway for cycloheptadiene formation. **TS21-SIPr** is 4.6 kcal/mol more stable than **TS27-SIPr**, suggesting that C-C reductive elimination and  $\beta$ -hydride elimination pathways (**TS21** and **TS23**) are the selectivity-determining steps for (5+2) cycloaddition and homo-ene reaction.



**Figure 2.4.** Optimized structures and bond distances of selected intermediates and transition states in Figure 2.3.

### 2.4.3 The Catalytic Cycle



**Figure 2.5.** Gibbs free energies of preferred mechanism for [Ni(NHC)]-catalyzed (5+2) cycloaddition (black) and homo-ene reaction (blue). Energies are Gibbs free energies given in kcal/mol.

The full catalytic cycles for [Ni(NHC)]-catalyzed (5+2) cycloaddition and homo-ene reaction are shown in Figure 2.5. The substrate coordinated nickel complex **10**, is the most stable intermediate in both catalytic cycles and the resting state. Complex **10** undergoes alkyne-alkene cyclization to form a metallacyclopentene intermediate **12**. Subsequent cyclopropane cleavage of **12** leads to metallacyclooctadiene intermediate **14**. From intermediate **14**, the reductive elimination produces the cycloheptadiene complex **22** or  $\beta$ -hydride elimination occurs through transition state **TS23** to eventually give triene complex **26**. The isomerization from **22** is facile and further produces the observed cycloheptadiene coordinated complex **32**. The liberation of the product

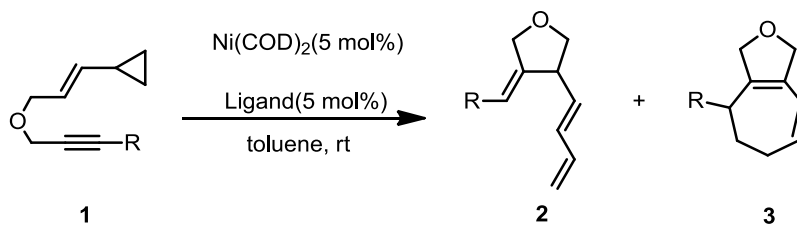
from product complexes **32** and **26** to regenerate the Ni-reactant complex **10** are both highly exothermic. The predicted barrier of 20.1 kcal/mol is consistent with experimental conditions.<sup>26</sup>

#### 2.4.4 Selectivities between (5+2) and Homo-Ene Products with SIPr Ligand

When the SIPr ligand is employed, the preference for the formation of **2** or **3** relies on the terminal alkyne substituent in the substrate (Table 2.1).<sup>5</sup> When the alkyne substituent is small, e.g. methyl or ethyl, the major product is triene **2**. With a bulky substituent, such as isopropyl or tertiary-butyl, cycloheptadiene **3** is formed. The catalytic cycles (shown in Figure 2.5) indicated the selectivity of the triene (**2**) and cycloaddition (**3**) products is determined by the energy difference between **TS23** and **TS21**. The transition states in reactions with the SIPr ligand and substrates with various alkyne substituents were computed.

Table 2.1 shows the computational and experimental selectivities between **2** and **3**. Computations predicted the same trend of selectivity as the experiment. In the reactions with the SIPr ligand, bulkier alkyne substituents (e.g. R = *t*-Bu or TMS, entries 4 and 5) prefer the cycloaddition product **3**, while in the reaction with the *I*tBu ligand, the triene product **2** is favored (entry 6). In cases where moderate selectivities were observed experimentally (entries 2 and 3), computation showed a greater preference for **3** than experiment.

**Table 2.1.** Theoretical and experimental selectivities between triene **2** and cycloheptadiene **3** with SIPr and *It*Bu ligands and substrates with various terminal substituents.<sup>a</sup> Energies are in kcal/mol.



entry	R	Ligand	$\Delta\Delta G^\ddagger(2-3)^b$	2:3 <sup>theo</sup>	2:3 <sup>exp</sup>
1 <sup>c</sup>	Me	SIPr	-0.8	85:15	100:0
2	Et	SIPr	2.0	5:95	60:40
3	<i>i</i> -Pr	SIPr	2.6	1:99	33:67
4	<i>t</i> -Bu	SIPr	3.5	0:100	0:100
5	TMS	SIPr	6.1	0:100	0:100
6	<i>t</i> -Bu	<i>It</i> Bu	-1.2	90:10	100:0

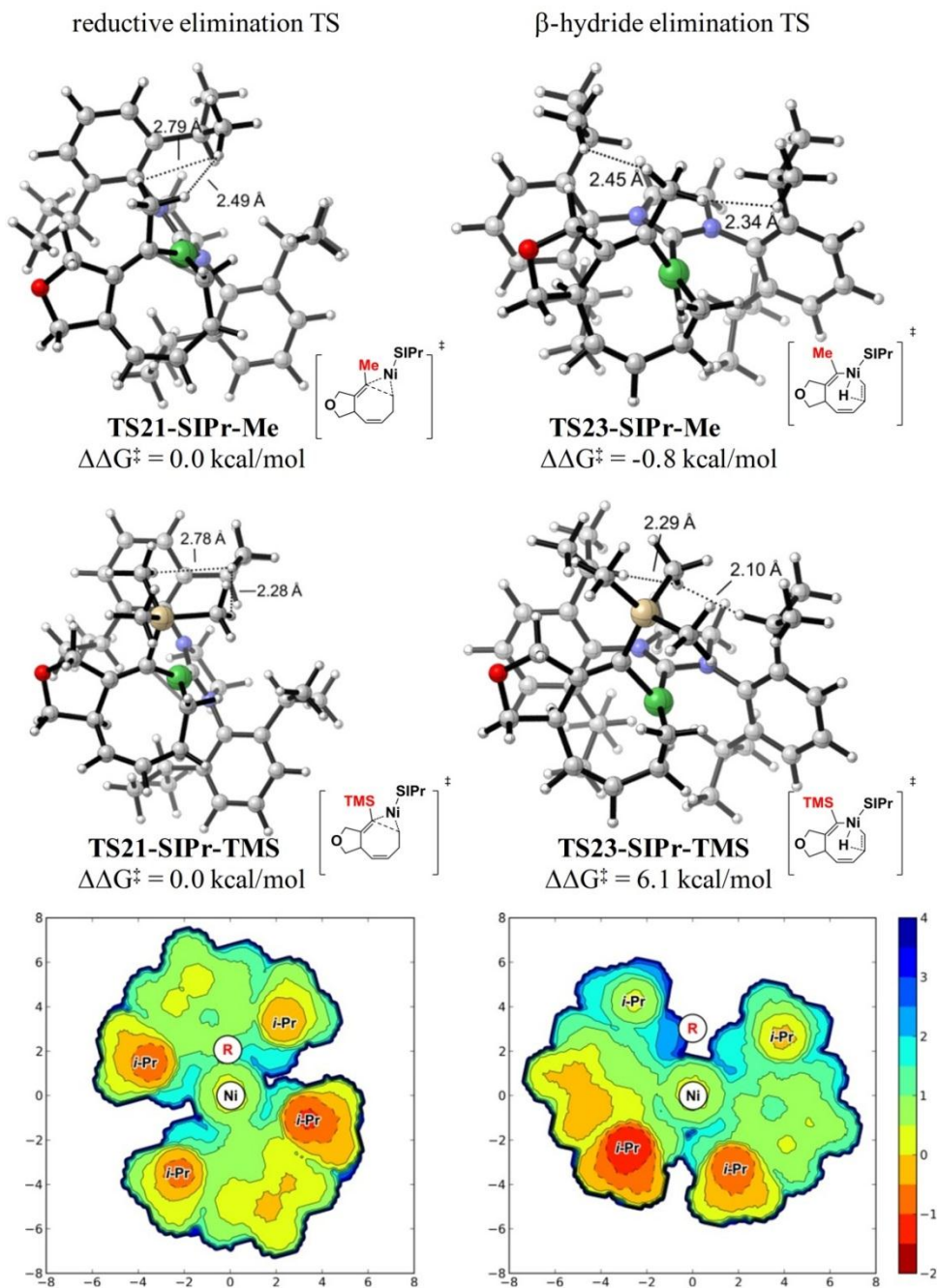
<sup>a</sup> M06 method also produces the same trend with a small preference to (5+2) cycloaddition, detailed results are listed in SI.

<sup>b</sup> The selectivity between pathways leading to products **2** and **3** is calculated from the activation free energy difference between **TS23** and **TS21**.

<sup>c</sup> Replacing the oxygen by NTs in the tether changed the  $\Delta\Delta G^\ddagger(2-3)$  to 0.2 kcal/mol. Detailed results are listed in the SI.

Figure 2.6 shows the transition states in the reactions with Me and TMS substituted substrates and the SIPr ligand. For each reaction, both the reductive elimination transition state (**TS21**) leading to the (5+2) cycloaddition product and the  $\beta$ -hydride elimination transition state

(**TS23**) leading to the homo-ene product are shown. The conformation of the metallacycle in **TS21** and **TS23** are similar, while the orientations of the SIPr ligand are noticeably different. In the reductive elimination transition state (**TS21**), the imidazolidine ring is in the same plane with the Ni and the forming carbon–carbon bond. In contrast, in the  $\beta$ -hydride elimination transition state (**TS23**), the imidazolidine ring is perpendicular to the plane of Ni and the two  $\alpha$ -carbon atoms. To illustrate the different orientations of the NHC ligands, 2D contour maps of the van der Waals surface of the SIPr ligand in transition states **TS21** and **TS23** are generated and shown in Figure 2.6. The red region in the contour plot indicates the ligand is closer to the substrate and the blue region indicates the ligand is farther away from the substrate. The “R” marks the  $\alpha$ -positions of the terminal alkyne substituent. In the  $\beta$ -hydride elimination transition state (**TS23**), the alkyne substituent (R) is placed adjacent to two *i*-Pr groups. In contrast, in the reductive elimination transition state (**TS21**), the alkyne substituent (R) is placed under the phenyl rings and the distances between R and *i*-Pr groups are greater than those in **TS23**. In reactions with bulky alkyne substituents, the  $\beta$ -hydride elimination transition state is disfavored due to steric repulsions with the *i*-Pr groups on the ligand. For example, in **TS23-SIPr-TMS** (R = TMS), the shortest H-H distance between TMS and *i*-Pr groups is only 2.10 Å. In **TS21-SIPr-TMS**, the distance between TMS and *i*-Pr become longer, the shortest H-H distance is 2.28 Å. Thus,  $\beta$ -hydride elimination (**TS23-SIPr-TMS**) is disfavored by 6.1 kcal/mol. When the alkyne substituent is small (*e.g.* R = Me), the steric effects are diminished and  $\beta$ -hydride elimination becomes favorable over reductive elimination.<sup>27</sup>

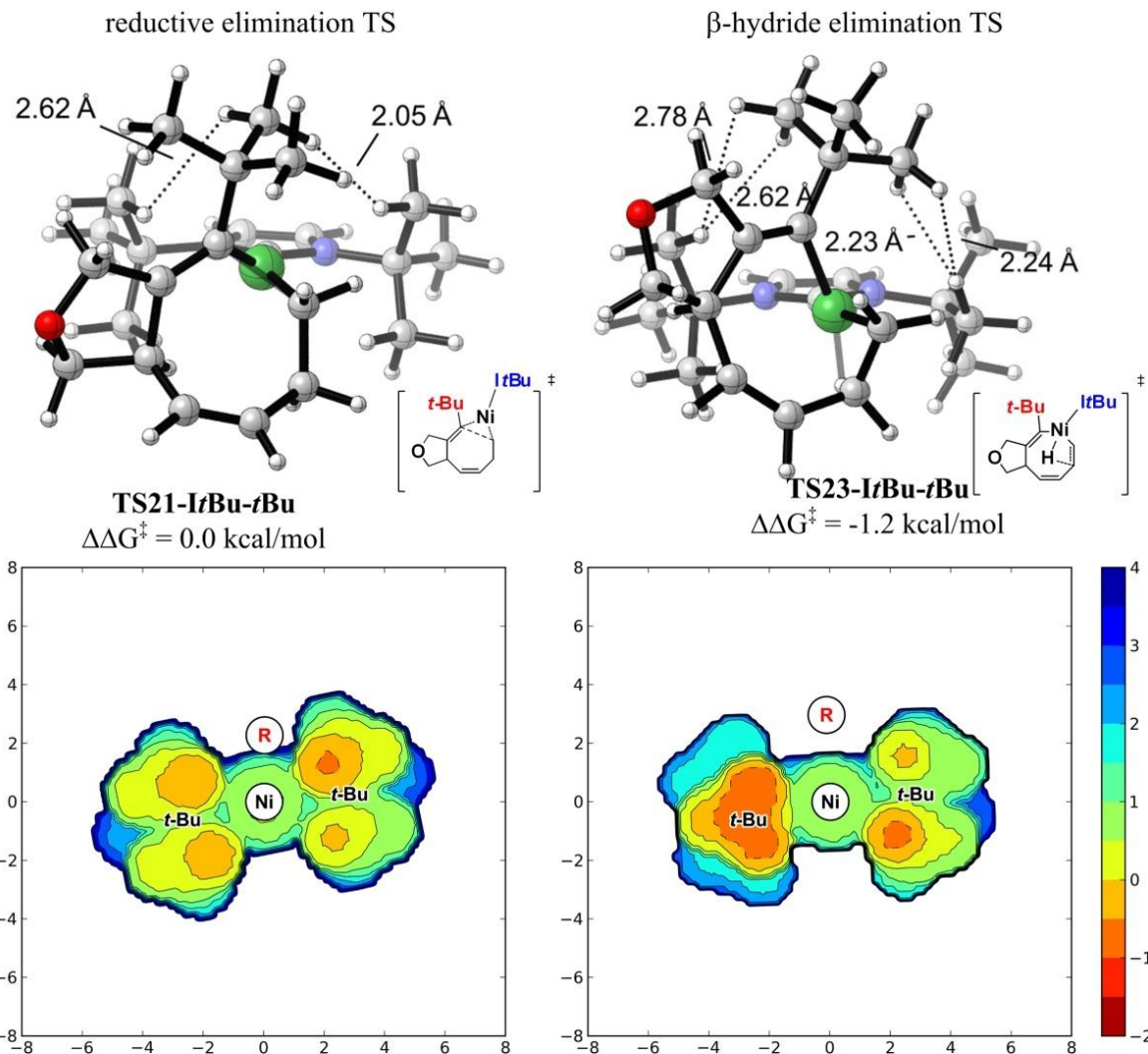


**Figure 2.6.** Optimized transition structures of Me and TMS substituted **TS21** (reductive elimination in the (5+2) pathway) and **TS23** ( $\beta$ -hydride elimination in the homo-ene pathway) with the SIPr ligand. Steric contour plots of the SIPr ligand are shown for both TSs and illustrate the different orientations of the NHC ligand in **TS21** and **TS23**. Ni is located at the origin of the coordinate system in the contour plots. Contour line of zero is defined as in the same plane of the Ni atom. Negative distance (red) indicates the ligand is closer to the substrate; positive distance (blue) indicates the ligand is farther away from substrate. Distances are in Å.



#### 2.4.5 Selectivities between (5+2) and Homo-Ene Products with *ItBu* Ligand

The buried volume of the *ItBu* ligand (35.5%) is almost identical to that of SIPr (35.7%). This suggests the overall bulkiness of these ligands is similar. However, the reaction with the *ItBu* ligand gives reversed selectivity compared to the SIPr ligand (entries 6 and 4, Table 2.1). The  $\beta$ -hydride elimination transition state **TS23-*ItBu-tBu*** is favored by 1.2 kcal/mol, leading to the homo-ene product, while in the reaction with SIPr ligand,  $\beta$ -hydride elimination is disfavored by 3.5 kcal/mol. The optimized transition structures of reductive elimination and  $\beta$ -hydride elimination with the *ItBu* ligand are shown in Figure 2.7. Ligand steric contour plots for these transition states are also illustrated. The ligand contour plots indicated the shape of the *ItBu* ligand is very different from the SIPr ligand, although their buried volume and overall bulkiness are similar. The most bulky regions on the *ItBu* ligand are the two *t*-Bu groups located in the same plane with the imidazolylidene ring. In the  $\beta$ -hydride elimination transition state (**TS23-*ItBu-tBu***), the orientation of the *ItBu* ligand is the same as the SIPr ligand (**TS23-SIPr-Me** and **TS23-SIPr-TMS**, Figure 2.6) and the smaller model ligand SIME (**TS23**, Figure 2.4): the alkyne substituent (marked with a red “R” in the contour plot) is placed perpendicular to the imidazolylidene ring, and thus no obvious steric repulsions with the ligand are observed. In the reductive elimination transition state (**TS21-*ItBu-tBu***), the *ItBu* ligand adopts a different orientation from those in the reductive elimination with the SIPr and SIME ligands (**TS21-SIPr-Me** and **TS21-SIPr-TMS**, Figure 2.6 and **TS21**, Figure 2.4). Steric repulsions with the *t*-Bu groups in the imidazolylidene plane forced the *ItBu* ligand to rotate almost 90 ° to place the alkyne substituent perpendicular to the imidazolylidene. The distance between the alkyne substituent and the *t*-Bu groups on the ligand is shorter in the reductive elimination TS than that in the  $\beta$ -hydride elimination TS.



**Figure 2.7.** Optimized transition structures of *t*-Bu substituted **TS21** (reductive elimination in the (5+2) pathway) and **TS23** ( $\beta$ -hydride elimination in the homo-ene pathway) with the *ItBu* ligand. Steric contour plots of the *ItBu* ligand are shown for both TSs and illustrate the orientations of the NHC ligand in **TS21** and **TS23**. Ni is located at the origin of the coordinate system in the contour plots. Contour line of zero is defined as in the same plane of the Ni atom. Negative distance (red) indicates the ligand is closer to the substrate; positive distance (blue) indicates the ligand is farther away from substrate. Distances are in Å.

## 2.5 Conclusions

The mechanism and selectivities of [Ni(NHC)]-catalyzed (5+2) cycloadditions and homo-ene reactions were studied theoretically. The origins of the selectivity of the cycloaddition and homo-ene products in reactions with different alkyne substituents and ligands were elucidated. The preferred catalytic cycle involves oxidative cyclization to form a metallacyclopentene intermediate, followed by cyclopropane cleavage to yield a metallacyclooctadiene intermediate. Subsequent direct C–C reductive elimination leads to the cycloheptadiene product, while  $\beta$ -hydride elimination and C–H reductive elimination lead to the homo-ene product. The selectivity is controlled by the shape and orientation of the NHC ligand. With the SIPr ligand, larger terminal alkyne substituents destabilize the  $\beta$ -hydride elimination transition state, leading to the (5+2) cycloaddition product. This is attributed to the steric repulsions with the *i*-Pr groups located perpendicular to the imidazolidine ring. With the *It*Bu ligand, the  $\beta$ -hydride elimination transition state leading to the homo-ene product is preferred.

## 2.6 References

(1) For recent reviews of transition-metal catalyzed (5+2) cycloadditions: (a) Wender, P. A.; Gamber, G. G.; Williams, T. J. in: *Modern Rhodium-Catalyzed Organic Reactions*, (Ed.: Evans, P. A.), Wiley-VCH, Weinheim, **2005**, pp 263-299. (b) Wender, P. A.; Croatt, M. P.; Deschamps, N. M. in: *Comprehensive Organometallic Chemistry III vol. 10*, (Eds.: Crabtree, R.H.; Mingos, D. M. P.), Elsevier, Oxford, **2007**, pp 603-647. (c) Butenschön, H. *Angew. Chem., Int. Ed.* **2008**, *47*, 5287. (d) Pellissier, H. *Adv. Synth. Catal.* **2011**, *353*, 189.

(2) Wender, P. A.; Takahashi, H.; Witulski, B. *J. Am. Chem. Soc.* **1995**, *117*, 4720.

(3) (a) Wender, P. A.; Rieck, H.; Fuji, M. *J. Am. Chem. Soc.* **1998**, *120*, 10976. (b) Wender, P. A.; Sperandio, D. *J. Org. Chem.* **1998**, *63*, 4164. (c) Gilbertson, S. R.; Hoge, G. S. *Tetrahedron Lett.* **1998**, *39*, 2075. (d) Wender, P. A.; Dyckman, A. J.; Husfeld, C. O.; Scanio, M. J. C. *Org. Lett.* **2000**, *2*, 1609. (e) Wang, B.; Cao, P.; Zhang, X. *Tetrahedron Lett.* **2000**, *41*, 8041. (f) Wender, P. A.; Barzilay, C. M.; Dyckman, A. J. *J. Am. Chem. Soc.* **2001**, *123*, 179. (g) Wender, P. A.; Gamber, G. G.; Scanio, M. J. C. *Angew. Chem., Int. Ed.* **2001**, *40*, 3895. (h) Wender, P. A.; Williams, T. J. *Angew. Chem., Int. Ed.* **2002**, *41*, 4550. (i) Wender, P. A.; Love, J. A.; Williams, T. J. *Synlett* **2003**, 1295. (j) Wegner, H. A.; de Meijere, A.; Wender, P. A. *J. Am. Chem. Soc.* **2005**, *127*, 6530. (k) Wender, P. A.; Haustedt, L. O.; Lim, J.; Love, J. A.; Williams, T. J.; Yoon, J.-Y. *J. Am. Chem. Soc.* **2006**, *128*, 6302. (l) Lee, S. I.; Park, Y.; Park, J. H.; Jung, G.; Choi, S. Y.; Chung, Y. K.; Lee, B. Y. *J. Org. Chem.* **2006**, *71*, 91. (m) Saito, A.; Ono, T.; Hanzawa, Y. *J. Org. Chem.* **2006**, *71*, 6437. (n) Gomez, F. J.; Kamber, N. E.; Deschamps, N. M.; Cole, A. P.; Wender, P. A.; Waymouth, R. M. *Organometallics* **2007**, *26*, 4541. (o) Shintani, R.; Nakatsu, H.; Takatsu, K.; Hayashi, T. *Chem. Eur. J.* **2009**, *15*, 8692. (p) Liu, P.; Sirois, L. E.; Cheong, P. H. Y.; Yu, Z. X.; Hartung, I. V.; Rieck, H.; Wender, P. A.; Houk, K. N. *J. Am. Chem. Soc.* **2010**, *132*, 10127. (q) Wender, P. A.; Stemmler, R. T.; Sirois, L. E. *J. Am. Chem. Soc.* **2010**, *132*, 2532. (r) Wender, P. A.; Sirois, L. E.; Stemmler, R. T.; Williams, T. J. *Org. Lett.* **2010**, *12*, 1604. (s) Wender, P. A.; Lesser, A. B.; Sirois, L. E. *Org. Synth.*, **2011**, *88*, 109.

(4) (a) Trost, B. M.; Toste, F. D.; Shen, H. *J. Am. Chem. Soc.* **2000**, *122*, 2379. (b) Trost, B. M.; Shen, H. C. *Org. Lett.* **2000**, *2*, 2523. (c) Trost, B. M.; Shen, H. C. *Angew. Chem., Int. Ed.* **2001**, *40*, 2313. (d) Trost, B. M.; Toste, F. D.; *Angew. Chem., Int. Ed.* **2001**, *40*, 1114. (e) Trost, B. M.; Shen, H. C.; Schulz, T.; *Org. Lett.* **2003**, *5*, 4149. (f) Trost, B. M.; Shen, H. C.; Horne, D. B.; Toste,

E. D.; Steinmetz, B. G.; Koradin, C. *Chem. Eur. J.* **2005**, *11*, 2577.

(5) Zuo, G.; Louie, J. *J. Am. Chem. Soc.* **2005**, *127*, 5798.

(6) Fürstner, A.; Majima, K.; Martin, R.; Krause, H.; Kattnig, E.; Goddard, R.; Lehmann, C. W. *J. Am. Chem. Soc.* **2008**, *130*, 1992.

(7) (a) Wender, P. A.; Gamber, G. G.; Hubbard, R. D.; Zhang, L. *J. Am. Chem. Soc.* **2002**, *124*, 2876. (b) Wender, P. A.; Gamber, G. G.; Hubbard, R. D.; Pham, S. M.; Zhang, L. *J. Am. Chem. Soc.* **2005**, *127*, 2836. (c) Wang, Y.; Wang, J.; Su, J.; Huang, F.; Jiao, L.; Liang, Y.; Yang, D.; Zhang, S.; Wender, P. A.; Yu, Z.-X. *J. Am. Chem. Soc.* **2007**, *129*, 10060. (d) Jiao, L.; Ye, S. Y.; Yu, Z.-X. *J. Am. Chem. Soc.* **2008**, *130*, 7178. (e) Huang, F.; Yao, Z.-K.; Wang, Y.; Wang, Y.; Zhang, J.; Yu, Z.-X. *Chem. Asian J.* **2010**, *5*, 1555. (f) Jiao, L.; Lin, M.; Yu, Z.-X. *Chem. Commun.* **2010**, *46*, 1059. (g) Jiang, G.-J.; Fu, X.-F.; Li, Q.; Yu, Z.-X., *Org. Lett.* **2012**, *14*, 692. (h) Lin, M.; Li, F.; Jiao, L.; Yu, Z.-X.; *J. Am. Chem. Soc.* **2011**, *133*, 1690. (i) Lin, M.; Kang, G.-Y.; Guo, Y.-A.; Yu, Z.-X. *J. Am. Chem. Soc.* **2012**, *134*, 398. (j) Liang, Y.; Jiang, X.; Fu, X.-F.; Ye, S.; Wang, T.; Yuan, J.; Wang, Y.; Yu, Z.-X. *Chem. Asian J.* **2012**, *7*, 593.

(8) (a) Yu, Z.-X.; Wender, P. A.; Houk, K. N. *J. Am. Chem. Soc.* **2004**, *126*, 9154. (b) Yu, Z.-X.; Cheong, P. H.-Y.; Liu, P.; Legault, C. Y.; Wender, P. A.; Houk, K. N. *J. Am. Chem. Soc.* **2008**, *130*, 2378. (c) Liu, P.; Cheong, P. H.-Y.; Yu, Z.-X.; Wender, P. A.; Houk, K. N. *Angew. Chem., Int. Ed.* **2008**, *47*, 3939. (d) Montero-Campillo, M. M.; Cabaleiro-Lago, E. M.; Rodriguez-Otero, J. *J. Phys. Chem. A* **2008**, *112*, 9068. (e) Xu, X.-F.; Liu, P.; Lesser, A.; Sirois, L. E.; Wender, P.

A.; Houk, K. N. *J. Am. Chem. Soc.* **2012**, *134*, 11012.

(9) Other products from different  $\beta$ -hydride eliminations can be formed through rhodium and ruthenium catalysts with various preferences. For rhodium catalyst, see: Wender, P. A.; Husfeld, C. O.; Langkopf, E.; Love, J. A. *J. Am. Chem. Soc.* **1998**, *120*, 1940-1941. For ruthenium catalyst, see ref 4.

(10) The oxygen, carbon and nitrogen tethers give similar selectivities with the same ligand and terminal alkyne substituent; see ref 5. Similar tether effects have also been found in many other related experimental studies on the transition-metal-catalyzed intramolecular cycloadditions involving VCP and  $2\pi$  components with Rh and Ru catalysts. Switching the tether only has limited effects on the selectivities; see ref 3(k), 4(f), 7(h) and 7(i).

(11) (a) Matas, I.; Campora, J.; Palma, P.; Alvarez, E. *Organometallics* **2009**, *28*, 6515. (b) Lan, Y.; Liu, P.; Newman, S. G.; Lautens, M.; Houk, K. N. *Chem. Sci.* **2012**, *3*, 1987.

(12) (a) Eisch, J. J.; Shi, X.; Owuor, F. A. *Organometallics* **1998**, *17*, 5219. (b) Eisch, J. J.; Owuor, F. A.; Shi, X. *Organometallics* **1999**, *18*, 1583. (c) Eisch, J. J.; Adeosun, A. A.; Dutta, S.; Fregene, P. O. *Eur. J. Org. Chem.* **2005**, 2657. (d) Hong, S. H.; Day, M. W.; Grubbs, R. H. *J. Am. Chem. Soc.* **2004**, *126*, 7414. (e) Rensburg, W. J.; Steynberg, P. J.; Meyer, W. H.; Kirk, M. M.; Forman, G. S. *J. Am. Chem. Soc.* **2004**, *126*, 14332. (f) Hong, S. H.; Wenzel, A. G.; Salguero, T. T.; Day, M. W.; Grubbs, R. H. *J. Am. Chem. Soc.* **2007**, *129*, 7961. (g) Herbert, M. B.; Lan, Y.; Keitz, B. K.; Liu, P.; Endo, K.; Day, M. W.; Houk, K. N.; Grubbs, R. H. *J. Am. Chem. Soc.* **2012**, *134*, 7861.

(13) For a recent view, see: Hartwig, J. *Inorg. Chem.* **2007**, *46*, 1936.

(14) For a recent review, see: Lu, X. -Y. *Top. Catal.* **2005**, *35*, 73.

(15) (a) Netherton, M. R.; Dai, C. -Y.; Neuschütz, K.; Fu, G. C. *J. Am. Chem. Soc.* **2001**, *123*, 10099. (b) Zhou, J.; Fu, G. C. *J. Am. Chem. Soc.* **2003**, *125*, 14726. (c) Han, C.; Buchwald, S. L. *J. Am. Chem. Soc.* **2009**, *131*, 7532. (d) Kambe, N.; Iwasaki, T.; Terao, J. *J. Chem. Soc. Rev.* **2011**, *40*, 4937.

(16) The buried volume of a ligand (%V<sub>bur</sub>) is defined as the percentage of volume occupied by the ligand in the first coordination sphere of the metal, see: (a) Hillier, A. C.; Sommer, W. J.; Yong, B. S.; Petersen, J. L.; Cavallo, L.; Nolan, S. P. *Organometallics* **2003**, *22*, 4322. (b) Dorta, R.; Stevens, E. D.; Scott, N. M.; Costabile, C.; Cavallo, L.; Hoff, C. D.; Nolan, S. P. *J. Am. Chem. Soc.* **2005**, *127*, 2485. (c) Cavallo, L.; Correa, A.; Costabile, C.; Jacobsen, H. *J. Organomet. Chem.* **2005**, *690*, 5407. (d) Poater, A.; Cavallo, L. *Dalton Trans.* **2009**, 8878. (e) Poater, A.; Cosenza, B.; Correa, A.; Giudice, S.; Ragone, F.; Scarano, V.; Cavallo, L. *Eur. J. Inorg. Chem.* **2009**, 1759. (f) Clavier, H.; Nolan, S. P. *Chem. Commun.* **2010**, *46*, 841. (g) Ragone, F.; Poater, A.; Cavallo, L. *J. Am. Chem. Soc.* **2010**, *132*, 4249.

(17) Liu, P.; Montgomery, J.; Houk, K. N.; *J. Am. Chem. Soc.*, **2011**, *133*, 6956.

(18) (a) Ragone, F.; Poater, A.; Cavallo, L., *J. Am. Chem. Soc.* **2010**, *132*, 4249. (b) Poater, A.;

Ragone, F.; Mariz, R.; Dorta, R.; Cavallo, L., *Chem. Eur. J.* **2010**, *16*, 14348. (c) Wucher, P.; Caporaso, L.; Roesle, P.; Ragone, F.; Cavallo, L.; Mecking, S.; Gottker-Schnetmann, I. *Proc. Natl. Acad. Sci.* **2011**, *108*, 8955.

(19) Gaussian 09, *Rev. B.01*: Frisch, M. J.; *et al.*, Gaussian, Inc., Wallingford CT, **2010**.

(20) For dispersion correction, see: (a) Grimme, S. *J. Comput. Chem.* **2006**, *27*, 1787. (b) Grimme, S.; Antony, J.; Ehrlich, S.; Krieg, H. *J. Chem. Phys.* **2010**, *132*, 154104. For examples of employing dispersion corrected DFT calculations: (c) Lonsdale, R.; Harvey, J. N.; Mulholland, A. *J. J. Phys. Chem. Lett.* **2010**, *1*, 3232. (d) McMullin, C. L.; Jover, J.; Harvey, J. N.; Fey, N. *Dalton Trans.* **2010**, *39*, 10833. (e) Comas-Vives, A.; Harvey, J. N. *Eur. J. Inorg. Chem.* **2011**, 5025. (f) Jacobsen, H.; Cavallo, L. *Chemphyschem.* **2012**, *13*, 562.

(21) Legault, C. Y. CYLView, 1.0b; Université de Sherbrooke, Canada, 2009; <http://www.cylview.org>.

(22) In the study of the mechanisms, 1,3-dimethylimidazolidine (SIME) was used as model ligand, which is represented by L in Figures 1, 3, and 5. The SIPr ligand was employed in test calculations for **TS11** and **TS19**. **TS11** is more than 20 kcal/mol more stable than **TS19** with the SIPr ligand, in agreement with calculations with the model ligand.



(23) For related discussion of the possible pathways: (a) Saito, N.; Tanaka, D.; Mori, M.; Sato, Y. *Chem. Rec.* **2011**, *11*, 186. (b) see ref 4(f).

(24) Wang, S. C.; Troast, D. M.; Conda-Sheridan, M.; Zuo, G.; LaGarde, D.; Louie, J.; Tantillo, D. J. *J. Org. Chem.*, **2009**, *74*, 7822.

(25) For related Ni-catalyzed cyclization of alkynes, see: (a) Kumar, P.; Prescher, S.; Louie, J. *Angew. Chem., Int. Ed.* **2011**, *50*, 10694. (b) Kumar, P.; Troast, D. M.; Cella, R.; Louie, J. *J. Am. Chem. Soc.* **2011**, *133*, 7719. (c) Stolley, R. M.; Maczka, M. T.; Louie, J. *Eur. J. Org. Chem.* **2011**, *20*, 3815. (d) Kumar, P.; Louie, J. *Org. Lett.* **2012**, *14*, 2026.

(26) Experimentally, the reaction is complete at room temperature within several hours, suggesting the overall barrier of reaction is around 20 kcal/mol.

(27) For recent examples of DFT studies, in which the steric effect of ligand or substrate is crucial for the selectivity, see: (a) Zhou, J.-L.; Liang, Y.; Deng, C.; Zhou, H.; Wang, Z.; Sun, X.-L.; Zheng, J.-C.; Yu, Z.-X.; Tang, Y. *Angew. Chem., Int. Ed.* **2011**, *50*, 7874. (b) Qu, J.-P.; Liang, Y.; Xu, H.; Sun, X.-L.; Yu, Z.-X.; Tang, Y. *Chem. Eur. J.* **2012**, *18*, 2196. (c) Yu, H.-Z.; Jiang, Y.-Y.; Fu, Y.; Liu, L. *J. Am. Chem. Soc.*, **2010**, *132*, 18078.

## Chapter 3. The Terminal Methyl Effects in Rh(I)-catalyzed Intermolecular (5+2)

### Cycloadditions of Vinylcyclopropanes: Origins of Substituent Effects on Reactivity and Chemoselectivity of Allenes

#### 3.1 Abstract

Allenenes constitute one of the four major classes of pi-reactive building blocks in organic synthesis. They engage as 2-carbon components in a wide range of metal-catalyzed reactions. Wender and co-workers discovered that the methyl substituents of terminal allene double bond are critical for reactivities of allenenes in  $[\text{Rh}(\text{CO})_2\text{Cl}]_2$ -catalyzed intermolecular (5+2) cycloadditions with vinylcyclopropanes (VCPs). Such terminal methyl effects also present in Rh(I)-catalyzed intermolecular (4+2) cycloadditions of allene-enes and alkenes. This unique reactivity of allene contrasts many reported Rh(I)-catalyzed intramolecular ( $m+n$ ) and ( $m+n+o$ ) cycloadditions because both substituted and unsubstituted allenenes generally work well. Through density functional theory (DFT) calculations and experiment, we explored the enigmatic reactivity and selectivity of allenenes in  $[\text{Rh}(\text{CO})_2\text{Cl}]_2$ -catalyzed intermolecular (5+2) cycloadditions with VCPs. The apparently low reactivity of terminally unsubstituted allenenes is due to a competing allene dimerization that irreversibly sequesters rhodium. With terminally substituted allenenes, steric repulsions between the terminal substituents significantly increase the barrier of allene dimerization while the barrier of (5+2) cycloaddition is not affected, and thus the cycloaddition prevails. Computations also revealed the origins of chemoselectivities of (5+2) cycloadditions with allene-ynes. Although simple allene and acetylene have similar insertion barriers, intermolecular

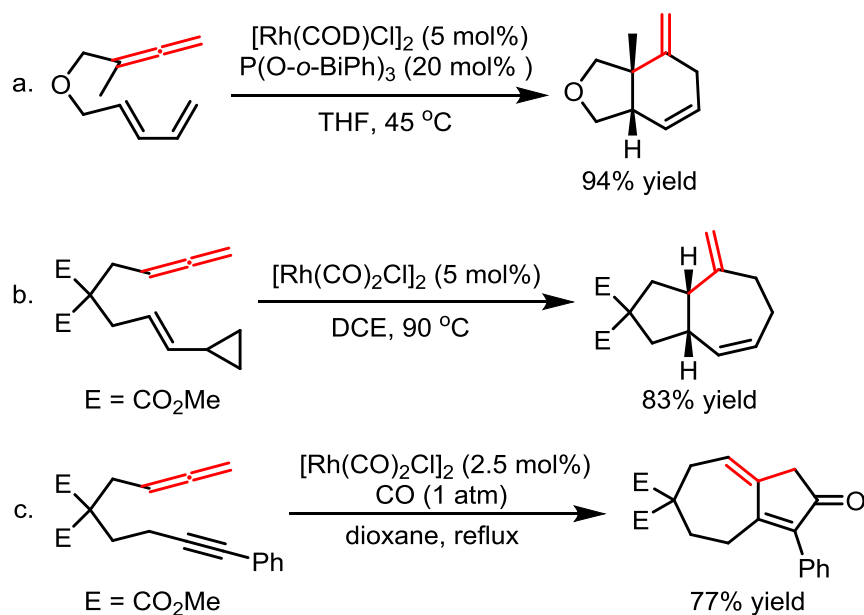
(5+2) cycloadditions of allene-yne occur exclusively at the terminal allene double bond. The terminal double bond is more reactive due to the enhanced  $d \rightarrow \pi^*$  backdonation from rhodium to the conjugated enyne. At the same time, addition to the internal double bond of allene-yne has a higher barrier as it would break the  $\pi$  conjugation. Substituted allenes are easier to distort into the transition state geometry than substituted alkynes. This leads to the greater reactivity of the allene double bond than the alkynyl group in allene-yne.

### 3.2 Introduction

A preeminent goal of organic synthesis is to achieve structural complexity with functional value in a safe, simple, environmentally acceptable and step, atom, and time economical fashion.<sup>1</sup> As exemplified by the Diels-Alder reaction, cycloadditions represent uniquely powerful processes to achieve this goal. They proceed in one operation with the convergent assembly of often commercially or readily available small molecule components and produce a new ring system with generally up to four new stereocenters, enabling a rapid build up of target relevant complexity. Prompted by the exceptional and growing importance of natural and designed targets based on seven-membered rings,<sup>2</sup> such as tumor promoting phorbol esters and latency activating prostratin analogs, the latter leads for HIV/AIDS eradication,<sup>3</sup> Wender *et al.* reported in 1995 the first examples of transition-metal-catalyzed (5+2) cycloadditions of vinylcyclopropanes (VCPs) and  $\pi$ -systems.<sup>4</sup> Due to contributions from several groups in recent years, the (5+2) cycloaddition has advanced impressively and become a versatile, practical, and efficient route to various functionalized seven-membered rings.<sup>5,6</sup> Among the current transition metal catalysts, rhodium

complexes are found to exhibit high catalytic activity and provide often exceptional chemo-, regio- and enantioselectivity. Rhodium catalysts are thus far the only systems to effect intermolecular (5+2) cycloadditions.

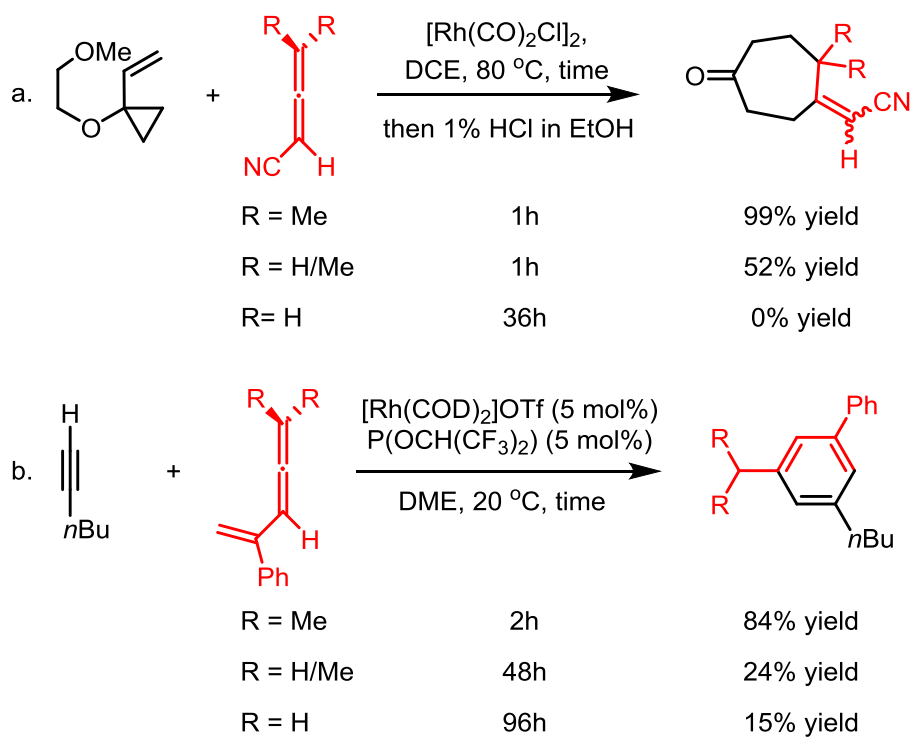
Allenes, one of the most common components in cycloadditions, have been widely employed in Rh(I)-catalyzed intramolecular ( $m+n$ ) and ( $m+n+o$ ) cycloadditions.<sup>7</sup> For example, Wender and co-workers discovered the Rh(I)-catalyzed intramolecular (4+2) cycloadditions of 1,3-dienes and allenes, affording the 6,5-, 6,6-, and 6,7-fused ring systems in an efficient fashion (Scheme 3.1a).<sup>8</sup> The same group also discovered the Rh(I)-catalyzed intramolecular (5+2) cycloadditions of VCPs and allenes (Scheme 3.1b).<sup>9</sup> The reaction works with mono-, di-, and trisubstituted allenes, producing the seven-membered ring products with an exocyclic double bond that cannot otherwise be accessed through the corresponding cycloaddition of alkenes or alkynes. In addition, Brummond,<sup>10</sup> and Mukai<sup>11</sup> and Wender<sup>12</sup> have independently studied the Rh(I)-catalyzed intramolecular Pauson-Khand type (2+2+1) cycloadditions with allenes, providing effective routes to functionalized cyclopentanones and cyclopentenones (Scheme 3.1c).<sup>13</sup>



**Scheme 3.1.** Selected examples of Rh(I)-catalyzed intramolecular ( $m+n$ ) and ( $m+n+o$ ) cycloadditions with allenes.

In 2005, Wegner, de Meijere and Wender reported the first  $[\text{Rh}(\text{CO})_2\text{Cl}]_2$ -catalyzed intermolecular (5+2) cycloadditions of VCPs and allenes with alkynyl, alkenyl, cyano, and cyanoalkyl substituents.<sup>5j</sup> In this work, the sterically encumbering methyl substituents on terminal allene double bond were found necessary to achieve the intermolecular (5+2) cycloaddition, while terminally mono- and unsubstituted allenes produce the cycloadduct much less efficiently (Scheme 3.2a). More importantly, this “terminal methyl effect” not only presents in the Rh(I)-catalyzed intermolecular (5+2) cycloadditions, it also exists in Rh(I)-catalyzed intermolecular (4+2) cycloadditions of allene-enes and alkenes (Scheme 3.2b).<sup>14</sup> The methyl substituents on terminal allene double bond are necessary for the desired (4+2) cycloadditions, while terminally mono- and unsubstituted allene-enes have much lower reactivities. Such enigmatic methyl effect limits the usage of allenes and contrasts many reported Rh(I)-catalyzed intramolecular ( $m+n$ ) and ( $m+n+o$ )

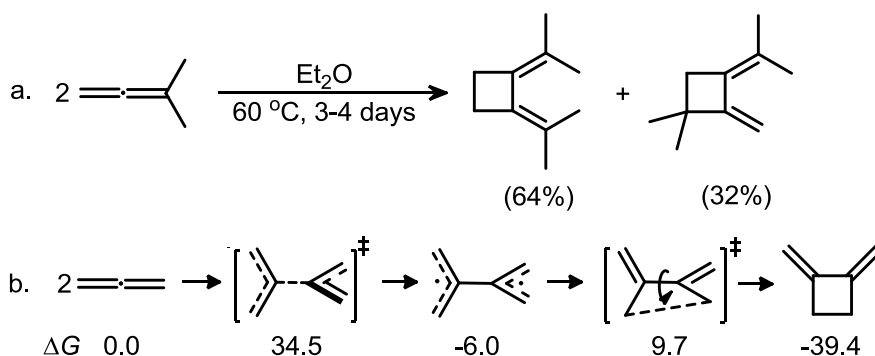
cycloadditions because both substituted and unsubstituted allenes generally work well. Our DFT calculations also indicated that allenes with or without terminal methyl substituents have similar activation barriers of (5+2) cycloaddition (see discussion below). Therefore, it was surmised that methyl substituents on allene might promote the (5+2) cycloadditions and other cycloadditions via preventing side reactions or catalyst inhibition.



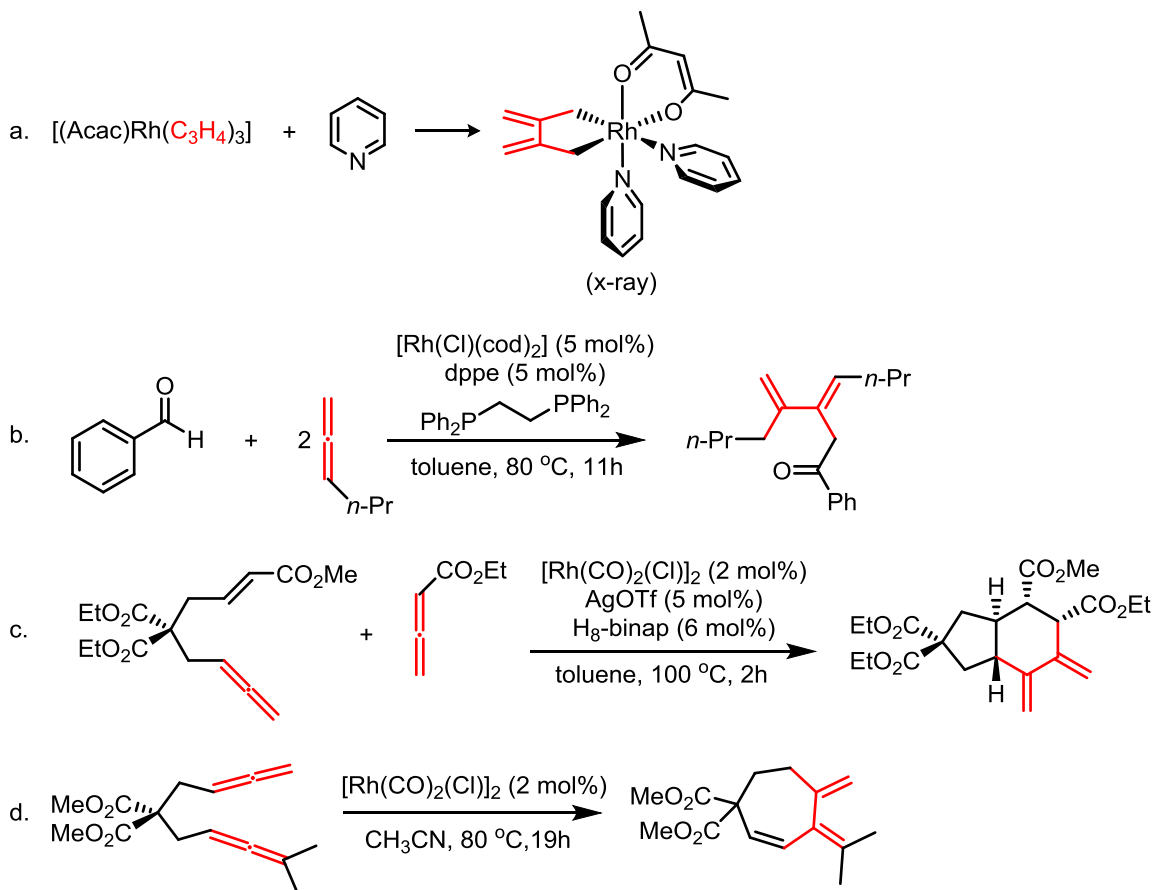
**Scheme 3.2.** Examples of terminal methyl effects on allene reactivities in Rh(I)-catalyzed intermolecular cycloadditions.

Allene dimerization has been reported under similar reaction conditions. For example, 1,1-dimethyl allene slowly dimerizes under mild conditions to form cyclobutane derivatives.<sup>15</sup> Johnson's calculations show that the dimerization of simple allene occurs via a stepwise mechanism with an activation barrier of 34.5 kcal/mol (Scheme 3.3).<sup>16</sup> More interestingly,

rhodium complexes have been found to catalyze several processes related to allene dimerization. In 1973, Ingrosso discovered that addition of pyridine ligand induces the allene dimerization in  $[(\text{Acac})\text{Rh}(\text{C}_3\text{H}_4)_3]$  complex to form  $[(\text{Acac})\text{Rh}(\text{C}_6\text{H}_8)(\text{pyridine})_2]$ , which has been characterized by X-ray crystallography (Scheme 3.4a).<sup>17</sup> Murakami recently reported Rh(I)-catalyzed 1:2 coupling between aldehydes and allenes (Scheme 3.4b).<sup>18</sup> Himo's computational study confirms that the reaction occurs via an initial dimerization of allene with rhodium catalyst.<sup>19</sup> Alexanian discovered a Rh(I)-catalyzed ene-allene-allene (2+2+2) cycloadditions which proceeds through allene dimerization and alkene insertion, giving direct access to stereochemically rich six-membered carbocycles (Scheme 3.4c).<sup>20</sup> Also, Ma reported  $[\text{Rh}(\text{CO})_2\text{Cl}]_2$ , the same catalyst used in the (5+2) cycloaddition, catalyzes intramolecular dimerization of allene, followed by  $\beta$ -hydride elimination to yield a seven-membered ring product (Scheme 3.4d).<sup>21</sup> Based on these previous studies on Rh(I)-catalyzed cycloadditions and allene dimerizations, we propose that the allene dimerization could be a hidden catalyst-poisoning pathway in the Rh(I)-catalyzed intermolecular (5+2) cycloadditions and possibly many other ( $m+n$ ) and ( $m+n+o$ ) cycloadditions.



**Scheme 3.3.** Experimental and theoretical studies of uncatalyzed thermal dimerization of allenes, Gibbs free energies in kcal/mol.

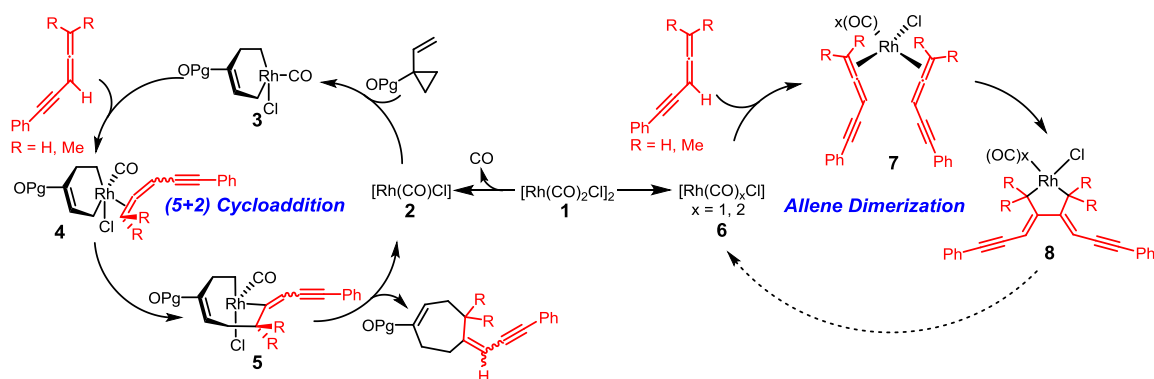


**Scheme 3.4.** Selected examples of Rh(I)-catalyzed dimerization of allenes and derived methodologies.

The competing (5+2) cycloaddition and allene dimerization pathways with allene-ynes are described in Scheme 3.5. From the precatalyst  $[\text{Rh}(\text{CO})_2\text{Cl}]_2$  (**1**), the (5+2) cycloaddition pathway occurs with the active catalyst  $[\text{Rh}(\text{CO})\text{Cl}]$  (**2**). Initial cyclopropane cleavage gives a metallacyclohexene intermediate **3**, and subsequent allene insertion produces a metallacyclooctadiene intermediate **5**. From **5**, C-C reductive elimination gives the seven-

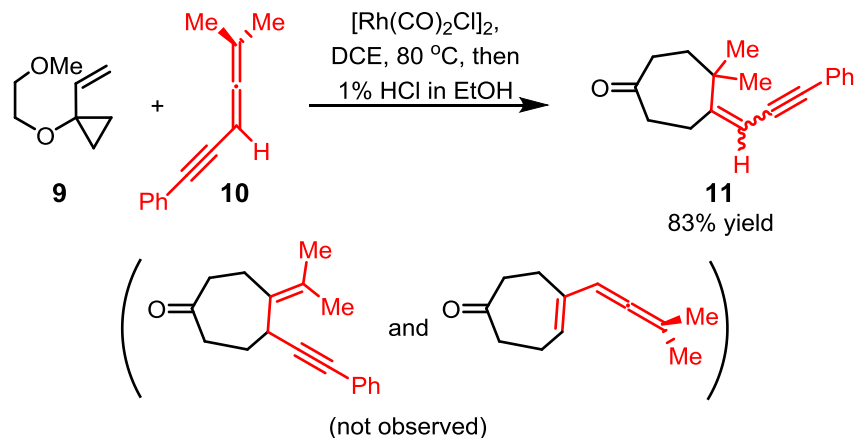


membered ring product. Alternatively, the  $[\text{Rh}(\text{CO})_x\text{Cl}]$  ( $x = 1, 2$ ) active catalyst **6** can catalyze the allene dimerization. The dimerization produces rhodium complex **8** which could be very stable and thus poison the rhodium catalyst.



**Scheme 3.5.** Proposed competing mechanisms for the Rh(I)-catalyzed (5+2) cycloaddition and allene dimerization with allene-ynes.

Besides the unique reactivity observed for the (5+2) cycloaddition of VCPs with variously substituted allene-ynes, the chemoselectivity is also intriguing. Although alkynes are typically more reactive than allenes in (5+2) cycloadditions as documented in all prior work, reactions with conjugated allene-ynes occur exclusively at the terminal double bond of allene (Scheme 3.6). To understand the origins of the unique reactivity and selectivity of these allene-based reactions, a subject pertinent to many other metal catalyzed reactions of allenes, we initiated DFT calculations and experimental studies on the contrasting behavior of allenes in intermolecular Rh(I)-catalyzed (5+2) cycloadditions with VCPs.



**Scheme 3.6.** Chemoselectivity of  $[\text{Rh}(\text{CO})_2\text{Cl}]_2$ -catalyzed intermolecular (5+2) cycloaddition of VCP **9** and allene-yne **10**.

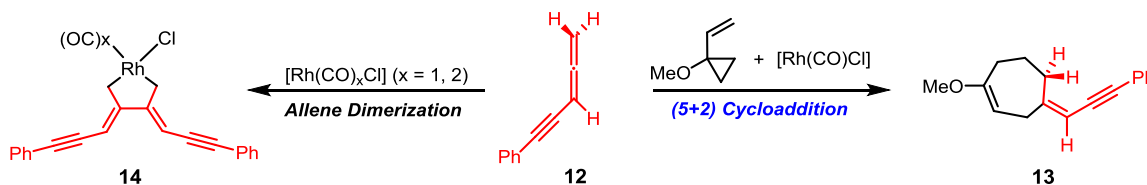
### 3.3 Computational Details

Geometry optimizations, frequencies, and thermal energy corrections were performed with the B3LYP functional, 6-31G(d) basis set for all main group elements and SDD basis set for rhodium implemented in Gaussian 09.<sup>22</sup> Energies were evaluated with the M06 method,<sup>23</sup> the 6-311+G(2d,p) basis set for all main group elements and SDD basis set for ruthenium. All reported free energies involve zero-point vibrational energy corrections and thermal corrections to Gibbs free energy at 298 K. The solvation free energy corrections were computed with CPCM model on gas-phase optimized geometries and dichloroethane was chosen as the solvent for consistency with the experiment.

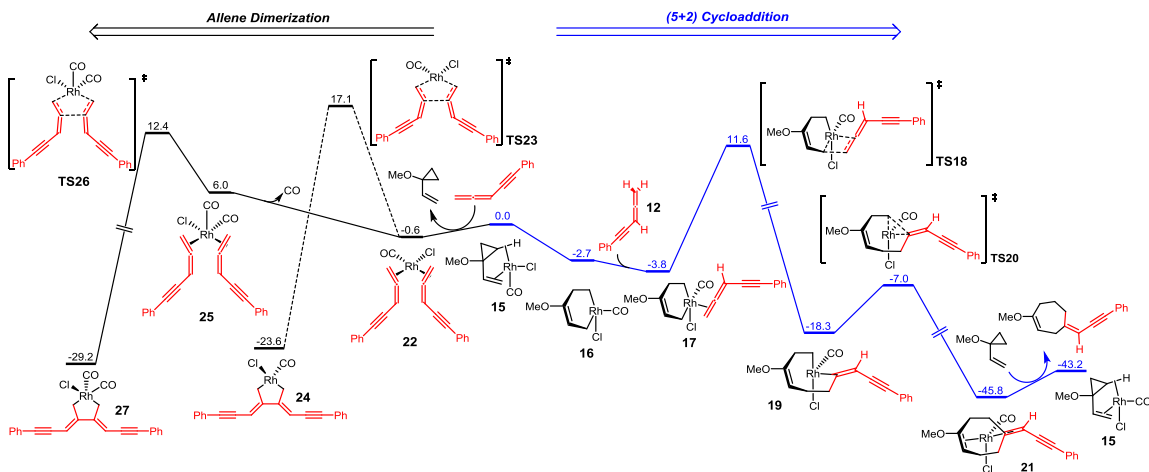
### 3.4 Results and Discussion

#### 3.4.1 Reactions with Terminally Unsubstituted Allene

We first studied the (5+2) cycloaddition and allene dimerization pathways with allene-yne **12**, which lacks the terminal allene substituents and experimentally yields no (5+2) cycloaddition product (Scheme 3.7). The 2-methoxyethoxy group on the VCP was replaced with a methoxy group in the calculations. With the  $[\text{Rh}(\text{CO})\text{Cl}]$  active catalyst, the (5+2) cycloaddition of 1-methoxyl-1-vinylcyclopropane and **12** gives the seven-membered ring product **13**. Alternatively, the  $[\text{Rh}(\text{CO})_x\text{Cl}]$  ( $x = 1, 2$ ) complex can catalyze the dimerization of **12** and form the rhodacyclopentane complex **14**. The calculated free energy surface for both pathways is shown in Figure 3.1 and optimized structures of selected intermediates and transition states are shown in Figure 3.2.



**Scheme 3.7.** The computational model of Rh(I)-catalyzed (5+2) cycloaddition and dimerization of the terminally unsubstituted allene-yne.

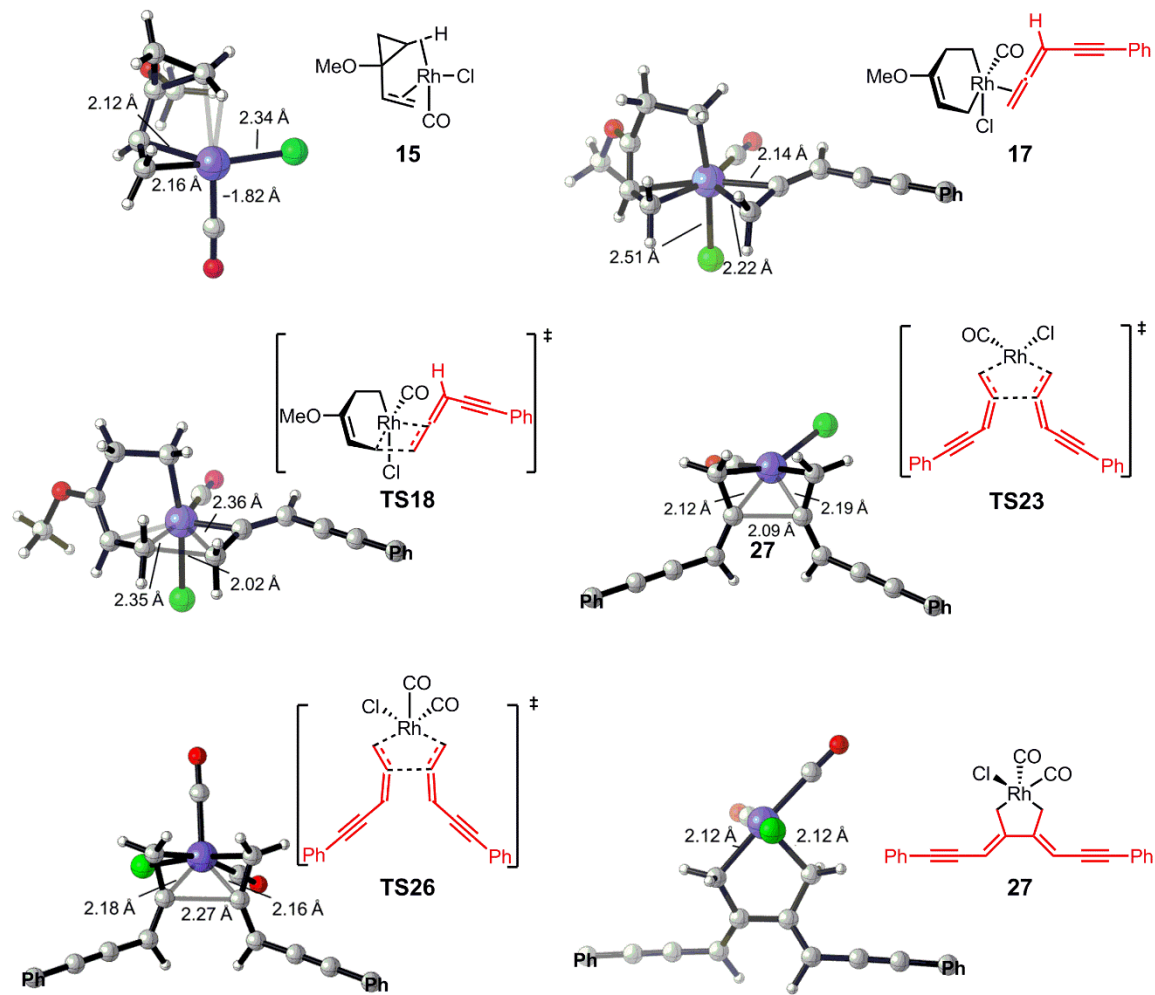


**Figure 3.1.** Free energy surface of favored pathways of  $[\text{Rh}(\text{CO})_2\text{Cl}]_2$ -catalyzed (5+2) cycloaddition and allene dimerization with terminally unsubstituted allene-yne **12**. Free energies (298 K) with respect to **15** are shown in kcal/mol.

Based on previous computational studies,<sup>24</sup> the active catalyst for (5+2) cycloaddition is  $[\text{Rh}(\text{CO})\text{Cl}]$ , which is formed via dissociation of the dimeric  $[\text{Rh}(\text{CO})_2\text{Cl}]_2$  precatalyst and elimination of CO. From the  $[\text{Rh}(\text{CO})\text{Cl}]$ -VCP complex **15**, cyclopropane cleavage occurs to give a metallacyclohexene intermediate **16**, and subsequent exergonic coordination of allene-yne produces  $\pi$  complex **17**. Insertion of the terminal double bond of allene-yne via **TS18** requires an activation barrier of 15.4 kcal/mol with respect to **17** and produces a metallacyclooctadiene intermediate **19**. Insertion of the internal allene double bond or the alkyne requires a higher barrier (see later for discussions on chemoselectivity). The subsequent reductive elimination via **TS20** gives the product-coordinated complex **21**. Therefore, the  $2\pi$  insertion of allene-yne via **TS18** is the rate-determining step of the (5+2) cycloaddition pathway.

Because the exact mechanism of allene dimerization is still unclear, we computed both mechanisms involving  $[\text{Rh}(\text{CO})_2\text{Cl}]$  or  $[\text{Rh}(\text{CO})\text{Cl}]$  as the active catalyst (shown in solid and

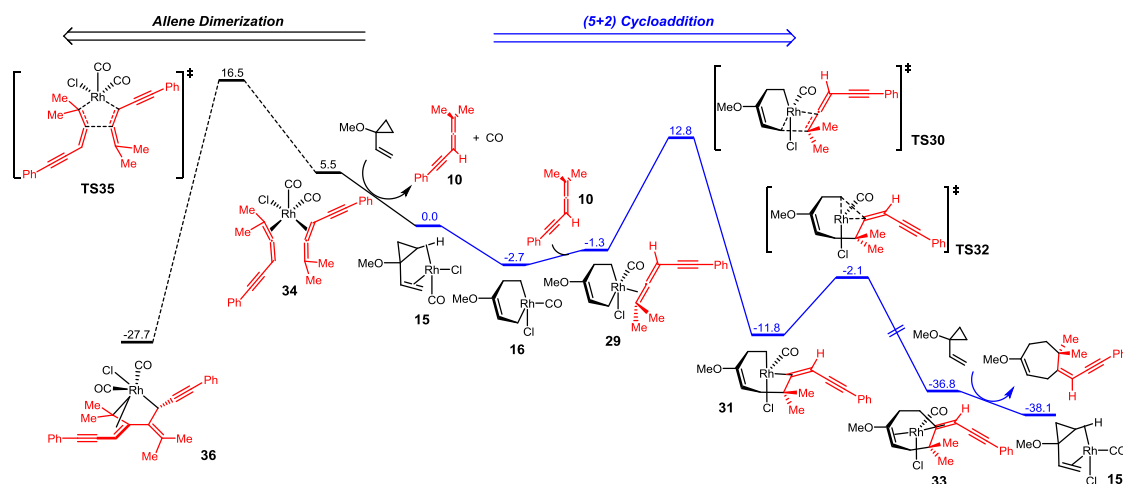
dashed black lines respectively in Figure 3.1). If the  $[\text{Rh}(\text{CO})\text{Cl}]$  complex is the active catalyst, substitution of VCP coordination by two allene-ynes converts **15** to intermediate **22**. From **22**, the oxidative cyclization of allene-ynes via **TS23** requires a 17.7 kcal/mol barrier and the formed intermediate **24** is very stable. Alternatively, oxidative cyclization of allene-ynes with  $[\text{Rh}(\text{CO})_2\text{Cl}]$  occurs from intermediate **25**. Although **25** is less stable than **22**, **TS26** is more favorable than **TS23**. This indicates that allene dimerization occurs more rapidly with  $[\text{Rh}(\text{CO})_2\text{Cl}]$ . The resultant intermediate **27** is very stable compared to the Rh-allene complex **25**, making the allene dimerization irreversible.<sup>25</sup> Comparing the two reaction pathways, the overall barrier of allene dimerization (**TS26**) is only 0.8 kcal/mol higher than (5+2) cycloaddition (**TS18**). These calculations indicate that the (5+2) cycloaddition and allene dimerization pathways are competitive with terminally unsubstituted allene-ynes. Therefore, the competitive and irreversible allene dimerization pathway poisons the rhodium catalyst, preventing its participation in the desired (5+2) cycloaddition.



**Figure 3.2.** Optimized structures of selected intermediates and transition states in the favored pathways of  $[\text{Rh}(\text{CO})_2\text{Cl}]_2$ -catalyzed (5+2) cycloaddition and allene dimerization with terminally unsubstituted allene-yne **12** (only the  $\alpha$ -carbon of phenyl group is shown for simplicity).

### 3.4.2 Terminal Methyl Effects on Allene Dimerization

We also studied the (5+2) cycloaddition and allene dimerization pathways with terminally dimethyl-substituted allene-yne **10**. The computed free energy surface is shown in Figure 3.3. From the [Rh(CO)Cl]-VCP complex **15**, cyclopropane cleavage gives the metallacyclohexene intermediate **16** and subsequent endergonic allene-yne coordination produces intermediate **29**. The  $2\pi$  insertion of terminal double bond of allene-yne occurs via **TS30**, and the formed metallacyclooctadiene intermediate **31** undergoes a facile C-C reductive elimination to generate the product-coordinated complex **33**. Similar to the unsubstituted allene-yne **12**, the rate determining step of (5+2) cycloaddition pathway with methyl-substituted allene-yne **10** is  $2\pi$  insertion and the overall barrier is 15.5 kcal/mol. The overall barriers of (5+2) cycloaddition pathway with allene-ynes are not affected by the terminal methyl substituents (15.4 kcal/mol with allene-yne **12** and 15.5 kcal/mol with methyl-substituted allene-yne **10**). Despite their similar reactivities in (5+2) cycloaddition, the methyl-substituted allene-yne **10** has a much higher barrier for allene dimerization. The dimerization transition state **TS35** is 3.7 kcal/mol higher in free energy than the  $2\pi$  insertion transition state **TS30**. Therefore, the competing allene dimerization pathway in this case is disfavored relative to the experimentally observed (5+2) cycloaddition.

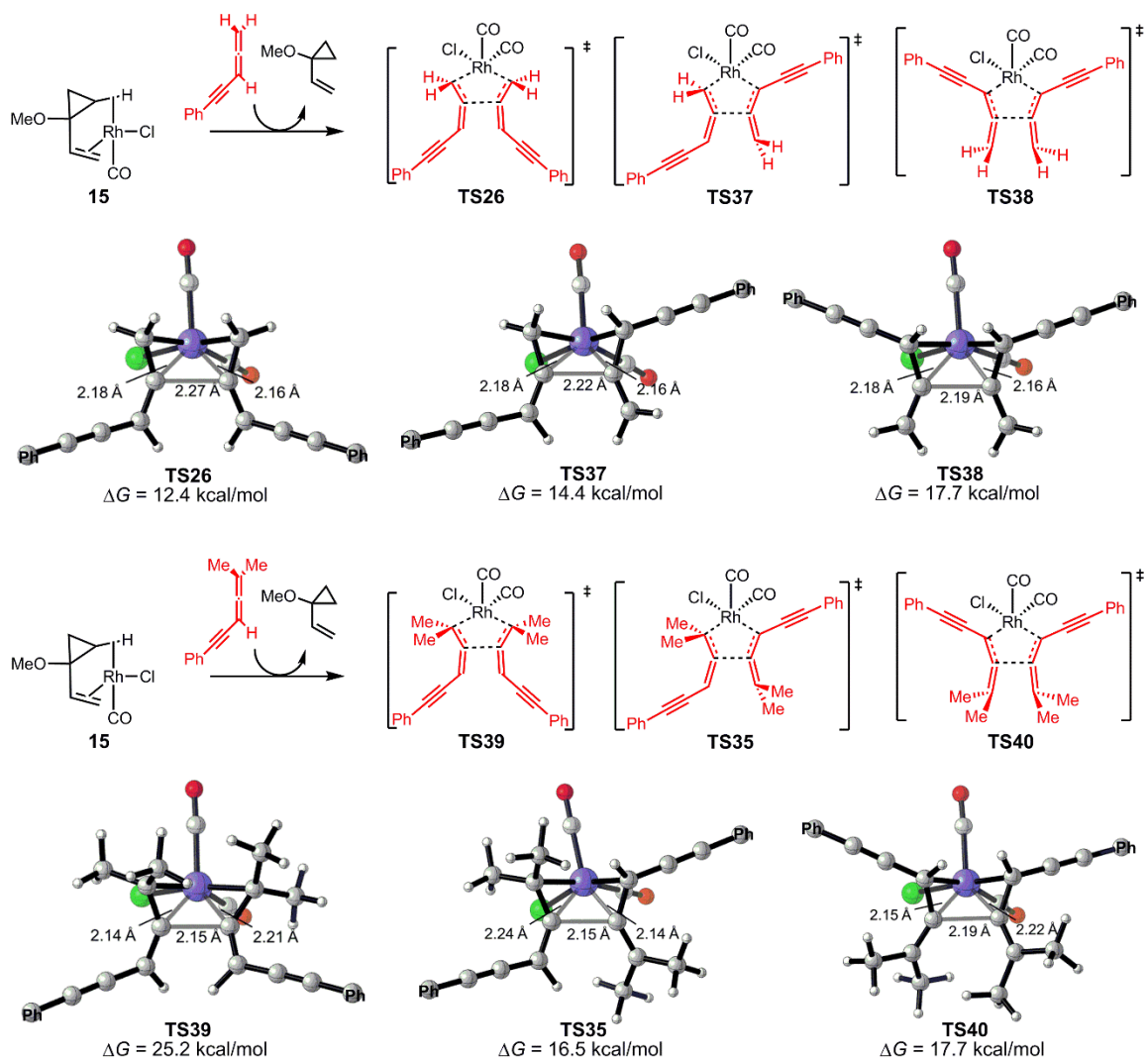


**Figure 3.3.** Free energy surface of  $[\text{Rh}(\text{CO})_2\text{Cl}]_2$ -catalyzed (5+2) cycloaddition and allene dimerization with dimethyl-substituted allene-yne **10**. All energies are Gibbs free energies at 298K with respect to complex **15**.

In order to understand the terminal methyl effects on the allene dimerization reactivity, all possible dimerization transition states are located and shown in Figure 3.4. Allene-yne have a terminal double bond and an internal double bond, so there are three possible dimerization transition states. For allene-yne **12**, it can dimerize with both the terminal double bonds via **TS26**, one terminal and one internal double bond via **TS37**, or both the internal double bonds via **TS38**. Calculation indicates that **TS26** is the most favorable transition state. Dimerization with the internal double bond (**TS37** and **TS38**) will break the conjugation with the alkynyl group and raises the activation barrier. Therefore, the dimerization of allene-yne **12** occurs with the two terminal double bonds and requires an activation barrier of 12.4 kcal/mol compared to the  $[\text{Rh}(\text{CO})\text{Cl}]$ -VCP complex **12**.



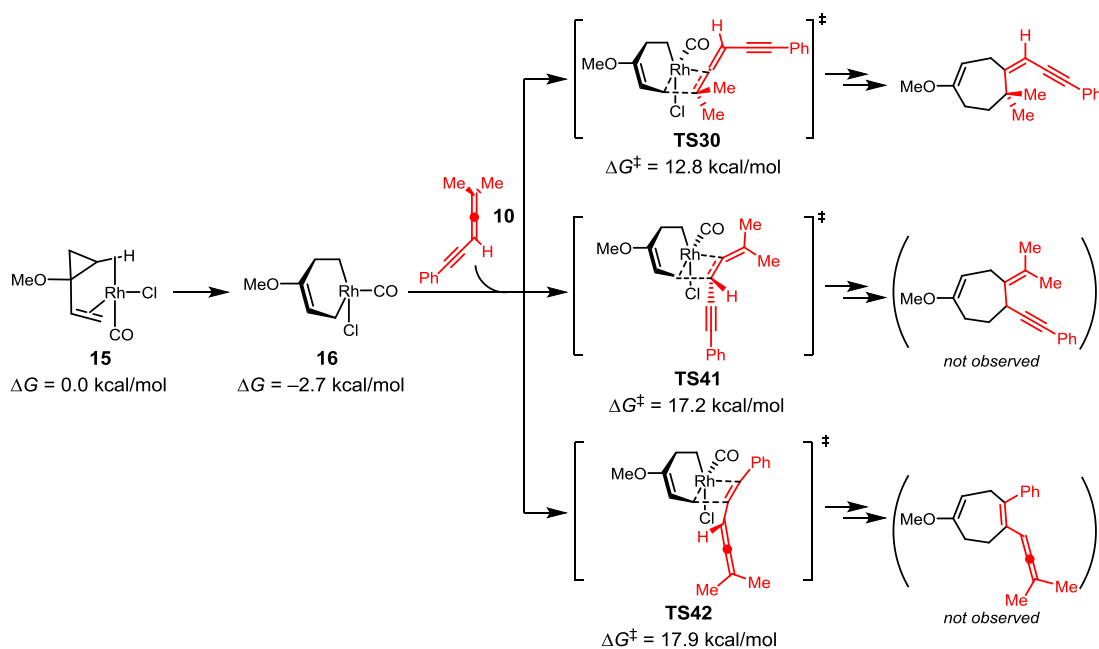
For the dimethyl-substituted allene-yne **10**, the preference between the three possible dimerization transition states is altered by the steric repulsions with methyl substituents (Figure 3.4). The dimerization with the two terminal double bonds via **TS39** is no longer favored and the barrier is 25.2 kcal/mol. On the other hand, dimerization of one terminal and one internal double bond via **TS35** is now the most favorable transition state and the activation barrier is 16.5 kcal/mol. Still, steric repulsions with the methyl substituents lead to higher barrier for dimerization compared to the unsubstituted allene-yne (**TS37**, 14.4 kcal/mol). These results indicate the high barrier of dimerization of terminally substituted allenes are due to steric repulsions with the terminal allene substituents and the rhodium catalyst.



**Figure 3.4.** Transition states of [Rh(CO)<sub>2</sub>Cl]-catalyzed dimerization of allene-ynes **12** and **10** (only the  $\alpha$ -carbon of phenyl group is shown for simplicity).

### 3.4.3 Origins of Chemoselectivities

Although allene-yne have three possible  $\pi$ -bonds that could engage in a (5+2) cycloaddition, the reaction occurs exclusively with the terminal double bond of allene. The chemoselectivity is determined in the  $2\pi$  insertion step, which is rate-limiting and irreversible. We calculated the three possible insertion transition states with allene-yne **10**. The most favorable TS isomers in each pathway and their activation barriers are shown in Scheme 3.8. Consistent with the experiment, the insertion of terminal double bond via **TS31** requires a barrier of 12.8 kcal/mol relative to the [Rh(CO)Cl]-VCP complex **15**. The  $2\pi$  insertion of the internal double bond via **TS41** requires a 17.2 kcal/mol barrier and the insertion of triple bond via **TS42** requires a 17.9 kcal/mol barrier, both are much higher than the  $2\pi$  insertion barrier of terminal double bond. Therefore, the (5+2) cycloadditions occur exclusively with the terminal double bond of allene-yne.



**Scheme 3.8.** Possible  $2\pi$  insertion transition states in the (5+2) cycloaddition pathway with allene-ynone **10**.

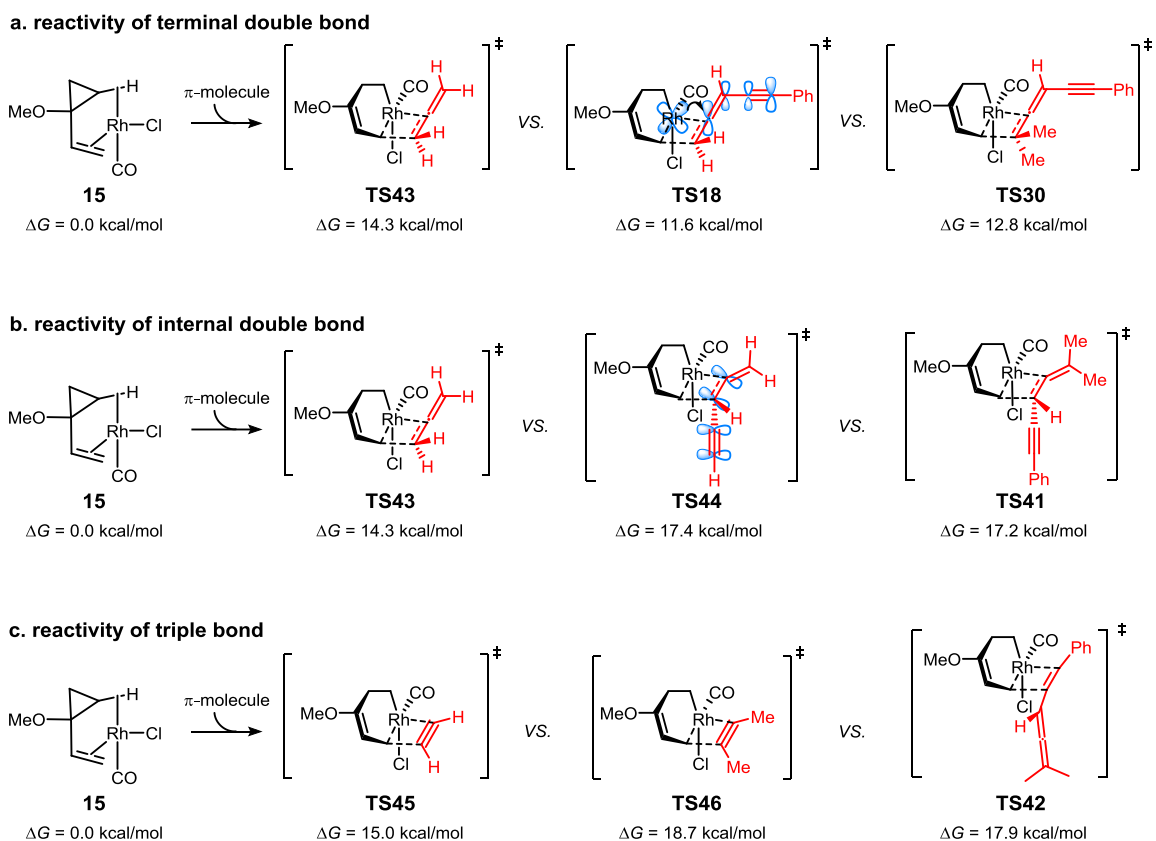
In order to understand the origins of chemoselectivity, we calculated the insertion barriers of simple allene and acetylene and explored the steric and electronic effects of substituents on the insertion barriers with different  $\pi$  bonds (Scheme 3.9). Scheme 3.9a shows the substituent effects on the reactivity of terminal double bond of allene-ynone. The insertion with simple allene requires a 14.3 kcal/mol barrier via **TS43** with respect to the  $[\text{Rh}(\text{CO})\text{Cl}]\text{-VCP}$  complex **15**. The terminal double bond in allene-ynone **12** is more reactive in  $2\pi$  insertion than simple allenes. In **TS18**, the phenylalkynyl substituent on allene-ynone **12** lowers the  $2\pi$  insertion barrier by 2.7 kcal/mol. This is presumably due to the increased  $d \rightarrow \pi^*$  back donation from rhodium to the conjugated  $\pi^*$  orbital of the allene-ynone. Interestingly, the terminal methyl substituents show only moderate steric repulsions around the forming C–C bond in  $2\pi$  insertion. **TS30** is only 1.2 kcal/mol higher in

energy than the unsubstituted **TS18**. This indicates the terminal allene substituents prevent the substrates from dimerization but have only minor effects on the rates of (5+2) cycloadditions.

In contrast to the activation of terminal double bond, a conjugated alkynyl group leads to higher  $2\pi$  insertion barrier in reactions with the internal allenyl double bond (Scheme 3.9b). The  $2\pi$  insertion with internal double bonds of allene-ynes via **TS44** and **TS41** requires about 3 kcal/mol higher barriers than the insertion of simple allene via **TS43**. The low reactivity of the internal double bond of allene-yne is due to the  $\pi$  conjugation between the allene and the alkyne. Insertion into the internal double bonds breaks the conjugation and raises the barrier dramatically.

Although acetylene and simple allene have similar  $2\pi$  insertion barriers (15.0 kcal/mol, **TS45** versus 14.3 kcal/mol, **TS43**), substituted alkynes in general have a much higher barrier for  $2\pi$  insertion. The  $2\pi$  insertion with the triple bond of allene-yne **12** requires 17.9 kcal/mol (**TS42**, Scheme 3.9c), which is comparable to that of 2-butyne (18.7 kcal/mol, **TS46**). The lower reactivity of internal alkynes in  $2\pi$  insertion is because the two  $C_{sp}-C$  bonds are more difficult to distort than the  $C_{sp}-H$  bonds of acetylene.

In summary, the terminal double bond of allene-yne is selectively activated in the  $2\pi$  insertion step due to the electronic effects of the conjugated alkynyl group, while the internal double bond and triple bond are deactivated. This leads to the exclusive formation of (5+2) cycloadduct with terminal double bond of the allene-ynes.



**Scheme 3.9.**  $2\pi$  insertion barriers (5+2) cycloaddition pathway with different allenes, alkynes and allene-ynes.

### 3.5 Conclusions

DFT calculations have revealed the mechanism and origins of substituent effects on reactivity and chemoselectivity of allene-ynes in Rh(I)-catalyzed intermolecular (5+2) cycloadditions with VCP. The Rh(I)-catalyzed (5+2) cycloaddition and allene dimerization are found to be competitive when allene-ynes lack methyl substituents on the terminal double bond. The competing allene dimerization is irreversible, generating a very stable rhodium complex,

thereby effectively poisoning the rhodium catalyst and shutting down the desired (5+2) cycloaddition. With the terminal methyl substituents, the barrier for allene dimerization of allene-ynes increase significantly while the (5+2) cycloaddition pathway is not affected, so the allene-ynes with the terminal methyl substituents are able to undergo the (5+2) cycloaddition. The hidden allene dimerization pathway explains the enigmatic reactivities of allenes in Rh(I)-catalyzed inter- and intramolecular cycloadditions and provide mechanistic insights to many other Rh(I)-catalyzed  $(m+n)$  and  $(m+n+o)$  cycloadditions.

The chemoselectivity that (5+2) cycloaddition occurs exclusively on the terminal double bond of allene-ynes are also studied. The rate-limiting  $2\pi$  insertion step with the terminal double bond of allene-yne requires much lower barrier than the barriers with the internal double bond or triple bond. Comparing to the insertion of a simple allene, the insertion of the terminal double bond of allene-yne has a stronger d- $\pi^*$  interaction between rhodium and the enyne from allene-yne, so the insertion barrier is lower. On the other hand, the internal double bond of allene-yne is conjugated with the alkynyl group, the insertion of this  $\pi$ -bond breaks its conjugation and significantly increases the barrier. In addition, the insertion of the triple bond of allene-ynes requires the distortion of two  $C_{sp}-C$  bonds, which is more difficult than the distortion of two C-H bonds of acetylene. Therefore, the substituent effects differentiate the similar intrinsic reactivities of simple allene and acetylene, leading to the exclusive (5+2) cycloaddition with the terminal double bond of allene-ynes.

### 3.6 References

(1) For a definition of the “ideal synthesis” incorporating the increasingly important issues of safety, step and atom count, waste stream, environmental, operational and time considerations. (a) Wender, P. A.; Miller, B. L. *Nature* **2009**, *460*, 197. (b) Wender, P. A. *Natural Products Reports* **2014**, *31* (4), 433. (c) P. A. Wender, B. L. Miller, in *Organic Synthesis: Theory & Applications*, Vol. 2 (Ed: T. Hudlicky), JAI, Greenwich, 1993, pp. 27 – 66; (d) R. A. Sheldon, *Chem. Commun.* **2008**, 3352. (e) P. T. Anastas, *Green Chemistry: Theory and Practice*, Oxford University Press, Oxford, 1998. For discussion of step and time economy, see: (f) Wender, P. A.; Handy, S. T.; Wright, D. L. *Chem. Ind.* **1997**, 765. (g) Wender, P. A.; Croatt, M. P.; Witulski, B. *Tetrahedron* **2006**, *62*, 7505, references therein. (h) Wender, P. A.; Verma, V. A.; Paxton, T. J.; Pillow, T. H. *Acc. Chem. Res.* **2008**, *41*, 40. For a discussion of atom economy, see: (i) Trost, B. M. *Science* **1991**, *254*, 1471; (j) B. M. Trost, *Angew. Chem. Int. Ed.* **1995**, *34*, 259.

(2) (a) Yet, L. *Chem. Rev.* **2000**, *100*, 2963. (b) Battiste, M. A.; Pelphrey, P. M.; Wright, D. L. *Chem. -Eur. J.* **2006**, *12*, 3438. (c) Wender, P. A.; Croatt, M. P.; Deschamps, N. M. In *Comprehensive Organometallic Chemistry III*; Crabtree, R. H., Mingos, D. M. P., Eds.; Elsevier: Oxford, 2007; Vol. 10, pp 603-648. (d) Butenschön, H. *Angew. Chem. Int. Ed.* **2008**, *47*, 5287. (e) Pellissier, H. *Adv. Synth. Catal.* **2011**, *353*, 189. (f) Ylijoki, K. E. O.; Stryker, J. M. *Chem. Rev.*, **2013**, *113*, 2244.

(3) For recent studies and lead references, see: (a) Wender, P. A.; Kee, J.-M.; Warrington, J. M. *Science* **2008**, *320*, 649. (b) Beans, E. J.; Fournogerakis, D.; Gauntlett, C.; Heumann, L. V.;



Kramer, R.; Marsden, M. D.; Chun, T.-W.; Zack, J. A.; Wender, P. A. *Proc. Natl. Acad. Sci.* **2013**, *110*, 11698.

(4) Wender, P. A.; Takahashi, H.; Witulski, B. *J. Am. Chem. Soc.* **1995**, *117*, 4720.

(5) For rhodium catalysts, see: (a) Wender, P. A.; Rieck, H.; Fuji, M. *J. Am. Chem. Soc.* **1998**, *120*, 10976. (b) Wender, P. A.; Sperandio, D. *J. Org. Chem.* **1998**, *63*, 4164. (c) Gilbertson, S. R.; Hoge, G. S. *Tetrahedron Lett.* **1998**, *39*, 2075. (d) Wender, P. A.; Dyckman, A. J.; Husfeld, C. O.; Scanio, M. J. C. *Org. Lett.* **2000**, *2*, 1609. (e) Wang, B.; Cao, P.; Zhang, X.; *Tetrahedron Lett.* **2000**, *41*, 8041. (f) Wender, P. A.; Barzilay, C. M.; Dyckman, A. J. *J. Am. Chem. Soc.* **2001**, *123*, 179. (g) Wender, P. A.; Gamber, G. G.; Scanio, M. J. C. *Angew. Chem., Int. Ed.* **2001**, *40*, 3895. (h) Wender, P. A.; Williams, T. J. *Angew. Chem. Int. Ed.* **2002**, *41*, 4550. (i) Wender, P. A.; Love, J. A.; Williams, T. J., *Synlett* **2003**, 1295. (j) Wegner, H. A.; de Meijere, A.; Wender, P. A. *J. Am. Chem. Soc.* **2005**, *127*, 6530. (k) Wender, P. A.; Haustedt, L. O.; Lim, J.; Love, J. A.; Williams, T. J.; Yoon, J.-Y. *J. Am. Chem. Soc.* **2006**, *128*, 6302. (l) Lee, S. I.; Park, Y.; Park, J. H.; Jung, G.; Choi, S. Y.; Chung, Y. K.; Lee, B. Y. *J. Org. Chem.* **2006**, *71*, 91. (m) Saito, A.; Ono, T.; Hanzawa, Y. *J. Org. Chem.* **2006**, *71*, 6437. (n) Gomez, F. J.; Kamber, N. E.; Deschamps, N. M.; Cole, A. P.; Wender, P. A.; Waymouth, R. M. *Organometallics* **2007**, *26*, 4541. (o) Shintani, R.; Nakatsu, H.; Takatsu, K.; Hayashi, T. *Chem. -Eur. J.* **2009**, *15*, 8692. (p) Liu, P.; Sirois, L. E.; Cheong, P. H. Y.; Yu, Z. X.; Hartung, I. V.; Rieck, H.; Wender, P. A.; Houk, K. N. *J. Am. Chem. Soc.* **2010**, *132*, 10127. (q) Wender, P. A.; Stemmler, R. T.; Sirois, L. E. *J. Am. Chem. Soc.* **2010**, *132*, 2532. (r) Wender, P. A.; Sirois, L. E.; Stemmler, R. T.; Williams, T. J. *Org. Lett.* **2010**, *12*, 1604. (s) Wender,

P. A.; Lesser, A. B.; Sirois, L. E. *Org. Synth.*, **2011**, 88, 109. (t) Wender, P. A.; Lesser, A. B.; Sirois, L. E. *Angew. Chem. Int. Ed.* **2012**, 124, 2790.

(6) For a ruthenium catalyst, see: (a) Trost, B. M.; Toste, F. D.; Shen, H. *J. Am. Chem. Soc.* **2000**, 122, 2379. (b) Trost, B. M.; Shen, H. C. *Org. Lett.* **2000**, 2, 2523. (c) Trost, B. M.; Shen, H. C. *Angew. Chem. Int. Ed.* **2001**, 40, 2313. (d) Trost, B. M.; Toste, F. D.; *Angew. Chem. Int. Ed.* **2001**, 40, 1114. (e) Trost, B. M.; Shen, H. C.; Schulz, T.; *Org. Lett.* **2003**, 5, 4149. (f) Trost, B. M.; Shen, H. C.; Horne, D. B.; Toste, E. D.; Steinmetz, B. G.; Koradin, C. *Chem. -Eur. J.* **2005**, 11, 2577. For a nickel catalyst, see: (g) Zuo, G.; Louie, J. *J. Am. Chem. Soc.* **2005**, 127, 5798. For an iron catalyst, see: (h) Fürstner, A.; Majima, K.; Martin, R.; Krause, H.; Kattnig, E.; Goddard, R.; Lehmann, C. W. *J. Am. Chem. Soc.* **2008**, 130, 1992.

(7) For reviews, see: (a) Kitagaki, S.; Inagaki, F.; Mukai, C. *J. Synth. Org. Chem. Jpn.* **2009**, 67, 618. (b) Ma, S. *Aldrichimica Acta* **2007**, 40, 91. (c) Croatt, M. P.; Wender, P. A. *Eur. J. Org. Chem.* **2010**, 19. For selected examples of Rh(I)-catalyzed intramolecular cycloadditions with allenes, see: (d) Sugikubo, K.; Omachi, F.; Miyanaga, Y.; Inagaki, F.; Matsumoto, C.; Mukai, C. *Angew. Chem. Int. Ed.* **2013**, 52, 11369. (e) Mukai, C.; Ohta, Y.; Oura, Y.; Kawaguchi, Y.; Inagaki, F. *J. Am. Chem. Soc.* **2012**, 134, 19580. (f) Inagaki, F.; Sugikubo, K.; Oura, Y.; Mukai, C. *Chem. -Eur. J.* **2011**, 17, 9062. (g) Inagaki, F.; Sugikubo, K.; Miyashita, Y.; Mukai, C. *Angew. Chem. Int. Ed.* **2010**, 49, 2206. (h) Oonishi, Y.; Yokoe, T.; Hosotani, A.; Sato, Y. *Angew. Chem. Int. Ed.* **2014**, 53, 1135. (i) Oonishi, Y.; Hosotani, A.; Sato, Y. *Angew. Chem. Int. Ed.* **2012**, 51, 11548. (j) Oonishi, Y.; Hosotani, A.; Sato, Y. *J. Am. Chem. Soc.* **2011**, 133, 10386.

(8) Wender, P. A.; Jenkins, T. E.; Suzuki, S. *J. Am. Chem. Soc.* **1995**, 117, 1843.

(9) Wender, P. A.; Glorius, F.; Husfeld, C. O.; Langkopf, E.; Love, J. A. *J. Am. Chem. Soc.* **1999**, *121*, 5348.

(10) (a) Brummond, K. M.; Chen, H.; Fisher, K. D.; Kerekes, A. D.; Rickards, B.; Sill, P. C.; Geib, S. J. *Org. Lett.* **2002**, *4*, 1931. (b) Brummond, K. M.; Sill, P. C.; Rickards, B.; Geib, S. J. *Tetrahedron Lett.* **2002**, *43*, 3735. (c) Brummond, K. M.; Mitasev, B. *Org. Lett.* **2004**, *6*, 2245. (d) Bayden, A. S.; Brummond, K. M.; Jordan, K. D. *Organometallics* **2006**, *25*, 5204. (e) Brummond, K. M.; Chen, D. *Org. Lett.* **2008**, *10*, 705. (f) Brummond, K. M.; Davis, M. M.; Huang, C. *J. Org. Chem.* **2009**, *74*, 8314. (g) Grillet, G.; Huang, C.; Brummond, K. M. *Org. Lett.* **2011**, *13*, 6304. (h) Grillet, F.; Brummond, K. M. *J. Org. Chem.* **2013**, *78*, 3737.

(11) (a) Mukai, C.; Nomura, I.; Yamanishi, K.; Hanaoka, M. *Org. Lett.* **2002**, *4*, 1755. (b) Mukai, C.; Nomura, I.; Kitagaki, S. *J. Org. Chem.* **2003**, *68*, 1376. (c) Mukai, C.; Inagaki, F.; Yoshida, T.; Kitagaki, S. *Tetrahedron* **2004**, *45*, 4117. (d) Mukai, C.; Hirose, T.; Teramoto, S.; Kitagaki, S. *Tetrahedron* **2005**, *61*, 10983. (e) Mukai, C.; Inagaki, F.; Yoshida, T.; Yoshitani, K.; Hara, Y.; Kitagaki, S. *J. Org. Chem.* **2005**, *70*, 7159. (f) Inagaki, F.; Mukai, C. *Org. Lett.* **2006**, *8*, 1217. (g) Inagaki, F.; Kawamura, T.; Mukai, C. *Tetrahedron* **2007**, *63*, 5154. (h) Hirose, T.; Miyakoshi, N.; Mukai, C. *J. Org. Chem.* **2008**, *73*, 1061. (i) Inagaki, F.; Narita, S.; Hasegawa, T.; Kitagaki, S.; Mukai, C. *Angew. Chem. Int. Ed.* **2009**, *48*, 2007. (j) Inagaki, F.; Kitagaki, S.; Mukai, C. *Synlett* **2011**, 594. (k) Inagaki, F.; Itoh, N.; Hayashi, Y.; Matsui, Y.; Mukai, C. *Beilstein J. Org. Chem.* **2011**, *7*, 404. (l) Hayashi, Y.; Ogawa, K.; Inagaki, F.; Mukai, C. *Org. Biomol. Chem.* **2012**, *10*, 4747. (m) Shafawati, M. T. S.; Inagaki, F.; Kawamura, T.; Mukai, C. *Tetrahedron* **2013**, *69*, 1509.

(n) Iwata, T.; Inagaki, F.; Mukai, C. *Angew. Chem. Int. Ed.* **2013**, *52*, 11138. (o) Mukai, C.; Takahashi, Y.; Ogawa, K.; Hayashi, Y.; Inagaki, F. *Chem. Pharm. Bull.* **2014**, *62*, 84.

(12) Wender, P. A.; Croatt, M. P.; Deschamps, N. M. *Angew. Chem. Int. Ed.* **2006**, *45*, 2459.

(13) For reviews on allenic Pauson-Khand reactions, see: (a) Alcaide, B.; Almendros, P. *Eur. J. Org. Chem.* **2004**, 3377.

(14) Murakami, M.; Ubukata, M.; Itami, K.; Ito, Y. *Angew. Chem. Int. Ed.* **1998**, *37*, 2248.

(15) Alcaide, B.; Almendros, P.; Aragoncillo, C. *Chem. Soc. Rev.* **2010**, *39*, 783, references therein.

(16) For Johnson's work, see: (a) Skraba, S. L.; Johnson, R. P. *J. Org. Chem.* **2012**, *77*, 11096. For other related works, see: (a) Siebert, M. R.; Osbourn, J. M.; Brummond, K. M.; Tantillo, D. J. *J. Am. Chem. Soc.* **2010**, *132*, 11952. (b) Soriano, E.; Fernández, I. *Chem. Soc. Rev.* **2014**, DOI: 10.1039/c3cs60457h.

(17) Ingrosso, G.; Immirzi, A.; Porri, L. *J. Organomet. Chem.* **1973**, *60*, C35.

(18) Toyoshima, T.; Miura, T.; Murakami, M. *Angew. Chem. Int. Ed.* **2011**, *50*, 10436.

(19) Huang, G.; Kalek, M.; Himo, F. *J. Am. Chem. Soc.* **2013**, *135*, 7647.

(20) (a) Brusoe, A. T.; Alexanian, E. J. *Angew. Chem. Int. Ed.* **2011**, *50*, 6596. (b) Brusoe, A. T.; Edwankar, R. V.; Alexanian, E. J. *Org. Lett.* **2012**, *14*, 6096.

(21) (a) Lu, P.; Ma, S. *Org. Lett.* **2007**, *9*, 2095. (b) Ma, S.; Lu, P.; Lu, L.; Hou, H.; Wei, J.; He, Q.; Gu, Z.; Jiang, X.; Jin, X. *Angew. Chem., Int. Ed.* **2005**, *44*, 5275. (c) Jiang, X.; Cheng, X.; Ma, S. *Angew. Chem., Int. Ed.* **2006**, *45*, 8009. (d) Ma, S.; Lu, L. *Chem. Asian J.* **2007**, *2*, 199. (e) Chen, G.; Jiang, X.; Fu, C.; Ma, S. *Chem. Lett.* **2010**, *39*, 78. (f) Lu, P.; Ma, S. *Chin. J. Chem.* **2010**, *28*, 1600. (g) Aubert, C.; Fensterbank, L.; Garcia, P.; Malacria, M. Simonneau, A. *Chem. Rev.* **2011**, *111*, 1954.

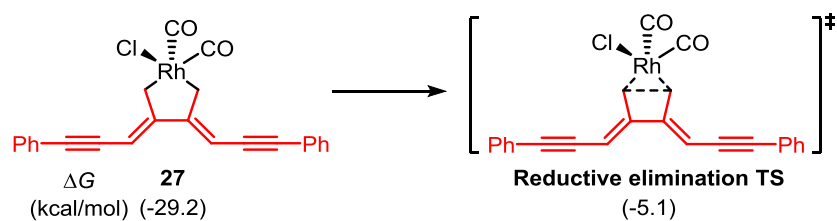
(22) Gaussian 09, Rev. B.01: Frisch, M. J.; *et al.*, Gaussian, Inc., Wallingford CT, 2010.

(23) Zhao, Y.; Truhlar, D. G. *Theor. Chem. Acc.* **2008**, *120*, 215.

(24) For computational studies on rhodium-catalyzed (5+2) cycloadditions, see: (a) Yu, Z. –X.; Wender, P. A.; Houk, K. N. *J. Am. Chem. Soc.* **2004**, *126*, 9154. (b) Liu, P.; Cheong, P. H. –Y.; Yu, Z. –X.; Wender, P. A.; Houk, K. N. *Angew. Chem. Int. Ed.* **2008**, *47*, 3939. (c) Wang, Y. Wang, J.; Su, J.; Huang, F.; Jiao, L.; Liang, Y.; Yang, D.; Zhang, S.; Wender, P. A.; Yu, Z. –X. *J. Am. Chem. Soc.* **2007**, *129*, 10060. (d) Yu, Z. –X.; Cheong, P. H. –Y.; Liu, P.; Legault, C. Y.; Wender, P. A.; Houk, P. A. *J. Am. Chem. Soc.* **2008**, *130*, 2378. (e) Xu, X.; Liu, P.; Lesser, A.; Sirois, L. E.; Wender, P. A.; Houk, K. N. *J. Am. Chem. Soc.* **2012**, *134*, 11012. For computational studies on other metal-catalyzed (5+2) cycloadditions, see: (f) Hong, X.; Liu, P.; Houk, K. N. *J. Am. Chem. Soc.* **2013**, *135*, 1456. (g) Hong, X.; Trost, B. M.; Houk, K. N. *J. Am. Chem. Soc.* **2013**, *135*, 6588. For other related mechanistic studies, see: (h) Wang, H.; Sawyer, J. R.; Evans, P. A.; Baik, M. –

H. *Angew. Chem. Int. Ed.* **2008**, *47*, 342. (i) Jiao, L.; Lin, M.; Yu, Z. -X. *J. Am. Chem. Soc.* **2011**, *133*, 447. (j) Zhang, Q.; Yu, H. -Z.; Li, Y. -T.; Liu, L.; Huang, Y.; Fu, Y. *Dalton Trans.* **2013**, *42*, 4175. (k) Inglesby, P. A.; Bacsa, J.; Negru, D. E.; Evans, P. A. *Angew. Chem. Int. Ed.* **2014**, *53*, 3952.

(25) We studied the C-C reductive elimination from **27**, the barrier is 24.1 kcal/mol, which is significantly higher than the barrier of observed (5+2) cycloaddition with allene-yne **10** under the same conditions (15.4 kcal/mol).



## Chapter 4. Distortion-accelerated Cycloadditions and Strain-Release-Promoted

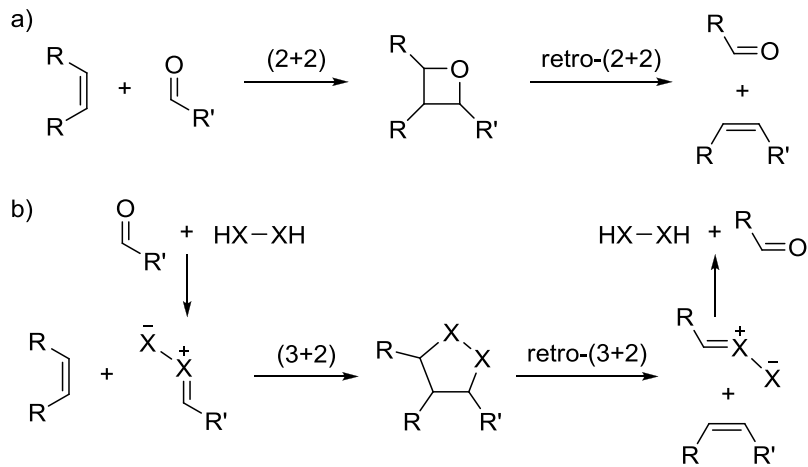
### Cycloreversions in the Organocatalytic Carbonyl-Olefin Metathesis

#### 4.1 Abstract

The mechanism of hydrazine-catalyzed carbonyl-olefin metathesis relying on a novel (3+2) strategy is studied by density functional theory (DFT) calculations. The origins of the special reactivity of cyclopropene in this transformation are revealed, and the reactivities of different alkenes in the (3+2) cycloadditions and cycloreversions are compared. It is found that the ease of distortion of reactants accelerates cycloadditions, and that the strain release is the controlling factor for cycloreversions.

#### 4.2 Introduction

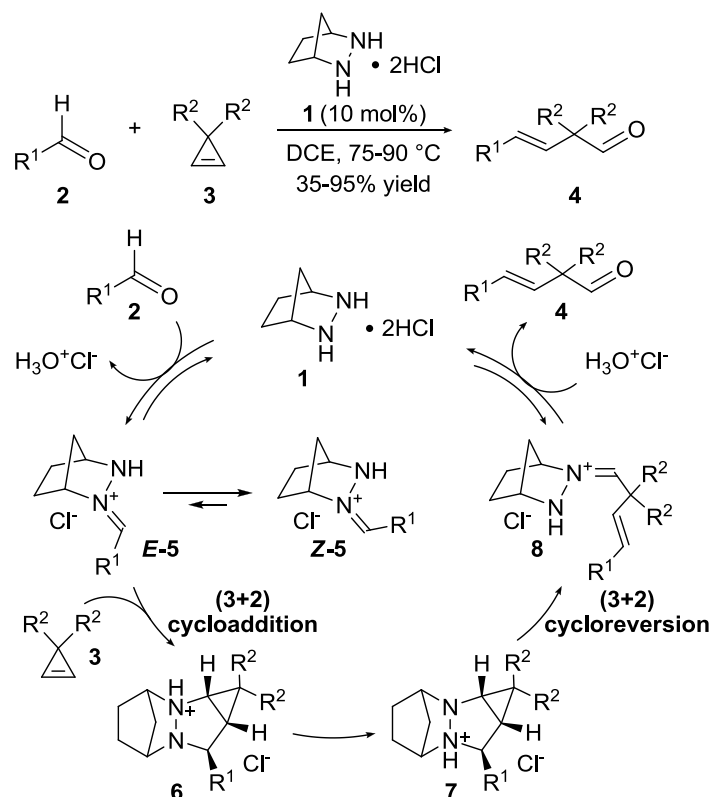
The carbonyl-olefin metathesis relying on various (2+2) cycloaddition/cycloreversion strategies (Scheme 4.1a) has been established for decades, but these reactions usually require photochemical promotion<sup>1</sup> or stoichiometric amounts of transition-metal reagents.<sup>2</sup> The catalytic and thermally allowed carbonyl-olefin metathesis has recently become reality through the experimental elaboration of a new (3+2) cycloaddition/cycloreversion strategy (Scheme 4.1b) from one of our laboratories.<sup>3</sup> The new route involves the ring-opening metathesis of cyclopropenes with aldehydes using a simple hydrazine organocatalyst.<sup>4</sup> Here we have determined the origins of the special reactivity of cyclopropene<sup>5</sup> and quantitated the reactivities of different alkenes in the (3+2) cycloadditions and cycloreversions. We show that the ease of distortion of reactants accelerates the cycloaddition, while the strain release of cycloadducts is the key to a facile retro-(3+2) reaction.



**Scheme 4.1.** The (2+2) and (3+2) strategies for carbonyl-olefin metathesis.

In the previous experimental study,<sup>3</sup> the ring-opening metathesis of cyclopropenes **3** with aldehydes **2** under the catalysis of the bis HCl salt of hydrazine **1** gave products **4** with complete *E*-olefin selectivity in moderate to good yields (Scheme 4.2). Mechanistically, the protonated azomethine imine **5** rather than the 1,3-dipolar azomethine imine was found to be a key intermediate in the catalytic cycle, which is supported by the preparation of putative intermediate and <sup>1</sup>H NMR observations.<sup>3</sup> As shown in Scheme 4.2, the catalytic cycle starts from the condensation of aldehyde **2** with hydrazine catalyst **1**, and then the reactive intermediate **E-5** undergoes cycloaddition with cyclopropene **3**. After the conversion of cycloadduct **6** to **7** by proton transfer, the orthogonal (3+2) cycloreversion of **7** produces hydrazonium **8**. The subsequent hydrolysis of **8** liberates the metathesis product **4** and regenerates catalyst **1**. Cyclopropenes work well, but norbornene and stilbene among other olefins do not undergo metathesis with aldehydes under the same conditions.<sup>3</sup> To gain mechanistic insights into this novel (3+2) cycloaddition/cycloreversion metathesis strategy, especially the origins of differing reactivities of various olefin substrates, we have conducted a density functional theory (DFT) study of this process.





**Scheme 4.2.** Catalytic carbonyl-olefin metathesis between aldehydes and cyclopropenes and the proposed mechanism.

### 4.3 Computational Details

Geometry optimizations, frequencies, and thermal energy corrections were performed with the M062X functional,<sup>6,7</sup> 6-31G(d) basis set for all elements implemented in Gaussian 09. Energies were evaluated with the M062X method, the 6-311+G(d,p) basis set for all elements.<sup>8</sup> All reported free energies involve zero-point vibrational energy corrections and thermal corrections to Gibbs free energy at 298 K. The solvation free energy corrections were computed with CPCM model on gas-phase optimized geometries and dichloroethane was chosen as the solvent for consistency with the experiment.

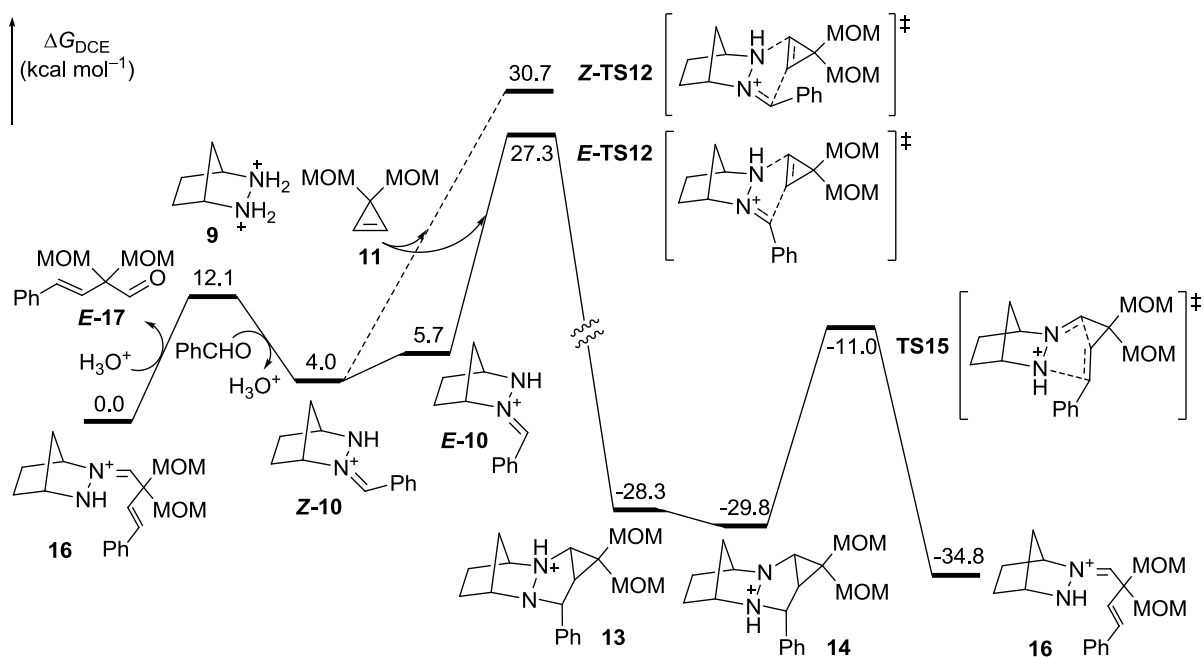
## 4.4 Results and Discussion

### 4.4.1 The Mechanism of Organocatalytic Carbonyl-Olefin Metathesis

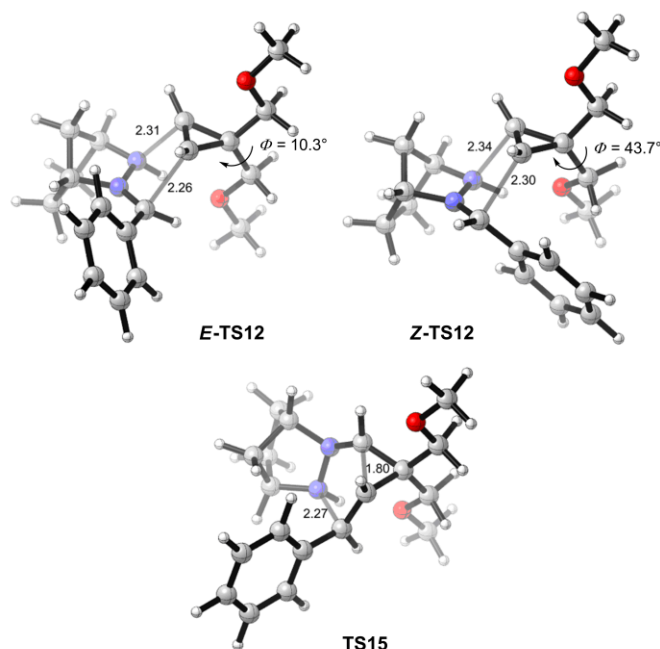
The Gibbs free energies for the catalytic cycle proposed in Scheme 4.2 are shown in Figure 4.1. From the cationic catalyst **9**, the condensation with benzaldehyde is exergonic by 8.1 kcal mol<sup>-1</sup> in dichloroethane, giving protonated azomethine imine **Z-10**. Compared to its isomer **E-10**, the **Z-10** is more stable by 1.7 kcal mol<sup>-1</sup>, which is consistent with the experimental isolation of **Z-10**.<sup>3</sup> Although azomethine imine is a well-known 1,3-dipole in the 1,3-dipolar cycloaddition, its cationic species (hydrazonium, such as **E-10** and **Z-10**) is also a good 4 $\pi$  component for cycloadditions.<sup>9</sup> From **Z-10** and **E-10**, there are eight possible (3+2) cycloaddition transition states with cyclopropene **11**. Calculations indicate that the transition state **E-TS12** generated from the less stable intermediate **E-10** is the most favorable one with an activation free energy of 21.6 kcal mol<sup>-1</sup>. The formation of the (3+2) cycloadduct **13** is highly exergonic, making the cycloaddition step irreversible. The subsequent proton transfer converts **13** into the retro-(3+2) cycloaddition precursor **14**. The cycloreversion step via transition state **TS15** (Figure 4.2) is facile, requiring an activation free energy of 18.8 kcal mol<sup>-1</sup> to form another protonated azomethine imine **16**. The hydrolysis of **16** to liberate the metathesis product **E-17** and to regenerate catalyst **9** is endergonic by 12.1 kcal mol<sup>-1</sup>, suggesting that the resting state of the catalytic cycle is the hydrazonium **16**. The overall barrier for the catalytic ring-opening metathesis of cyclopropene **11** with benzaldehyde is 27.3 kcal mol<sup>-1</sup>, which arises from: (1) the 4.0 kcal mol<sup>-1</sup> exchange energy of reactant benzaldehyde and product aldehyde **E-17** with catalyst **9**, (2) the 1.7 kcal mol<sup>-1</sup> isomerization energy from hydrazonium **Z-10** to **E-10**, and (3) the 21.6 kcal mol<sup>-1</sup> activation free energy of the (3+2) cycloaddition between **E-10** and

cyclopropene **11**. The DFT-computed free energy barrier (27.3 kcal mol<sup>-1</sup>) for the whole reaction in dichloroethane is consistent with the experimental reaction temperatures of 75-90 °C (Scheme 4.2).

Complete *E*-selectivity is observed in the experiments (Scheme 4.2). Computational results show that the lowest-energy pathway for the generation of *Z*-olefin metathesis product is through the (3+2) cycloaddition of hydrazone **Z-10** with cyclopropene **11** via **Z-TS12** (Figure 4.2). The free energy of transition state **Z-TS12** from **Z-10** is 3.4 kcal mol<sup>-1</sup> higher than that of transition state **E-TS12** leading to the *E*-olefin metathesis product (30.7 versus 27.3 kcal mol<sup>-1</sup>, Figure 4.1).<sup>10</sup> This predicts an *E*-/*Z*-olefin ratio of more than 100:1, in agreement with the experimental observation. In the transition state **Z-TS12**, to avoid steric clashes between the phenyl group of **Z-10** and the substituent on cyclopropene **11**, the dihedral angle of the methoxymethyl group at the 3-position of cyclopropene increases to 43.7°, which is 33.4° larger than the corresponding value in **E-TS12** (Figure 4.2). This greatly increases the distortion energy of cyclopropene **11**, making transition state **Z-TS12** unfavourable.



**Figure 4.1.** DFT-computed Gibbs free energies for the ring-opening metathesis of cyclopropene **11** with benzaldehyde using catalyst **9** (MOM = methoxymethyl).

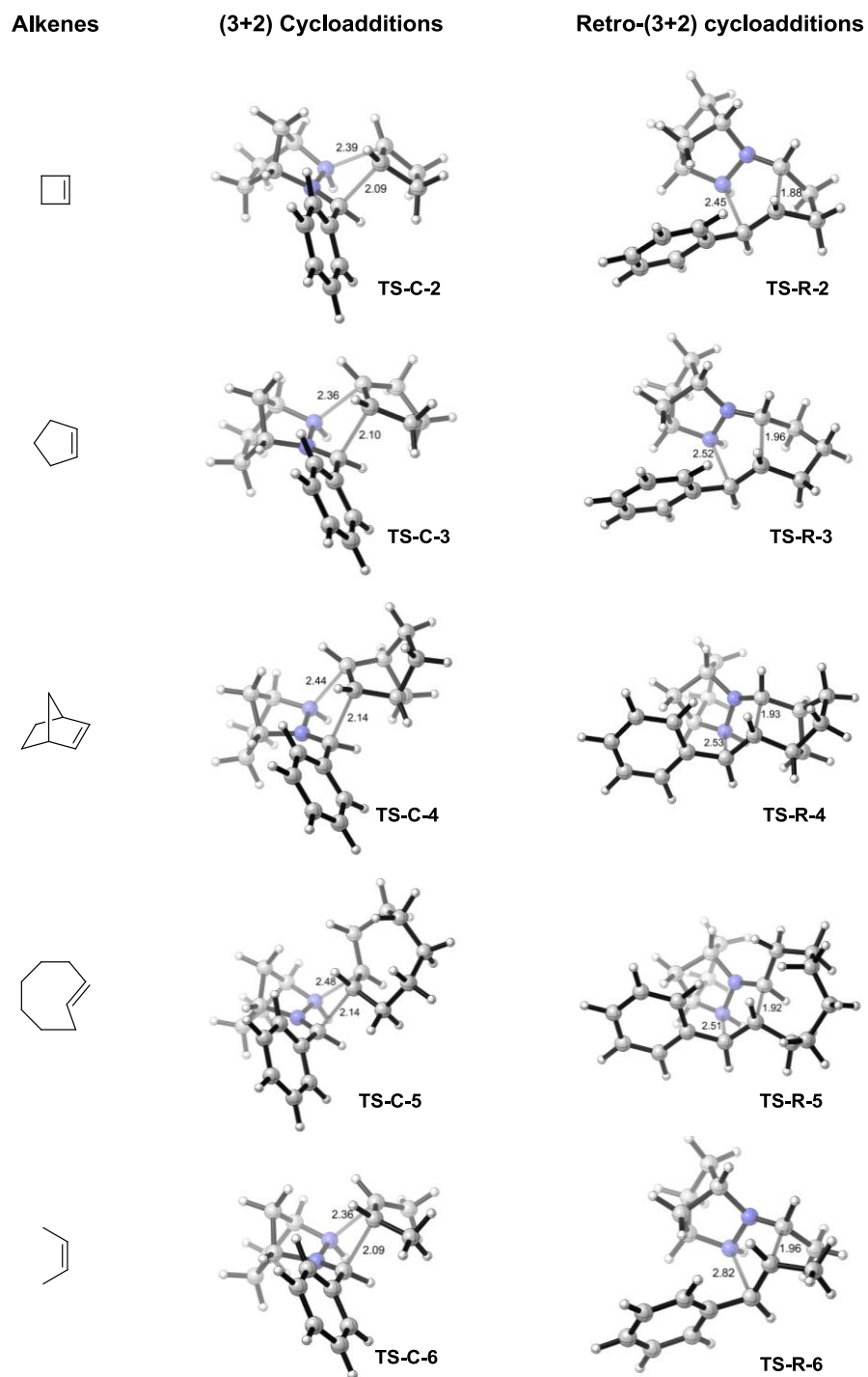


**Figure 4.2.** The (3+2) cycloaddition transition states *E*-TS12 and *Z*-TS12 and the cycloreversion transition state TS15 (Distances are in Å; atoms distant from the observer are “fogged out”).

#### 4.4.2 The Distortion Control of Cycloadditions

We further explored the origins of reactivity of different olefin substrates. For the current hydrazine-catalyzed carbonyl-olefin metatheses involving different olefins, the free energy difference between the resting state and the reactive hydrazone *E*-10 should be similar (about 6 kcal mol<sup>-1</sup>), so the overall reaction rate depends on the barriers of the (3+2) cycloaddition and cycloreversion. We have investigated the (3+2) cycloadditions of various alkenes with *E*-10 and the corresponding retro-(3+2) cycloadditions (Figure 4.3). The computational results are summarized in Tables 4.1 and 4.2. We also analyzed the activation barriers of the (3+2) cycloadditions using the distortion/interaction model.<sup>11</sup> This model relates the activation energy to the distortion energy required for the geometrical deformation of the reactants to achieve their

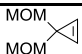

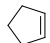
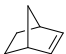
transition-state conformations, and to the interaction energy arising from the interactions between the two distorted reactants in the transition state.



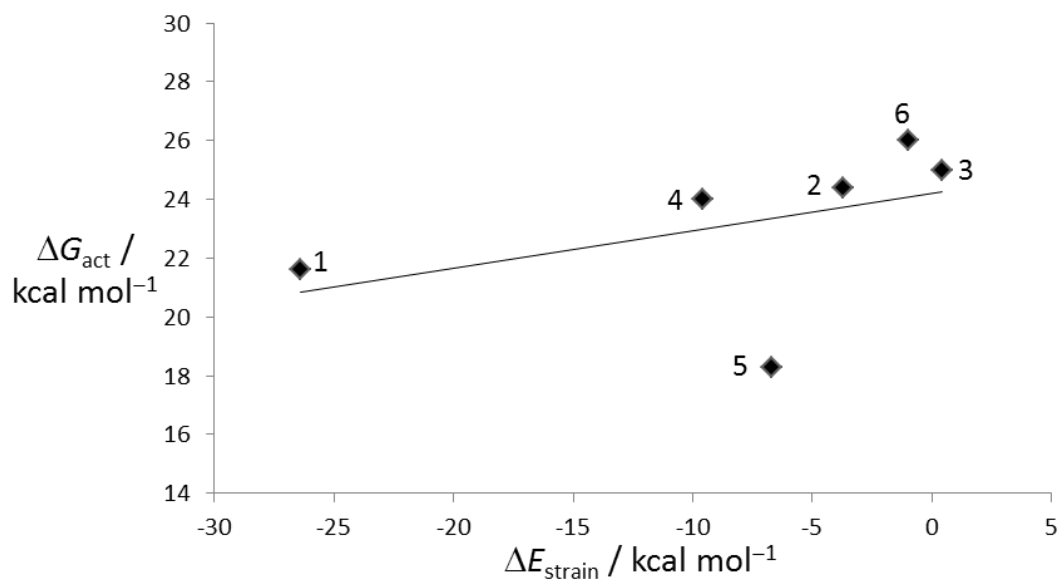
**Figure 4.3.** Optimized transition-state structures of the (3+2) cycloadditions of various alkenes with *E*-10 and the corresponding retro-(3+2) cycloadditions (Distances are in Å; atoms distant from the observer are “fogged out”).

Table 4.1 shows that the (3+2) cycloadditions of hydrazone **E-10** with various alkenes are all exergonic by more than 10 kcal mol<sup>-1</sup> with the activation barriers varying from 18.3 to 26.0 kcal mol<sup>-1</sup>. The activation free energies correlate poorly ( $r^2 = 0.20$ ) with the strain release from these reactions (Figure 4.4).<sup>12</sup> *Trans*-cyclooctene is the most reactive olefin, but the strain release is moderate. Therefore, the strain release is not the main factor promoting the (3+2) cycloaddition. The transition-state distortion energies play a predominant role in the cycloaddition reactivity. Figure 4.5 shows a good correlation ( $r^2 = 0.84$ ) between activation barriers and reactant distortion energies. *Trans*-cyclooctene is highly pre-distorted toward its cycloaddition transition-state geometry, and cyclopropene has very easy distortion of the C-H bonds out of the C=C bond plane,<sup>13</sup> which is a prominent distortion in the transition state. Consequently, they are the two most reactive olefins in the (3+2) cycloaddition step.

**Table 4.1.** Activation free energy ( $\Delta G_{\text{act}}$ ) and reaction free energy ( $\Delta G_{\text{rxn}}$ ) for the (3+2) cycloadditions of hydrazonium **E-10** with various alkenes in dichloroethane, the strain release ( $\Delta E_{\text{strain}}$ ) from the alkene to the corresponding alkane, and the transition-state distortion energy ( $\Delta E_{\text{dist}}$ )

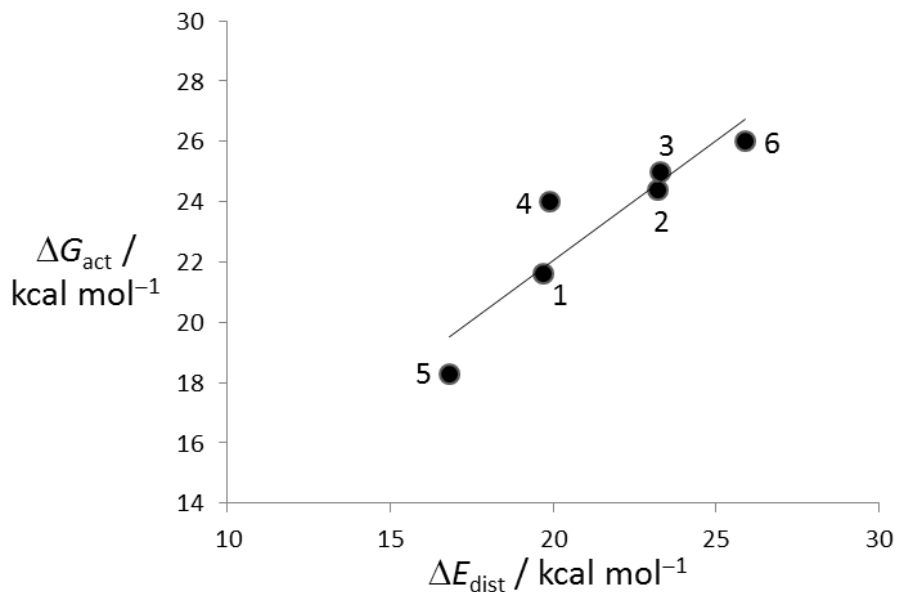
Entry <sup>a</sup>	Alkene	$\Delta G_{\text{act}}$	$\Delta G_{\text{rxn}}$	$\Delta E_{\text{strain}}$	$\Delta E_{\text{dist}}$
1		21.6	-34.0	-26.4	19.7
2		24.4	-18.9	-3.7	23.2
3		25.0	-13.8	0.4	23.3
4		24.0	-20.3	-9.6	19.9
5		18.3	-21.3	-6.7	16.8
6		26.0	-13.6	-1.0	25.9

<sup>a</sup> All energies are in kcal mol<sup>-1</sup>.



**Figure 4.4.** Plot of activation free energy  $\Delta G_{\text{act}}$  for cycloadditions versus strain release  $\Delta E_{\text{strain}}$  ( $\Delta G_{\text{act}} = 0.13\Delta E_{\text{strain}} + 24.22$ ,  $r^2 = 0.20$ ). See Table 4.1 for meaning of symbols.



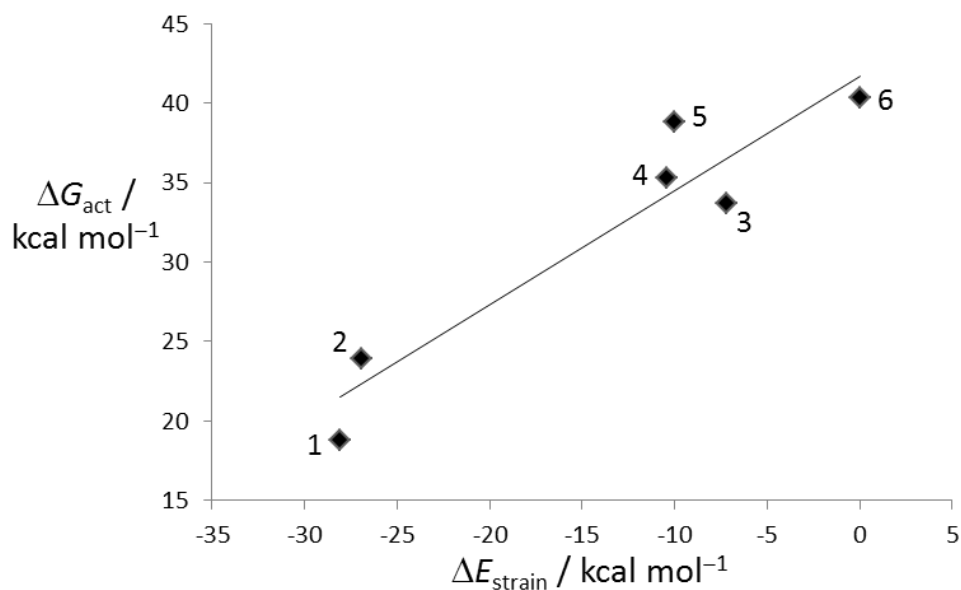


**Figure 4.5.** Plot of activation free energy  $\Delta G_{\text{act}}$  for cycloadditions versus distortion energy  $\Delta E_{\text{dist}}$  ( $\Delta G_{\text{act}} = 0.79\Delta E_{\text{dist}} + 6.23$ ,  $r^2 = 0.84$ ). See Table 4.1 for meaning of symbols.

#### 4.4.3 The Strain-Release Control of Cycloreversions

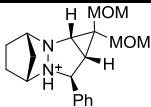
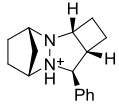
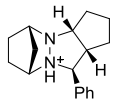
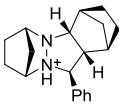
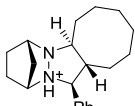
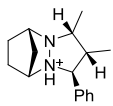
Table 4.2 provides the energetics for the cycloreversion step, which may also control the overall rate of reactions. For most substrates (Table 4.2, entries 3-6), the (3+2) cycloreversion is thermodynamically disfavored, and the activation barrier is very high. This indicates that the retro-(3+2) cycloaddition is the bottleneck for this carbonyl-olefin metathesis using other olefins. For instance, the activation barrier for the (3+2) cycloreversion of the substrate generated from norbornene is  $35.3 \text{ kcal mol}^{-1}$  (Table 4.2, entry 4), which is  $8.0 \text{ kcal mol}^{-1}$  higher than the overall barrier for the carbonyl-cyclopropene metathesis ( $27.3 \text{ kcal mol}^{-1}$ , Figure 4.1). This explains why norbornene cannot undergo metathesis with aldehydes under the same conditions. The strain release of the alkane moiety from the alkene is the key factor controlling the cycloreversion reactivity, as demonstrated by the good correlation ( $r^2 = 0.89$ ) between activation barriers and released

strain energies (Figure 4.6).<sup>12</sup> For the carbonyl-cyclopropene metathesis, the retro-(3+2) cycloaddition is accompanied by the energy release of 28.1 kcal mol<sup>-1</sup> from the highly strained cyclopropane skeleton. This is the driving force for the cycloreversion step as well as the whole reaction.



**Figure 4.6.** Plot of activation free energy  $\Delta G_{\text{act}}$  for cycloreversions versus strain release  $\Delta E_{\text{strain}}$  ( $\Delta G_{\text{act}} = 0.72\Delta E_{\text{strain}} + 41.71$ ,  $r^2 = 0.89$ ). See Table 4.2 for meaning of symbols.

**Table 4.2** Activation free energy ( $\Delta G_{\text{act}}$ ) and reaction free energy ( $\Delta G_{\text{rxn}}$ ) for the (3+2) cycloreversions in dichloroethane and the strain release ( $\Delta E_{\text{strain}}$ ) of the alkane moiety from the alkene

Entry <sup>a</sup>	Substrate	$\Delta G_{\text{act}}$	$\Delta G_{\text{rxn}}$	$\Delta E_{\text{strain}}$
1		18.8	-5.0	-28.1
2		23.9	-3.6	-26.9
3		33.7	9.3	-7.2
4		35.3	11.2	-10.4
5		38.8	8.4	-10.0
6		40.3	5.5	0.0

<sup>a</sup> All energies are in kcal mol<sup>-1</sup>.

## 4.5 Conclusions

We have studied the mechanism of hydrazine-catalyzed carbonyl-olefin metathesis using density functional theory (DFT) calculations. Through comparing the reactivities of different alkenes in the (3+2) cycloadditions and cycloreversions, we explain the origins of the special reactivity of cyclopropene in this transformation. The ease of distortion of reactants (cyclopropene has very easy distortion of the C-H bonds out of the C=C bond

plane) can accelerate cycloadditions, and the strain release (cyclopropane skeleton has a high strain energy) is the controlling factor for cycloreversions. To achieve both is the key to a successful carbonyl-olefin metathesis with hydrazine catalyst. Further computation-guided designs of new catalysts and reactions in the field of carbonyl-olefin metathesis are ongoing in our laboratories.

#### 4.6 References

(1) (a) Perez-Ruiz, R.; Gil, S.; Miranda, M. A. *J. Org. Chem.* 2005, **70**, 1376; (b) Valiulin, R. A.; Kutateladze, A. G. *Org. Lett.* 2009, **11**, 3886; (c) Valiulin, R. A.; Arisco, T. M.; Kutateladze, A. G. *J. Org. Chem.* 2011, **76**, 1319.

(2) (a) Fu, G. C.; Grubbs, R. H. *J. Am. Chem. Soc.* 1993, **115**, 3800; (b) Nicolaou, K. C.; Postema, M. H. D.; Claiborne, C. F. *J. Am. Chem. Soc.* 1996, **118**, 1565; (c) Rainier, J. D.; Allwein, S. P.; Cox, J. M. *J. Org. Chem.* 2001, **66**, 1380; (d) Iyer, K.; Rainier, J. D. *J. Am. Chem. Soc.* 2007, **129**, 12604.

(3) Griffith, A. K.; Vanos, C. M.; Lambert, T. H. *J. Am. Chem. Soc.* 2012, **134**, 18581.

(4) For a recent highlight, see: Lee, A.-L. *Angew. Chem., Int. Ed.* 2013, **52**, 4524.

(5) For reviews on the cyclopropene chemistry, see: (a) Rubin, M.; Rubina, M.; Gevorgyan, V. *Synthesis* 2006, 1221; (b) Zhu, Z.-B.; Wei, Y.; Shi, M. *Chem. Soc. Rev.* 2011, **40**, 5534; (c) Wilson, M. R.; Taylor, R. E. *Angew. Chem., Int. Ed.* 2013, **52**, 4078.

(6) Frisch, M. J. and et al., *Gaussian 09*, Revision C.01, Gaussian, Inc., Wallingford CT, 2010.

(7) (a) Zhao, Y.; Truhlar, D. G. *Theor. Chem. Acc.* 2008, **120**, 215; (b) Zhao, Y.; Truhlar, D. G. *Acc. Chem. Res.* 2008, **41**, 157.

(8) (a) Paton, R. S.; Mackey, J. L.; Kim, W. H.; Lee, J. H.; Danishefsky, S. J.; Houk, K. N. *J. Am. Chem. Soc.* 2010, **132**, 9335; (b) Lan, Y.; Zou, L.; Cao, Y.; Houk, K. N. *J. Phys. Chem. A* 2011, **115**, 13906.

(9) Rueping, M.; Maji, M. S.; Küçük, H. B.; Atodiresei, I. *Angew. Chem., Int. Ed.* 2012, **51**, 12864, and references therein.

(10) The reactions of cyclopropene itself with hydrazoniums (**E-10** and **Z-10**) are also computed. Without the substituents at the 3-position, the reactions become faster (1-2 kcal mol<sup>-1</sup> decrease in the barrier), and the *E*-olefin metathesis product is still favored, although the free energy difference of two transition states drops from 3.4 to 2.2 kcal mol<sup>-1</sup>.

(11) (a) Ess, D. H.; Houk, K. N. *J. Am. Chem. Soc.* 2007, **129**, 10646; (b) Ess, D. H.; Houk, K. N. *J. Am. Chem. Soc.* 2008, **130**, 10187; (c) van Zeist, W.-J.; Bickelhaupt, F. M. *Org. Biomol. Chem.*

2010, **8**, 3118; (d) Fernández, I.; Cossó, F. P.; Bickelhaupt, F. M. *J. Org. Chem.* 2011, **76**, 2310; (e) Lan, Y.; Wheeler, S. E.; Houk, K. N. *J. Chem. Theory Comput.* 2011, **7**, 2104; (f) Paton, R. S.; Kim, S.; Ross, A. G.; Danishefsky, S. J.; Houk, K. N. *Angew. Chem., Int. Ed.* 2011, **50**, 10366; (g) Fernández, I.; Bickelhaupt, F. M. *J. Comput. Chem.* 2012, **33**, 509; (h) Gordon, C. G.; Mackey, J. L.; Jewett, J. C.; Sletten, E. M.; Houk, K. N.; Bertozzi, C. R. *J. Am. Chem. Soc.* 2012, **134**, 9199; (i) Liang, Y.; Mackey, J. L.; Lopez, S. A.; Liu, F.; Houk, K. N. *J. Am. Chem. Soc.* 2012, **134**, 17904; (j) Lopez, S. A.; Munk, M. E.; Houk, K. N. *J. Org. Chem.* 2013, **78**, 1576; (k) Lopez, S. A.; Houk, K. N. *J. Org. Chem.* 2013, **78**, 1778; (l) Zou, L.; Paton, R. S.; Eschenmoser, A.; Newhouse, T. R.; Baran, P. S.; Houk, K. N. *J. Org. Chem.* 2013, **78**, 4037; (m) Fernández, I.; Sola, M.; Bickelhaupt, F. M. *Chem. Eur. J.* 2013, **19**, 7416; (n) Kamber, D. N.; Nazarova, L. A.; Liang, Y.; Lopez, S. A.; Patterson, D. M.; Shih, H.-W.; Houk, K. N.; Prescher, J. A. *J. Am. Chem. Soc.* 2013, **135**, 13680.

(12) Strain energies are taken from: Schleyer, P. v. R.; Williams, J. E.; Blanchard, K. R. *J. Am. Chem. Soc.* 1970, **92**, 2377.

(13) Liu, F.; Paton, R. S.; Kim, S.; Liang, Y.; Houk, K. N. *J. Am. Chem. Soc.* 2013, **135**, 15642.

## Chapter 5. Distortion-Acceleration Effect of Alkynyl Substituents in the Hexadehydro-Diels-Alder Reaction

### 5.1 Abstract

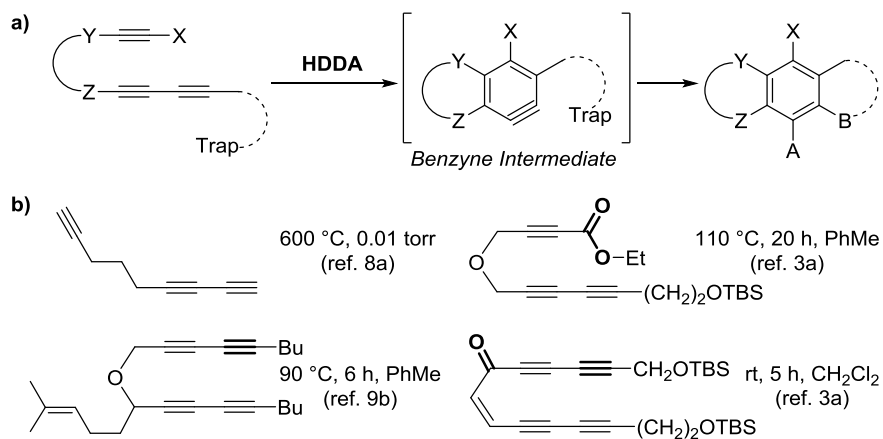
The intramolecular hexadehydro-Diels-Alder (HDDA) reactions between 1,3-diynes and alkynes produce highly reactive benzyne under thermal conditions without catalysts or other reagents. Experiments show that the substituents, especially the alkynyl group, on the yne moiety have a dramatic influence on the HDDA reactivity. Density functional theory (DFT) calculations and the distortion/interaction analysis show that, for the activated substrates, the stepwise diradical pathway is more favorable than the concerted [4+2] process. The mechanism for the synthetically useful HDDA reactions differs from the concerted mechanism favored by most conventional DA reactions. The alkynyl substituent dramatically accelerates the HDDA reaction mainly by decreasing the distortion energy required to achieve the diradical transition state. However, this distortion-acceleration effect does not exist in the concerted DA reactions.

### 5.2 Introduction

The Diels-Alder (DA) reaction mechanism has a long history of controversy.<sup>1</sup> The parent reaction of butadiene and ethene is concerted,<sup>1a</sup> and the concerted mechanism is more favorable for most DA reactions employed in organic synthesis.<sup>2</sup> The cycloaddition between butadiyne and ethyne to generate benzyne is the most highly oxidized DA variant, which is named the hexadehydro-Diels-Alder (HDDA) reaction.<sup>3a,4</sup> The reverse process of this reaction is believed to play an important role in combustion chemistry of aromatic compounds.<sup>5</sup> According to the high-level *ab initio* computations, the concerted retro-HDDA route from benzyne to butadiyne and

ethyne is consistent with the experimental observations.<sup>5a</sup> However, it was also pointed out that the competitive stepwise route through a singlet diradical intermediate awaits elucidation.<sup>5a</sup> In 2011, Johnson and co-workers reported the (U)CCSD(T)//M05-2X computational results for the cycloaddition of butadiyne with ethyne.<sup>6</sup> It was found that the concerted and stepwise routes to benzyne have very similar energetics, with only a 0.5 kcal mol<sup>-1</sup> advantage for the concerted one.<sup>6</sup>

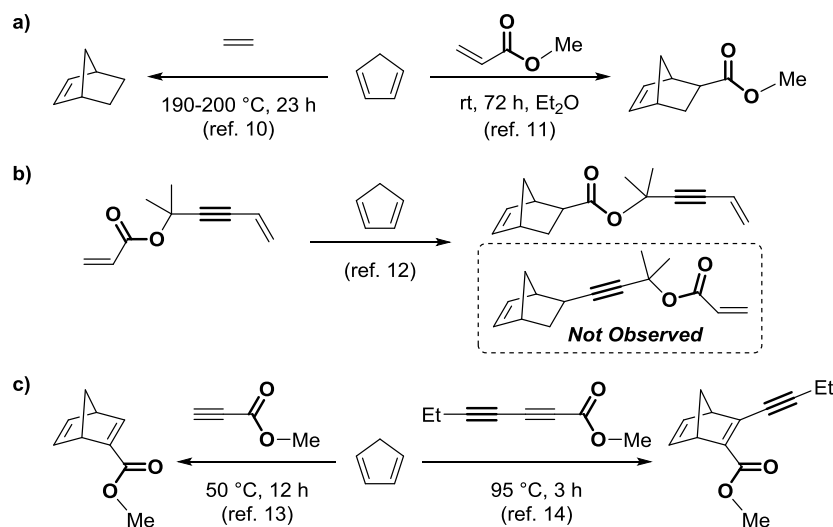
The power of the intramolecular hexadehydro-Diels-Alder (HDDA) reaction in synthetic chemistry was greatly expanded through the recent discovery by Hoyer and co-workers.<sup>3a</sup> As shown in Scheme 5.1a, a 1,3-diyne undergoes the [4+2] cycloaddition with an alkyne to produce the benzyne intermediate, which can be trapped *in situ* to give structurally complex benzenoid products in an atom- and step-economical fashion.<sup>7</sup> Experimental explorations by the Hoyer,<sup>3</sup> Johnson,<sup>8a</sup> and Lee<sup>9</sup> groups indicated that the substituents on the yne moiety affect the HDDA reactivities dramatically. Four representative HDDA substrates with their reaction conditions are given in Scheme 5.1b. The unactivated diyne-yne [4+2] cycloaddition requires harsh conditions (600 °C, 0.01 torr) to occur.<sup>8a</sup> When the alkyne is activated by the ester group, the reaction temperature is decreased to 110 °C.<sup>3a</sup> The use of alkynyl substituted diynophile further lowers the temperature required for the HDDA reaction to 90 °C.<sup>9b</sup> The combination of alkynyl and carbonyl activation makes the reaction occur even at room temperature.<sup>3a</sup>





**Scheme 5.1.** a) Formation of benzyne through the HDDA reactions and subsequent trapping reactions to generate various benzene derivatives. b) Representative substrates and conditions for the HDDA reactions.

For normal electron demand Diels-Alder (DA) reactions between diene and dienophile, the use of strong electron-withdrawing groups to activate the dienophile is a well-known strategy to lower the reaction temperature (Scheme 5.2a).<sup>10,11</sup> This strategy also works well when the dienophile is activated by the ester group in the HDDA reaction (Scheme 5.1b). Dramatic activation by an alkynyl group is also observed (Scheme 5.1b). However, the alkynyl activation is not observed in the DA reactions of cyclopentadiene. As shown in Scheme 5.2b-c, the DA reactivity of enyne with cyclopentadiene is much lower than that of acrylate,<sup>12</sup> and additional alkynyl substitution does not improve the reactivity of propiolate.<sup>13,14</sup> These phenomena are significantly different from the observations for HDDA reactions (Scheme 5.1b). To better understand the mechanism and substituent effects of the HDDA reaction, especially the origins of the unique activation by alkynyl groups, we conducted a density functional theory (DFT) study of this intriguing process.<sup>15-17</sup> Here we have found that, for the synthetically useful HDDA reactions, the stepwise diradical mechanism is more favorable than the concerted mechanism. The alkynyl substituent dramatically accelerates the HDDA reaction mainly by decreasing the distortion energy required to achieve the diradical transition state.



**Scheme 5.2.** Effects of the ester and alkynyl groups on the DA reactivities of dienophiles with cyclopentadiene.

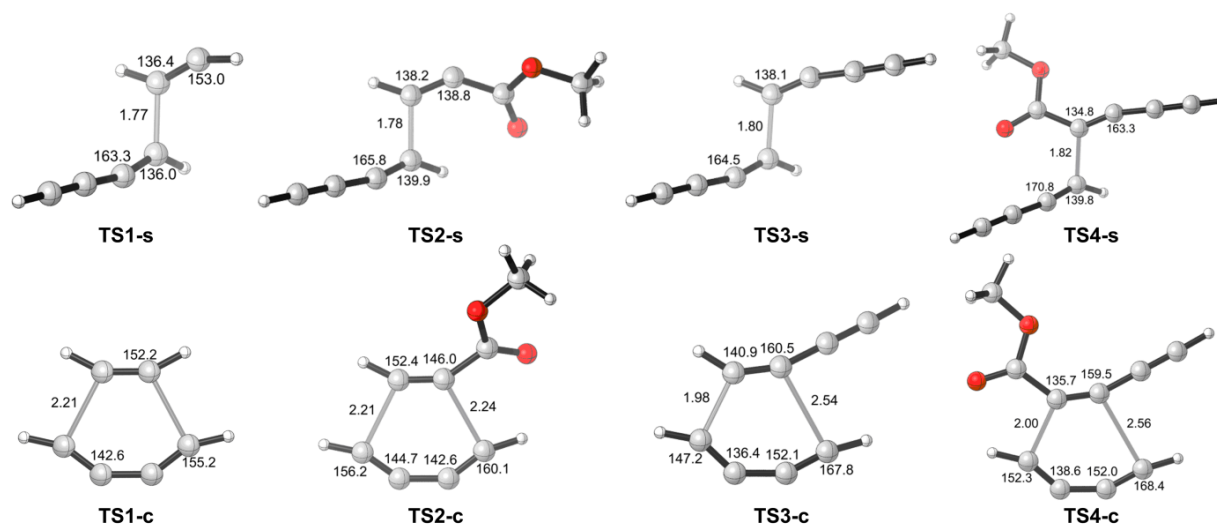
### 5.3 Computational Details

Geometry optimizations were performed with the (U)M062X functional, 6-311+G(d,p) basis set for all elements implemented in Gaussian 09. Energies were evaluated with the (U)M062X method, the 6-311+G(d,p) basis set for all elements. Computed structures are illustrated using CYLVIEW drawings.

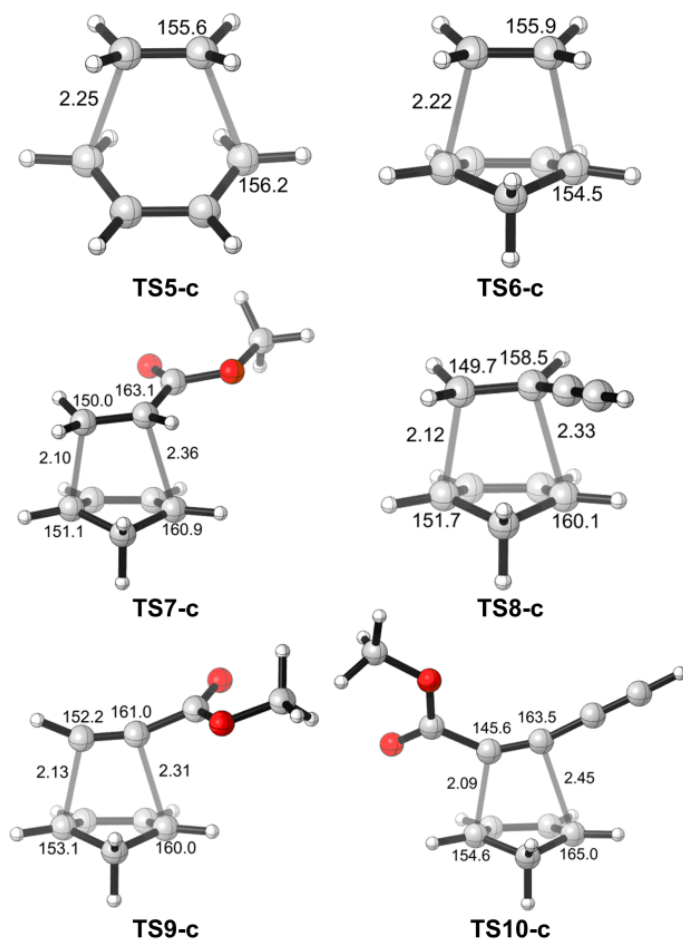
### 5.4 Results and Discussion

Figure 5.1 shows the transition-state structures **TS1-4-s** for the formation of diradical intermediates from butadiyne and four dienophiles with different reactivities (ethyne, methyl propiolate, butadiyne, and methyl pentadiynoate). This step is rate-determining in the stepwise HDDA reactions. The transition-state structures **TS1-4-c** for the concerted reactions are also shown in Figure 5.1. The DA reactions of butadiene with ethene and cyclopentadiene with five

dienophiles(ethene, methyl acrylate, butenyne, methyl propiolate, and methyl pentadiynoate) via transition states **TS5-10-c** were investigated for comparison (Figure 5.2).<sup>18</sup> We also analyzed the activation barriers using the distortion/interaction model<sup>19</sup> (or activation strain model<sup>20</sup>). This model relates the activation energy ( $E_{act}$ ) to the distortion energy ( $E_{dist}$ ) required for the geometrical deformation of the reactants to achieve their transition-state conformations and the interaction energy ( $E_{int}$ ) arising from the interactions between two distorted reactants in the transition state.<sup>21</sup> All of these results are summarized in Table 5.1.



**Figure 5.1.** (U)M06-2X/6-311+G(d,p)-optimized transition-state structures for the stepwise or concerted HDDA reactions of butadiyne with diynophiles (distances in Å, angles in deg).



**Figure 5.2.** M06-2X/6-311+G(d,p)-optimized transition-state structures for the concerted DA reactions of butadiene with ethene and cyclopentadiene with dienophiles (distances in Å, angles or dihedral angles in deg).

**Table 5.1.** (U)M06-2X/6-311+G(d,p)-computed activation, distortion, and interaction energies (in kcal mol<sup>-1</sup>).

Entry	TS	$E_{\text{act}}$	$E_{\text{dist-2}}$	$E_{\text{dist-4}}$	$E_{\text{dist}}$	$E_{\text{int}}$
1	<b>TS1-s</b>	35.2	14.6	12.9	27.5	7.7
2	<b>TS2-s</b>	28.8	18.8	10.7	29.5	-0.7
3	<b>TS3-s</b>	28.4	11.6	11.6	23.2	5.2
4	<b>TS4-s</b>	25.7	14.2	10.1	24.3	1.4
5	<b>TS1-c</b>	36.0	14.0	29.3	43.3	-7.3
6	<b>TS2-c</b>	32.4	17.2	26.7	43.9	-11.5
7	<b>TS3-c</b>	35.4	16.1	27.9	44.0	-8.6
8	<b>TS4-c</b>	31.6	20.4	24.9	45.3	-13.7
9	<b>TS5-c</b>	19.6(33.0 <sup>[a]</sup> )	7.3	18.7	26.0	-6.4
10	<b>TS6-c</b>	16.1(29.7 <sup>[a]</sup> )	7.4	16.2	23.6	-7.5
11	<b>TS7-c</b>	10.1(26.0 <sup>[a]</sup> )	8.1	15.2	23.3	-13.2
12	<b>TS8-c</b>	14.0(28.8 <sup>[a]</sup> )	8.8	15.8	24.6	-10.6
13	<b>TS9-c</b>	14.0(28.4 <sup>[a]</sup> )	10.5	15.2	25.7	-11.7
14	<b>TS10-c</b>	13.3(27.7 <sup>[a]</sup> )	13.1	12.7	25.8	-12.5

[a] Activation free energy in the gas phase at 298 K.

The formation of benzyne from butadiyne and ethyne requires activation energies of 35.2 and 36.0 kcal mol<sup>-1</sup> for the stepwise and concerted reactions via transition states **TS1-s** and **TS1-c**, respectively (Table 5.1, entries 1 and 5). This suggests that the stepwise and concerted pathways are very competitive for the unactivated diyne-yne [4+2] cycloaddition, in accordance with the conclusion from the (U)CCSD(T)//M05-2X computations by Johnson and co-workers.<sup>6,22</sup> The barrier for the generation of cyclohexene from butadiene and ethene via concerted transition state **TS5-c** is 19.6 kcal mol<sup>-1</sup> (Table 5.1, entry 9). Interestingly, this reaction is 9.7 kcal mol<sup>-1</sup> less exothermic than the HDDA reaction of butadiyne and ethyne (-47.6 versus -57.3 kcal mol<sup>-1</sup>). This shows that the much higher barrier for the HDDA reaction cannot be explained by the reaction exothermicity. As shown in Figure 5.1, an enormous deformation for the linear diyne is required to achieve the concerted HDDA transition state **TS1-c**. The bend of two internal bond angles from 180 ° to 143 ° destroys the conjugative stabilization of diyne<sup>23</sup> and results in the repulsive orbital interactions between two distorted yne moieties. This makes the distortion energy of **TS1-c** about

17 kcal mol<sup>-1</sup> larger than that of the DA transition state **TS5-c** (43.3 versus 26.0 kcal mol<sup>-1</sup>), while the interaction energies are almost identical (-7.3 and -6.4 kcal mol<sup>-1</sup>; Table 5.1, entries 5 and 9). For the stepwise HDDA transition state **TS1-s** (Figure 5.1), the distortion energy is decreased by 15.8 kcal mol<sup>-1</sup> (27.5 versus 43.3 kcal mol<sup>-1</sup>; Table 5.1, entries 1 and 5) due to the much smaller geometrical change required for the diyne. However, the favorable interaction energy is also greatly reduced by 15.0 kcal mol<sup>-1</sup> (7.7 versus -7.3 kcal mol<sup>-1</sup>) because of the smaller orbital overlap between diyne and diynophile.

With activated diynophiles, the stepwise HDDA reactions are found to be more favorable, and the barriers are 3.6 to 7.0 kcal mol<sup>-1</sup> lower than those for the concerted [4+2] process (Table 5.1, entries 2-4 and 6-8). Introducing an ester group on ethyne decreases the activation energy by 6.4 kcal mol<sup>-1</sup> (28.8 versus 35.2 kcal mol<sup>-1</sup>; Table 5.1, entries 1-2). This is consistent with the much lower temperature required in the experiment (Scheme 5.1b). The distortion/interaction analysis showed that the reduction in the barrier is due to the elimination of the repulsive interaction energy (-0.7 versus 7.7 kcal mol<sup>-1</sup>). Such an interaction-acceleration effect also exists in the concerted DA reactions of cyclopentadiene with methyl acrylate and ethene: the methoxycarbonyl substituent increases the interaction energy by 5.7 kcal mol<sup>-1</sup> (Table 5.1, entries 10-11). These results indicate that the strong electronegativity of the ester group enhances the favorable interactions from the electron donor (diene or diyne) to acceptor (dienophile or diynophile) regardless of the mechanism (concerted or stepwise).

Experimentally, the alkynyl substituent improves the HDDA reactivity dramatically (Scheme 5.1b), and calculations reproduce this phenomenon. The stepwise HDDA reaction between two butadiynes has an activation barrier of 28.4 kcal mol<sup>-1</sup> (Table 5.1, entry 3), 6.8 kcal mol<sup>-1</sup> lower than that for the reaction between butadiyne and ethyne (35.2 kcal mol<sup>-1</sup>; Table 5.1, entry 1). This

suggests that the alkynyl substituent accelerates the HDDA reaction by about 5 orders of magnitude. The much higher reactivity of the diyne-diyne cycloaddition mainly comes from the lower distortion energy (23.2 versus 27.5 kcal mol<sup>-1</sup>; Table 5.1, entries 1 and 3). Previous study showed that an ethynyl group stabilizes the methyl radical by 12.1 kcal mol<sup>-1</sup>.<sup>[24]</sup> This is consistent with our calculations that the isodesmic reaction of butenyne with the vinyl radical is exothermic by 9.0 kcal mol<sup>-1</sup>. Therefore, much less distortion is required for the diyne to reach its conformation in the diradical transition state **TS3-s** (Figure 5.1). Besides the distortion-acceleration effect, the alkynyl substituent, as a weak electron-withdrawing group, enhances the interaction energy by 2.5 kcal mol<sup>-1</sup> (5.2 versus 7.7 kcal mol<sup>-1</sup>; Table 5.1, entries 1 and 3).

For the reaction between butadiyne and methyl pentadiynoate, the activation energy via diradical transition state **TS4-s** is 25.7 kcal mol<sup>-1</sup>, about 10 kcal mol<sup>-1</sup> lower than that required for the unactivated HDDA reaction (Table 5.1, entries 1 and 4). This dramatic reduction in the barrier results from both decrease of distortion energy and increase of interaction energy, accounting for the very mild conditions for the intramolecular HDDA reaction with both alkynyl and carbonyl activation (Scheme 5.1b).

Notably, calculations show that the distortion-acceleration effect by the alkynyl group does not exist in the concerted HDDA reactions (Table 5.1, entries 5-8). The reactivities are controlled by the interaction energy. As the electronegativity of the alkynyl group is much smaller than that of ester, the reactivity of butadiyne is much lower than that of propiolate (35.4 versus 32.4 kcal mol<sup>-1</sup>), and adding an alkynyl substituent slightly improves the reactivity of propiolate (31.6 versus 32.4 kcal mol<sup>-1</sup>). This is inconsistent with the experimental results (Scheme 5.1b), showing that the concerted mechanism does not operate in the activated diyne-yne [4+2] cycloadditions. For the DA reactions of cyclopentadiene with dienophiles, the alkynyl activation is not observed (Scheme

5.2b-c). This is in agreement with the computational results that there is no reduction in the distortion energy by alkynyl substituents in the concerted transition states (Table 5.1, entries 10-14). Therefore, the effects of the alkynyl substituent are closely related to the reaction pathway.

## 5.5 Conclusion

We have found that the HDDA reactions of the activated diynophiles occur through the stepwise diradical mechanism. This differs from the concerted mechanism favored by most conventional DA reactions. The alkynyl substituent accelerates the HDDA reaction by about 5 orders of magnitude mainly by decreasing the distortion energy required to achieve the diradical transition state. This is because the alkynyl group stabilizes the developing vinyl radical in the transition state. The distortion-acceleration effect of the alkynyl group does not exist in the concerted DA reactions.

## 5.6 References

- (1) (a) Goldstein, E.; Beno, B.; Houk, K. N. *J. Am. Chem. Soc.* **1996**, *118*, 6036; (b) Houk, K. N.; Gonzalez, J.; Li, Y. *Acc. Chem. Res.* **1995**, *28*, 81; (c) Houk, K. N.; Li, Y.; Evanseck, J. D. *Angew. Chem. Int. Ed.* **1992**, *31*, 682.
- (2) Nicolaou, K. C.; Snyder, S. A.; Montagnon, T.; Vassilikogiannakis, G. *Angew. Chem. Int. Ed.* **2002**, *41*, 1668.
- (3) (a) Hoye, T. R.; Baire, B.; Niu, D.; Willoughby, P. H.; Woods, B. P. *Nature* **2012**, *490*, 208; (b) Niu, D.; Willoughby, P. H.; Woods, B. P.; Baire, B.; Hoye, T. R. *Nature* **2013**, *501*, 531; (c)



Niu, D.; Hoye, T. R. *Nature Chem.* **2014**, *6*, 34; (d) Hoye, T. R.; Baire, B.; Wang, T. *Chem. Sci.* **2014**, *5*, 545; (e) Niu, D.; Wang, T.; Woods, B. P.; Hoye, T. R. *Org. Lett.* **2014**, *16*, 254.

(4) For reviews on the dehydro-Diels-Alder reaction, see: (a) Johnson, R. P. *J. Phys. Org. Chem.* **2010**, *23*, 283; (b) Wessig, P.; Müller, G. *Chem. Rev.* **2008**, *108*, 2051.

(5) (a) Zhang, X.; Maccarone, A. T.; Nimlos, M. R.; Kato, S.; Bierbaum, V. M.; Ellison, G. B.; Ruscic, B.; Simmonett, A. C.; Allen, W. D.; Schaefer III, H. F. *J. Chem. Phys.* **2007**, *126*, 044312; (b) Moskaleva, L. V.; Madden, L. K.; Lin, M. C. *Phys. Chem. Chem. Phys.* **1999**, *1*, 3967; (c) Deng, W.-Q.; Han, K.-L.; Zhan, J.-P.; He, G.-Z. *Chem. Phys. Lett.* **1998**, *288*, 33.

(6) Ajaz, A.; Bradley, A. Z.; Burrell, R. C.; Li, W. H. H.; Daoust, K. J.; Bovee, L. B.; DiRico, K. J.; Johnson, R. P. *J. Org. Chem.* **2011**, *76*, 9320.

(7) (a) Hoffmann, R. W.; Suzuki, K. *Angew. Chem. Int. Ed.* **2013**, *52*, 2655; (b) Baire, B.; Niu, D.; Willoughby, P. H.; Woods, B. P.; Hoye, T. R. *Nature Protoc.* **2013**, *8*, 501; (c) Yeoman, J. T. S.; Reisman, S. E. *Nature* **2012**, *490*, 179; (d) Wender, P. A.; Miller, B. L. *Nature* **2009**, *460*, 197; (e) Wender, P. A.; Verma, V. A.; Paxton, T. J.; Pillow, T. H. *Acc. Chem. Res.* **2008**, *41*, 40; (f) Trost, B. M. *Angew. Chem. Int. Ed.* **1995**, *34*, 259; (g) Trost, B. M. *Science* **1991**, *254*, 1471.

(8) For early examples of the HDDA reactions, see: (a) Bradley, A. Z.; Johnson, R. P. *J. Am. Chem. Soc.* **1997**, *119*, 9917; (b) Miyawaki, K.; Suzuki, R.; Kawano, T.; Ueda, I. *Tetrahedron Lett.* **1997**, *38*, 3943; (c) Miyawaki, K.; Kawano, T.; Ueda, I. *Tetrahedron Lett.* **1998**, *39*, 6923; (d) Kawano, T.; Inai, H.; Miyawaki, K.; Ueda, I. *Tetrahedron Lett.* **2005**, *46*, 1233; (e) Kimura, H.; Torikai, K.; Miyawaki, K.; Ueda, I. *Chem. Lett.* **2008**, *37*, 662; (f) Tsui, J. A.; Sterenberg, B. T. *Organometallics* **2009**, *28*, 4906.

- (9) (a) Yun, S. Y.; Wang, K. P.; Lee, N. K.; Mamidipalli, P.; Lee, D. *J. Am. Chem. Soc.* **2013**, *135*, 4668; (b) Karmakar, R.; Mamidipalli, P.; Yun, S. Y.; Lee, D. *Org. Lett.* **2013**, *15*, 1938; (c) Wang, K. P.; Yun, S. Y.; Mamidipalli, P.; Lee, D. *Chem. Sci.* **2013**, *4*, 3205; (d) R. Karmakar, S. Y. Yun, K. P. Wang, D. Lee, *Org. Lett.* **2014**, *16*, 6; (e) Lee, N.-K.; Yun, S. Y.; Mamidipalli, P.; Salzman, R. M.; Lee, D.; Zhou, T.; Xia, Y. *J. Am. Chem. Soc.* **2014**, *136*, DOI: 10.1021/ja500292x; (f) Mamidipalli, P.; Yun, S. Y.; Wang, K.-P.; Zhou, T.; Xia, Y.; Lee, D. *Chem. Sci.* **2014**, *5*, DOI: 10.1039/c3sc53478b.
- (10) Joshel, L. M.; Butz, L. W. *J. Am. Chem. Soc.* **1941**, *63*, 3350.
- (11) Diego-Castro, M. J.; Hailes, H. C. *Tetrahedron Lett.* **1998**, *39*, 2211.
- (12) Mamedov, E. G. *Russ. J. Appl. Chem.* **2004**, *77*, 1316.
- (13) Adam, W.; de Lucchi, O.; Pasquato, L.; Will, B. *Chem. Ber.* **1987**, *120*, 531.
- (14) Jones, E. R. H.; Thompson, J. M.; Whiting, M. C. *J. Chem. Soc.* **1957**, 2012.
- (15) Frisch, M. J. et al. *Gaussian 09*, Revision D.01, Gaussian, Inc., Wallingford CT, **2013**. Computational details and references are given in the Supporting Information.
- (16) (a) Zhao, Y.; Truhlar, D. G. *Theor. Chem. Acc.* **2008**, *120*, 215; (b) Zhao, Y.; Truhlar, D. G. *Acc. Chem. Res.* **2008**, *41*, 157.
- (17) (a) Pieniazek, S.; Houk, K. N. *Angew. Chem. Int. Ed.* **2006**, *45*, 1442; (b) Pieniazek, S.; Clemente, F. R.; Houk, K. N. *Angew. Chem. Int. Ed.* **2008**, *47*, 7746; (c) Paton, R. S.; Mackey, J. L.; Kim, W. H.; Lee, J. H.; Danishefsky, S. J.; Houk, K. N. *J. Am. Chem. Soc.* **2010**, *132*, 9335;

(d) Lan, Y.; Zou, L.; Cao, Y.; Houk, K. N. *J. Phys. Chem. A* **2011**, *115*, 13906; (e) Paton, R. S.; Kim, S.; Ross, A. G.; Danishefsky, S. J.; Houk, K. N. *Angew. Chem. Int. Ed.* **2011**, *50*, 10366.

(18) The *exo* cycloaddition between cyclopentadiene and methyl acrylate via **TS7-c-x** is 0.5 kcal mol<sup>-1</sup> less favorable than the *endo* one via **TS7-c**, while the *exo* cycloaddition between cyclopentadiene and butenyne via **TS8-c** is 0.5 kcal mol<sup>-1</sup> more favorable than the *endo* one via **TS8-c-n**. For a related study, see: Min, S.-J.; Jones, G. O.; Houk, K. N.; Danishefsky, S. J. *J. Am. Chem. Soc.* **2007**, *129*, 10078.

(19) (a) Ess, D. H.; Houk, K. N. *J. Am. Chem. Soc.* **2007**, *129*, 10646; (b) Legault, C. Y.; Garcia, Y.; Merlic, C. A.; Houk, K. N. *J. Am. Chem. Soc.* **2007**, *129*, 12664; (c) Ess, D. H.; Houk, K. N. *J. Am. Chem. Soc.* **2008**, *130*, 10187.

(20) For a review, see: van Zeist, W.-J.; Bickelhaupt, F. M. *Org. Biomol. Chem.* **2010**, *8*, 3118.

(21) For recent examples, see: (a) Fernández, I.; Bickelhaupt, F. M. *J. Comput. Chem.* **2012**, *33*, 509; (b) Gordon, C. G.; Mackey, J. L.; Jewett, J. C.; Sletten, E. M.; Houk, K. N.; Bertozzi, C. R. *J. Am. Chem. Soc.* **2012**, *134*, 9199; (c) Liang, Y.; Mackey, J. L.; Lopez, S. A.; Liu, F.; Houk, K. N. *J. Am. Chem. Soc.* **2012**, *134*, 17904; (d) Fernández, I.; Bickelhaupt, F. M.; Cossío, F. P. *Chem. Eur. J.* **2012**, *18*, 12395; (e) Lopez, S. A.; Munk, M. E.; Houk, K. N. *J. Org. Chem.* **2013**, *78*, 1576; (f) Lopez, S. A.; Houk, K. N. *J. Org. Chem.* **2013**, *78*, 1778; (g) Zou, L.; Paton, R. S.; Eschenmoser, A.; Newhouse, T. R.; Baran, P. S.; Houk, K. N. *J. Org. Chem.* **2013**, *78*, 4037; (h) Fernández, I.; Sola, M.; Bickelhaupt, F. M. *Chem. Eur. J.* **2013**, *19*, 7416; (i) Kamber, D. N.; Nazarova, L. A.; Liang, Y.; Lopez, S. A.; Patterson, D. M.; Shih, H.-W.; Houk, K. N.; Prescher, J. A. *J. Am. Chem. Soc.* **2013**, *135*, 13680; (j) Liu, F.; Paton, R. S.; Kim, S.; Liang, Y.; Houk, K. N. *J. Am. Chem. Soc.* **2013**, *135*, 15642; (k) Usharani, D.; Lacy, D. C.; Borovik, A. S.; Shaik, S. *J. Am. Chem. Soc.* **2013**,

135, 17090; (l) Fernández, I.; Bickelhaupt, F. M. *J. Comput. Chem.* **2014**, *35*, 371; (m) Hong, X.; Liang, Y.; Griffith, A. K.; Lambert, T. H.; Houk, K. N. *Chem. Sci.* **2014**, *5*, 471; (n) Yang, Y.-F.; Cheng, G.-J.; Liu, P.; Leow, D.; Sun, T.-Y.; Chen, P.; Zhang, X.; Yu, J.-Q.; Wu, Y.-D.; Houk, K. N. *J. Am. Chem. Soc.* **2014**, *136*, 344; (o) Hong, X.; Liang, Y.; Houk, K. N. *J. Am. Chem. Soc.* **2014**, *136*, 2017; (p) Yang, J.; Liang, Y.; Šečkutè, J.; Houk, K. N.; Devaraj, N. K. *Chem. Eur. J.* **2014**, *20*, 3365.

(22) For other DA reactions, UM06-2X has been found to slightly overestimate the energies of the diradical transition states, see: James, N. C.; Um, J. M.; Padias, A. B.; Hall, Jr., H. K.; Houk, K. N. *J. Org. Chem.* **2013**, *78*, 6582.

(23) Jarowski, P. D.; Wodrich, M. D.; Wannere, C. S.; Schleyer, P. v. R.; Houk, K. N. *J. Am. Chem. Soc.* **2004**, *126*, 15036.

(24) Zipse, H. *Top. Curr. Chem.* **2006**, *263*, 163.

## Chapter 6. The Mechanism and Selectivity of N-triflylphosphoramidate Catalyzed (3<sup>+</sup>+2)

### Cycloaddition between Hydrazones and Alkenes

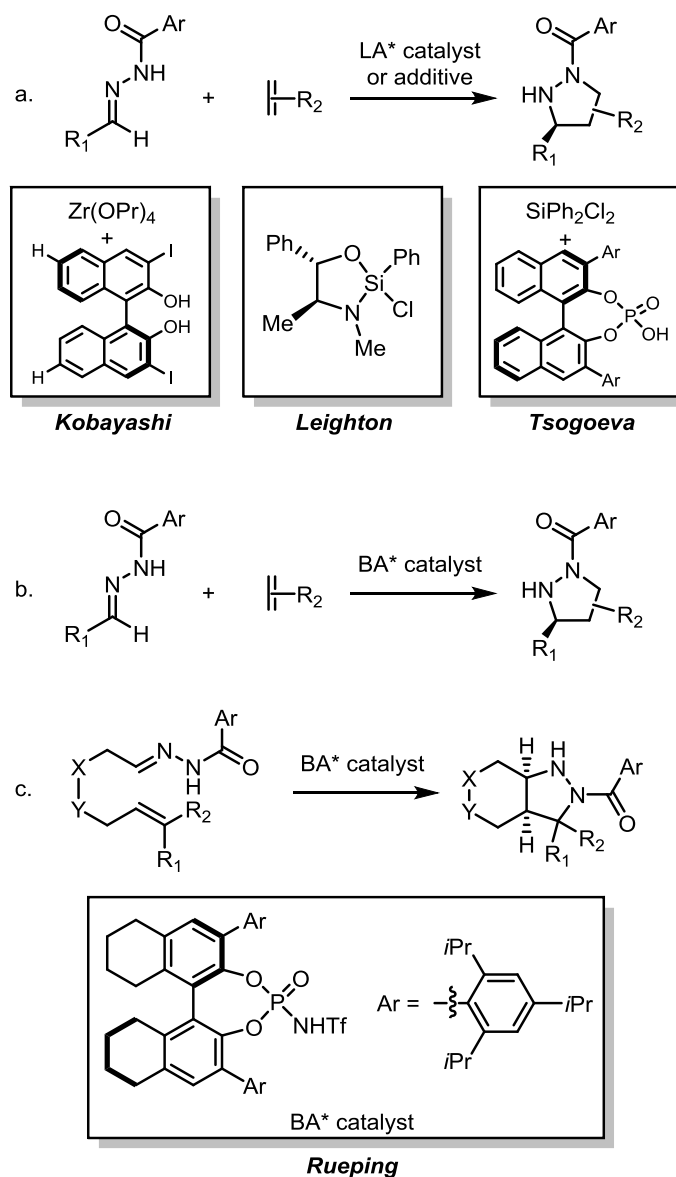
#### 6.1 Abstract

Brønsted acid catalyzed (3+2) cycloadditions between hydrazones and alkenes provide a general approach to pyrazolidines. The acidity of Brønsted acid is crucial for the catalytic efficiency: the less acidic phosphoric acids are ineffective, while the highly acidic N-triflylphosphoramidates are very efficient and can promote highly enantioselective cycloadditions. The mechanism and origins of catalytic efficiencies and selectivities have been explored with density functional theory (DFT) calculations. Protonation of hydrazones by N-triflylphosphoramidate produces hydrazone-phosphoramidate anion complexes. These ion-pair complexes are very reactive in (3<sup>+</sup>+2) cycloadditions with alkenes, producing pyrazolidine products. The alternative 1,3-dipolar (3+2) cycloaddition pathway with azomethine imine is much less favorable due to the endergonic isomerization from hydrazone to azomethine imine. Only a small distortion of the ion-pair complex is required to achieve its geometry in the (3<sup>+</sup>+2) cycloaddition transition state. In contrast, the weak phosphoric acid is not able to protonate the hydrazone, and only a hydrogen-bonded complex is formed. A larger distortion energy is required for the hydrogen-bonded complex to achieve the “ion-pair” geometry in the cycloaddition transition state, and a significant barrier is found. Based on the mechanism, we have also explained the origins of enantioselectivities when a chiral N-triflylphosphoramidate catalyst is employed.

#### 6.2 Introduction

Pyrazolidines are very important and valuable compounds for their widespread natural occurrence, impressive biological properties,<sup>1</sup> and application in material science<sup>2</sup>. The 1, 3-dipolar cycloaddition between hydrazones and alkenes provides an atom- and step-economic access to pyrazolidines,<sup>3</sup> and extensive efforts have been devoted to the development of enantioselective catalysts for this transformation.<sup>4,5</sup> For example, Kobayashi discovered the chiral zirconium/binol complexes as efficient enantioselective Lewis acid catalysts for both inter- and intramolecular (3+2) cycloaddition between hydrazones and alkenes (Scheme 6.1a).<sup>4a,4c</sup> In addition, Leighton and Tsogoeva individually reported that chiral silanes could serve as an alternative enantioselective Lewis acid for similar reactions (Scheme 6.1a).<sup>4d,5c</sup> Rueping and co-workers recently discovered a general and highly enantioselective N-triflylphosphoramidate catalyst for the intermolecular (3+2) cycloaddition between various hydrazones and alkenes, affording the pyrazolidine derivatives with the Brønsted acid catalyzed approach (Scheme 6.1b).<sup>6</sup>

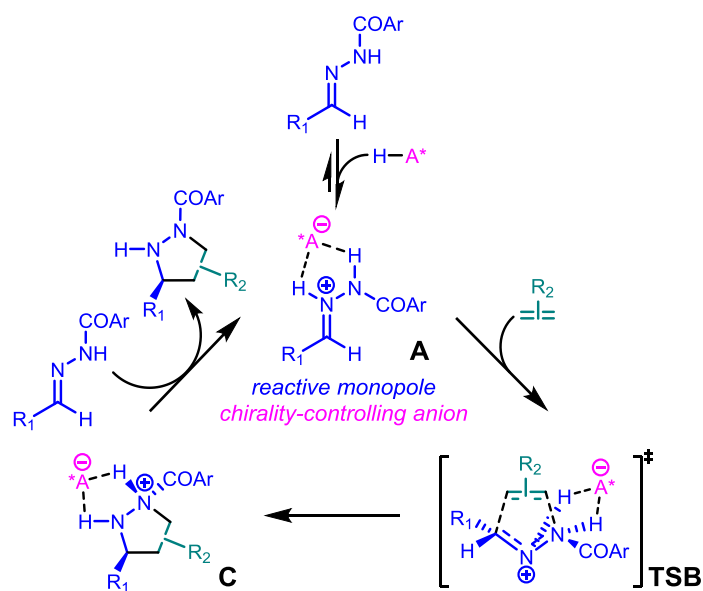
The acidity of Brønsted acid catalysts is crucial for cycloadditions between hydrazones and alkenes. Less acidic phosphoric acids ( $pK_a = 13-14$  in acetonitrile) give low yields of product irrespective of the reaction conditions, while the more acidic N-triflylphosphoramidate<sup>7</sup> ( $pK_a = 6-7$  in acetonitrile) are much more reactive catalysts with good to excellent enantioselectivities.<sup>6,8</sup> In addition, Rueping and co-workers find that the same catalyst is also effective for the enantioselective intramolecular cycloadditions. The cycloadditions occur smoothly between various N-benzoylhydrazones and alkenes with broad substrate scope and good to excellent enantioselectivities (Scheme 6.1c).



**Scheme 6.1.** Lewis acid and Brønsted acid facilitated enantioselective (3+2) cycloadditions between hydrazones and alkenes (LA: Lewis acid; BA: Brønsted acid).

Because of the necessity of highly acidic Brønsted acid catalysts, we surmise that phosphoramides may not play a role like the classical Lewis acid catalysts in activating the 1, 3-dipole.<sup>4e,9</sup> Instead, the Brønsted acid catalyst could protonate hydrazone and form an ion-pair complex **A** (Scheme 6.2). The ion pair complex **A** has a reactive monopolar hydrazone and a

chirality-controlling phosphoramidate anion. This makes the subsequent ( $3^++2$ ) cycloaddition mild and selective via **TSB**, generating the pyrazolidine-phosphoramidate complex **C**. Subsequently, complex **C** releases the pyrazolidine product, regenerating the complex **A** with another molecule of hydrazone. Although the monopolar ( $3^++2$ ) cycloadditions with hydrazone cations have been documented since the 70s, the synthetic applications and especially the catalytic reactions are rare.<sup>10</sup> Does the N-triflylphosphoramidate really protonate the hydrazones and catalyze the ( $3^++2$ ) cycloadditions with alkenes? How does the chiral phosphoramidate control the regio- and enantioselectivity? In order to answer the above questions and provide the mechanistic basis for designing future Brønsted acid catalyzed ( $3^++2$ ) cycloadditions with hydrazones, we have carried out density functional theory (DFT) calculations to explore the mechanism and selectivity of the N-triflylphosphoramidate catalyzed ( $3+2$ ) cycloadditions between hydrazones and alkenes.



**Scheme 6.2.** Proposed monopolar ( $3^++2$ ) pathway of Brønsted acid catalyzed cycloaddition between hydrazones and alkenes.



### 6.3 Computational Details

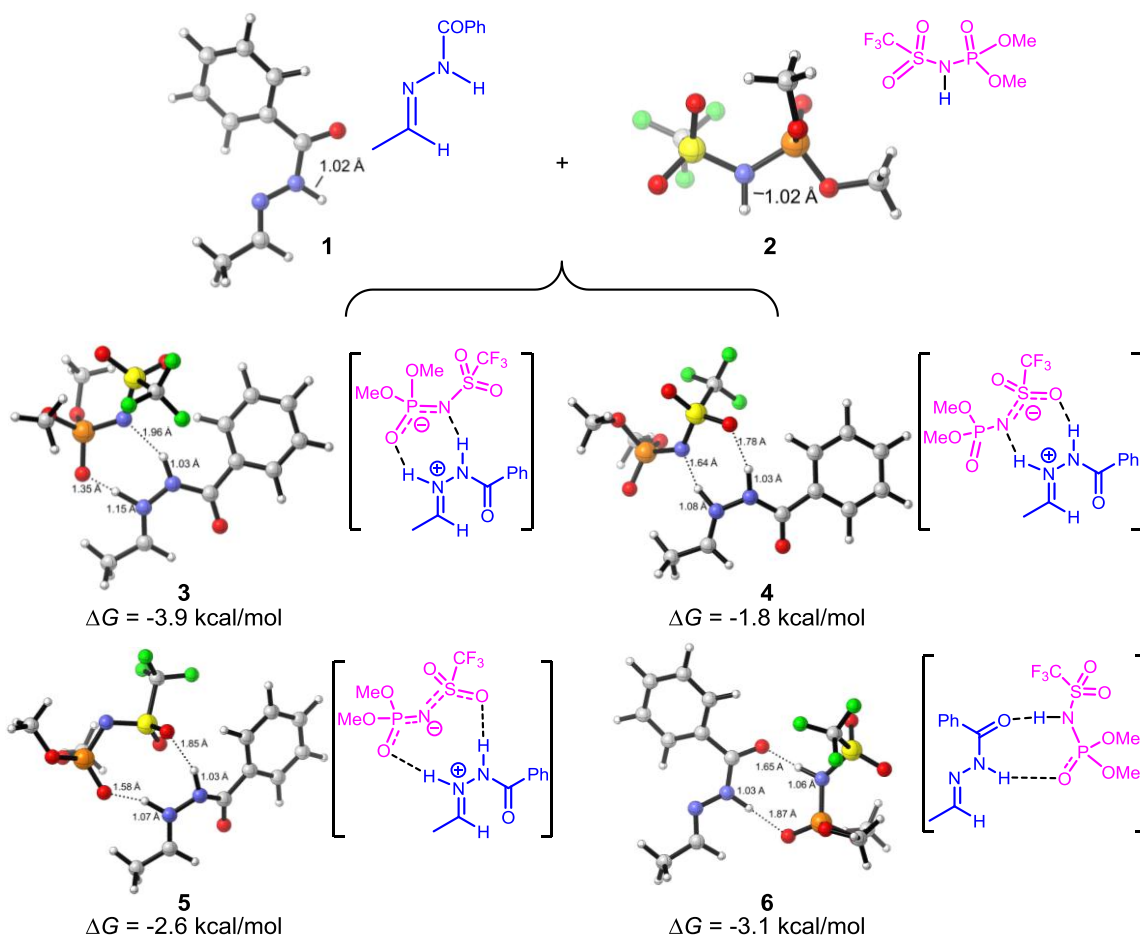
All density functional theory (DFT) calculations were performed with Gaussian 09. Geometry optimization of all the minima and transition states involved was carried out at the M062X level of theory with the 6-31G(d) basis set. The vibrational frequencies were computed at the same level to check whether each optimized structure is an energy minimum or a transition state and to evaluate its zero-point vibrational energy (ZPVE) and thermal corrections at 298 K. The single-point energies and solvent effects in chloroform were computed at the M062X level of theory with the 6-311+G(d,p) basis set, based on the gas-phase optimized structures. Solvation energies were evaluated by a self-consistent reaction field (SCRF) using the CPCM model (UFF Radii). Fragment distortion and interaction energies and bond dissociation energies were computed at the M062X/6-311+G(d,p) level using the B3LYP/6-31G(d) geometries in the gas phase. Extensive conformational searches for the hydrazone, phosphoramidate, and hydrazone-phosphoramidate/phosphate complexes have been conducted, and only the most stable conformers and isomers are discussed.

### 6.4 Results and Discussion

#### 6.4.1 Complexation between Hydrazone and Phosphoramidate

We first studied various complexes between the model hydrazone **1** and the achiral model phosphoramidate **2**. The optimized structures and Gibbs free energies of these complexes are shown in Figure 6.1. The complexation between hydrazone and phosphoramidate can occur with or without proton transfer. When proton transfer occurs, there are three possible hydrogen-bonding complexes, and these complexes (**3**, **4** and **5**) are shown in Figure 6.1. The N-H distances of

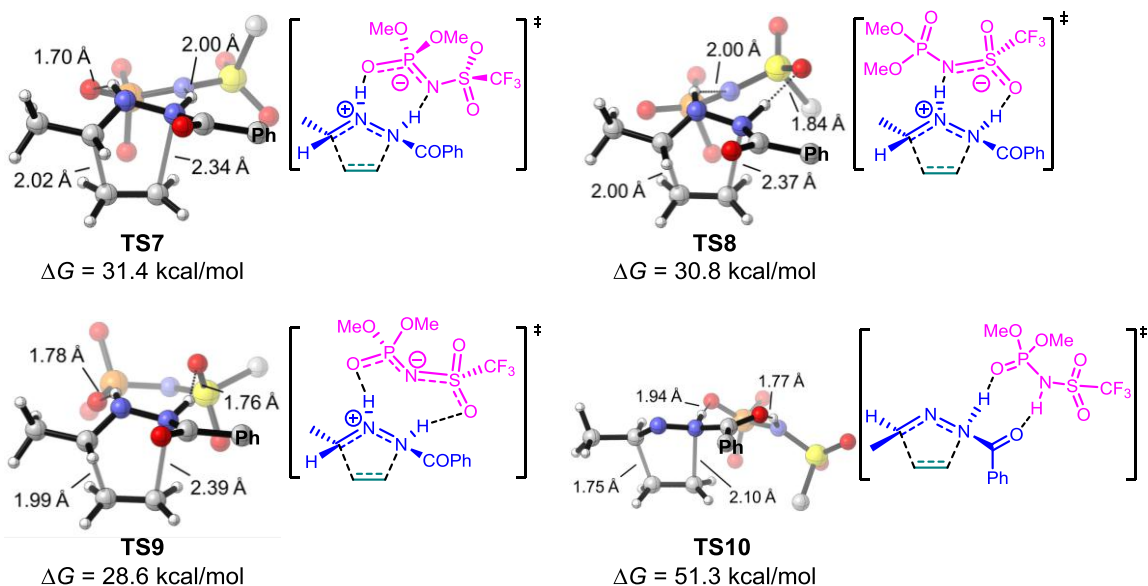
hydrazonium in the ion-pair complexes are generally smaller than 1.1 Å, and the distances between phosphoramidate anion and hydrogens from hydrazonium are at least 1.6 Å. The proton transfer complexes support the hypothesis that the Brønsted acid facilitates the (3<sup>+</sup>+2) cycloaddition by generating the hydrazonium cation. Alternatively, only hydrogen-bonding complexation occur in complex **6**.<sup>11</sup> The N-H distances are similar to those of the separate hydrazone and phosphoramidate. Although the ion-pair and hydrogen-bonded complexes are quite different, the complexation are all exergonic, and the four complexes have similar stabilities.



**Figure 6.1.** Optimized structures and Gibbs free energies of complexes between hydrazone **1** and phosphoramidate **2**.

The (3+2) cycloaddition between the hydrazone-phosphoramidate complexes and ethylene was explored, and the optimized structures and Gibbs free energies of transition states (compared to the most stable complex **3**) are shown in Figure 6.2. **TS7**, **TS8** and **TS9** are the transition states

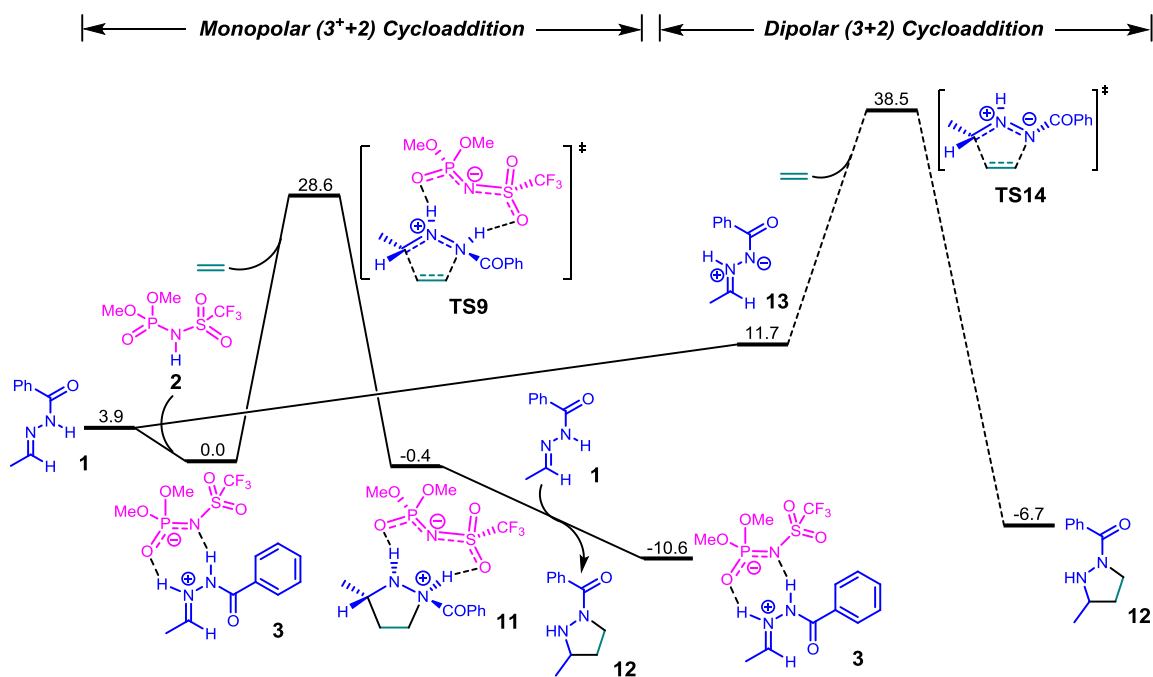
with the ion-pair complexes (**3**, **4** and **5**), and **TS10** is the transition state with the hydrogen-bonded complex **6**. The ion-pair complexes are much more reactive than the hydrogen-bonded complex in the (3+2) cycloaddition with ethylene. The reaction barriers of the ion-pair complexes (**TS7**, **TS8** and **TS9**) are around 30 kcal/mol, while the hydrogen-bonded complex has a significant higher barrier via **TS10** (51.3 kcal/mol).<sup>12</sup> Only the ion-pair complexes are reactive in the (3+2) cycloaddition with alkenes, and the ion-pair complexes have similar reactivities to the hydrazonium cation we investigated earlier.<sup>13</sup> The N-triflylphosphoramidate catalyzed cycloaddition between hydrazones and alkenes is, indeed, a (3<sup>+</sup>+2) cycloaddition. Among the transition states with the ion-pair complexes, **TS9** is the most favorable one with 28.6 kcal/mol barrier, while **TS7** and **TS8** are at least 2 kcal/mol higher in terms of Gibbs free energy. This suggests that the phosphoramidate anion uses the two terminal oxygens (one from phosphine, the other from sulfur) to bind the hydrazonium cation in the (3<sup>+</sup>+2) cycloaddition transition state.



**Figure 6.2.** Optimized structures and Gibbs free energies of (3+2) cycloaddition transition states between the hydrazone-phosphoramidate complexes and ethylenes (the free energies changes are compared to the most stable complex **3**; the phenyl group from hydrazone, and the methyl groups and fluorines from phosphoramidate are hidden for simplicity).

We also studied the whole catalytic cycle of the (3<sup>+</sup>+2) cycloaddition and the competing 1, 3-dipolar (3+2) cycloaddition pathway with the model hydrazone **1** and phosphoramidate **2**. From hydrazone **1**, the complexation with phosphoramidate **2** is exergonic by 3.9 kcal/mol, giving the ion-pair complex **3**. Subsequent (3<sup>+</sup>+2) cycloaddition with ethylene requires a barrier of 28.6 kcal/mol via **TS9**, giving the pyrazolidine-phosphoramidate complex **11**. The pyrazolidine product **12** is less basic than the hydrazone **1**, so the product extrusion from complex **11** to regenerate the ion-pair complex **3** is exergonic, making the overall reaction exergonic by 10.6 kcal/mol. The ion-pair complex **3** is the resting state of the whole catalytic cycle, and the overall barrier is 28.6 kcal/mol

via transition state **TS9**.<sup>14</sup> Alternatively, the hydrazone can isomerize to the less stable azomethine imine **13** and undergo the 1, 3-dipolar (3+2) cycloaddition with ethylene. Although the azomethine imine is a reactive dipole and the cycloaddition barrier with ethylene is only 26.8 kcal/mol, the overall barrier of the 1, 3-dipolar cycloaddition pathway is 38.5 kcal/mol because of endergonic isomerization. Therefore, the phosphoramidate catalyzed (3<sup>+</sup>+2) cycloaddition pathway is much more favorable than the 1, 3-dipolar cycloaddition pathway.



**Figure 6.3.** Free energy changes of the phosphoramidate **2** catalyzed monopolar (3<sup>+</sup>+2) cycloaddition pathway and the 1, 3-dipolar cycloaddition pathway between hydrazone **1** and ethylene.

#### 6.4.2 Catalytic Activities of Phosphoramidate and Phosphoric Acid

Recent experiments have shown that the N-triflylphosphoramidate is a much more effective catalyst than phosphoric acid for the cycloaddition between hydrazones and alkenes. We have used DFT calculations to explain the different catalytic activities of the two Brønsted acids, and the results are shown in Figure 4. As described above, the N-triflylphosphoramidate catalyzed (3+2) cycloaddition between hydrazone **1** and ethylene requires a 28.6 kcal/mol barrier via **TS9**. In contrast, the same reaction catalyzed by the less acidic phosphoric acid, modeled by the dimethyl phosphate **15**, is much more difficult. From the hydrazone **1**, the complexation with phosphate is exergonic by 4.4 kcal/mol, generating the hydrazone-phosphate complex **16**. The subsequent (3+2) cycloaddition with ethylene via **TS17** requires a barrier of 36.8 kcal/mol, which is substantially higher than the barrier of N-triflylphosphoramidate catalyzed pathway.

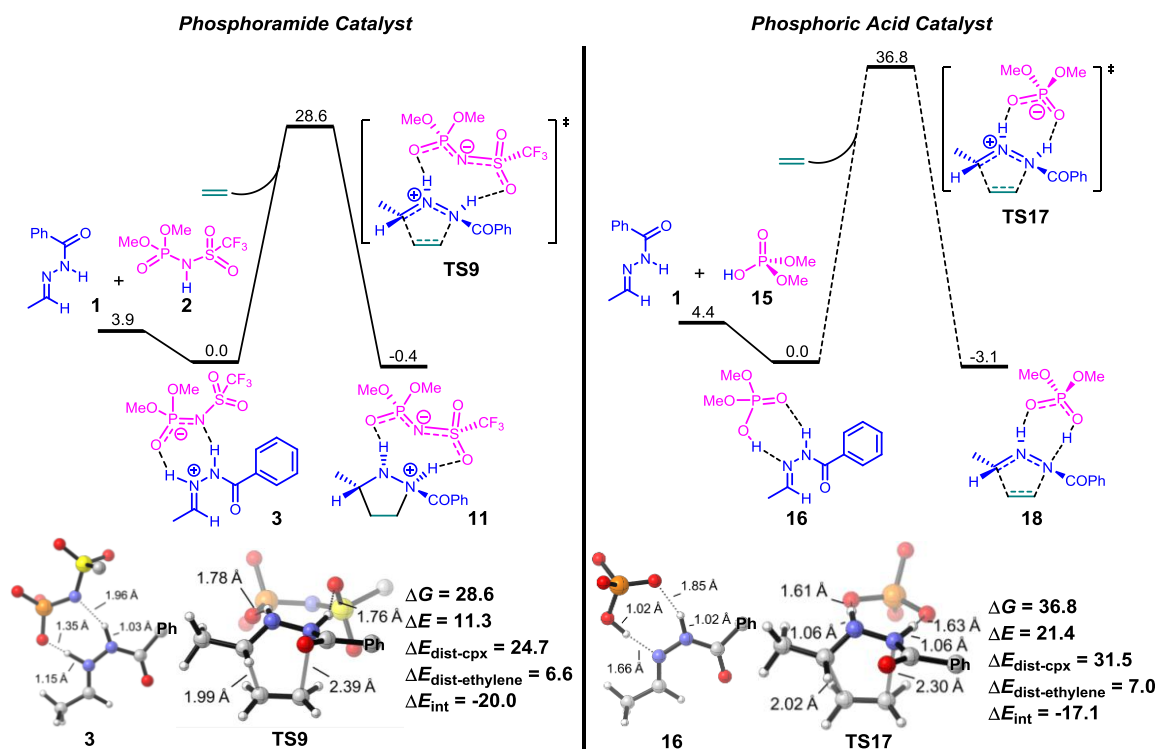
In order to understand the different catalytic efficiencies of phosphoric acid and N-triflylphosphoramidate, we applied the distortion/interaction model on the cycloaddition transition states (**TS9** and **TS17**). Both transition states are separated into two fragments (the distorted complex and ethylene), followed by single point energy calculations on each distorted fragment. The energy differences between the distorted structures and optimized ground state structures are the distortion energy of the ion pair complex ( $\Delta E_{\text{dist-cpx}}$ ) and ethylene ( $\Delta E_{\text{dist-ethylene}}$ ), respectively. The interaction energy ( $\Delta E_{\text{int}}$ ) is the difference between the activation energy and the total distortion energy ( $\Delta E_{\text{dist-cpx}} + \Delta E_{\text{dist-ethylene}}$ ).

We find that the distortion of complex ( $\Delta E_{\text{dist-cpx}}$ ) is the determining factor for the barrier differences. Both transition states have similar  $\Delta E_{\text{dist-ethylene}}$  and  $\Delta E_{\text{int}}$ , while the  $\Delta E_{\text{dist-cpx}}$  of phosphoric acid (31.5 kcal/mol) is 6.8 kcal/mol higher than that of phosphoramidate (24.7 kcal/mol). The difference of  $\Delta E_{\text{dist-cpx}}$  is the major contribution to the 10.1 kcal/mol difference of the electronic barriers (11.3 kcal/mol of **TS9** and 21.4 kcal/mol of **TS17**). The high  $\Delta E_{\text{dist-cpx}}$  with dimethylphosphate means that the ground state structure of phosphoric acid complex is very different to its structure in the transition state (**TS17**), and a large energy penalty is required for that structural change. The large structural difference arises from the low acidity of phosphoric acid. In the hydrazone-dimethylphosphate complex **16**, the hydrazone is not protonated, and the O-H bond of dimethylphosphate is 1.02 Å. Thus the complex **16** is a hydrogen-bonded complex, instead of an ion-pair complex. While in **TS17**, in order to undergo the facile ( $3^++2$ ) cycloaddition, the complex is distorted to a “ion pair” structure and the same O-H bond of dimethylphosphate is stretched to 1.61 Å (Figure 6.4). Therefore, significant distortion is required for the hydrazone-phosphoric acid complex to achieve its structure in the ( $3^++2$ ) cycloaddition transition state with alkenes.

Different from the phosphoric acid, N-triflylphosphoramidate is acidic enough to protonate the hydrazone. Spontaneously, it requires much less energy to distort the ion-pair complex **3** to the similar geometry in the transition state **TS9**, and a smaller barrier is found. In addition, to directly compare the acidity of the model phosphoric acid and N-triflylphosphoramidate, we also calculated the free energy change of proton transfer from the N-triflylphosphoramidate **2** to dimethylphosphate anion. The reaction is exergonic by 11.7 kcal/mol, which is consistent with the difference of  $\Delta E_{\text{dist-}}$



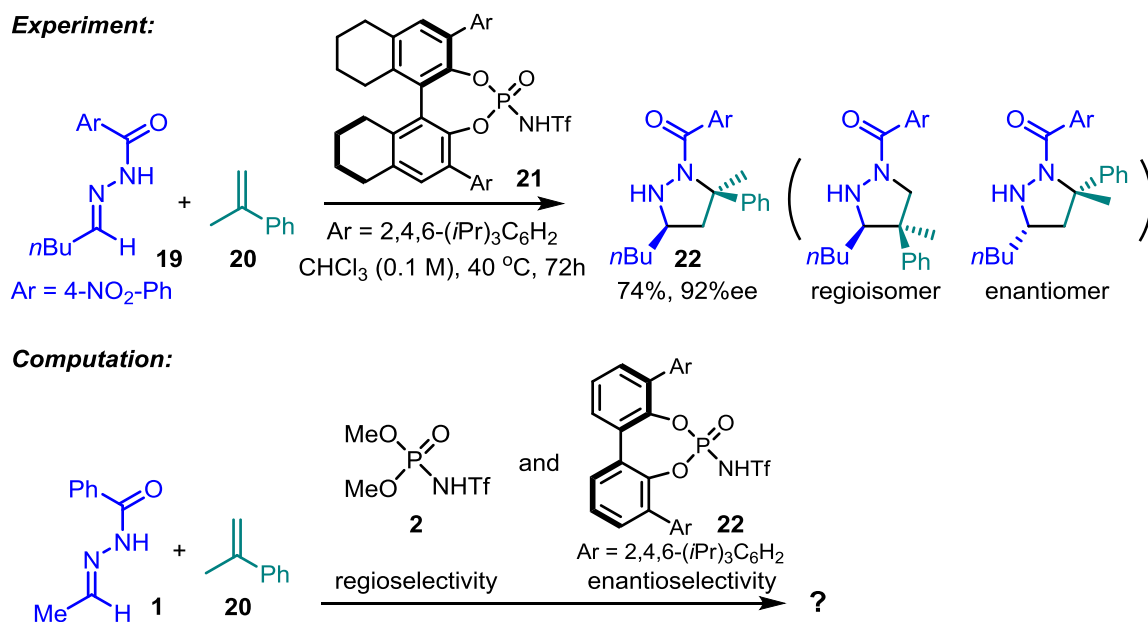
cpx as well as the experimental  $pK_a$  difference of similar compounds measured by Rueping and coworkers.<sup>8</sup>



**Figure 6.4.** Free energy changes and distortion/interaction analysis of transition states of phosphoramidate (2) and phosphoric acid (dimethylphosphate) catalyzed (3+2) cycloadditions between hydrazone 1 and ethylene (the phenyl group from hydrazone, the methyl groups and fluorines from phosphoramidate, and the methyl groups from phosphate are hidden for simplicity).

### 6.4.3 Origins of Regioselectivity

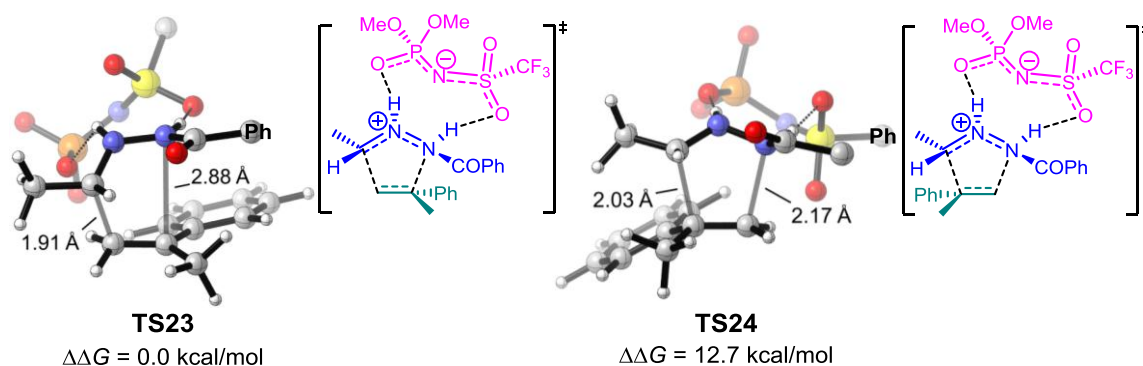
The chiral N-triflylphosphoramidate **21** gives high regio- and enantioselectivity in experiment. We employed the achiral phosphoramidate **2** and chiral phosphoramidate **22** to explore the regio- and enantioselectivity computationally (Scheme 6.3).



**Scheme 6.3.** Experimental results and computational models of selectivities of chiral phosphoramidate **21** catalyzed cycloaddition between hydrazone **19** and  $\alpha$ -methylstyrene **20**.

With the model phosphoramidate **2**, we have studied the regioselectivity of cycloaddition between hydrazone **1** and  $\alpha$ -methylstyrene **20** (Figure 6.5). **TS23** has the phenyl group of  $\alpha$ -methylstyrene proximal to the forming C-N bond, generating the product that has been found in experiment. Computationally, we also find that **TS23** is 12.7 kcal/mol more stable than **TS24**. The

regioselectivity mainly arises from the different orbital interactions between the hydrazone and alkene in the transition states. The hydrazone is electrophilic and styrene is nucleophilic, thus stronger interaction can be generated when the more electrophilic terminus (carbon) of hydrazone is proximal to the more nucleophilic terminus (terminal carbon) of styrene. The preference can also be rationalized by FMO theory, the major HOMO-LUMO interaction is from the HOMO of styrene to the LUMO of hydrazone, and **TS23** allows the most favorable interaction.



**Figure 6.5.** Transition states and relative Gibbs free energies of phosphoramidate **2** catalyzed cycloaddition between hydrazone **1** and  $\alpha$ -methylstyrene **20**.

#### 6.4.4 Origins of Enantioselectivity

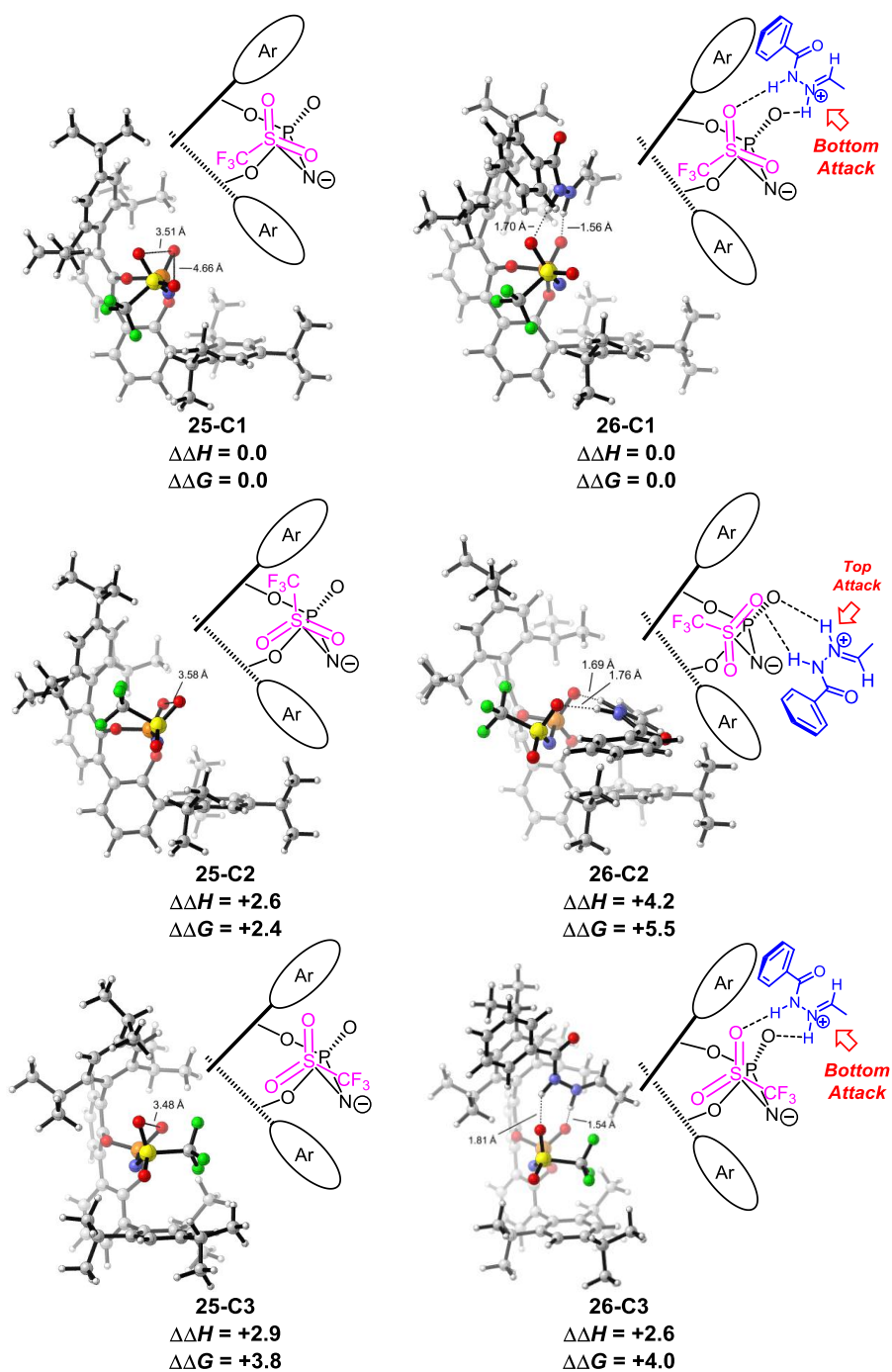
We also studied the enantioselectivity of (3+2) cycloaddition between hydrazone **1** and  $\alpha$ -methylstyrene **20** with the model chiral N-triflylphosphoramidate **22** (Scheme 6.3). Anion **25** has three major conformations by rotating the substituents of sulfur (Figure 6.6). The **25-C1** has the  $\text{CF}_3$  group

pointing away from the two bulky 2, 4, 6-*i*Pr)<sub>3</sub>C<sub>6</sub>H<sub>2</sub> substituents, and this conformer is the most stable. The other two conformers (**25-C2** and **25-C3**) have the CF<sub>3</sub> group closer to the bulky aryl substituents, and are higher in energy.

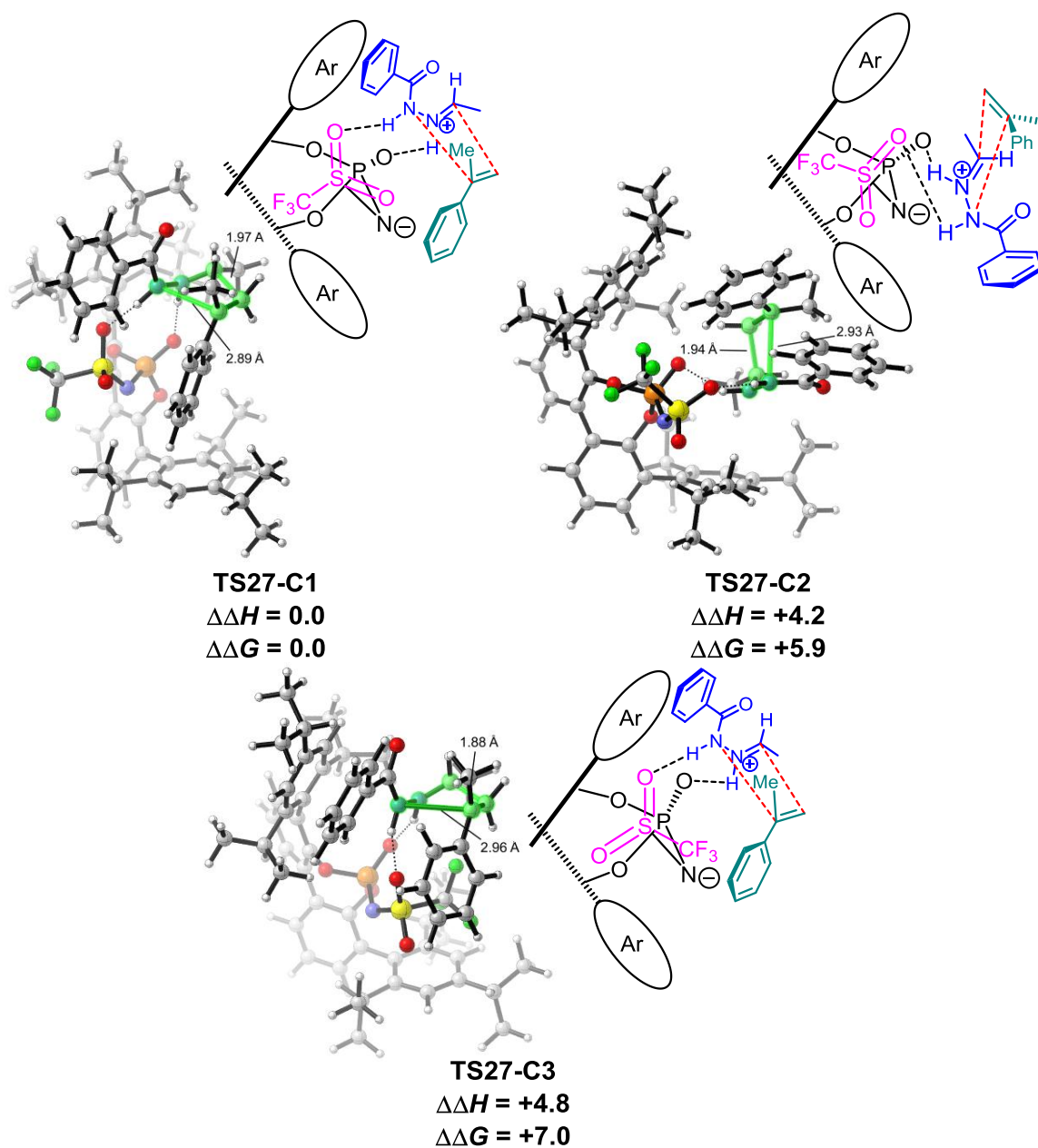
As discussed above, we showed that the phosphoramidate anion uses the two terminal oxygens to bind the hydrazone in the (3+2) cycloaddition transition state with alkenes. Using the same binding mode, we studied the ion-pair complexes with the three conformers of **25** (Figure 6.6). From **25-C1**, only one pair of oxygens (with the distance of 3.51 Å) are possible to form a stable complex with hydrazone because of the distance between the oxygens, and the formed complex is **26-C1**. Similarly, **26-C2** and **26-C3** are found with the corresponding conformers of **25**. Interestingly, all the three conformers of ion-pair complex (**26-C1** to **26-C3**) have only one face available for alkenes to approach. **26-C1** has the top of hydrazone protected by the bulky aryl substituent, and alkene can only approach from the bottom. **26-C3** also has the bottom face available, thus **26-C1** and **26-C3** give the same cycloaddition product. Alternatively, **26-C2** has the bottom of the hydrazone hindered, and this conformer leads to the minor enantiomer in experiment. Because the binding between hydrazone and phosphoramidate anion is very similar in the three conformers, **26-C1** is the most stable.

The (3+2) cycloaddition transition states between the three conformers of ion-pair complex and  $\alpha$ -methylstyrene were located, and the computational selectivity is consistent with the experimental results (Figure 6.7). We find **TS27-C1** is more favorable than **TS27-C2**, and the preference is similar to the relative stabilities of the corresponding conformers of ion-pair complex (**26**) and

phosphoramidate anion (**25**). Therefore, the two bulky aryl substituents of the chiral N-triflylphosphoramidate differentiate the stabilities of the anion conformers, and the ion-pair complexation with hydrazone transfers the chirality of catalyst to the cycloaddition transition state, generating the enantioselectivity.



**Figure 6.6.** Optimized structures and relative stabilities of chiral N-triflylphosphoramidate **22** anion and anion-hydrazone complex.



**Figure 6.7.** Optimized structures and relative stabilities of chiral N-triflylphosphoramidate **22** catalyzed (3+2) cycloaddition transition states between hydrazone and  $\alpha$ -methylstyrene.

## 6.5 Conclusions

The mechanism and origins of catalytic efficiencies and selectivities of chiral N-triflylphosphoramidate catalyzed (3+2) cycloaddition between hydrazones and alkenes have been studied through DFT calculations. The acidic N-triflylphosphoramidate protonates the hydrazone, and a hydrazonium-phosphoramidate anion complex is formed. The ion-pair complex is very reactive in the subsequent (3<sup>+</sup>+2) cycloaddition with alkenes, generating the pyrazolidine product. The alternative 1, 3-dipolar (3+2) cycloaddition pathway with azomethine imine is less favorable because of the endergonic isomerization from hydrazone to azomethine imine. The Brønsted acid catalyzed (3+2) cycloaddition with hydrazone is essentially a (3<sup>+</sup>+2) cycloaddition with hydrazonium, thus the protonation of hydrazone by the Brønsted acid is crucial for the catalytic efficiency. The less acidic phosphoric acid is not able to protonate the hydrazone, and a hydrogen-bonded complex is formed. This leads to a large distortion for the hydrogen-bonded complex to achieve the “ion-pair” geometry in the (3+2) cycloaddition transition state, resulting in a significant reaction barrier. In addition, we have explained the origins of enantioselectivities when the chiral bulky N-triflylphosphoramidate is employed. The steric-demanding substituents of phosphoramidate catalyst is able to differentiate the stabilities of the conformers of hydrazone-chiral phosphoramidate complex. The most favorable conformer only has one face of the hydrazonium available for the alkene to approach, which transfers the chirality of the catalyst to the (3<sup>+</sup>+2) cycloaddition transition state, generating the enantioselectivity.



## 6.6 References

(1) (a) Gürsپی, A.; Demirayak, S.; Capan, G.; Erol, K.; Vural, K. *Eur. J. Med. Chem.* **2000**, *35*, 359. (b) Brzozowski, Z.; Saczewski, F.; Gdaniec, M. *Eur. J. Med. Chem.* **2000**, *35*, 1053. (c) Jeong, T.-S.; Kim, K. S.; An, S.-J.; Cho, K.-H.; Lee, S.; Lee, W. S. *Bioorg. Med. Chem. Lett.* **2004**, *14*, 2715. (d) Camacho, M. E.; Leon, J.; Entrena, A.; Velasco, G.; Carrion, M. D.; Escames, G.; Vivo, A.; Acuna-Castroviejo, D.; Gallo, M. A.; Espinosa, A. *J. Med. Chem.* **2004**, *47*, 5641. (e) Prasad, Y. J.; Rao, A. L.; Prasoon, L.; Murali, K.; Kumar, P. R. *Bioorg. Med. Chem. Lett.* **2005**, *15*, 5030. (f) Goodell, J. R.; Puig-Basagoiti, F.; Forshey, B. M.; Shi, P.-Y.; Ferguson, D. M. *J. Med. Chem.* **2006**, *49*, 2127. (g) Özdemir, Z.; Kandilci, H. B.; Gumusel, B.; Calis, U.; Bilgin, A. A. *Eur. J. Med. Chem.* **2007**, *42*, 373. (h) Özdemir, A.; Turan-Zitouni, G.; Kaplancikli, Z. A.; Revial, G.; Guven, K. *Eur. J. Med. Chem.* **2007**, *42*, 403. (i) Zhang, X.; Li, X.; Allan, G. F.; Sbriscia, T.; Linton, O.; Lundeen, S. G.; Sui, Z. *J. Med. Chem.* **2007**, *50*, 3857.

(2) (a) Gao, X. C.; Cao, H.; Zhang, L. Q.; Zhang, B.W.; Cao, Y.; Huang, C. H. *J. Mater. Chem.* **1999**, *9*, 1077. (b) Fu, H. B.; Yao, J. N. *J. Am. Chem. Soc.* **2001**, *123*, 1434. (c) Oh, S. W.; Zhang, D. R.; Kang, Y. S. *Mater. Sci. Eng. C* **2004**, *24*, 131.

(3) For recent reviews on 1, 3-dipolar cycloadditions, see: (a) Pellissier, H. *Tetrahedron* **2007**, *63*, 3235. (b) Nair, V.; Suja, T. D. *Tetrahedron* **2007**, *63*, 12247. (c) Zhang, W. *Chemistry Letters* **2013**, *42*, 676. For thermal (3+2) cycloadditions, see: (d) Grigg, R.; Kemp, J.; Thompson, N. *Tetrahedron Lett.* **1978**, *19*, 2827. (e) Le Fevre, G.; Hamelin, J. *Tetrahedron Lett.* **1979**, *20*, 1757. (f) Snider, B. B.; Conn, R. S. E.; Sealfon, S. *J. Org. Chem.* **1979**, *44*, 218. (g) Grigg, R.; Dowling, M.; Jordan,

M.W.; Sridharan, V. *Tetrahedron* 1987, 43, 5873. (h) Khau, V. V.; Martinelli, M. J. *Tetrahedron Lett.* **1996**, 37, 4323.

(4) For Lewis acid catalyzed (3+2) cycloadditions with hydrazones, see: (a) Kobayashi, S.; Shimizu, H.; Yamashita, Y.; Ishitani, H.; Kobayashi, J. *J. Am. Chem. Soc.* **2002**, 124, 13678. (b) Kobayashi, S.; Hirabayashi, R.; Shimizu, H.; Ishitani, H.; Yamashita, Y. *Tetrahedron Lett.* **2003**, 44, 3351. (c) Yamashita, Y.; Kobayashi, S. *J. Am. Chem. Soc.* **2004**, 126, 11279. (d) Shirakawa, S.; Lombardi, P. J.; Leighton, J. L. *J. Am. Chem. Soc.* **2005**, 127, 9974. (e) Frank, E.; Mucsi, Z.; Zupko, I.; Rethy, B.; Falkay, G.; Schneider, G.; Wöfling, J. *J. Am. Chem. Soc.* **2009**, 131, 3894. (f) Zamfir, A.; Schenker, S.; Bauer, W.; Clark, T.; Tsogoeva, S B. *Eur. J. Org. Chem.* **2011**, 3706. (g) Xie, H.; Zhu, J.; Chen, Z.; Li, S.; Wu, Y. *Synthesis* **2011**, 2767.

(5) For recent catalytic asymmetric syntheses of pyrazolines and pyrazolidines, see: (a) LaLonde, R. L.; Wang, Z. J.; Mba, M.; Lackner, A. D.; Toste, F. D. *Angew. Chem. Int. Ed.* **2010**, 49, 598. (b) Hashimoto, T.; Maeda, Y.; Omote, M.; Nakatsu, H.; Maruoka, K. *J. Am. Chem. Soc.* **2010**, 132, 4076. (c) Zamfir, A.; Tsogoeva, S. B. *Synthesis* **2011**, 1988. (d) Hashimoto, T.; Omote, M.; Maruoka, K. *Angew. Chem. Int. Ed.* **2011**, 50, 3489. (e) Fernández, M.; Reyes, E.; Vicario, J. L.; Bad á, D.; Carrillo, L. *Adv. Synth. Catal.* **2012**, 354, 371. (f) Hashimoto, T.; Kimura, H.; Kawamata, Y.; Maruoka, K. *Nat. Chem.* **2011**, 3, 642. (g) Deiana, L.; Zhao, G.-L.; Leijonmarck, H.; Sun, J.; Lehmann, C. W.; Córdova, A. *ChemistryOpen* **2012**, 1, 134.

(6) Rueping, M.; Maji, M. S.; K üçük, H. B.; Atodiresei, I. *Angew. Chem. Int. Ed.* **2012**, 51, 12864.

(7) For related work in the field of chiral binol-based Ntriflylphosphoramides, see (a) Yamamoto, S. A.; Nakashima, D.; Yamamoto, H. *J. Am. Chem. Soc.* **2006**, 128, 9626. For an overview, see (b) Rueping, M.; Nachtsheim, B. J.; Ieawsuwan, W.; Atodiresei, I. *Angew. Chem. Int. Ed.* **2011**, 50, 6706. For further examples, see (c) Rueping, M.; Ieawsuwan, W.; Antonchick, A. P.; Nachtsheim,

B. J. *Angew. Chem. Int. Ed.* **2007**, *46*, 2097. (d) Rueping, M.; Nachtsheim, B. J.; Moreth, S. A.; Bolte, M. *Angew. Chem. Int. Ed.* **2008**, *47*, 593. (e) Rueping, M.; Theissmann, T.; Kuenkel, A.; Koenigs, R. M. *Angew. Chem. Int. Ed.* **2008**, *47*, 6798. (f) Enders, D.; Narine, A. A.; Toulgoat, F.; Bisschops, T. *Angew. Chem. Int. Ed.* **2008**, *47*, 5661. (g) Zeng, M.; Kang, Q.; He, Q.-L.; You, S.-L. *Adv. Synth. Catal.* **2008**, *350*, 2169. (h) Rueping, M.; Ieawsuwan, W.; *Adv. Synth. Catal.* **2009**, *351*, 78. (i) Rueping, M.; Nachtsheim, B. J.; Koenigs, R. M.; Ieawsuwan, W. *Chem. Eur. J.* **2010**, *16*, 13116. (j) Rueping, M.; Lin, M.-Y. *Chem. Eur. J.* **2010**, *16*, 4169. (k) Rueping, M.; Nachtsheim, B. J. *Synlett* **2010**, 119. (l) Rueping, M.; Merino, E.; Koenigs, R. M. *Adv. Synth. Catal.* **2010**, *352*, 2629. (m) Cheon, C. H.; Yamamoto, H. *Org. Lett.* **2010**, *12*, 2476. (n) Rueping, M.; Uria, U.; Lin, M.-Y.; Atodiresei, I. *J. Am. Chem. Soc.* **2011**, *133*, 3732. (o) Hashimoto, T.; Nakatsu, H.; Yamamoto, K.; Maruoka, K. *J. Am. Chem. Soc.* **2011**, *133*, 9730. (p) Rueping, M.; Ieawsuwan, W. *Chem. Commun.* **2011**, *47*, 11450.

(8) Kaupmees, K.; Tolstoluzhsky, N.; Raja, S.; Rueping, M.; Leito, I. *Angew. Chem. Int. Ed.* **2013**, *51*, 11569.

(9) (a) Domingo, L. R. *Eur. J. Org. Chem.* **2000**, 2265. (b) Tanaka, J.; Kanemasa, S. *Tetrahedron* **2001**, *57*, 899. (c) Wagner, G. *Chem. Eur. J.* **2003**, *9*, 1503. (d) Kuznetsov, M. L.; Kukushkin, V. Y.; Haukka, M.; Pombeiro, A. J. L. *Inorg. Chim. Acta* **2003**, *356*, 85. (e) Castillo, R.; Andrés, J.; Domingo, L. R. *Eur. J. Org. Chem.* **2005**, 4705. (f) Domingo, L. R.; Benchouk, W.; Mekelleche, S. M. *Tetrahedron* **2007**, *63*, 4464. (g) Wagner, G.; Danks, T. N.; Vullo, V. *Tetrahedron* **2007**, *63*, 5251. (h) Bădoiu, A.; Bernardinelli, G.; Mareda, J.; Kündig, E. P.; Viton, F. *Chem. Asian J.* **2008**, *3*, 1298. (i) Wagner, G.; Danks, T. N.; Desai, B. *Tetrahedron* **2008**, *64*, 477. (j) Frank, É.; Mucsi, Z.; Szécsi, M.; Zupkó, I.; Wölfling, J.; Schneider, G. *New J. Chem.* **2010**, *34*, 2671. (k) Chaudhuri,

T.; Banerjee, M. *J. Lumin.* **2012**, *132*, 1456. (l) N. Acharjee, A. Banerji, T. Prang *Monatsh, Chem.* **2012**, *143*, 1687. (m) Śniezek, M.; Stecko, S.; Panfil, I.; Furman, B.; Urbańczyk-Lipkowska, Z.; Chmielewski, M. *Tetrahedron: Asymmetry* **2013**, *24*, 89.

(10) (a) Hesse, K.-D.; *Justus Liebigs Ann. Chem.* **1970**, *743*, 50. (b) Le Fevre, G.; Sinbandhit, S.; Hamelin, J. *Tetrahedron* **1979**, *35*, 1821. (c) Wilson, R. M.; Rekers, J. W. *J. Am. Chem. Soc.* **1979**, *101*, 4005. (d) Fouchet, B.; Joucla, M.; Hamelin, J. *Tetrahedron Lett.* **1981**, *22*, 1333. (e) Shimizu, T.; Hayashi, Y.; Nakano, M.; Teramura, K. *Bull. Chem. Soc. Jpn.* **1982**, *55*, 2456. (f) Shimizu, T.; Hayashi, Y.; Teramura, K. *Bull. Chem. Soc. Jpn.* **1985**, *58*, 397. (g) Shimizu, T.; Hayashi, Y. Y.; Miki, M.; Teramura, K. *J. Org. Chem.* **1987**, *52*, 2277. (h) Griffith, A. K.; Vanos, C. M.; Lambert, T. H. *J. Am. Chem. Soc.* **2012**, *134*, 18581. (i) Davis, L. O.; Daniel, W. F. M.; Tobey, S. L. *Tetrahedron Lett.* **2012**, *53*, 522. (j) Lin, G.-Q.; Lei, X.; Liu, P.; Xu, Q.-Q.; Dong, C. *Synlett* **2012**, *23*, 2087.

(11) The double hydrogen-bond formations are only possible in complex **6** and its less stable regioisomer.

(12) We find the barrier of (3+2) cycloaddition between hydrazone and ethylene (without the hydrogen-bonded phosphoramidate) is 47.4 kcal/mol, 3.9 kcal/mol lower than the barrier with the hydrogen-bonded complex **6**.

(13) The (3+2) cycloaddition barrier between hydrazone cation and ethylene is 26.0 kcal/mol. For related computational study on the (3+2) cycloaddition with hydrazone cation, see: Hong, X.; Liang, Y.; Griffith, A. K.; Lambert, T. H.; Houk, K. N. *Chem. Sci.* **2014**, *5*, 471.

(14) In experiment, more reactive cyclopentadiene and styrene derivatives are used, and the calculated cycloaddition barrier between hydrazone **1** and  $\alpha$ -methylstyrene is 22.2 kcal/mol, which is consistent with the experimental conditions (RT, 18h).

## Chapter 7. The Mechanisms and Origins of Switchable Chemoselectivity of Ni-catalyzed

### C(aryl)-O and C(acyl)-O Activation of Aryl Esters with Phosphine Ligands

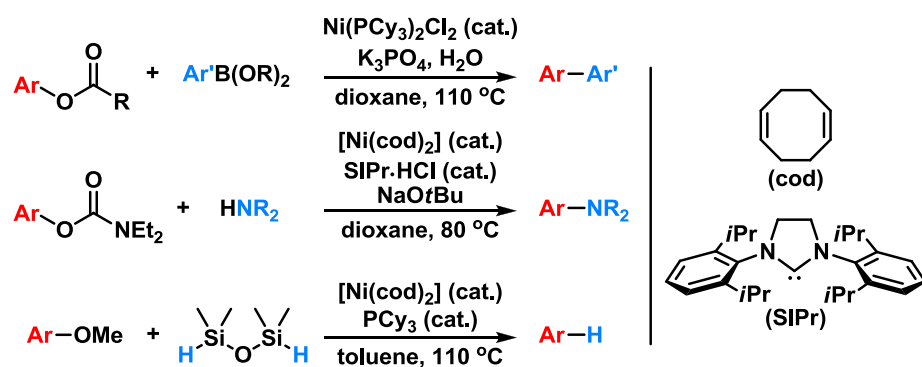
#### 7.1 Abstract

Many experiments have shown that nickel with monodentate phosphine ligands favors the C(aryl)-O activation over the C(acyl)-O activation for aryl esters. However, Itami and co-workers recently discovered that nickel with bidentate phosphine ligands can selectively activate the C(acyl)-O bond of aryl esters of aromatic carboxylic acids. The chemoselectivity with bidentate phosphine ligands can be switched back to C(aryl)-O activation when aryl pivalates are employed. To understand the mechanisms and origins of this switchable chemoselectivity, density functional theory (DFT) calculations have been conducted. For aryl esters, nickel with bidentate phosphine ligands cleaves C(acyl)-O and C(aryl)-O bonds via three-centered transition states. The C(acyl)-O activation is more favorable due to the lower bond dissociation energy (BDE) of C(acyl)-O bond, which translates into a lower transition-state distortion energy. However, when monodentate phosphine ligands are used, a vacant coordination site on nickel creates an extra Ni-O bond in the five-centered C(aryl)-O cleavage transition state. The additional interaction energy between the catalyst and substrate makes C(aryl)-O activation favorable. In the case of aryl pivalates, nickel with bidentate phosphine ligands still favors the C(acyl)-O activation over the C(aryl)-O activation at the cleavage step. However, the subsequent decarbonylation generates a very unstable *t*Bu-Ni(II) intermediate, and this unfavorable step greatly increases the overall barrier for generating the

C(acyl)-O activation products. Instead, the subsequent C-H activation of azoles and C-C coupling in the C(aryl)-O activation pathway are much easier, leading to the observed C(aryl)-O activation products.

## 7.2 Introduction

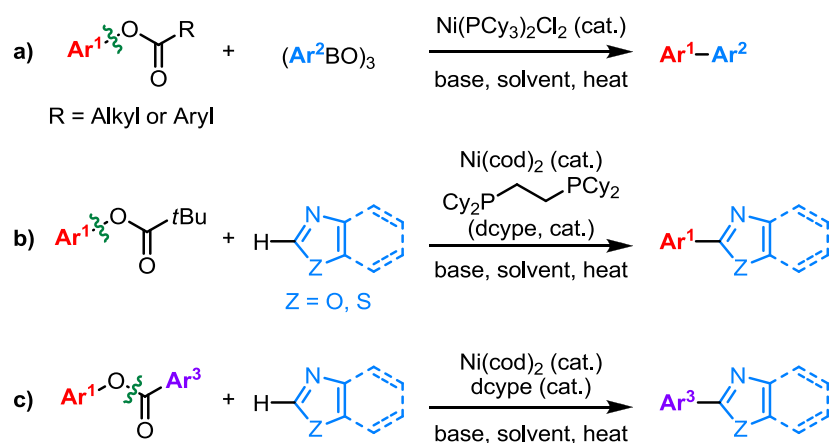
Transition-metal-catalyzed cross-coupling reactions have become important tools for laboratory and industrial carbon-carbon and carbon-heteroatom bond formation because of the efficiency and broad applicability of such reactions.<sup>1</sup> Despite the great success of cross-couplings using aryl halides and palladium catalysts,<sup>2</sup> extensive efforts toward environmentally friendly electrophiles and low-cost catalysts have led to the discovery of nickel-catalyzed C(aryl)-O activation.<sup>3</sup> In 2008, Garg and Shi independently reported the first nickel-catalyzed C(aryl)-O activation using aryl esters,<sup>4</sup> and other carbon electrophiles, such as carbamates,<sup>5</sup> sulfamates,<sup>6</sup> phosphates,<sup>7</sup> and even phenolates,<sup>8</sup> have seen increased use over the past few years. In addition, the design of nucleophiles for the C(aryl)-Ni intermediate has enabled not only C-C but also C-N and C-H bonds formation (Scheme 7.1).<sup>5g,6c,7b,9</sup>



**Scheme 7.1.** Representative Reactions Involving Ni-Catalyzed C(aryl)-O Activation.

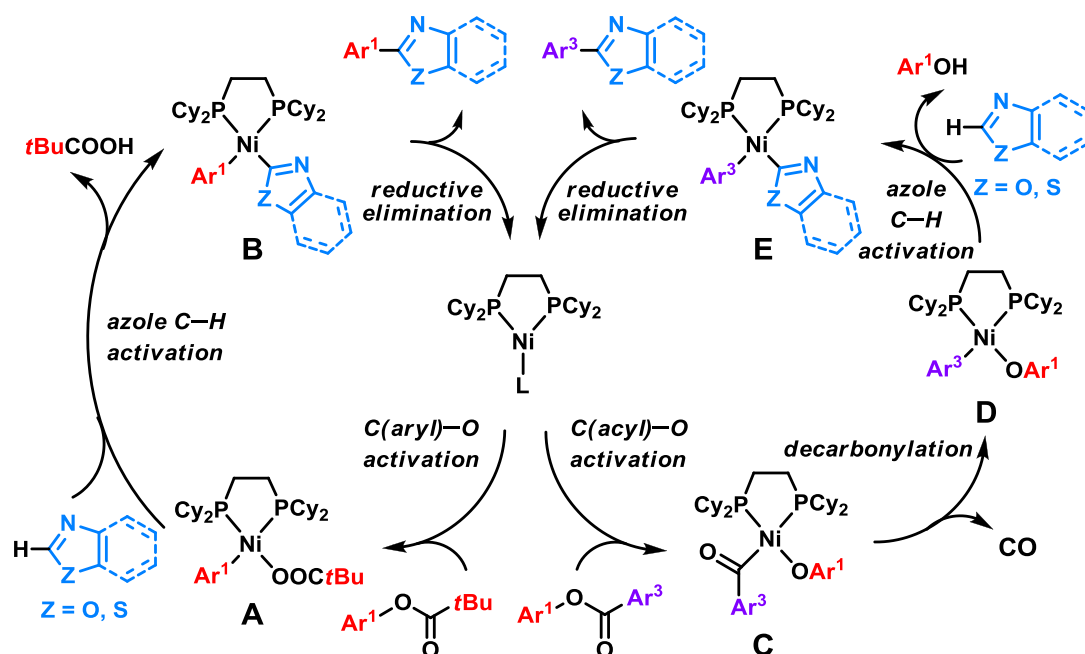
Among the developed methodologies of Ni-catalyzed C-O activation of aryl esters using monodentate phosphine ligands, only the cleavage of C(aryl)-O bond occurs (Scheme 7.2a).<sup>5f,9a,10</sup> In addition, Itami and co-workers reported that nickel with a bidentate phosphine ligand, 1,2-bis(dicyclohexylphosphino)ethane (dcype), can also favor the C(aryl)-O activation of aryl pivalates (Scheme 7.2b).<sup>11</sup> However, they later discovered that the same catalyst can achieve an unexpected C(acyl)-O activation and decarbonylation when aryl esters of aromatic carboxylic acids are employed (Scheme 7.2c).<sup>12</sup> Based on this strategy, a wide variety of heteroaromatic esters were smoothly coupled with azoles to generate bis(heteroaryl) scaffolds in a straightforward fashion.<sup>13</sup>





**Scheme 7.2.** Chemoselectivity of Ni-Catalyzed C-O Activation of Aryl Esters with Phosphine Ligands

There are two possible catalytic cycles for the Ni/dcppe catalyzed C-O activation of aryl esters (Scheme 7.3). For the pivalic ester, the C(aryl)-O activation occurs to give intermediate **A**. Subsequent azole C-H activation generates intermediate **B**, which undergoes the  $C_{sp^2}$ - $C_{sp^2}$  reductive elimination to produce the observed cross-coupling product. Alternatively, aromatic ester undergoes the C(acyl)-O activation to give intermediate **C**. Subsequent decarbonylation generates the aryl-nickel intermediate **D**. After the azole C-H activation, intermediate **E** undergoes reductive elimination to produce the cross-coupling product. Although the proposed mechanisms are plausible, the resting states, rate-determining steps, and especially the origins of chemoselectivity are not known. Therefore, we have used density functional theory (DFT) calculations to explore the mechanisms and origins of switchable chemoselectivity of Ni-catalyzed C(aryl)-O and C(acyl)-O activation of aryl esters with phosphine ligands.



**Scheme 7.3.** Proposed Mechanisms for Ni-Catalyzed C-O Activation of Aryl Esters and Subsequent C-C Coupling with Azoles.

### 7.3 Computational Details

All density functional theory (DFT) calculations were performed with Gaussian 09.<sup>14</sup> Geometry optimization of all the minima and transition states involved was carried out at the B3LYP level of theory<sup>15</sup> with the SDD basis set<sup>16</sup> for nickel and the 6-31G(d) basis set<sup>17</sup> for the other atoms (keyword 5D was used in the calculations). The vibrational frequencies were computed at the same level to check whether each optimized structure is an energy minimum or a transition state and to

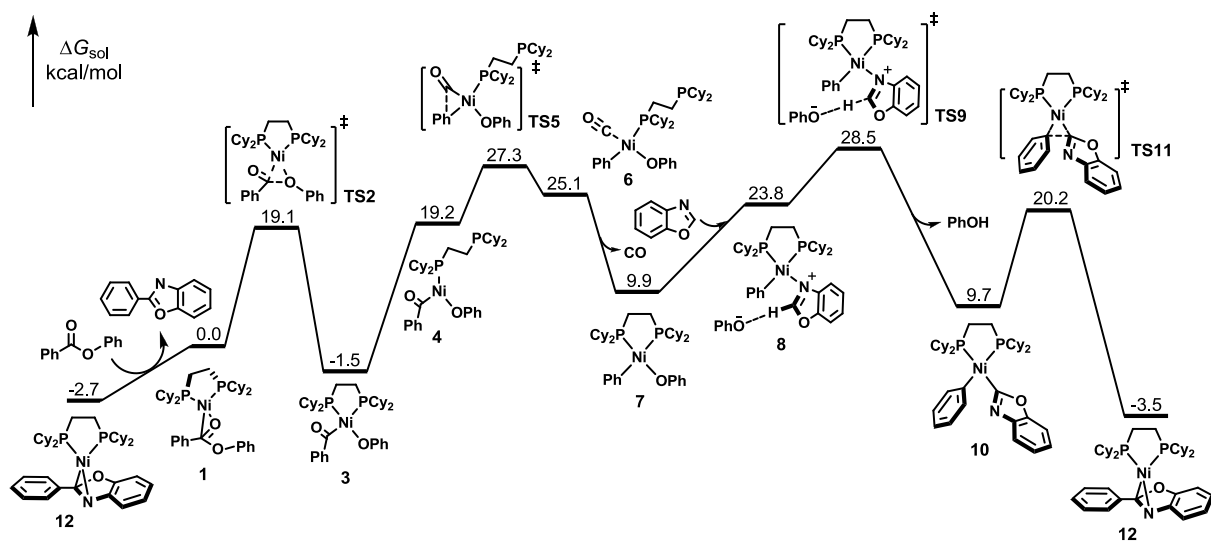
evaluate its zero-point vibrational energy (ZPVE) and thermal corrections at 298 K. The single-point energies and solvent effects in 1,4-dioxane were computed at the M06 level of theory<sup>18</sup> with the SDD basis set for nickel and the 6-311+G(d,p) basis set for the other atoms, based on the gas-phase optimized structures. Solvation energies were evaluated by a self-consistent reaction field (SCRF) using the SMD model.<sup>19</sup> Fragment distortion and interaction energies and bond dissociation energies were computed at the M06/6-311+G(d,p)-SDD level using the B3LYP/6-31G(d)-SDD geometries in the gas phase.

## 7.4 Results and Discussion

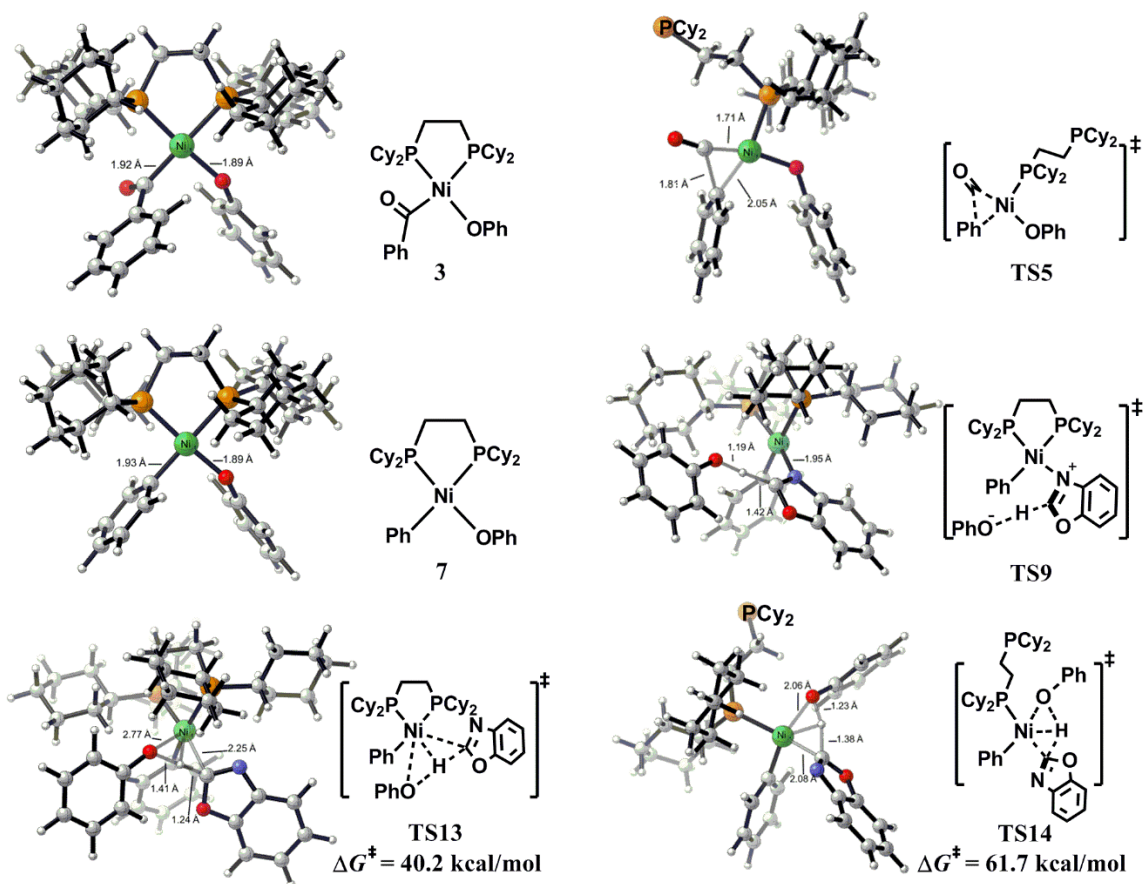
### 7.4.1. Aryl Esters of Aromatic Carboxylic Acids: Origins of Ligand-Controlled Chemoselectivity of C-O Activation

Using phenyl benzoate and benzoxazole as model reactants, we first explored the mechanism of Ni/dcype catalyzed C-O activation of aromatic esters and subsequent C-C couplings with azoles. The free energy profile is shown in Figure 7.1, and optimized structures of selected intermediates and transition states are shown in Figure 7.2. From the substrate coordinated complex **1**, the C(acyl)-O activation via **TS2** requires an activation free energy of 19.1 kcal/mol to generate the C(acyl)-Ni intermediate **3**. For the C-O activation, three possible pathways were explored, and the origins of preferences are discussed in detail later. After the C(acyl)-O activation, dissociation of one phosphine ligand from nickel is necessary to provide a coordination site for the carbonyl migration

through transition state **TS5**. The loss of one phosphine ligand is endergonic by 20.7 kcal/mol, and this contributes to the high overall barrier (28.8 kcal/mol) for carbonyl migration. After carbonyl migration, a barrierless decarbonylation occurs to produce the tetracoordinated nickel complex **7**. From **7**, the substitution of phenoxide by benzoxazole gives the N-coordinated nickel intermediate **8**. This step is endergonic by 13.9 kcal/mol. The following deprotonation of benzoxazole using phenoxide as base via **TS9** is facile, requiring an activation free energy of only 4.7 kcal/mol. Besides **TS9**, two additional transition states of four-centered  $\sigma$ -bond metathesis, **TS13** and **TS14**, are also located (Figure 7.2). Comparing **TS13** with **TS14**, **TS13** is significantly more stable because it maintains the bidentate coordination of dcype ligand. However, the  $\sigma$ -bond metathesis pathway via **TS13** is disfavored by 11.7 kcal/mol in terms of free energy than the stepwise deprotonation pathway via **TS9** (40.2 versus 28.5 kcal/mol). The similar preference was also reported in previous studies of Pd-catalyzed C-H activation of oxazoles and thiazoles.<sup>20</sup> After the C-H activation, intermediate **10** undergoes a  $C_{sp^2}$ - $C_{sp^2}$  reductive elimination to give the product coordinated complex **12**. Subsequent product extrusion from **12** to regenerate substrate coordinated complex **1** is endergonic by 2.7 kcal/mol, suggesting that **12** is the resting state of the catalytic cycle. Therefore, the overall barrier for this reaction is 31.2 kcal/mol, which is consistent with the experimental conditions.<sup>12</sup>



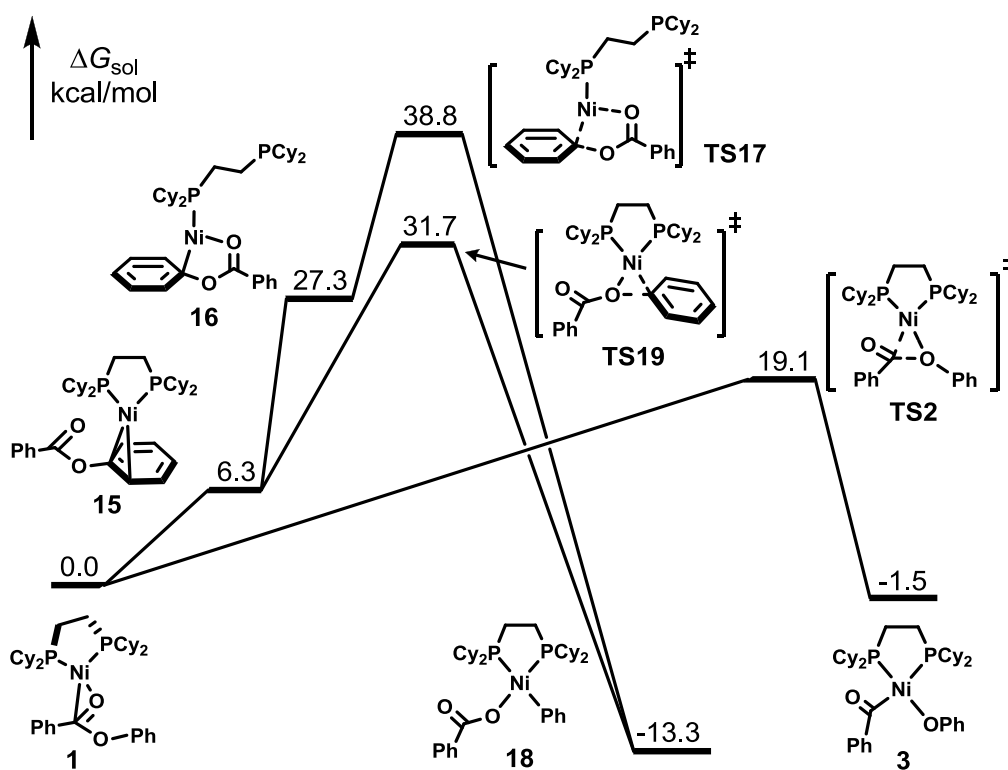
**Figure 7.1.** DFT-computed Gibbs free energies for the Ni/dcype-catalyzed decarbonylative C-C coupling of benzoxazole and phenyl benzoate.



**Figure 7.2.** DFT-optimized structures of selected intermediates and transition states for the Ni/dcype-catalyzed decarbonylative C-C coupling of benzoxazole and phenyl benzoate.

Besides the C(acyl)-O activation of aryl esters of aromatic carboxylic acids, the competing C(aryl)-O activation was also explored. The free energy profile is shown in Figure 7.3. There are two possible C(aryl)-O activation pathways with dcype acting as either a mono- or bidentate ligand. When dcype acts as a bidentate ligand, nickel migrates to the oxygenated phenyl group in **15** in order to undergo the C(aryl)-O bond cleavage via **TS19**. The migration is endergonic by 6.3

kcal/mol, and the C(aryl)-O bond cleavage requires an activation free energy of 25.4 kcal/mol, resulting in an overall barrier of 31.7 kcal/mol. If dcype acts as a monodentate ligand, the coordination of acyl oxygen leads to the five-centered transition state **TS17**. Although the barrier for the cleavage step from intermediate **16** is only 11.5 kcal/mol, the formation of **16** is very endergonic, making the overall barrier as high as 38.8 kcal/mol. Therefore, compared with the C(aryl)-O activation via **TS17** or **TS19**, the Ni/dcype catalyst significantly favors the C(acyl)-O activation via the three-centered transition state **TS2** (19.1 kcal/mol, Figure 7.3).



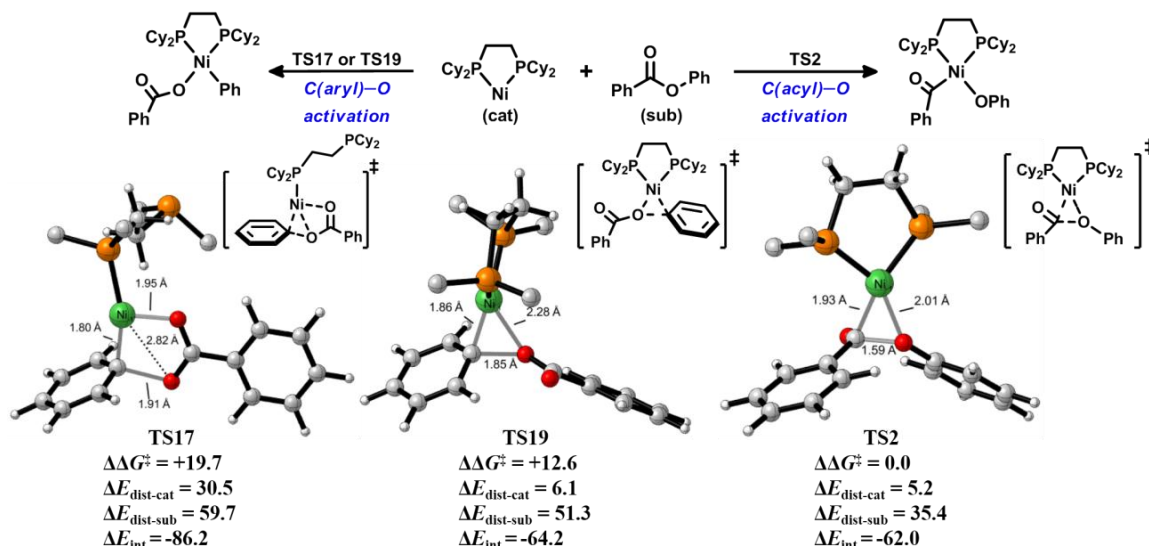
**Figure 7.3.** DFT-computed Gibbs free energies for the Ni/dcype-catalyzed C(acyl)-O and C(aryl)-O activation pathways of phenyl benzoate.

To gain insights into the origins of chemoselectivity of Ni/dcype-catalyzed C-O activation of aryl esters, we analyzed the C(acyl)-O and C(aryl)-O activation transition states using the distortion/interaction model,<sup>21-23</sup> as shown in Figure 7.4. Each transition structure was separated into two fragments (the distorted catalyst and substrate), followed by single point energy calculations on each distorted fragment. The energy differences the distorted structures and optimized ground-state structures are the distortion energy of Ni(dcype) catalyst ( $\Delta E_{\text{dist-cat}}$ ) and aryl ester substrate ( $\Delta E_{\text{dist-sub}}$ ), respectively. The interaction energy ( $\Delta E_{\text{int}}$ ) is the difference between the activation energy and the total distortion energy ( $\Delta E_{\text{dist-cat}} + \Delta E_{\text{dist-sub}}$ ).

For the C(aryl)-O activation transition states, **TS17** and **TS19**, the distortion energy of the Ni(dcype) catalyst,  $\Delta E_{\text{dist-cat}}$ , causes **TS19** to be lower in energy. Although the interaction energy,  $\Delta E_{\text{int}}$ , is larger in **TS17** because of the extra Ni-O(acyl) bond, the loss of one phosphine coordination from nickel results in a very high distortion energy of catalyst (30.5 kcal/mol, Figure 7.4) and makes the five-centered transition state **TS17** unfavorable for the C(aryl)-O activation. Comparing the three-centered C(acyl)-O and C(aryl)-O activation transition states, **TS2** and **TS19**, they have similar  $\Delta E_{\text{dist-cat}}$  and  $\Delta E_{\text{int}}$ , but very different distortion of substrate,  $\Delta E_{\text{dist-sub}}$ . The lower  $\Delta E_{\text{dist-sub}}$  of **TS2** (35.4 versus 51.3 kcal/mol, Figure 7.4) leads to the preference for the C(acyl)-O activation. The computed homolytic dissociation energy of C(aryl)-O bond of phenyl benzoate is 101.3 kcal/mol, and the value of C(acyl)-O bond is 78.2 kcal/mol. This indicates that the C(acyl)-O bond is much weaker than the C(aryl)-O bond. The weaker C(acyl)-O bond requires less distortion of the



substrate in the three-centered C-O cleavage transition state. Therefore, the C(acyl)-O activation is favorable using nickel catalysts with bidentate phosphine ligands.

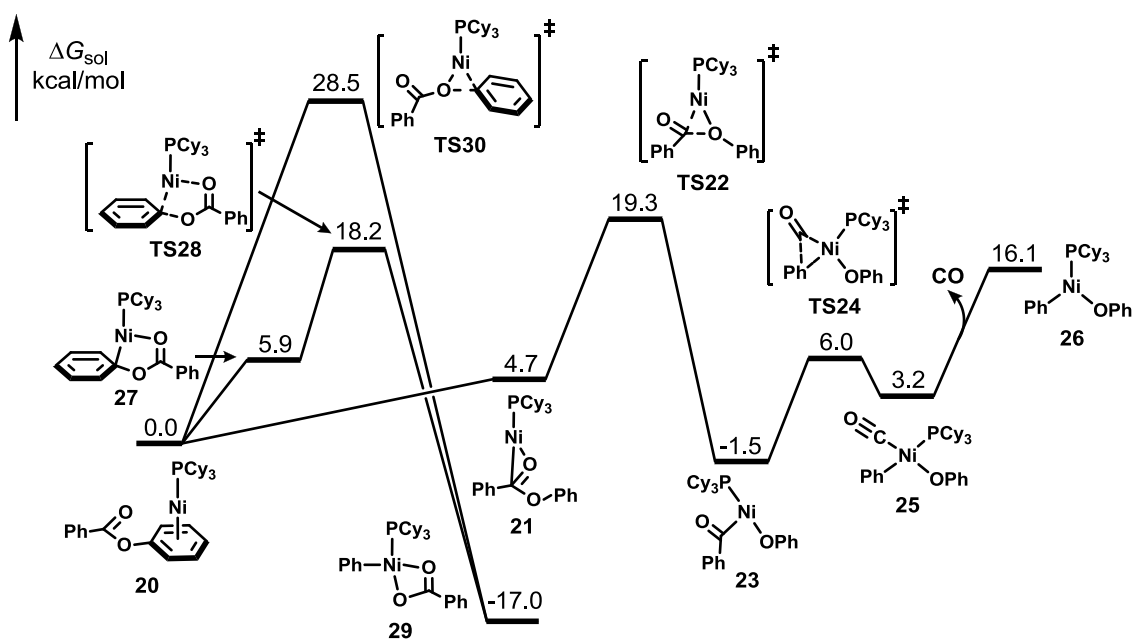


**Figure 7.4.** The distortion/interaction analysis of the C(aryl)-O and C(acyl)-O activation transition states involving the Ni/dcype catalyst (Only the  $\alpha$ -carbon of cyclohexyl group is shown for simplicity; energies are in kcal/mol).

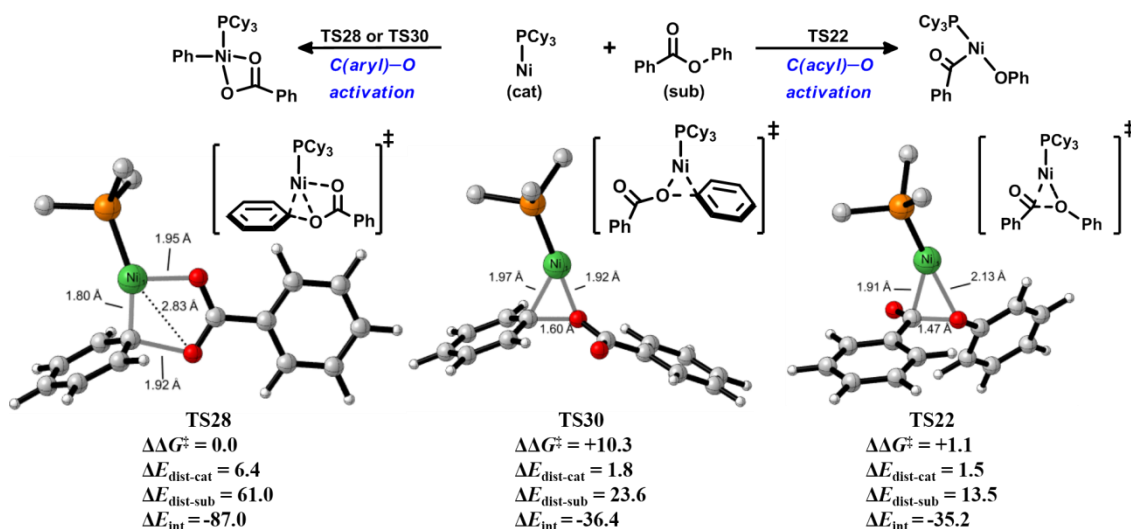
We also investigated the possible C-O activation pathways with the Ni/PCy<sub>3</sub> catalyst. The free energy profile is shown in Figure 7.5. From the substrate coordinated complex **20**, the C(acyl)-O cleavage via **TS22** requires an activation free energy of 19.3 kcal/mol. The subsequent decarbonylation gives a relatively unstable intermediate **26** for transmetalation. For the C(aryl)-O activation, the three-centered transition state **TS30** is much less stable than the five-centered transition state **TS28**. The overall barrier for the C(aryl)-O activation pathway via **TS28** is 18.2 kcal/mol, which is 1.1 kcal/mol lower than that of the C(acyl)-O activation with the monodentate

PCy<sub>3</sub> ligand(**TS22**: 19.3 kcal/mol, Figure 7.5).<sup>24</sup> In addition to the preference for the C(aryl)-O activation transition state, the different stabilities of the generated intermediates, **26** (16.1 kcal/mol) and **29** (-17.0 kcal/mol), could lead to even larger preference for the C(aryl)-O activation pathway when the subsequent transformations are not facile. A previous computational study by Liu and co-workers showed that the transmetalation of boron reagents could have an barrier of over 30 kcal/mol.<sup>10</sup> In this case, the preference to the C(aryl)-O activation mainly arises from the much better stability of intermediate **29**.

The distortion/interaction analysis revealed the origins of the reversed chemoselectivity with the monodentate phosphine ligand (Figure 7.6). Comparing the three-centered transition states **TS30** and **TS22**, the weaker C(acyl)-O bond leads to the lower  $\Delta E_{\text{dist-sub}}$  in **TS22** (13.5 versus 23.6 kcal/mol, Figure 7.6) and a 9.2 kcal/mol preference to break this bond. However, in the case of five-centered C(aryl)-O cleavage transition state **TS28**, the Ni(PCy<sub>3</sub>) catalyst does not require as much distortion energy as the Ni(dcybe) catalyst in **TS17** (30.5 kcal/mol, Figure 7.4), and thus the larger  $\Delta E_{\text{int}}$  from the additional Ni-O bond (-87.0 kcal/mol, Figure 7.6) overrides the distortion penalty and leads to the overall preference to the C(aryl)-O bond activation with the Ni/PCy<sub>3</sub> catalyst.



**Figure 7.5.** DFT-computed Gibbs free energies for the Ni/PCy<sub>3</sub>-catalyzed C(acyl)-O and C(aryl)-O activation pathways of phenyl benzoate.

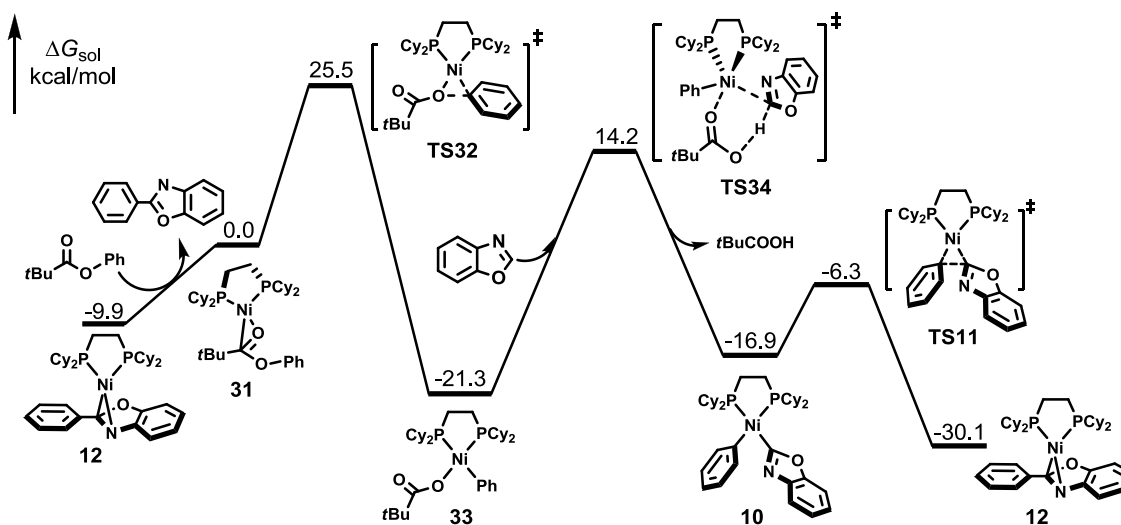


**Figure 7.6.** The distortion/interaction analysis of the C(aryl)-O and C(acyl)-O activation transition states involving the Ni/PCy<sub>3</sub> catalyst (Only the  $\alpha$ -carbon of cyclohexyl group is shown for simplicity; energies are in kcal/mol).

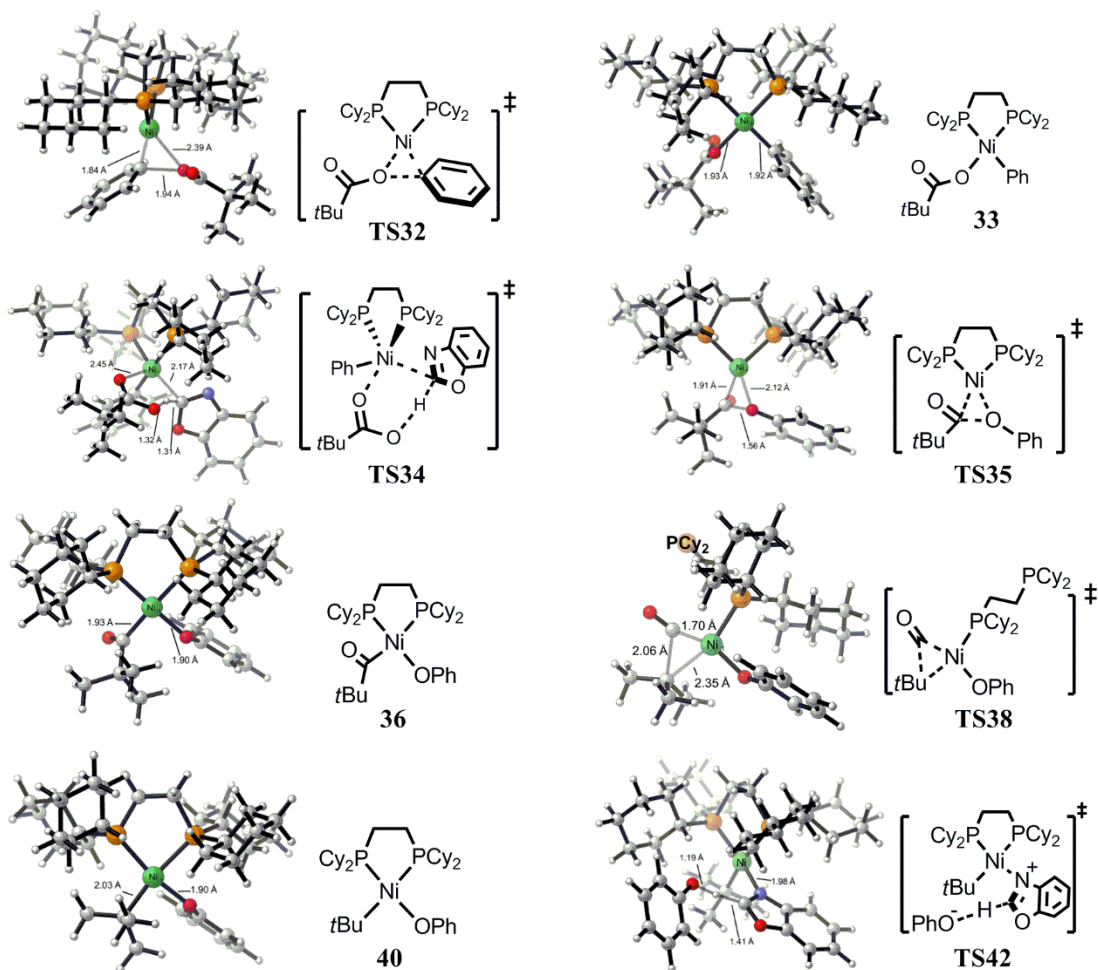
#### 7.4.2. Aryl Pivalates: Origins of Substrate-Dependent Chemoselectivity of C-O Activation

Unlike the Ni/dcype catalyzed C(acyl)-O activation of aryl esters of aromatic carboxylic acids, the C(aryl)-O activation of aryl pivalates was observed with the same catalyst (Scheme 7.2c). Using phenyl pivalate and benzoxazole as the model reactants, we studied the mechanism and origins of chemoselectivity of the Ni/dcype-catalyzed C-C couplings between azoles and aryl pivalates. The free energy profile is shown in Figure 7.7, and optimized structures of selected intermediates and transition states are shown in Figure 7.8. From the substrate-coordinated complex **31**, the C(aryl)-O activation via **TS32** requires an activation free energy of 25.5 kcal/mol. This step is exergonic by 21.3 kcal/mol, suggesting that the resulting intermediate **33** is very stable. Then intermediate **33**

undergoes a six-centered concerted metalation-deprotonation (CMD) pathway through transition state **TS34** to realize the benzoxazole C-H activation. The subsequent  $C_{sp^2}$ - $C_{sp^2}$  reductive elimination is facile with a barrier of 10.6 kcal/mol, giving the product coordinated complex **12**. The product extrusion from **12** is endergonic by 9.9 kcal/mol. For the whole catalytic cycle, both the C(aryl)-O activation and the benzoxazole C-H activation have high barriers, and the overall free energy span is 35.5 kcal/mol.



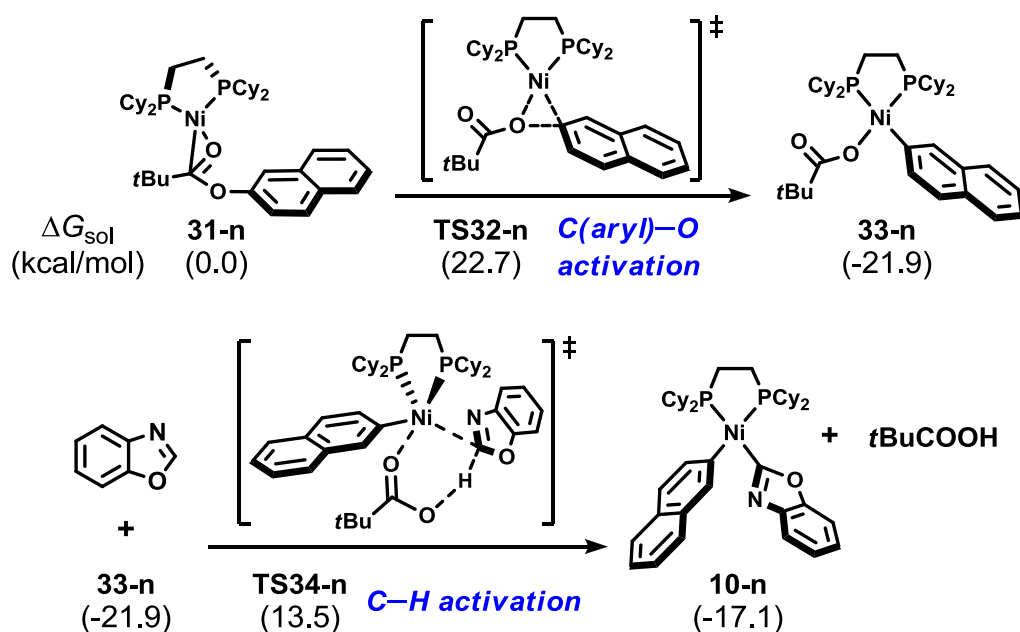
**Figure 7.7.** DFT-computed Gibbs free energies for the Ni/dcype-catalyzed C-C coupling between benzoxazole and phenyl pivalate.



**Figure 7.8.** DFT-optimized structures of selected intermediates and transition states for the C(acyl)-O and C(aryl)-O activation pathways of the Ni/dcype-catalyzed C-C coupling between benzoxazole and phenyl pivalate.

Very recently, Itami and co-workers reported an experimental mechanistic study of the same reaction.<sup>25</sup> They found that the stoichiometric reaction of naphthalen-2-yl pivalate with Ni(cod)<sub>2</sub>/dcype gives an arylnickel(II) pivalate complex **33-n** (Scheme 7.4), which is proved an

isolatable intermediate in the catalytic cycle. This is in good agreement with our computational results (Figure 7.7). Furthermore, kinetic studies reveal that the C-H activation of benzoxazole is the rate-determining step in the reaction using naphthalen-2-yl pivalate.<sup>25</sup> For a direct comparison, we also studied the C(aryl)-O activation pathway of naphthalen-2-yl pivalate (Scheme 7.4). It was found that naphthalen-2-yl pivalate is more reactive toward oxidative addition. The C(aryl)-O activation barrier is now 22.7 kcal/mol, which is 2.8 kcal/mol lower than the corresponding value for phenyl pivalate (25.5 kcal/mol, Figure 7.7). On the other hand, the C-H activation barrier is not affected by switching the phenyl group (35.5 kcal/mol, Figure 7.7) to the naphthalen-2-yl group (35.4 kcal/mol, Scheme 7.4). Therefore, the rate-determining step of the reaction using naphthalen-2-yl pivalate is the C-H activation of benzoxazole.

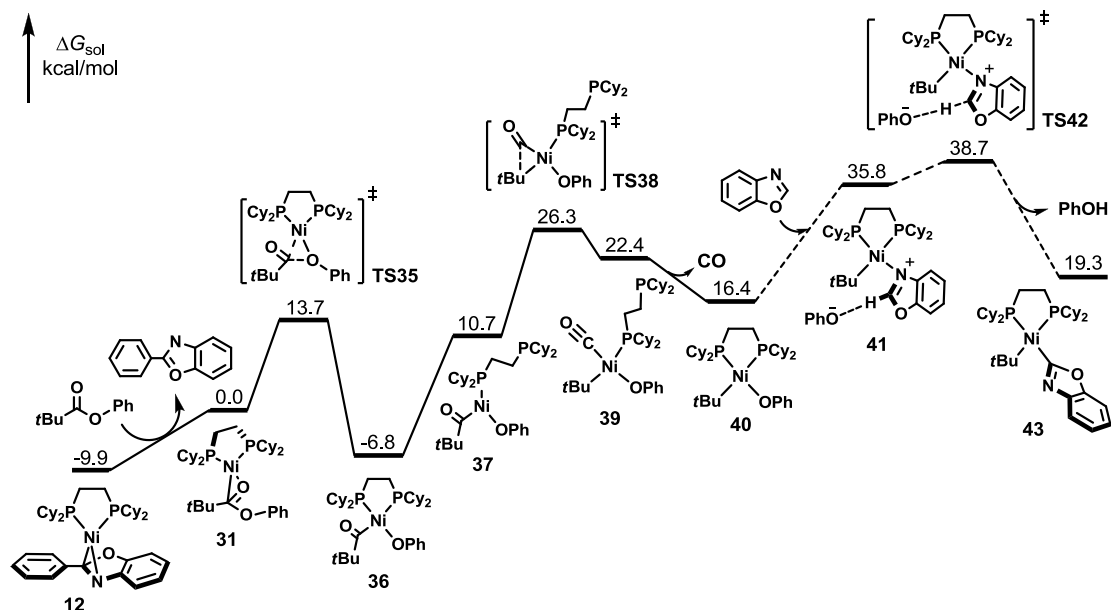


**Scheme 7.4.** DFT-Computed Gibbs Free Energies for Reaction Using Naphthalen-2-yl Pivalate

The possible C(acyl)-O activation and subsequent decarbonylative C-C coupling were also studied. The free energy profile is shown in Figure 7.9, and optimized structures of selected intermediates and transition states are shown in Figure 7.8. From the substrate coordinated complex **31**, the C(acyl)-O activation via **TS35** is very facile, requiring an activation free energy of 13.7 kcal/mol. The generated intermediate **36** is exergonic by only 6.8 kcal/mol, suggesting that the C(acyl)-O activation step is reversible. The dissociation of one phosphine ligand from nickel provides an open coordination site for carbonyl migration via **TS38**. Subsequent decarbonylation generates an unstable intermediate **40**. From **40**, the further transformation with benzoxazole would lead to a very high-energy transition state **TS42** (38.7 kcal/mol, Figure 7.9). Comparing the two C-



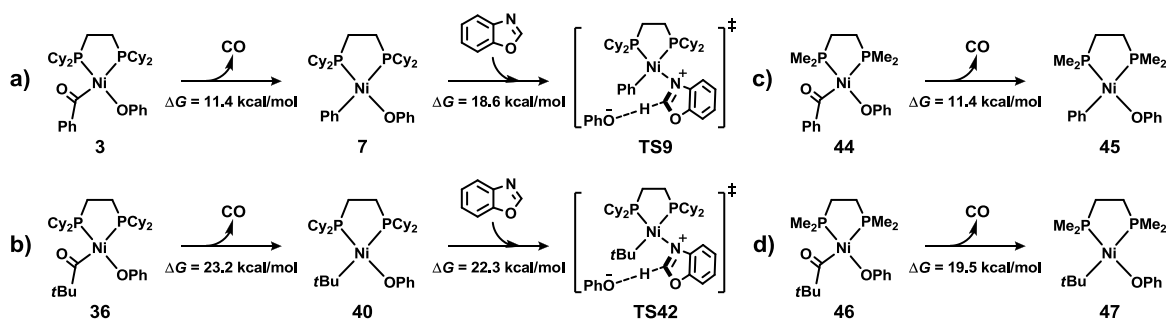
O activation transition states of phenyl pivalate, **TS32** (25.5 kcal/mol, Figure 7.7) and **TS35** (13.7 kcal/mol, Figure 7.9), the preference for the C(acyl)-O activation with bidentate phosphine ligands (Figure 7.4) still exists. However, the following C-H activation process requires an overall activation free energy of 45.5 kcal/mol (from **36** to **TS42**, Figure 7.9), which is 10.0 kcal/mol higher than that of the C-H activation after the C(aryl)-O bond cleavage shown in Figure 7.7. Therefore, when aryl pivalates are employed, the decarbonylative C-C coupling products are not observed.<sup>11</sup>



**Figure 7.9.** DFT-computed Gibbs free energies for the Ni/dcype-catalyzed decarbonylative C-C coupling of benzoxazole and phenyl pivalate.

We further studied the origins of different barriers for the C-H activation processes after the C(acyl)-O bond cleavage of aromatic and pivalic esters. In the case of phenyl benzoate, the overall barrier is 30.0 kcal/mol and includes two parts shown in Scheme 7.5a: the reaction free energy of

decarbonylation from intermediate **3** to **7** (11.4 kcal/mol) and the barrier for the deprotonation of benzoxazole from intermediate **7** to transition state **TS9** (18.6 kcal/mol). Similarly, the 45.5 kcal/mol barrier in the case of phenyl pivalate also includes these two parts (Scheme 7.5b), and the major difference comes from the reaction free energy of decarbonylation. For phenyl pivalate, this step is endergonic by 23.2 kcal/mol, significantly higher than that for phenyl benzoate (11.4 kcal/mol, Scheme 7.5a). When using a less steric demanding ligand, 1,2-bis(dimethylphosphino)ethane (dmpe), the decarbonylation is still endergonic by 11.4 kcal/mol for phenyl benzoate (Scheme 7.5c), while the reaction free energy for phenyl pivalate is 19.5 kcal/mol (Scheme 7.5d), 3.7 kcal/mol lower as compared to using the dcype ligand. This suggests that the steric repulsion between the bulky phosphine ligand and the *t*Bu group in intermediate **40** contributes to part of the difference between benzoate and pivalate. The electronic effect is the major reason for the extremely unfavorable decarbonylation in the case of pivalic esters. For both benzoate and pivalate, there are strong  $d_{\text{Ni}}-\pi^*_{\text{acyl}}$  interactions<sup>26</sup> in the C(acyl)-O activation products **3**, **36**, **44**, and **46**. After the decarbonylation, the phenyl group in intermediates **7** and **45** is a weak  $\pi$  acceptor, and the  $d_{\text{Ni}}-\pi^*$  interaction decreases, making this step endergonic by 11.4 kcal/mol (Scheme 5, a and c). However, the *t*Bu group in intermediates **40** and **47** are unlikely to accept the d electrons from nickel, and the lack of the  $d-\pi^*$  interaction leads to much more endergonic decarbonylations (Scheme 7.5, b and d).



**Scheme 7.5.** Comparisons of Reaction Free Energies of Decarbonylation Involving Benzoate and Pivalate.

## 7.5 Conclusions

Mechanisms and origins of the switchable chemoselectivity of the Ni-catalyzed C(acyl)-O and C(aryl)-O activation of aryl esters with phosphine ligands are revealed through DFT calculations. For aryl esters of aromatic carboxylic acids, the nickel with the bidentate dcype ligand cleaves the C-O bonds via three-centered transition states. The lower BDE of the C(acyl)-O bond leads to the lower distortion energy in the cleavage transition state, making the C(acyl)-O activation more favorable. After the facile C(acyl)-O activation, the endergonic dissociation of one phosphine ligand from nickel provides a coordination site for decarbonylation. Subsequently, the deprotonation of azoles by aryloxyde realizes the C-H activation process. The following  $C_{sp^2}$ - $C_{sp^2}$  reductive elimination generates the cross-coupling product. When the monodentate  $PCy_3$  ligand is used with aryl esters, a vacant coordination site on nickel creates an extra Ni-O bond in the five-centered C(aryl)-O cleavage transition state. This additional interaction energy overrides the distortion penalty and makes the C(aryl)-O activation preferred.

For aryl pivalates, the bidentate phosphine ligand still favors the C(acyl)-O cleavage. However, the subsequent decarbonylation generates a highly unstable *t*Bu-Ni(II) intermediate due to the lack of d- $\pi^*$  interaction between nickel and the *t*Bu group as well as the steric repulsion between the bulky phosphine ligand and the *t*Bu group. This very unfavorable step significantly increases the overall barrier for generating the C(acyl)-O activation products. Instead, the C-H activation of azoles and C-C coupling after the C(aryl)-O activation are much easier, leading to the observed C(aryl)-O activation products.

## 7.6 References

- (1) (a) *Topics in Current Chemistry*, Vol. 219; Miyaura, N., Ed.; Springer-Verlag: New York, 2002. (b) Hassan, J.; Sévignon, M.; Gozzi, C.; Schulz, E.; Lemaire, M. *Chem. Rev.* **2002**, *102*, 1359. (c) *Metal-Catalyzed Cross-Coupling Reactions*; Diederich, F., Meijere, A., Eds.; Wiley-VCH: Weinheim, 2004. (d) Corbet, J.; Mignani, G. *Chem. Rev.* **2006**, *106*, 2651. (e) Negishi, E. *Bull. Chem. Soc. Jpn.* **2007**, *80*, 233. (f) Molander, G. A.; Ellis, N. *Acc. Chem. Res.* **2007**, *40*, 275. (g) Alberico, D.; Scott, M. E.; Lautens, M. *Chem. Rev.* **2007**, *107*, 174. (h) Ackermann, L.; Vicente, R.; Kapdi, A. R. *Angew. Chem. Int. Ed.* **2009**, *48*, 9792. (i) Chen, X.; Engle, K. M.; Wang, D.-H.; Yu, J.-Q. *Angew. Chem. Int. Ed.* **2009**, *48*, 5094. (j) Yamaguchi, J.; Yamaguchi, A. D.; Itami, K. *Angew. Chem. Int. Ed.* **2012**, *51*, 8960.

(2) (a) Old, D. W.; Wolfe, J. P.; Buchwald, S. L. *J. Am. Chem. Soc.* **1998**, *120*, 9720. (b) Littke, A. F.; Fu, G. C. *Angew. Chem. Int. Ed.* **2002**, *41*, 4176. (c) Nicolaou, K. C.; Bulger, P. G.; Sarlah, D. *Angew. Chem. Int. Ed.* **2005**, *44*, 4442. (d) Chinchilla, R.; Nájera, C. *Chem. Rev.* **2007**, *107*, 874. (e) Yin, L.; Liebscher, J. *Chem. Rev.* **2007**, *107*, 133. (f) Ming, C.; Kwong, F. Y. *Chem. Soc. Rev.* **2011**, *40*, 4963. (g) Li, B.-J.; Yu, D.-G.; Sun, C.-L.; Shi, Z.-J. *Chem. Eur. J.* **2011**, *17*, 1728. (h) Seechurn, C. C. C. J.; Kitching, M. W.; Colacot, T. J.; Snieckus, V. *Angew. Chem. Int. Ed.* **2012**, *51*, 5062.

(3) For reviews, see: (a) Yu, D.-G.; Li, B.-J.; Shi, Z.-J. *Acc. Chem. Res.* **2010**, *43*, 1486. (b) Rosen, B. M.; Quasdorf, K. W.; Wilson, D. A.; Zhang, N.; Resmerita, A.-M.; Garg, N. K.; Percec, V. *Chem. Rev.* **2011**, *111*, 1346. (c) Han, F. -S. *Chem. Soc. Rev.* **2013**, *42*, 5270. (d) Yamaguchi, J.; Muto, K.; Itami, K. *Eur. J. Org. Chem.* **2013**, 19. (e) Mesganaw, T.; Garg, N. K. *Org. Process Res. Dev.* **2013**, *17*, 29. For related studies on mechanism, see: (f) Yoshikai, N.; Matsuda, H.; Nakamura, E. *J. Am. Chem. Soc.* **2008**, *130*, 15258. (g) Yoshikai, N.; Matsuda, H.; Nakamura, E. *J. Am. Chem. Soc.* **2009**, *131*, 9590. (h) Xue, L.-Q.; Lin, Z.-Y. *Chem. Soc. Rev.* **2010**, *39*, 1692. (i) Li, Z.; Jiang, Y.-Y.; Fu, Y. *Chem. Eur. J.* **2012**, *18*, 4345. (j) Yu, H.-Z. Fu, Y. *Chem. Eur. J.* **2012**, *18*, 16765. (k) Cornella, J.; Gómez-Bengoa, E.; Martín, R. *J. Am. Chem. Soc.* **2013**, *135*, 1997.

(4) (a) Quasdorf, K. W.; Tian, X.; Garg, N. K. *J. Am. Chem. Soc.* **2008**, *130*, 14422. (b) Guan, B.-T.; Wang, Y.; Li, B.-J.; Yu, D.-G.; Shi, Z.-J. *J. Am. Chem. Soc.* **2008**, *130*, 14468. (c) Li, B.-J.; Li, Y.-Z.; Lu, X.-Y.; Liu, J.; Guan, B.-T.; Shi, Z.-J. *Angew. Chem. Int. Ed.* **2008**, *47*, 10124. (d)

Shimasaki, T.; Tobisu, M.; Chatani, N. *Angew. Chem. Int. Ed.* **2010**, *49*, 2929. (e) Ehle, A. R.; Zhou, Q.; Watson, M. P. *Org. Lett.* **2012**, *14*, 1202.

(5) (a) Sengupta, S.; Leite, M.; Raslan, D. S.; Quesnelle, C.; Snieckus, V. *J. Org. Chem.* **1992**, *57*, 4066. (b) Dallaire, C.; Kolber, I.; Gingras, M. *Org. Synth.* **2002**, *78*, 42. (c) Quasdorf, K. W.; Riener, M.; Petrova, K. V.; Garg, N. K. *J. Am. Chem. Soc.* **2009**, *131*, 17748. (d) Antoft-Finch, A.; Blackburn, T.; Snieckus, V. *J. Am. Chem. Soc.* **2009**, *131*, 17750. (e) Xi, L.; Li, B.-J.; Wu, Z.-H.; Lu, X.-Y.; Guan, B.-T.; Wang, B.-Q.; Zhao, K.-Q.; Shi, Z.-J. *Org. Lett.* **2010**, *12*, 884. (f) Quasdorf, K. W.; Antoft-Finch, A.; Liu, P.; Silberstein, A. L.; Komaromi, A.; Blackburn, T.; Ramgren, S. D.; Houk, K. N.; Snieckus, V.; Garg, N. K. *J. Am. Chem. Soc.* **2011**, *133*, 6352. (g) Hie, L.; Ramgren, S. D.; Mesganaw, T.; Garg, N. K. *Org. Lett.* **2012**, *14*, 4182. (h) Ramgren, S. D.; Hie, L.; Ye, Y.-X.; Garg, N. K. *Org. Lett.* **2013**, *15*, 3950.

(6) (a) Macklin, T. K.; Snieckus, V. *Org. Lett.* **2005**, *7*, 2519. (b) Wehn, P. M.; Du Bois, J. *Org. Lett.* **2005**, *7*, 4685. (c) Ramgren, S. D.; Silberstein, A. L.; Yang, Y.; Garg, N. K. *Angew. Chem. Int. Ed.* **2011**, *50*, 2171. (d) Chen, G.-J.; Han, F.-S. *Eur. J. Org. Chem.* **2012**, 3575.

(7) (a) Chen, H.; Huang, Z.-B.; Hu, X.-M.; Tang, G.; Xu, P.-X.; Zhao, Y.-F.; Cheng, C.-H. *J. Org. Chem.* **2011**, *76*, 2338. (b) Huang, J.-H.; Yang, L. M. *Org. Lett.* **2011**, *13*, 3750.

(8) (a) Yu, D.-G.; Li, B.-J.; Zheng, S.-F.; Guan, B.-T.; Wang, B.-Q.; Shi, Z.-J. *Angew. Chem. Int. Ed.* **2010**, *49*, 4566. (b) Yu, D.-G.; Shi, Z.-J. *Angew. Chem. Int. Ed.* **2011**, *50*, 7097.

(9) For C-N bond formations, see: (a) Mesganaw, T.; Silberstein, A. L.; Ramgren, S. D.; Nathel, N. F. F.; Hong, X.; Liu, P.; Garg, N. K. *Chem. Sci.* **2011**, *2*, 1766. (b) Llies, L.; Matsubara, T.; Nakamura, E. *Org. Lett.* **2012**, *14*, 5570. For C-H bond formations, see: (c) Álvarez-Bercedo, P.; Martin, R. *J. Am. Chem. Soc.* **2010**, *132*, 17352. (d) Tobisu, M.; Chatani, N. *ChemCatChem* **2011**, *3*, 1410. (e) Tobisu, M.; Yamakawa, K.; Shimasaki, T.; Chatani, N. *Chem. Commun.* **2011**, *47*, 2946. (f) Mesganaw, T.; Nathel, N. F. F.; Garg, N. K. *Org. Lett.* **2012**, *14*, 2918.

(10) Li, Z.; Zhang, S.-L.; Fu, Y.; Guo, Q.-X.; Liu, L. *J. Am. Chem. Soc.* **2009**, *131*, 8815.

(11) Muto, K.; Yamaguchi, J.; Itami, K. *J. Am. Chem. Soc.* **2012**, *134*, 169.

(12) Amaike, K.; Muto, K.; Yamaguchi, J.; Itami, K. *J. Am. Chem. Soc.* **2012**, *134*, 13573.

(13) (a) Correa, A.; Cornella, J.; Martin, R. *Angew. Chem. Int. Ed.* **2013**, *52*, 1878. (b) Meng, L.-K.; Kamada, Y.; Muto, K.; Yamaguchi, J.; Itami, K. *Angew. Chem. Int. Ed.* **2013**, *52*, 10048.

(14) Frisch, M. J.; Trucks, G. W.; Schlegel, H. B.; Scuseria, G. E.; Robb, M. A.; Cheeseman, J. R.; Scalmani, G.; Barone, V.; Mennucci, B.; Petersson, G. A.; Nakatsuji, H.; Caricato, M.; Li, X.; Hratchian, H. P.; Izmaylov, A. F.; Bloino, J.; Zheng, G.; Sonnenberg, J. L.; Hada, M.; Ehara, M.; Toyota, K.; Fukuda, R.; Hasegawa, J.; Ishida, M.; Nakajima, T.; Honda, Y.; Kitao, O.; Nakai, H.; Vreven, T.; Montgomery, J. A., Jr.; Peralta, J. E.; Ogliaro, F.; Bearpark, M.; Heyd, J. J.; Brothers, E.; Kudin, K. N.; Staroverov, V. N.; Kobayashi, R.; Normand, J.; Raghavachari, K.; Rendell, A.; Burant, J. C.; Iyengar, S. S.; Tomasi, J.; Cossi, M.; Rega, N.; Millam, J. M.; Klene, M.; Knox, J. E.;

Cross, J. B.; Bakken, V.; Adamo, C.; Jaramillo, J.; Gomperts, R.; Stratmann, R. E.; Yazyev, O.; Austin, A. J.; Cammi, R.; Pomelli, C.; Ochterski, J. W.; Martin, R. L.; Morokuma, K.; Zakrzewski, V. G.; Voth, G. A.; Salvador, P.; Dannenberg, J. J.; Dapprich, S.; Daniels, A. D.; Farkas, O.; Foresman, J. B.; Ortiz, J. V.; Cioslowski, J.; Fox, D. J.; *Gaussian 09, revision C.01*; Gaussian Inc.: Wallingford, CT, 2010.

(15) (a) Becke, A. D. *J. Chem. Phys.* **1993**, *98*, 5648. (b) Lee, C.; Yang, W.; Parr, R. G. *Phys. Rev. B* **1988**, *37*, 785.

(16) (a) Szentpaly, L. V.; Fuentealba, P.; Preuss, H.; Stoll, H. *Chem. Phys. Lett.* **1982**, *93*, 555. (b) Dolg, M.; Wedig, U.; Stoll, H.; Preuss, H. *J. Chem. Phys.* **1987**, *86*, 866. (c) Schwerdtfeger, P.; Dolg, M.; Schwarz, W. H. E.; Bowmaker, G. A.; Boyd, P. D. W. *J. Chem. Phys.* **1989**, *91*, 1762.

(17) Hehre, W. J.; Radom, L.; Schleyer, P. v. R.; Pople, J. A. *Ab Initio Molecular Orbital Theory*; Wiley: New York, 1986.

(18) (a) Zhao, Y.; Truhlar, D. G. *Theor. Chem. Acc.* **2008**, *120*, 215. (b) Zhao, Y.; Truhlar, D. G. *Acc. Chem. Res.* **2008**, *41*, 157.

(19) Marenich, A. V.; Cramer, C. J.; Truhlar, D. G. *J. Phys. Chem. B* **2009**, *113*, 6378.

(20) (a) Verrier, C.; Martin, T.; Hoarau, C.; Marsais, F. *J. Org. Chem.* **2008**, *73*, 7383. (b) Gorelsky, S. I.; Lapointe, D.; Fagnou, K. *J. Am. Chem. Soc.* **2008**, *130*, 10848. (c) Théveau, L.; Verrier, C.;



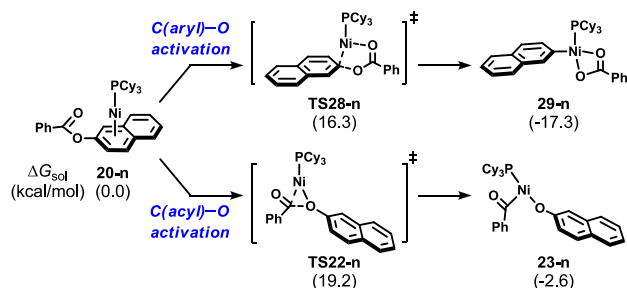
Lassalas, P.; Martin, T.; Dupas, G.; Querolle, O.; Hijfte, L. V.; Marsais, F.; Hoarau, C. *Chem. Eur. J.* **2011**, *17*, 14450.

(21) (a) Ess, D. H.; Houk, K. N. *J. Am. Chem. Soc.* **2007**, *129*, 10646. (b) Legault, C. Y.; Garcia, Y.; Merlic, G. A.; Houk, K. N. *J. Am. Chem. Soc.* **2007**, *129*, 12664. (c) Ess, D. H.; Houk, K. N. *J. Am. Chem. Soc.* **2008**, *130*, 10187.

(22) For a review, see: van Zeist, W.-J.; Bickelhaupt, F. M. *Org. Biomol. Chem.* **2010**, *8*, 3118.

(23) (a) Fernández, I.; Bickelhaupt, F. M. *J. Comput. Chem.* **2012**, *33*, 509. (b) Gordon, C. G.; Mackey, J. L.; Jewett, J. C.; Sletten, E. M.; Houk, K. N.; Bertozzi, C. R. *J. Am. Chem. Soc.* **2012**, *134*, 9199. (c) Liang, Y.; Mackey, J. L.; Lopez, S. A.; Liu, F.; Houk, K. N. *J. Am. Chem. Soc.* **2012**, *134*, 17904. (d) Fernández, I.; Bickelhaupt, F. M.; Cossío, F. P. *Chem. Eur. J.* **2012**, *18*, 12395. (e) Lopez, S. A.; Houk, K. N. *J. Org. Chem.* **2013**, *78*, 1778. (f) Zou, L.; Paton, R. S.; Eschenmoser, A.; Newhouse, T. R.; Baran, P. S.; Houk, K. N. *J. Org. Chem.* **2013**, *78*, 4037. (g) Fernández, I.; Sola, M.; Bickelhaupt, F. M. *Chem. Eur. J.* **2013**, *19*, 7416. (h) Kamber, D. N.; Nazarova, L. A.; Liang, Y.; Lopez, S. A.; Patterson, D. M.; Shih, H.-W.; Houk, K. N.; Prescher, J. A. *J. Am. Chem. Soc.* **2013**, *135*, 13680. (i) Liu, F.; Paton, R. S.; Kim, S.; Liang, Y.; Houk, K. N. *J. Am. Chem. Soc.* **2013**, *135*, 15642. (j) Usharani, D.; Lacy, D. C.; Borovik, A. S.; Shaik, S. *J. Am. Chem. Soc.* **2013**, *135*, 17090. (k) Hong, X.; Liang, Y.; Griffith, A. K.; Lambert, T. H.; Houk, K. N. *Chem. Sci.* **2014**, *5*, DOI: 10.1039/c3sc52882k.

(24) We also calculated the Ni/PCy<sub>3</sub>-catalyzed C-O activation pathways with naphthalen-2-yl benzoate, and the results are shown below. It was found that the C(aryl)-O activation for naphthalen-2-yl benzoate (**TS28-n**: 16.3 kcal/mol) is easier than that for phenyl benzoate (**TS28**: 18.2 kcal/mol, Figure 5). The C(acyl)-O activation barriers for these two benzoates are nearly identical.



(25) Muto, K.; Yamaguchi, J.; Lei, A.; Itami, K. *J. Am. Chem. Soc.* **2013**, *135*, 16384.

(26) (a) Bessac, F.; Alary, F.; Poteau, R.; Heully, J.-L.; Daudey, J.-P. *J. Phys. Chem. A* **2003**, *107*, 9393. (b) Ducéré, J.-M.; Lepetit, C.; Silvi, B.; Chauvin, R. *Organometallics* **2008**, *27*, 5263. (c) Kégl, T.; Ponec, R.; Kollár, L. *J. Phys. Chem. A* **2011**, *115*, 12463. (d) Lovitt, C. F.; Frenking, G.; Girolami, G. S. *Organometallics* **2012**, *31*, 4122.